C24

The Telecommunications and Data Acquisition Progress Report 42-59

July and August 1980

(NASA-CR-163608) THE TELECOMMUNICATIONS AND DATA ACQUISITION REPORT Progress Report, Jul. - Aug. 1980 (Jet Propulsion Lab.) 155 p HC A08/MF A01 CSCL 22A

N80-33427 THRU N80-33446 Unclas G3/12 35006

October 15, 1980

National Aeronautics and Space Administration

Jet Propulsion Laboratory
California Institute of Technology
Pasadena, California

REPRODUCED BY
NATIONAL TECHNICAL INFORMATION SERVICE
U.S. DEPARTMENT OF COMMERCE
SPRINGFIELD, VA. 22161

155

The Telecommunications and Data Acquisition Progress Report 42-59

July and August 1980

October 15, 1980

National Aeronautics and
Space Administration

Jet Propulsion Laboratory
California Institute of Technology
Pasadena, California

The research described in this publication was carried out by the Jet Propulsion Laboratory, California Institute of Technology, under NASA Contract No. NAS7-100.

Preface

This publication was formerly entitled *The Deep Space Network Progress Report*. Although the practice of reporting progress in the development and operations of the Deep Space Network continues, the report is expanded with this issue to include developments in Earth-based radio technology as applied to other research programs. These programs are:

(1) Geodynamics: For several years, the laboratory has been developing radio interferometry at microwave frequencies for application to geodetic measurements. This branch of telecommunications technology is now being applied to the study of geodynamics.

(2) Astrophysics: The deep space stations, individually and in pairs as an interferometer, have been used by radio astronomers for astrophysics research by direct observations of radio sources.

(3) An activity closely related to radio astronomy's use of the deep space stations is NASA's continuing program of radio search for extraterrestrial intelligence in the microwave region of the electromagnetic spectrum.

Each succeeding issue of this report will present material in some, but not all, of the following categories:

Radio Astronomy
Search for Extraterrestrial Intelligence
Radio Interferometry at Microwave Frequencies

- Geodetic Techniques Development
- Spacecraft Navigation
- Orbiting Very Long Baseline Interferometry

Deep Space Network

- Description
- Program Planning
- Planetary and Interplanetary Mission Support
- Advanced Systems
- Network and Facility Engineering and Implementation
- Operations
- Spacecraft Radio Science
- Planetary Radar
- Energy

In each issue, there will be a report on the current configuration of one of the seven DSN systems (Tracking, Telemetry, Command, Monitor and Control, Test Support, Radio Science, and Very Long Baseline Interferometry).

The work described in this report series is either performed or managed by the Telecommunications and Data Acquisition organization of JPL.

Contents

RADIO ASTRONOMY

The Table Mountain 8-mm-Wavelength Interferometer 1
M. A. Janssen, S. Gulkis, E. T. Olsen, B. L. Gary,
F.S.Soltis, and N. I. Yamane
NASA Code 196-41-73-01

Pattern Measurements of a Low-Sidelobe Horn Antenna 8
M. A. Janssen, S. Gulkis, S. M. Bednarczyk,
H. W. Marlin, and G. F. Smoot
NASA Code 685-20-04-02

SEARCH FOR EXTRATERRESTRIAL INTELLIGENCE

INSTRUMENT SYSTEMS DEVELOPMENT

The SETI Instrument Development Plan 15
B.Crow
NASA Code 199-50-52-01

OBSERVATORY OPERATIONS

A. Bimodal Search Strategy for SETI 23
S.Gulkis, E. T. Olsen, and J. Tarter
NASA Code 192-55-63-65

RADIO INTERFEROMETRY AT MICROWAVE FREQUENCIES

GEODETIC TECHNIQUES DEVELOPMENT

ORION

ORION S-Band Data Acquisition for S-X Calibration 33
S.C.Wu
NASA Code 692-40-20-01

THE DEEP SPACE NETWORK

DESCRIPTION OF THE DSN

Network Functions and Facilities 37
N.A.Renzetti

DSN Ground Communications Facility 40
R.H. Evans
NASA Code 311-06-40-00

The DSN Programming System 51
A.P.Irvine
NASA Code 311-03-41-15

Preceding page blank

PROGRAM PLANNING

Planning a DSN Support Section Technical Library 55
T. Bailey and C. C. Chatburn
NASA Code 311-03-32-10

PLANETARY AND INTERPLANETARY MISSION SUPPORT

Interplanetary Flight Projects

International Solar Polar Mission 62
R.B.Miller
NASA Code 311-03-22-80

ADVANCED SYSTEMS

Tracking and Ground-Based Navigation

A Study of the Processes in the RF Hydrogen Gas Dissociator 68
L. Maleki
NASA Code 310-10-62-15

Experimental Optical Fiber Communications Link 77
G.F.Lutes
NASA Code 310-10-62-18

Network Data Processing and Productivity

Open-Loop Radio Science With a Suppressed-Carrier Signal 86
C.A.Greenhall
NASA Code 310-40-73-19

NETWORK AND FACILITY ENGINEERING AND IMPLEMENTATION

Network

Noise Adding Radiometer Performance Analysis 98
C.Stelzried
NASA Code 311-03-41-05

OPERATIONS

Network Operations

Networks Consolidation Program 107
M. L. Yeater, D. T. Herrman, and G. E. Sanner
NASA Code 311-03-31-10

DSN System Performance Test Software 121
F.B.Leppla
NASA Code 311-03-13-24

TRISCAN: A Method of Precision Antenna Positioning 126
R.C.Bunce
NASA Code 311-03-14-20

Deep Space Stations

Alternative to Surge Chambers for Goldstone Water Supply Distribution 134
J.L. Koh
NASA Code 311-03-14-01

PLANETARY RADAR

Planetary Radar 142
R.M. Taylor
NASA Code 310-30-70-50

ENERGY

Deep Space Network Energy Program 145
S.E.Friesema
NASA Code 311-03-31-30

SETI Bibliography 148

The Table Mountain 8-mm-Wavelength Interferometer

M. A. Janssen, S. Gulkis, and E. T. Olsen
Planetary Atmosphere Section

B. L. Gary, F. S. Soltis, and N. I. Yamane
Microwave Observational Systems Section

A two-element radio interferometer operating at 8.33-mm wavelength has been developed at the Jet Propulsion Laboratory's Table Mountain Observatory near Wrightwood, CA. The interferometer employs a 5.5-m and a 3-m-diameter antenna on an east-west baseline of 60 or 120 m, yielding fringe spacings at transit of 28″ or 14″, respectively. The broad intermediate-frequency bandpass of 100-350 MHz and the system noise temperature of 500 K provide high sensitivity for the measurement of continuum sources. The interferometer has been used for high-resolution studies of the planets and the Sun, and it is currently being adapted to study solar flare emissions at high spatial and time resolution.

I. Introduction

We describe a millimeter-wavelength interferometer which has been developed at the Jet Propulsion Laboratory's Table Mountain Observatory, located in the San Gabriel Mountain range near Wrightwood, CA. The interferometer was designed for the observation of continuum sources at the fixed frequency of 36 GHz (8.33-mm wavelength), with the primary goal of performing high-resolution studies of solar system objects. For example the two available baselines permit disk-resolved observation of Venus, Jupiter, and Saturn. The receivers employ the lowest noise uncooled mixers currently available and a broad intermediate-frequency bandwidth to achieve maximum sensitivity.

The interferometer became operational in May 1974, and has been used for the measurement of the 8-mm brightness temperature of Saturn's rings (Ref. 1), limb darkening studies of the atmospheric emission from Venus and Jupiter, and a high-resolution study of the chromospheric emission from the quiet Sun (Ref. 2). Current and future observational projects include an investigation of the thermophysical properties of Mercury's surface and a program to obtain data on millimetric solar flare emissions.

II. Description

A. General

The principal elements of the interferometer are a 5.5-m and a 3-m-diameter antenna. The 3-m antenna is movable to one of two fixed stations located 60 and 120 m to the west of the larger antenna. These stations provide east-west baselines of 7,000 and 14,000 wavelengths and yield resolutions (fringe spacings) of 28″ and 14″, respectively, at source transit. To date the 3-m antenna has only been used at the 60-m station.

The altitude is 2290 m above mean sea level, placing the interferometer above the major portion of the atmosphere's water vapor.

A schematic of the interferometer is given in Fig. 1. One linear polarization of the source continuum is received in the neighborhood of the 36-GHz local oscillator (LO) frequency. This is downconverted by double-sideband superheterodyne receivers into the intermediate-frequency (IF) passband of 100-350 MHz. After amplification the IF signals are brought together through underground cabling and correlated to produce the output signal. This signal depends upon the spatial brightness structure of the source and its geometric relationship to the baseline (cf. Ref. 3).

Coherence at the correlator inputs requires (1) coherence of the LO signals in each receiver and (2) equal delay in each signal path between the source and the correlator. Coherent LO signals at 36 GHz are passively generated in each receiver from a single 12-GHz signal provided by a centrally located oscillator. This scheme eliminates the need for independent local oscillators and active phase-lock loops. The relative signal delay depends upon the source-baseline geometry, which varies with the earth's rotation, and is equalized by a computer-controlled delay compensation network.

The correlator performs an analog multiplication of the instantaneous voltages appearing at its two input ports. Provided the two local oscillators are perfectly coherent, a source in the antenna beams produces a sinusoidal signal with a frequency varying from zero to approximately 1 Hz. This frequency is due to the motion of the source through the interferometer fringe pattern, which is determined by the source-baseline geometry. To simplify data processing, a constant correlator output signal frequency of 0.5 Hz is maintained by introducing a small frequency offset into one local oscillator signal.

B. Antennas

The 5.5-m antenna consists of an equatorially mounted parabolic reflector with a Cassegrain feed system and was originally operated as a single antenna telescope (Ref. 4). The 3-m antenna was installed specifically to provide an interferometer in conjunction with the first antenna. It consists of a surplus spun-aluminum reflector which was resurfaced for millimeter work and employs a prime focus feed. An altitude/azimuth mount was obtained by modification of a surplus Nike missile radar tracking mount and includes a transport trailer which allows the antenna to be readily moved. The aperture efficiency of each antenna is approximately 50 percent at 8 mm. The main beam of the interferometer (the product of the individual antenna voltage patterns) has a half-power beamwidth of 8′.

C. The LO System

A centrally located oscillator supplies 12-GHz signals to the receivers through waveguide transmission lines. These signals are tripled in the receivers to provide coherent 36-GHz signals to the mixers. The central oscillator consists of a Gunn diode phase-locked to a crystal standard to provide a 12-GHz output accurate to one part in 10^7. This signal is amplified by a Varian traveling wave tube to a level of approximately 1 W, divided, and transmitted underground through a flexible elliptical waveguide to each antenna site. At each antenna the signal is routed up to the receiver through a thermally insulated waveguide with rotary couplings at the antenna axes. The triplers provide in excess of 10 mW of power at 36 GHz to the mixers. A controlled frequency offset, variable within the range ±1 Hz, is introduced into one of the 12-GHz lines by means of a mechanical phase shifter following the power divider. The rotation of the phase shifter is computer-controlled so that the signal output frequency is precisely maintained at 0.5 Hz.

The relative phase of the 36-GHz signals appearing at the mixers changes due to variations in the effective electrical lengths of the transmission lines following the 12-GHz power division. No effort has been made to control the electrical length difference other than underground burial of the transmission lines and thermal insulation of the antennas where the signals are transported up to the receivers. The relative phase of the LO signals at the mixers is thus subject to slow variations related to ambient conditions. Extensive astronomical observations show that this instrumental phase drift rarely exceeds 20°/h.

D. Receivers

The receivers employ uncooled balanced mixers with Schottky-barrier diodes manufactured by Spacekom, Inc. The system noise temperature of each receiver is approximately 500 K (double sideband) with a rectangular 100-350 MHz IF bandpass flat to within ±0.5 dB. The resulting sensitivity in the measurement of flux density from a point source is better than 0.1 Jy/h. The current mixers were installed in August 1977, prior to which date the receiver characteristics were slightly different (Janssen and Olsen (Ref. 1)). Both antennas receive one linear polarization, with the polarization vector at zero position angle. The feed horn and receiver assembly of the 3-m antenna (which is azimuthally mounted) is rotated to track this polarization.

E. Delay Compensation Network

A gain-balanced network of delay segments is interposed in one IF path to equalize the relative signal delay as a source is tracked across the sky. The delay network consists of 10 cable

pairs and associated high-frequency switches. Each cable pair consists of a fixed length of low-loss coaxial cable and a shorter length of high-loss cable of matched attenuation. One member of each pair is switched into the 3-m antenna signal path as required. The differential delays in each pair form a binary sequence which allows a net delay in the range 0-512 ns to be selected with a resolution of 0.5 ns.

The differential delay of each pair was initially calibrated to an accuracy of ±0.03 ns. These errors were subsequently refined astronomically as described in a following section. With these calibrations we estimate that the net error in a given delay setting is typically about 0.06 ns, with a worst case error of 0.20 ns. These errors lead to signal amplitude losses due to decorrelation of 0.4 and 3 percent, respectively. The finite resolution of the delay network further leads to an average signal loss of less than 1 percent. Residual differences in the attenuations of each cable pair are about 1 percent and are calibrated to reduce the average error from this source to less than 0.5 percent.

F. Gain Calibration

A gas-discharge noise source is weakly coupled to the RF input of each receiver through a directional coupler. When switched on manually each noise source adds approximately 40 K to the total noise power of its associated IF channel. The gains of the IF-mixer networks exhibit slow drifts, of about 1 percent/h, and the noise sources provide a means of monitoring this gain drift. The net gain of the correlated output also depends upon parameters of the correlator itself, but gain variations caused by this component are not significant.

G. Computer Control and Signal Processing

Routine functions of the interferometer are automatically controlled by an Interdata Model 4A computer. These functions include antenna tracking, delay setting, phase shifter rotation, and orientation of the 3-m antenna polarization as well as the processing and analysis of the output signal. The basic cycle of the computer control program is 2 s, during which time the position of the source is recomputed, the interferometer control parameters are monitored and updated, and one complete 0.5-Hz signal cycle (fringe) is obtained. Absolute time-sequencing is provided by a crystal-controlled clock synchronized with the universal time broadcast by the National Bureau of Standards (WWV). The source position along with terms describing its relative motion during the course of the observation are obtained from externally provided ephemerides, and they are entered into the control program at the start of the observation.

The correlator output is integrated and digitized in contiguous 100-ms intervals, and in each 2-s program cycle a complete 20-point sample of the fringe is obtained and stored in the computer. Successive samples are stacked for a preselected number of cycles n, after which the accumulated fringe is analyzed to obtain one complete integration of $2n$-s duration. The fringe amplitude and phase are determined by least squares fit. The residuals of this fit are used to estimate directly the uncertainty of the result, and a record is thereby obtained of the instrumental noise in each individual integration.

III. Performance and Calibration

A. Baseline and Delay Calibration

The extragalactic source 3C273 was observed in May 1974, to obtain an initial determination of the baseline. The two orthogonal components of the baseline which lie in the earth's equatorial plane were subsequently determined by minimizing the diurnal phase drifts in the observation of several sources of known position. Uncertainties of 0.5 wavelengths are estimated for these components. The uncertainties are primarily due to the slow drift in the unregulated instrumental phase. The polar baseline component was determined to ±5 wavelengths by surveying, and this accuracy was verified astronomically by the measurement of delay decorrelation (see below) for sources widely spaced in declination. An effort is currently underway to reduce the uncertainty in this component by the more sensitive technique of astronomical phase measurements, a task which is considerably more difficult at millimeter than at centimeter wavelengths because of the relative scarcity of suitable point sources.

The broad IF bandwidth gives a correspondingly narrow correlation function in the net signal delay at the correlator inputs. Complete signal decorrelation occurs if the absolute delay difference is approximately 1.3 ns. The initial calibration of the delay compensation network was astronomically checked and improved. In principle the shape of the correlation function may be measured, and its center thus determined by adjusting a fixed delay offset in the tracking program while observing a source. In practice we used a technique in which a source was tracked across the sky at the alternate half-power points of the correlation function, where small delay errors produce maximum fluctuations in signal amplitude. Correlation of these fluctuations with the binary delay network setting permits the individual delay element errors to be determined, as well as allowing an upper limit to be placed on the "worst case" setting in which all of the errors are additive. Further, from measurements of several sources one may determine the variation of the correlation function center with declination, from which the polar baseline

component may be estimated. Using this technique we have obtained the above-quoted errors, which are valid for sources within ±30° of the ecliptic.

B. Phase and Amplitude Stability

There are several sources of error in the measurement of the signal phase. System noise causes a random phase error which approaches σ/a rad in the strong signal limit, where a and σ are the amplitude and amplitude uncertainty of a particular measurement. The instrumental phase is generally unknown, and its slow but unpredictable drift contributes to the long-term phase error. Control errors in the phase shifter may result in an instantaneous phase error of up to 2°. Finally, fluctuations in the atmospheric paths of the signals received at each antenna produce a spectrum of phase errors which tends to decorrelate the signal during individual integrations and may scatter phase measurements with a wide range of time scales.

System performance under varying conditions is illustrated by the measurements of Venus shown in Figs. 2 and 3. Near inferior conjunction Venus is one of the strongest millimeter-wavelength sources in the sky, although it is an extended source and is then "resolved" by the interferometer. Generally speaking, a two-element interferometer measures only a single Fourier component of the brightness distribution, the particular component measured depending upon the geometric relationship of the source to the baseline at the instant of observation. The signal produced by an extended source is thus always less than would be obtained if the object were a point source with the same total flux. The ratio, as it depends upon baseline projection, is known as the visibility function (or more correctly, the normalized visibility function). As a rule, the larger the baseline as projected onto the plane of the sky in the direction of the source, the more highly resolved is the source; i.e., the less the "visibility."

The data shown were obtained on two different days near the time of the 1975 inferior conjunction and consist of the signal amplitude and phase obtained in 1-min integrations. Venus rose off the end of the baseline and became progressively more resolved with increasing hour angle in the figures. The solid curves show the theoretical visibility functions and phases computed for a uniformly bright disk at the locations and with the semidiameters given for Venus in the American Ephemeris and Nautical Almanac on the dates of observation.

The amplitudes have been corrected for atmospheric attenuation, which has been taken from a theoretical model to be a constant 3 percent at the zenith, and to scale as the secant of the zenith angle. About two-thirds of this attenuation is due to atmospheric oxygen and is effectively constant, with water vapor accounting for the remainder. The variability of water vapor under typical observing conditions is expected to lead tc errors less than 1.5 percent in amplitude measurement. The phase data have been corrected to remove a small sinusoidal phase drift of 24-h period to allow for residual baseline errors and the diurnal component of the instrumental phase drift.

The amplitude scale of the data shown in Fig. 2 has been adjusted to give a least-squares fit to the calculated visibility function. These data were obtained under normal observing conditions when the weather was clear and stable. The amplitude scatter is small and uniform as the signal amplitude varies and is consistent with that expected due to receiver noise. Where the signal is small the phase scatter is generally consistent with the noise-to-signal ratio σ/a, with the phase becoming random at about the time the signal disappears. For signals of relative amplitude (visibility) greater than about 0.15, however, the rms phase scatter approaches a lower limit of about 3°, which reflects the combined effects of instrumental and atmospherically induced phase noise. This demonstrates that the instrumental performance is within expected bounds and that the atmosphere's influence under "good" weather conditions is minimal.

Because the real part of the index of refraction of air is very nearly constant with frequency throughout the microwave region, the atmospherically induced phase fluctuations for a given baseline will increase linearly with the observing frequency. One may therefore anticipate that atmospheric conditions are of greater concern at millimeter wavelengths than in the centimeter range. The data shown in Fig. 3 were obtained under poor observing conditions, with thick cumulus clouds over the interferometer. The observing parameters were substantially the same in both observations, and the curve shows the expected amplitude of the signal based on the calibration of the data of Fig. 2. The amplitude scatter is seen to depend on amplitude and indicates signal losses approaching 50 percent for individual 1-min integrations. We attribute this loss to large short-term phase fluctuations due to atmospheric inhomogeneities which decorrelate the signal on time scales less than 1 min. The phase scatter among the 1-min integrations, even where the signal is large, shows fluctuations up to 60°, and indicates that substantial atmospheric effects are present on time scales on the order of 1 min. These data illustrate the particular importance of weather conditions on interferometric observations at millimeter wavelengths.

C. Future Modifications

The interferometer is currently undergoing modification to accommodate a program of solar flare observations. The principal change will be the conversion of the receiver polarization from a single linear mode to dual circular modes in which either left- or right-circular polarizations may be selected. Rapid switching will permit alternate polarizations to be received in contiguous integrations as short as 2 s.

Acknowledgments

We gratefully acknowledge the participation of Glenn Berge in the initial planning stages of the interferometer and the technical assistance of Richard Wetzel in its construction. The Table Mountain interferometer was constructed and is operated under Contract NAS 7-100, sponsored by the National Aeronautics and Space Administration.

References

1. M. A. Janssen and E. T. Olsen, "A measurement of the brightness temperature of Saturn's rings at 8-mm wavelength," *Icarus*, vol. 33, pp. 263-278, Feb. 1978.
2. M. A. Janssen, E. T. Olsen, and K. R. Lang, "Interferometric observations of the quiet Sun at 8-mm wavelength," *Astrophys. J.*, vol. 228, pp. 616-628, March 1979.
3. W. N. Christiansen and J. N. Hogbom, *Radiotelescopes*. Cambridge: Cambridge University Press, 1969.
4. J. R. Cogdell, J. J. G. McCue, P. D. Kalachev, A. E. Salomonovich, I. G. Moiseev, J. J. Stacey, E. E. Epstein, E. E. Altshuler, G. Feix, J. W. B. Day, H. Hvatum, W. J. Welch, and F. T. Barath, "High resolution millimeter reflector antennas," *IEEE Trans. Antennas and Propagat.*, vol. AP-18, pp. 515-529, July 1970.

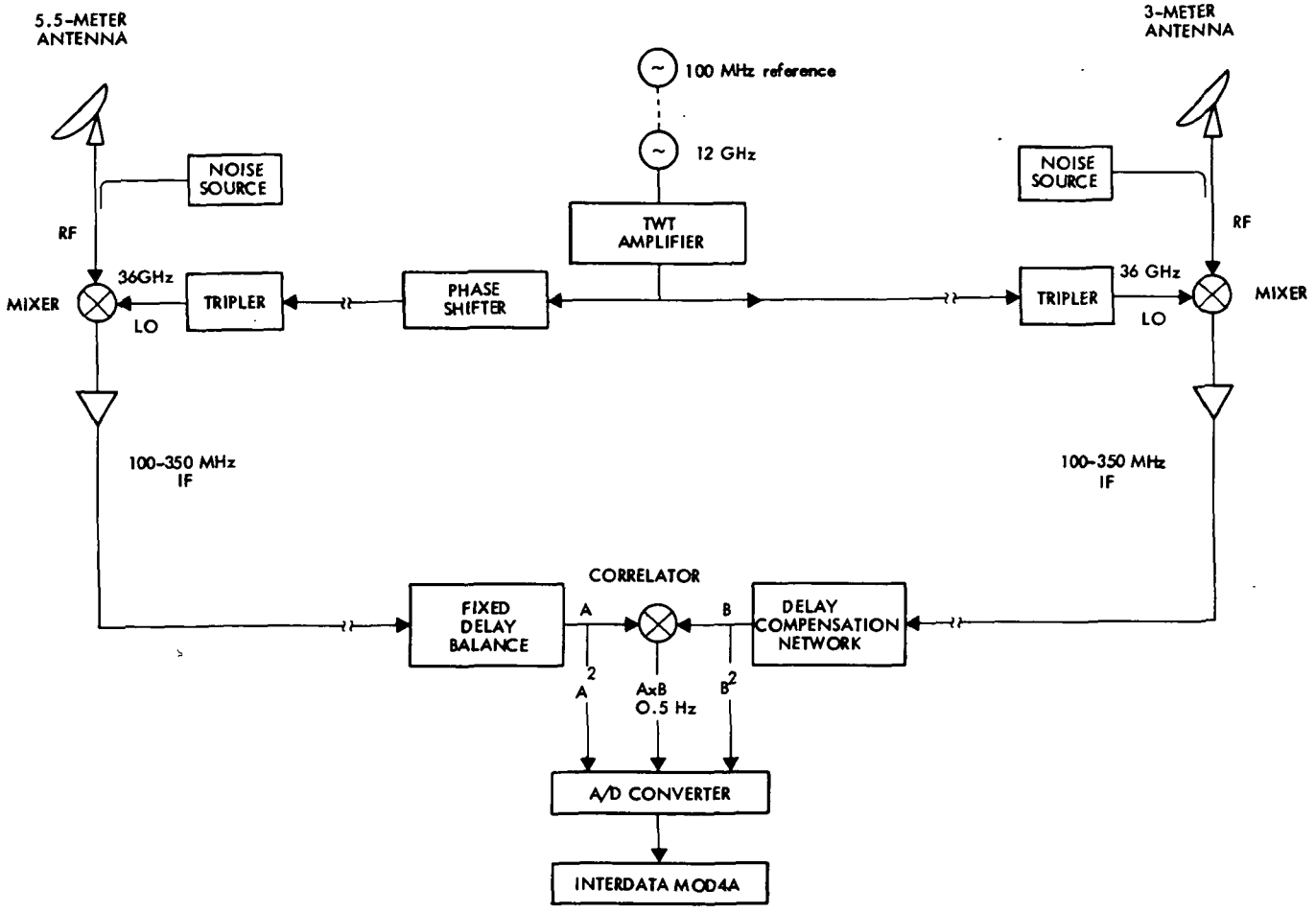

Fig. 1. Schematic diagram of the Table Mountain 8-mm interferometer system

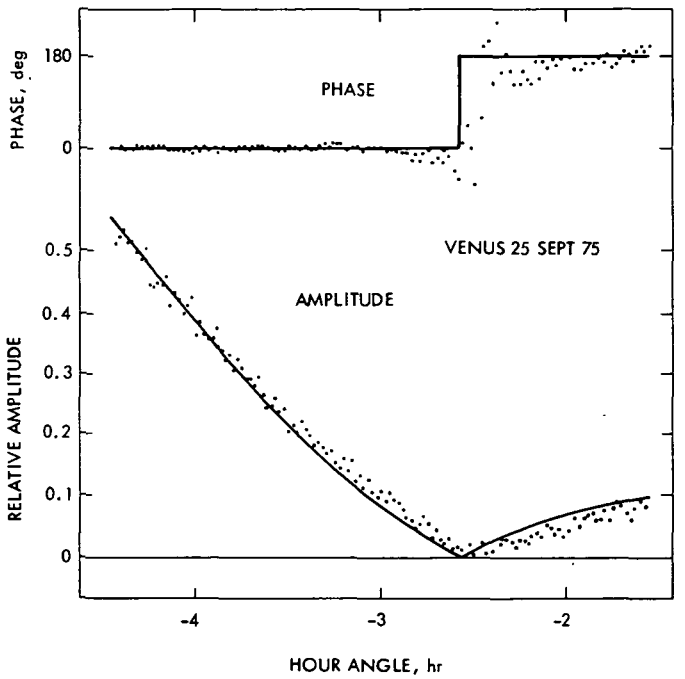

Fig. 2. Data from Venus observations September 25, 1975. Points show phase and amplitude obtained in contiguous 1-min integrations. Venus becomes progressively resolved during the course of the observations, with an amplitude null and 180° phase change near −2.5 h. Curves indicate the behavior expected according to a simple theoretical model; the systematic departure of the data from the amplitude curve is consistent with the expected amount of limb darkening on Venus

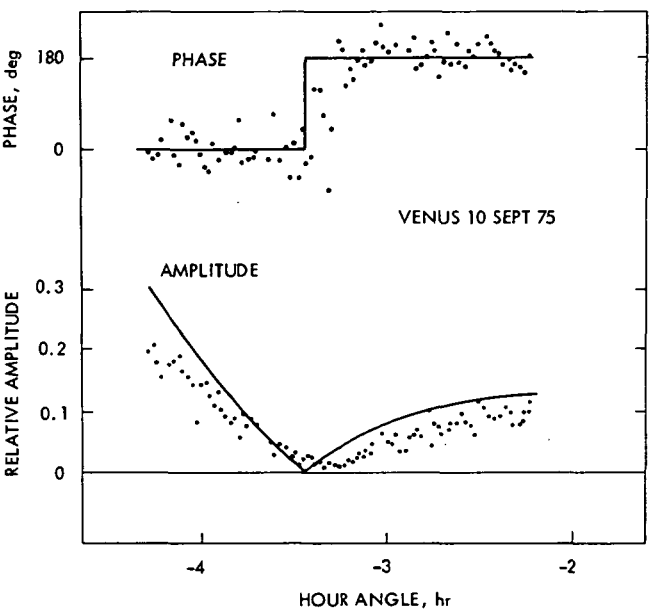

Fig. 3. Data from Venus observations September 10, 1975 which show the extreme effects produced by the atmosphere under poor weather conditions. The observing parameters were substantially the same as for the data of Fig. 2. The data show loss of signal amplitude as well as excessive scatter

N80-33429

Pattern Measurements of a Low-Sidelobe Horn Antenna

M. A. Janssen and S. Gulkis
Planetary Atmospheres Section

S. M. Bednarczyk
Microwave Observational Systems Section

H. W. Marlin
Spacecraft Telecommunications Equipment Section

G. F. Smoot
University of California, Berkeley

The power pattern of a corrugated horn antenna designed for low sidelobes was measured to levels 90 dB below the main beam maximum in both the E- and H-planes. The measured patterns were found to be in good agreement with theoretical predictions.

I. Introduction

Requirements for antennas with high off-axis rejection are rapidly growing, and the study of such antennas is topical in current antenna technology. Applications requiring antennas with low-level sidelobes exist in earth-based and satellite communications, in radar systems, and in radio astronomy. The work reported here was motivated by a requirement for an antenna with very low sidelobes to measure properties of the cosmic microwave background radiation from a satellite (Ref. 1). The particular application calls for horn antennas of approximately 7-deg beamwidth, operating at discrete frequencies in the range 20 to 90 GHz, which have far-sidelobe levels lower than 85 dB below the main beam peak to adequately reject stray radiation from the earth. While antennas that meet this requirement have been designed, the sidelobe levels have not (to our knowledge) been measured to levels lower than 75 dB below the main peak (Refs. 2 through 4). As our requirements exceed the capabilities of current state-of-the-art pattern measurement techniques, we undertook the task of extending these capabilities to meet our objectives.

We report the techniques and results of our antenna measurements here. The present work demonstrates that the sidelobes of horn antennas can be measured to significantly lower levels than has been achieved previously. The results should be of interest in both the measurement and further design of low-sidelobe antennas for other areas of application.

II. The Horn Antenna

A corrugated conical horn of the scalar feed horn antenna type was employed for the measurements. The horn, shown in Fig. 1, possesses a beamwidth of approximately 7 deg. It has been previously employed in an airborne experiment to measure the anistropy of the cosmic background radiation

(Ref. 5). The design is based on pioneering studies by Kay (Ref. 6) and Potter (Ref. 7) of low-sidelobe antennas. Several authors, most notably Clarricoats and Saha (Ref. 8), have investigated the theoretical properties of this type of antenna. The significant features of this horn are its broad bandwidth, the 10-deg flare angle, and moderate groove spacing (two grooves/wavelength), which permit compact and easy construction. The design frequency of the horn is 33 GHz, although the pattern was not predicted to be significantly different at the present test frequency of 31.4 GHz. A transition section is employed to match the circular input port of the horn with rectangular waveguide.

III. The Measurement Technique

The strategy for the measurements was to use a conventional pattern measurement technique, while taking special precautions to eliminate the main sources of extraneous signals that could confuse the far-sidelobe measurements. The chief sources of background signal were anticipated to be radiation scattered into the main beam or near sidelobes from nearby objects, and radio frequency (RF) leakage into the receiver behind the horn due to imperfect connectors and junctions. Particular care was taken to obtain a clean and uncluttered test geometry, while the RF portion of the receiver was made extremely compact and easy to shield.

The measurement geometry illustrated in Fig. 2 was achieved by mounting a receiver with the test horn and transmitter on towers, illuminating the test horn on a horizontal path. The transmitter-receiver plane was thus removed 6 m from the ground to isolate the test system from nearby sources of reflection. The receiver tower was located at the edge of a mesa, the terrain beyond falling off sharply. The transmitter employed an identical low-sidelobe horn to further reduce potential reflection paths. The test horn was rotated in a horizontal plane by rotating the receiver tower on an azimuth bearing located near ground level. The axis of azimuth rotation passed through the point where the horn axis intersects its aperture, so that the incident signal was uniformly sampled as the azimuth was rotated to measure the sidelobes. The mount holding the receiver and test horn also rotated around the test horn axis, allowing the test horn polarization to be set at any chosen angle. The close spacing between transmitter and test horn (4 m) gave a sufficiently uniform illumination of the test horn while allowing for maximum signal strength.

Fig. 3 gives a schematic of the test circuit. A fixed-frequency Gunn oscillator supplied a continuous wave (CW) signal at the test frequency. A calibrated attenuator in the transmitter circuit allowed the transmitter power to be varied from its maximum of 10 mW through a range of 50 dB. A series 1750 receiving system manufactured by Scientific-Atlanta Corporation was employed and consists in essence of a narrow-band receiver that is phase-locked to the transmitter signal. The local oscillator employs a relatively low frequency signal (~2.6 GHz), the 12th harmonic of which is locked to the transmitter frequency. The advantage of this system is that the RF portion of the receiver is limited to the harmonic mixer and is very compact. For the measurements, the mixer was well wrapped with microwave-absorbing material in a small cylindrical volume behind the test horn. The received signal power was recorded on one axis of a two-axis plotter, the second axis of which was synchronized with the horn rotation angle.

IV. The Horn Pattern

After a series of measurements to guarantee proper alignment of the test system and receiver linearity, the pattern of the test horn was measured in both the *H*- and *E*-planes. The results are shown in Figs. 4 and 5, respectively. Receiver linearity was checked by obtaining a series of *H*-plane patterns with the transmitter reduced in 10-dB increments through a range of 50 dB, making use of the calibrated attenuator. The measured main beam maximum was found to decrease in corresponding 10-dB increments to within ±1 dB in all cases. The measured patterns themselves were identical to within ±2 dB down to approximately the 85-dB level shown in Fig. 4, where system noise becomes significant. Hence, the system linearity was demonstrated to be at least ±2 dB over the full range 0 to 85 dB.

Receiver noise dominates the measurements below 90 dB. In the linearity measurements the noise level seen at angles beyond 100 deg in Fig. 4 was unchanged, while the patterns decreased in amplitude by up to 50 dB. If this noise were due in part to signal leakage, reflections, or receiver horn sidelobes, a relative decrease in this noise level would have been observed. As a further check, the receiver was wrapped with an additional layer of microwave-absorbing material, and the *H*-plane pattern was remeasured with no significant change observed. We conclude that the pattern measurements were limited by receiver noise alone.

The dashed curves in Figs. 4 and 5 show a theoretical calculation of the test horn pattern based on a computer program developed by Potter (Ref. 2). Although there are small deviations between the calculated and measured patterns, the overall agreement is excellent. The observed differences may be due to machining tolerances in the actual horn or to neglected contributions in the computations of the theoretical patterns.

IV. Conclusion

It is demonstrated that horn antenna patterns are measurable to levels less than 90 dB below the central peak with conventional range techniques. Further, existing theory for the performance of corrugated scalar feeds appears to give excellent predictions at these low-sidelobe levels. We believe that several factors contribute to the measurement success. First, the use of a relatively high frequency (31.4 GHz) maximizes the wavelength distances of unavoidable scattering objects in a given test environment, such as the ground and nearby buildings. In the present measurement, the receiver was located at the edge of a steep mesa so that the main power lobe of the transmitting antenna essentially disappeared into free space, with no chance for multipath reflections into the receiver for the vast bulk of the radiated signal. The power in such reflections was further reduced by using a low-sidelobe horn for the transmitter, identical to that measured in the experiment. Finally, the receiver RF path was maintained at a minimum by employing a well-shielded harmonic mixer immediately adjacent to the test horn output port.

The level of sensitivity reached in these measurements was limited by receiver noise, with no evidence to indicate the presence of extraneous signals. The test apparatus used had a fixed short time constant for signal integration, which limited the receiver sensitivity. A straightforward improvement could be achieved by allowing for longer signal integrations and incorporating a switched-reference measurement scheme to enable the accurate determination of very low signal levels.

Acknowledgments

We gratefully acknowledge the advice and assistance of Dan A. Bathker and Gerald S. Levy of the Jet Propulsion Laboratory. The pattern measurements were carried out at the Mesa Antenna Test Range Facility of the Jet Propulsion Laboratory.

References

1. J. C. Mather, "COBE-Explorer of the Primeval Explosion," *Astronaut. Aeronaut.*, pp. 60-66, Oct. 1978.

2. A. Ludwig, J. Hardy, and R. Norman, *Gain Calibration of a Horn Antenna Using Pattern Integration*. Technical Report 32-1572, Oct. 1972. Jet Propulsion Laboratory, Pasadena, California.

3. P. D. Potter, *A New Computer Program for the Design and Analysis of High Performance Conical Feed Horns*. Technical Report 32-1526, Vol. XIII, pp. 92-107, Feb. 1973. Jet Propulsion Laboratory, Pasadena, California.

4. H. P. Coleman, R. M. Brown, and B. D. Wright, "Paraboloidal Reflector Offset With a Corrugated Conical Horn," *IEEE Trans. Antennas Propagat.*, pp. 817-819, Nov. 1975.

5. G. F. Smoot, M. V. Gorenstein, and R. A. Muller, "Detection of Anisotropy in the Cosmic Blackbody Radiation," *Phys. Rev. Lett.*, Vol. 39, pp. 898-901, Oct. 1977.

6. A. F. Kay, *A Wide Flare Horn – A Novel Feed for Low Noise Broadband and High Aperture Efficiency Antennas*. Report 62-757. U.S. Air Force Cambridge Research Laboratory, Oct. 1962.

7. P. D. Potter, "A New Horn Antenna With Suppressed Sidelobes and Equal Beamwidths," *Microwave J.*, Vol. VI, No. 6, pp. 71-78, June 1963.

8. P. J. B. Clarricoats and P. K. Saha, "Propagation and Radiation Behavior of Corrugated Feeds: Part II – Corrugated-conical Horn Feed," *Proc. Inst. Elec. Eng.*, Vol. 118, pp. 1177-1186, Sept. 1971.

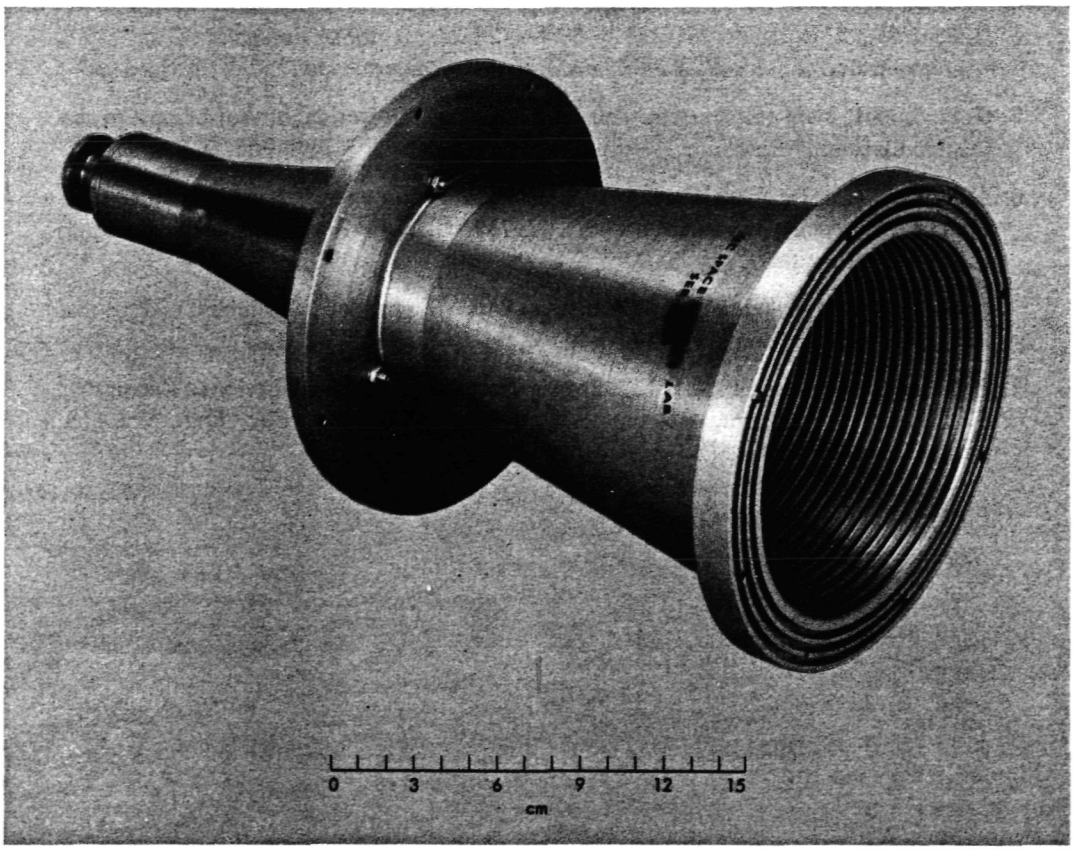

Fig. 1. Test horn—corrugated, conical scalar feed horn antenna. Flare angle is 10 deg, and groove spacing is approximately 0.5 wavelengths. Choke grooves on rim face are to suppress potential backlobe radiation.

ORIGINAL PAGE IS
OF POOR QUALITY

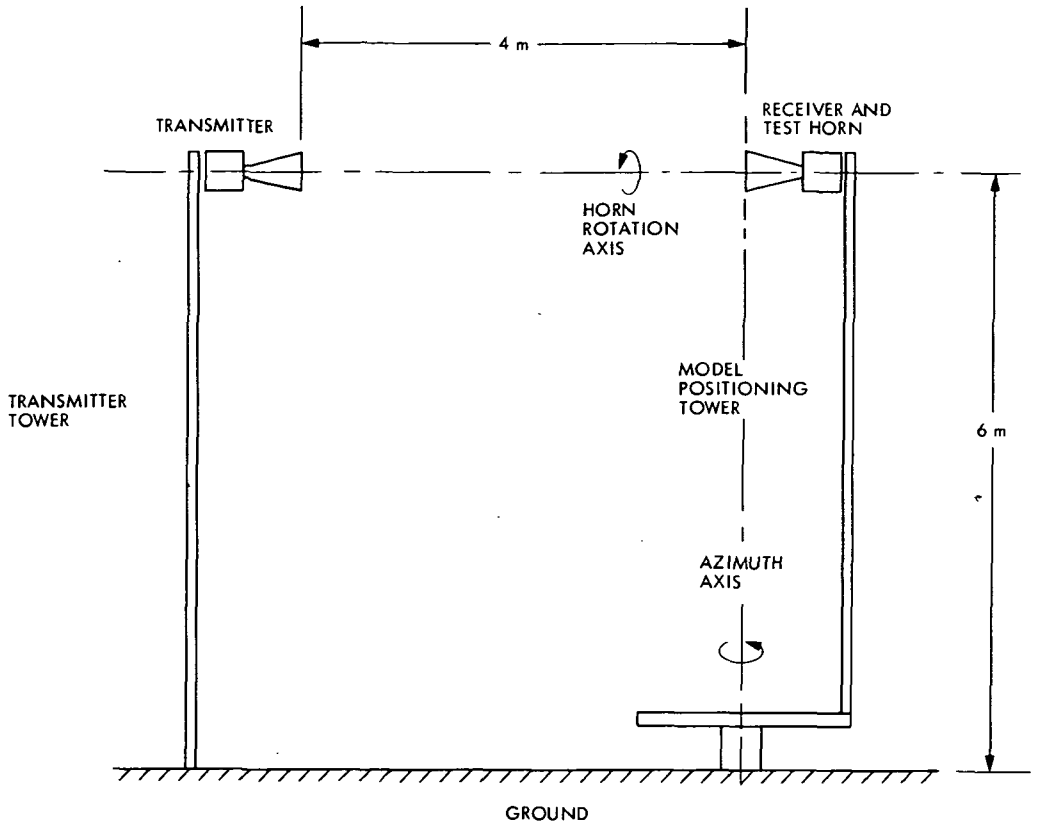

Fig. 2. Schematic of pattern measurement geometry

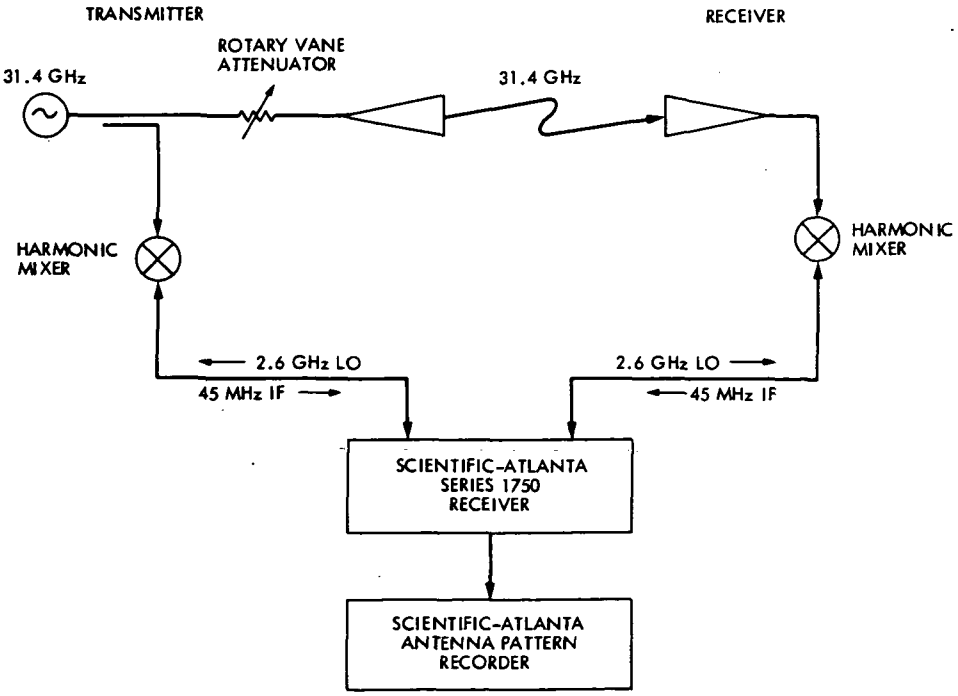

Fig. 3. Test circuit schematic

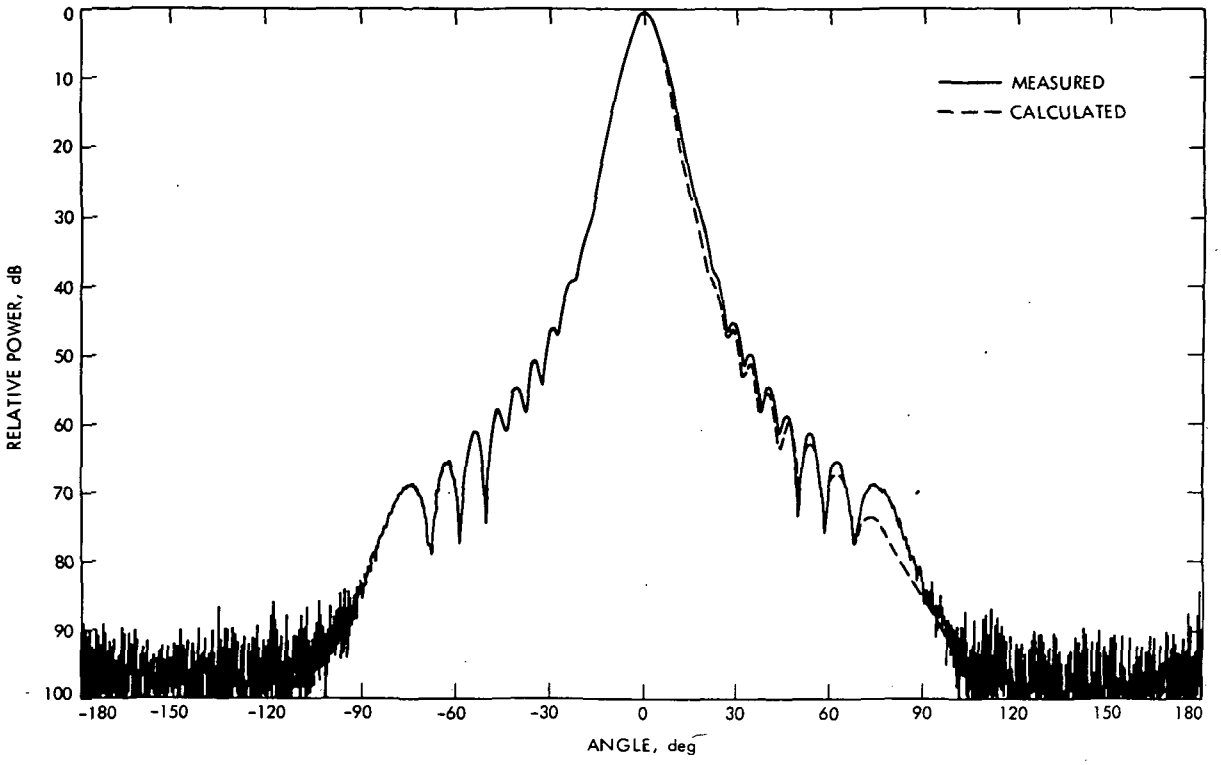

Fig. 4. *H*-plane radiation pattern of test horn. Receiver noise dominates below 90 dB.

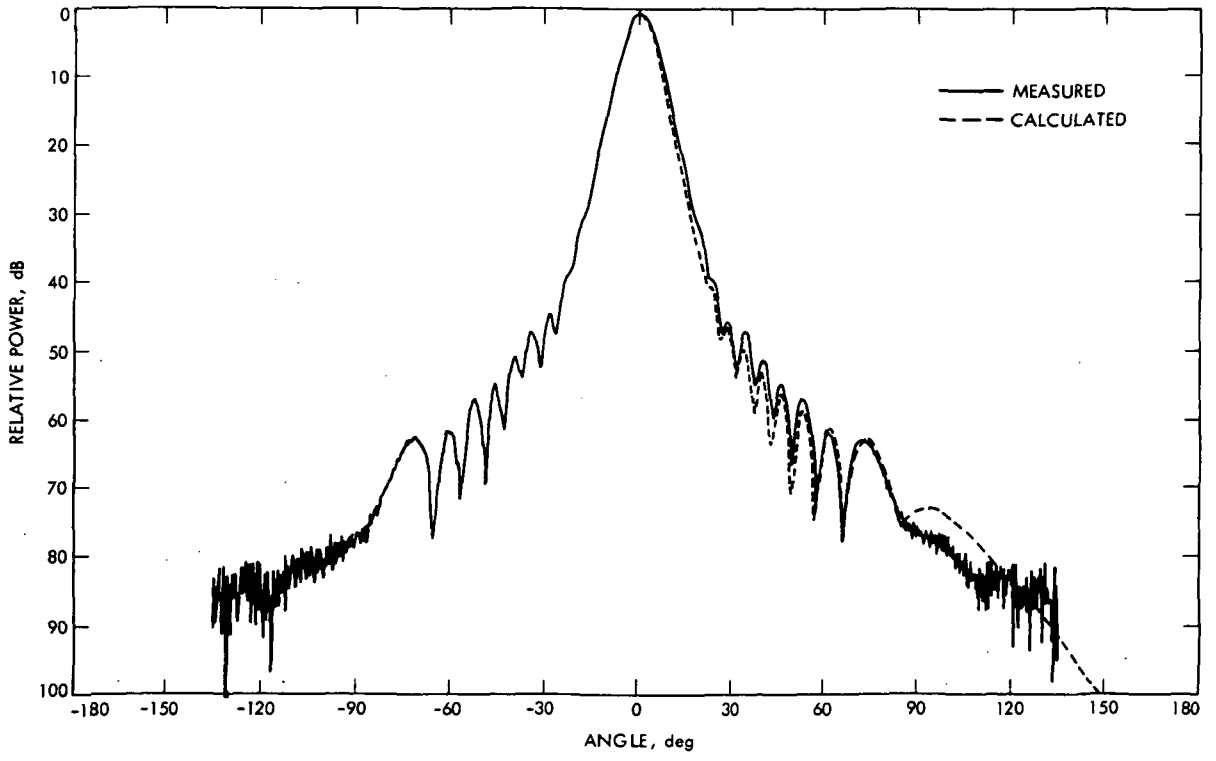

Fig. 5. *E*-plane radiation pattern of test horn

D3
55

N80-33430

The SETI Instrument Development Plan

R. B. Crow
Telecommunications Systems Section

The SETI (Search for Extraterrestrial Intelligence) Program is a NASA Research and Development Program that will search the microwave region of the spectrum for signals of extraterrestrial intelligent origin. The program includes two versions of an instrument system, a "target survey instrument" that will observe at a very high sensitivity a selected set of "interesting stars" that have particular a priori promise, and a "sky survey instrument" that will be used to observe the entire celestial sphere at a lower sensitivity. This article will briefly describe the architecture of the instrument system and reveal the development approach that will be used to implement the operational instruments.

I. Introduction

The target and sky survey instruments will be designed to be the most sensitive broadband radio telescopes on earth. From the high-efficiency antenna feed, to the cryogenically cooled preamplifiers, to the high-resolution spectrum analyzers, to the signal processor, the utmost care will be taken to deliver the best performance possible. The engineering task that is required will require considerable resources, but is within the state of the art. The SETI challenge, however, will be to handle the massive data output (gigabytes per second – see Table 1) in real time.

This problem is clearly several orders of magnitude beyond present general-purpose computer technology. It is anticipated that there will be several classes of special, high-speed digital processors that will carry out very selective algorithms and produce outputs with dramatically reduced data rates. The determination of the appropriate algorithms and the evaluation of their efficiencies when implemented in hardware is the task that will be accomplished during the SETI breadboard development.

II. Target Survey Instrument

The targeted survey will be conducted using the 305-meter antenna at Arecibo, Puerto Rico, a 64-meter DSN antenna, first at Goldstone and later in Australia, and other large radio telescopes. There are 244 solar-type stars that can be seen from Arecibo. Another 529 solar-type stars will be viewed (at lower sensitivity) by the smaller radio telescopes. The plan is to spend from 100 to 1000 seconds on each star while searching the frequency range from 1.2 to 3 GHz.

The Arecibo instrument (Fig. 1) will provide the highest sensitivity by virtue of the antenna gain. The antenna "line" feeds cover an instantaneous frequency range of 50 MHz (tunable over 100 MHz), while the multichannel spectrum analyzer/signal detector (MCSA/SD) will be capable of analyzing a frequency segment 16 MHz wide with a maximum resolution of 1 Hz. Since both continuously present and pulsed signals are considered reasonable extraterrestrial intelligence (ETI) signals, the MCSA/SD will be designed to have multiple resolutions (1, 2, 4, $\cdots$ 2048, 4092 Hz). These outputs represent an approximate set of matched filters to

optimally detect pulses while spectrum accumulators will enhance CW signal detection. These capabilities will be explored in more depth in the breadboard description.

At other locations, the target survey instruments (Fig. 2) will provide the facilities to view those stars not visible from Arecibo. The fundamental difference between the two-instrument configuration is that the non-Arecibo versions will be implemented with an 8-MHz bandwidth and offer less sensitivity due to smaller antenna sizes

The DSN is currently undergoing an evaluationary step in the form of the Network Consolidation Project (NCP). One key characteristic of the NCP will be reduced operations cost through automation. The SETI instruments will be designed to capitalize on the automation capability to improve its operational efficiency.

III. Sky Survey Instrument

The sky survey will be conducted first on a listen-only, 34-meter antenna at Goldstone and later in Australia. The sky survey instrument (Fig. 3) exhibits somewhat different characteristics from the target instrument due to its assigned task. The sky survey will cover the entire celestial sphere (at the slew rate of the antenna) over a much wider frequency band (1- to 10-GHz continuous coverage with spot coverage from 10 to 25 GHz). These two requirements modify the instrument characteristics since pulse detection is less practical (due to the slewing of the antenna) while greater analysis bandwidth is required (to search the frequency range in the allowed search time).

IV. SETI Breadboard Development

The SETI breadboard instrument will assist in the development of both the targeted and sky survey instrument systems. Figure 4 is a block diagram of the SETI breadboard instrument. It will be noted that the existing DSS 13 antenna feed, cooled preamplifier, and receiver will be used for the instrument while the development effort will concentrate on the MCSA/SD, signal processor, and SETI instrument automation.

The SETI downconverter (Fig. 5) provides the interface between either a Block III DSN receiver or the receivers at Arecibo to the MCSA/SD. The downconverter will be designed with an AGC circuit with selectable time constants. Computer control of the downconverter gain will also be possible.

The MCSA/SD will function not only as a multichannel spectrum analyzer, but will also provide specialized processing in a high-speed digital processor to reduce the data rate to the signal processor to manageable rates.

The overall architecture of the MCSA is shown in Fig. 6. This figure represents only one (of the 140) legs of the instrument. It will be noted that the design incorporates both digital bandpass filters and discrete Fourier transforms (DFT).

Several levels of "real" bandwidth (i.e., 1, 32, 1024 Hz) are available for use on the data bases shown in the figure along with their accumulators.

Figure 7 graphically represents the planned development approach of the MCSA/SD. It will be noted that the signal processor will be used to develop and test various algorithms in software. Once an algorithm has been selected, it is turned into hardware in the MCSA/SD in the next phase.

A few words should be said about the functions identified in Fig. 7.

(1) Baseline: A baseline determination must be made in order to apply any threshold criteria. The approach that will be taken early in the development will exponentially average the 1024-Hz data. The time constant for this average will be under computer control. A unique baseline value will be available for each 1024-Hz segment of the spectrum. Later work will investigate the use of other resolutions as the reference for the baseline along with possible arbitrary, user-defined baselines.

(2) Threshold: There will be a separate (computer-controlled) threshold for each bandwidth threshold. The threshold value for each particular resolution will be used across the entire analysis bandwidth. There will also be an "override" threshold feature where any 1024-Hz bandwidth segment can be squelched to prohibit known RFI from saturating the signal processor.

(3) Dedrift: This feature will be applied to the threshold data from the various bandwidth resolutions. The concept will be to store the threshold data from several (30 to 100) spectra to determine if there is a recognizable drifting (in frequency) pulse. This process can also be used to search for drifting CW signals by using the accumulator outputs as input to the dedrifters. A third alternative that will be evaluated in the breadboard is to store several complete spectra (before thresholding), dedrift, and then apply the threshold critera. This algorithm will offer the optimal sensitivity, however its cost efficiency must be assessed since it is very expensive in data memory.

(4) Pseudo Resolutions: To form the complete set of resolution bandwidths from 1 Hz to 4096 Hz, each of the "real" resolutions (i.e., output of the digital bandpass filter or DFT, i.e., 1 Hz, 32 Hz, 1024 Hz) are added in frequency to reduce the resolution (i.e., add 2 adjacent 32-Hz cells to get a 64-Hz cell, etc.) while adding the same resolution in time improves the resolution (i.e., adding two 32-Hz spectra with the proper overlap to produce a 16-Hz pseudo resolution).

Figure 8 represents the proposed layout of the breadboard instrument. The LSI-11 in the first equipment rack will be used as a functional part of the MCSA/SD to download programs into RAM memory for the bit-slice microcomputers in the MCSA, to run diagnostic tests, and to interface with the signal processor.

The magnetic tape unit and disc will be used to acquire and store data so that SETI algorithms may be evaluated in a nonreal-time environment.

Remote operation of the signal processor (and thereby the whole system through the signal processor station controller interface) will be possible from either JPL or Ames Research Center (ARC). This feature will allow development of a SETI algorithm on the same instruments in which they will be implemented and for remote SETI tests to be conducted from either JPL or ARC.

A graphic CRT and hardcopy will be available at the local site and at the remote JPL and ARC sites to provide efficient communication between the SETI scientists in their quest for the proper set of SETI algorithms.

The challenge to SETI is to search for extraterrestrial intelligence, and to provide significant improvements in the knowledge of radio astronomy. The instruments that will provide the tools for this search do not exist anywhere in this world, and represent the kind of challenge that JPL has met so well in the past. The breadboard phase has begun and should be available for preliminary testing a year from now. The search has begun.

Table 1. Unprocessed MCSA/SD output data rates

Signal type	Resolution, Hz	Data rate, bytes/s		
		Breadboard	Arecibo target instrument (two polarizations)	Sky instrument (two polarizations)
Power (one byte-floating point)				
Nonaccumulated	1	64k	32M	
	32	64k	32M	512M
	1024	64k	32M	512M
	1024 (baseline)	1k	0.4M	6.4M
	65k	64k	32M	512M
		257k	128.4M	1542M
Accumulated	1	64 to 4k	0.032M to 2M	
(16 < N < 1000)	32	64 to 4k	0.032M to 2M	0.512M to 32M
	1024	64 to 4k	0.032M to 2M	0.512M to 32M
		195 to 12k	0.096M to 6M	1.024M to 64M
Pulses 100 bins/spectra	1	0.4k	0.2M	NA[a]
(3-byte address,	32	12.8k	6.4M	78.6M
1-byte power)	1024	409.6k	209.5M	2514M
		422.8k	216.1M	2592.6M
Voltage (2 bytes per voltage)				
Nonaccumulated	1	256k	128M	NA
	32	256k	128M	2048M
	1024	256k	128M	2048M
		768k	384M	4096M

[a]Not applicable.

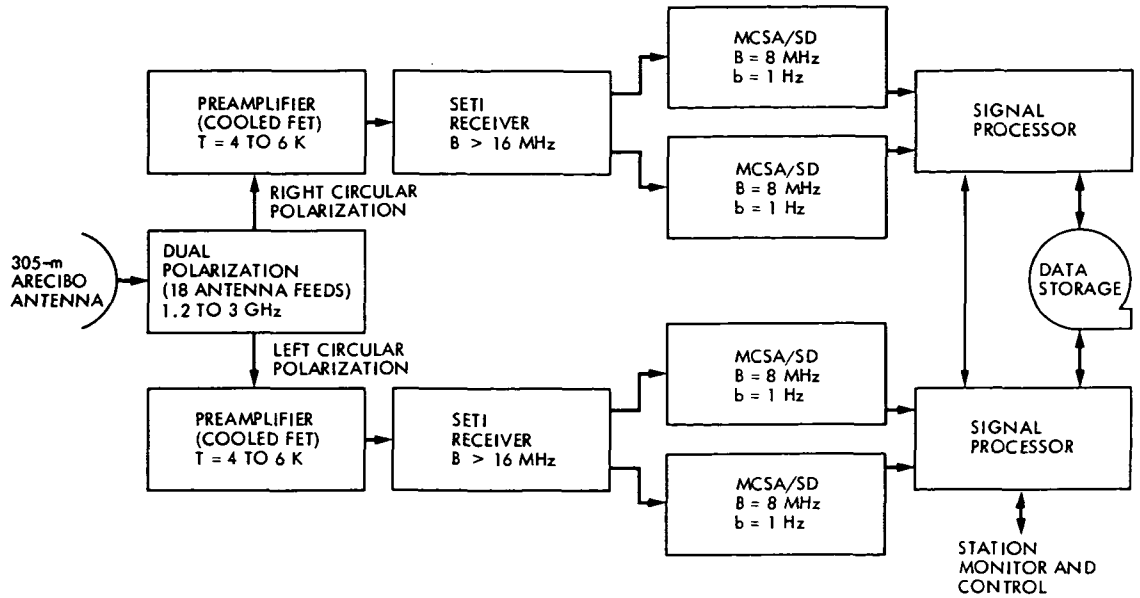

Fig. 1. Target survey instrument installation at Arecibo

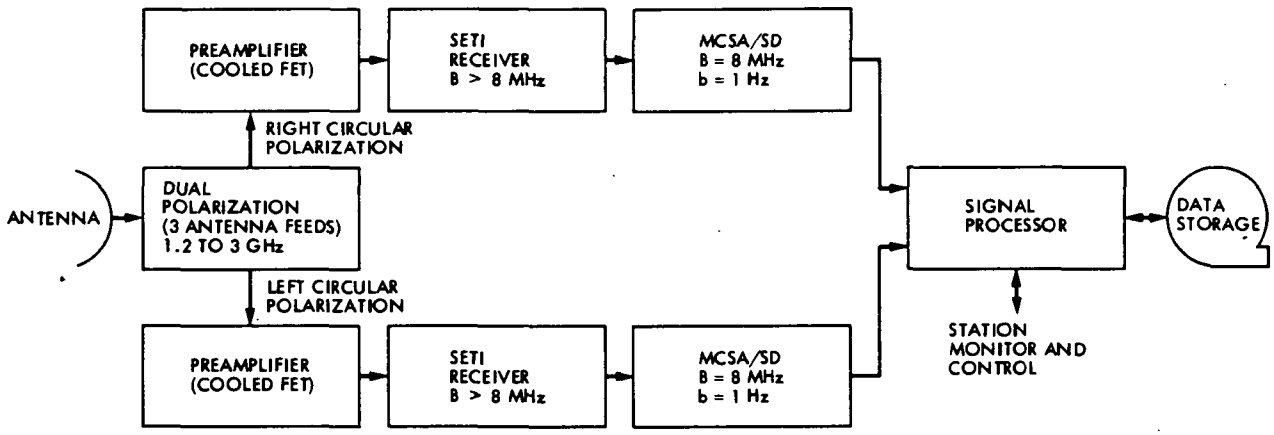

Fig. 2. Typical target survey instrument installation

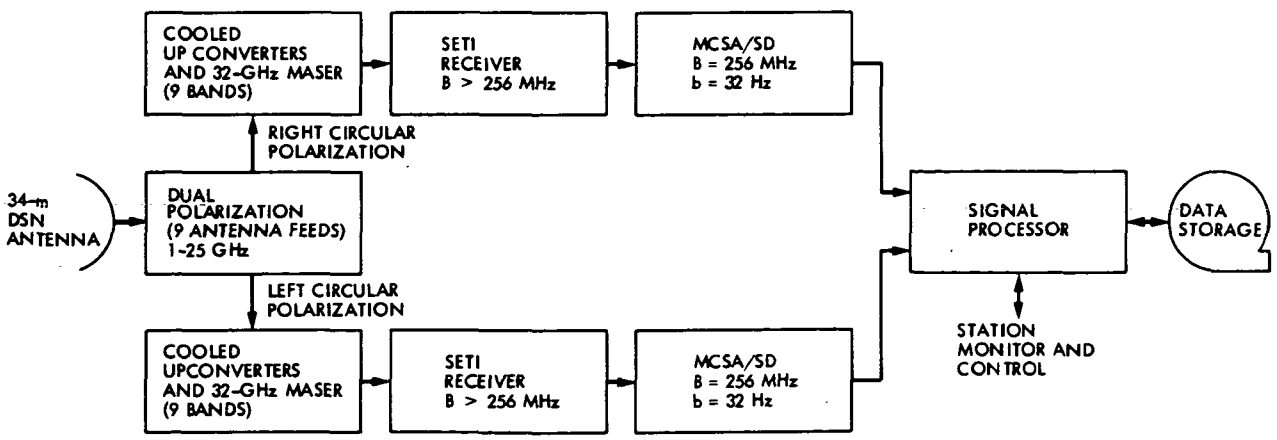

Fig. 3. Sky survey instrument installation at 34-m DSN antenna

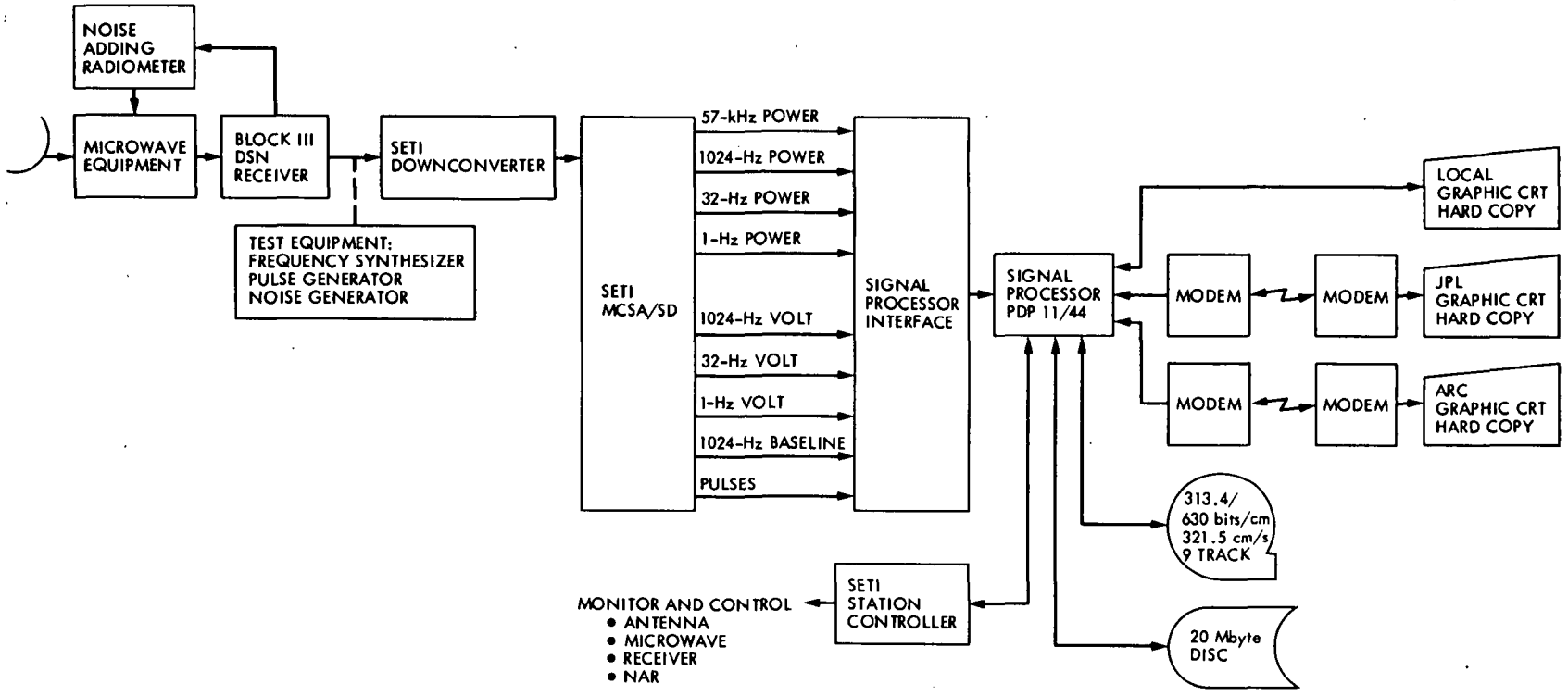

Fig. 4. Block diagram of SETI breadboard instrument

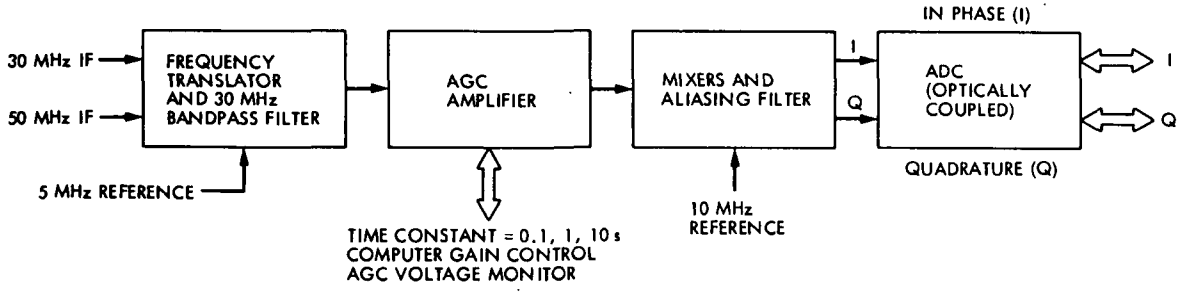

Fig. 5. Block diagram of SETI downconverter

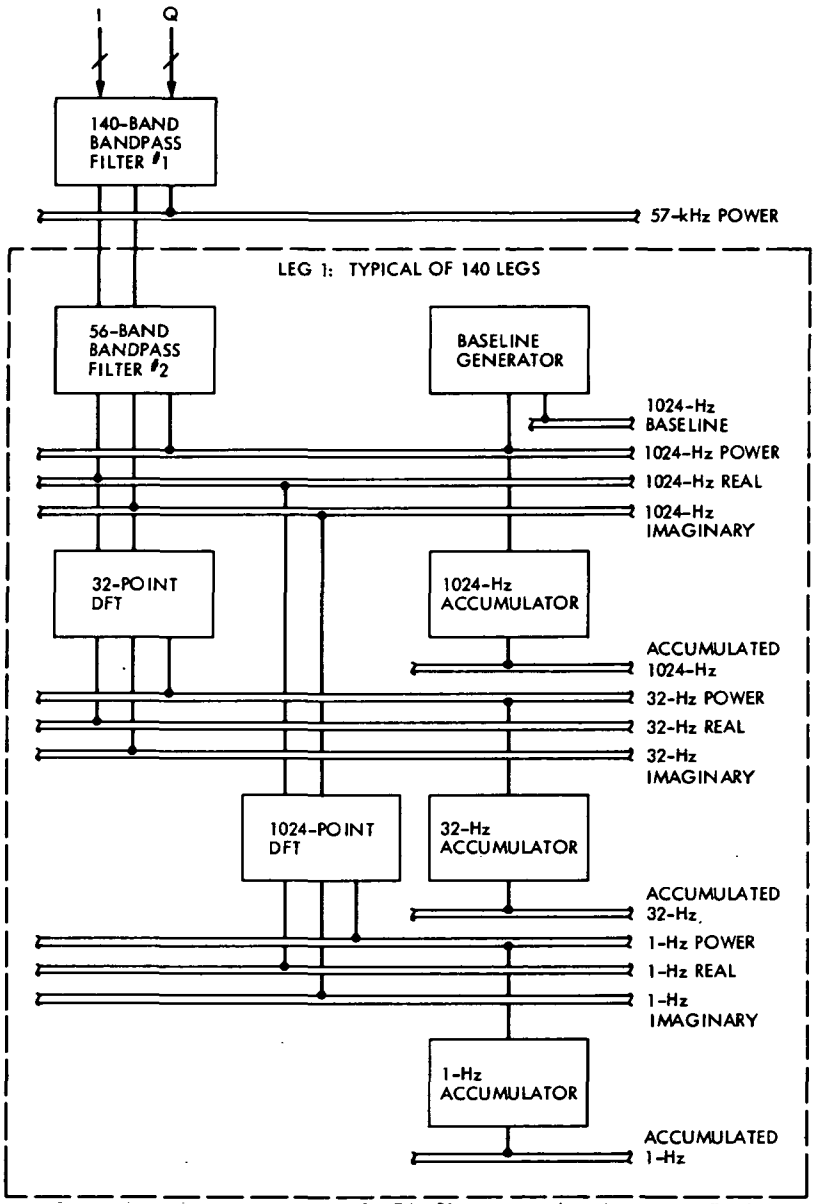

Fig. 6. Architecture of multichannel spectrum analyzer for SETI target instrument

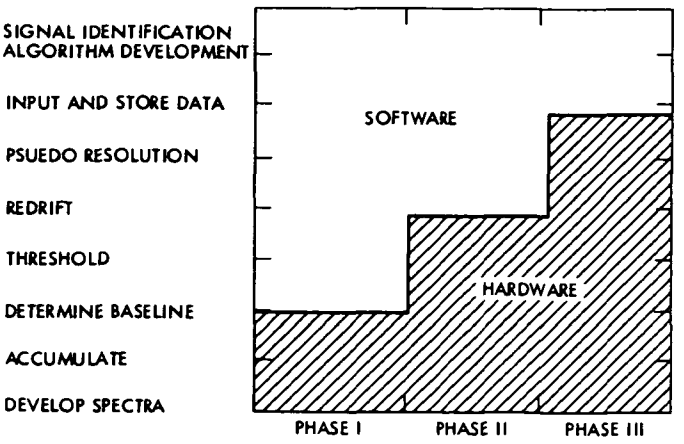

Fig. 7. SETI instrument development plan

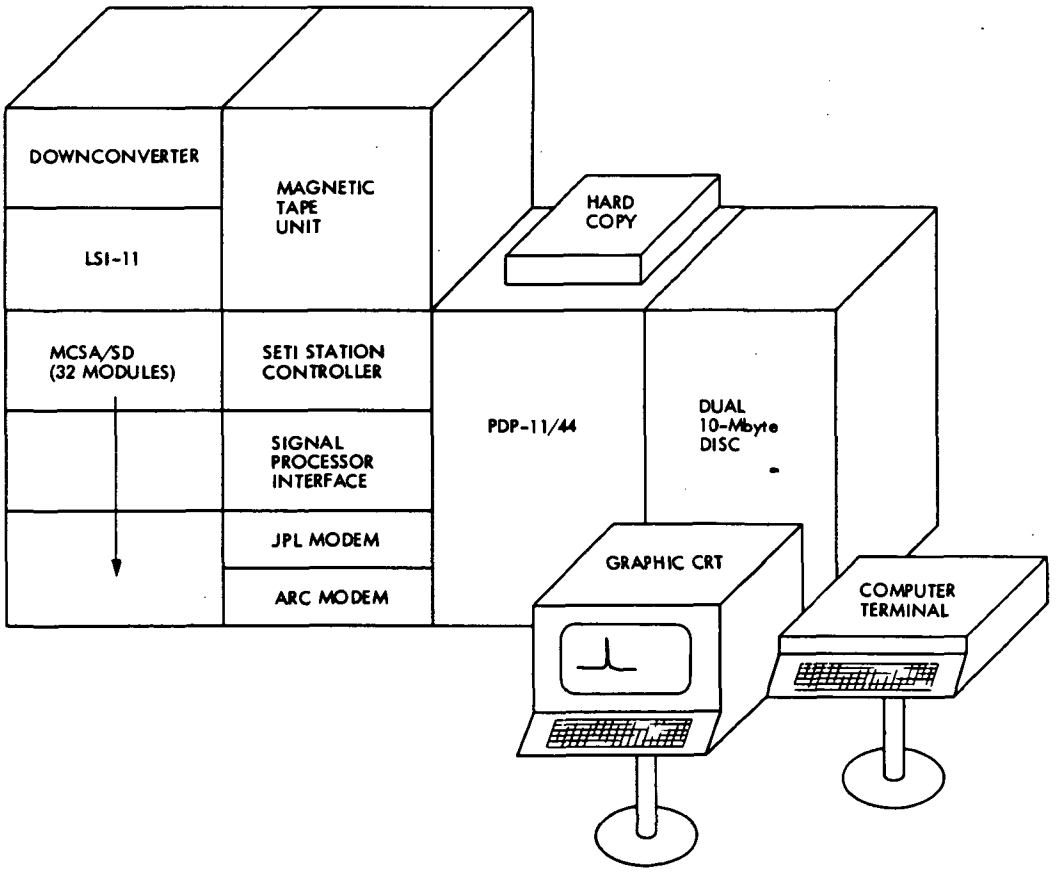

Fig. 8. Proposed layout for SETI breadboard instrument

D4
55

N80-33431

A Bimodal Search Strategy for SETI

S. Gulkis and E. T. Olsen
Planetary Atmospheres Section

J. Tarter
University of California, Berkeley

This report describes the search strategy and resultant observational plan which have been developed to carry out a comprehensive Search for Extraterrestrial Intelligence (SETI) over that portion of the electromagnetic spectrum known as the terrestrial microwave window. The limiting sensitivity achieved has been parameterized and calculated for DSN antennas as well as several radio astronomy observatories. A brief description of the instrumentation to be employed in the search and the classes of signals to be looked for is given.

I. Introduction

Since Coconni and Morrison (Ref. 1) first published their classic paper on the use and detectability of the 21-cm wavelength for SETI, there have been many theoretical investigations of the likelihood of intelligent life appearing in our galaxy and a few restricted search programs carried out. But regardless of the number of communicative civilizations in our galaxy, we still do not know where to point our antennas, what frequency to listen on, or what type of signal to search for. To determine these, we must engage in an extensive and systematic search program.

About four years ago, groups at the NASA Ames Research Center (ARC) in Mountain View, California, and at the Jet Propulsion Laboratory (JPL) in Pasadena, California set out jointly to develop a search strategy which had as its objective to greatly expand the parameter space which has been observed to date, and to accomplish this with existing telescopes. The search strategy developed by these groups is based on observations to be carried out primarily in the terrestrial microwave window (defined here to be the spectral range from 600 MHz to 25 GHz). This is the spectral region in which the sky brightness is minimum, which contains the "water hole" (Oliver, Ref. 2) and microwave water line frequencies, and for which instrumentation is readily available.

The search strategy assumes that signals of extraterrestrial origin may be narrowband transmissions which are continuously present or pulsed. The proposed strategy will be most successful at detecting those types of signals which are designed to be easily detectable but will nevertheless retain some sensitivity to more complex types of signals. The observational program embodied in the ARC/JPL plan is bimodal in character so as to cover a wide range of possibilities (Seeger, Ref. 3). One goal of the program is to survey the entire sky over a wide range of frequency to a relatively constant flux level (Murray et al., Ref. 4). This survey ensures that all potential life sites are observed to some limiting

equivalent isotropic radiated power (EIRP) depending upon their distance. A second goal is to survey a set of potential transmission sites selected *a priori* to be especially promising, achieving very high sensitivity over a smaller range of frequency (Oliver and Billingham, Ref. 5). The purpose of this paper will be to discuss the various aspects of these two complementary observational goals embodied in the ARC/JPL search strategy. Table 1 summarizes the principal observing parameters of these two approaches.

II. Sensitivity Limits for Existing Telescopes

It is presumed at the onset of the ARC/JPL program that existing radio telescopes, equipped with state-of-the-art receivers and data processing devices, will have both the sensitivity to explore the vicinity of nearby stars for transmitters similar to earth's, and to explore the entire galaxy for more powerful signals or for signals beamed at us. In this section, we examine this assumption on a quantitative basis.

An isotropic transmitter with power P_T at a distance r will create a flux

$$\phi = P_T/4\pi r^2 . \tag{1}$$

The power received by an antenna of physical area A and aperture efficiency η, from a source which produces a flux ϕ, is given by

$$P = \phi \eta A . \tag{2}$$

This power can be detected when it exceeds the inherent noise fluctuations of the system. For a postintegration power detection receiver with equivalent input noise temperature T and IF bandwidth b, the standard deviation of the noise fluctuations is given by

$$\sigma = kT \sqrt{\frac{b}{t}} . \tag{3}$$

where k is Boltzman's constant and t is the integration time. Thus, detection of a signal is possible when the signal power P exceeds the noise power σ by some specified factor α, determined by the allowable probability of a false alarm. Hence, we have the condition for detectability given by

$$P \geq \alpha \sigma = \alpha kT \sqrt{\frac{b}{t}} . \tag{4}$$

Combining Eqs. (2) and (4), we can write for the minimum detectable flux (in W/m^2)

$$\phi = \frac{\alpha kT}{\eta A} \sqrt{\frac{b}{t}} \tag{5}$$

Table 2 gives sensitivity limits for some existing telescopes instrumented with low noise receivers. The parameters used are as follows:

$\alpha = 5$

$b = 1$ Hz

$\tau = 1$ s and 1000 s

$\eta = 0.5$

If 1000 seconds is the integration time on each star, sensitivities in the range 4.9×10^{-27} W/m^2 to 3.3×10^{-25} W/m^2 are achievable from the largest to smallest telescope for spectral resolution of 1 Hz. The combined frequency resolution and sensitivity (1/2 jansky in a 1-Hz bandwidth for Arecibo) fall far outside that which has been used in radio astronomy.

From Eq. (1) the flux received at the earth from a transmitter r light-years away, per watt of equivalent isotropic radiated power, is

$$\phi = \frac{8.89 \times 10^{-34}\, EIRP}{r^2} \text{ W/m}^2 . \tag{6}$$

We may write for the range of a detectable signal

$$r = \left[\frac{8.89 \times 10^{-34}\, (EIRP)\,(\eta)\,(A)}{\alpha kT} \sqrt{\frac{t}{b}}\right]^{1/2} . \tag{7}$$

Figure 1 shows the minimum detectable EIRP as a function of distance for a typical sky survey ($\alpha = 5$, $b = 32$ Hz, $\tau = 1$ s) carried out with a 34-m telescope and for two telescopes used in a discrete source survey ($\alpha = 5$, $b = 1$ Hz, $\tau = 1000$ sec). We see from this figure that the Arecibo telescope can detect 10^8 W (EIRP) out to about 4 light-years, the distance to the nearest stars. Transmitters at the level of the strongest TV stations, $10^5 - 10^7$ W (EIRP), can be detected only if they are situated less than 2 light-years away. A transmitter equivalent to the most powerful radar systems used on earth, 10^{13} W (EIRP), can be detected by the sky survey at a distance of 22 light-years and by the discrete source survey at a distance of 1348 light-years.

III. Bimodal Observational Plan

A. Discrete Source Mode

The *a priori* site survey is designed to observe 773 stars which have been identified within 25 parsecs of the sun to be of spectral type F, G, or K and luminosity class V. The frequency range to be covered will be 1.2 to 3 GHz and as many spot bands between 3 and 25 GHz as time permits. This spectral region includes the water hole, 1.4 to 1.7 GHz, which has been suggested as a preferred frequency band for an interstellar search (Oliver, Ref. 2).

The sensitivity level which can be achieved depends on both the telescope used and the integration time. Table 2 gives typical sensitivities that can be achieved with the Arecibo antenna and with several smaller DSN antennas. Only 244 stars are visible to the Arecibo telescope; the other 529 stars must be observed using telescopes more than a factor of 3 smaller in diameter. The integration time required to achieve a constant sensitivity varies as the inverse fourth power of the telescope diameter. Thus, no attempt will be made to achieve a constant sensitivity search, as this would require ~260 times as much observing time on a 64-m antenna as on the Arecibo antenna. Rather, all stars shall be observed for approximately the same integration duration.

B. Sky Survey

The sky survey will search the entire celestial sphere over the frequency range $1.2 < f < 10$ GHz inclusive and as many spot bands between 10 and 25 GHz as time permits. In order to better understand the constraints on time and sensitivity of a sky survey, it is convenient to modify Eq. (5) by substituting for the integration time t the amount of time required to sweep the telescope primary beam past a location on the celestial sphere. Let ω be the angular tracking rate in deg/s. Then the time required to move a half-power beamwidth is

$$\xi = 70\, c/f D\, \omega \tag{8}$$

in seconds, where D is the diameter of the telescope, f is the observation frequency, and c is the velocity of light. Since $A = \pi D^2/4$ for a circular aperture, Eq. (5) becomes:

$$\phi = (4\alpha k T_s/\pi\eta)\sqrt{\omega\, bf/70\, cD^3} \tag{9}$$

in W/m^2.

Now the time required to survey a fraction g of the sky is

$$T_i = 4\pi g\xi/\Omega_i \tag{10}$$

where the solid angle of the beam is

$$\Omega_i = \epsilon c^2/\eta A f_i^2 \tag{11}$$

and ϵ is the beam efficiency. Substituting Eq. (11) into (10) and assuming a circular aperture, the time to survey at a particular frequency setting is found:

$$T_i = (70 g\pi^2\, \eta D f_i/(c\omega\epsilon)\,. \tag{12}$$

The time to carry out a complete survey between the frequency limits f_L and f_u depends on both the bandpass B of the multichannel spectrum analyzer and the scan rate. The bandpass B is equal to the product of the number of channels in the spectrum analyzer and the single channel bandwidth (b). An attractive operational procedure is to operate at a constant angular tracking rate. This choice results in a sensitivity which varies as the square root of the frequency. This leads to the following expression for the time to carry out a survey between the frequency limits f_L and f_u

$$T = [(70 g\pi^2\eta D)/(2c\omega B\epsilon)]\,(f_u^2 - f_L^2)\,. \tag{13}$$

Assuming that the survey is carried out using a 34-m telescope which scans at a rate of 0.2 °/s, the time required to survey the entire sky at a single frequency setting is

$$T_i = 3\sqrt{f_{GHz}} \text{ days} \tag{14}$$

if the scans are separated by one half-power beam width. The instantaneous bandpass of a 2^{23} channel analyzer operating at a spectral resolution of 32 Hz is 268.4 MHz. Thus the time required to survey the entire celestial sphere over the frequency range $1.2 \leqslant f \leqslant 10$ GHz is

$$T \approx 1.6 \text{ years}\,. \tag{15}$$

The sensitivity achieved in such a survey will be

$$\phi = 2.0 \times 10^{-24}\, \alpha\, \sqrt{f_{GHz}} \text{ W/m}^2\,. \tag{16}$$

C. Instrumentation

Figure 2 shows a block diagram of a system instrumented for SETI observations. The complete system consists of the radio telescope, orthogonally polarized feeds, low noise receivers, a large multichannel spectrum analyzer (MCSA) and associated accumulators, processor, and various recording devices.

The crucial new instrumentation which enables this search to greatly expand on previous searches is the large multichannel spectral analyzer. Such devices will make it possible to examine large numbers of frequencies simultaneously. A digital spectrum analyzer with 300 MHz of bandwidth and a million channels is currently under construction at the Jet Propulsion Laboratory (Morris and Wilck, Ref. 6). This device produces FFT transforms in 10-MHz sections with 300-Hz resolution. One such device designed at Stanford University in collaboration with the Ames Research Center and JPL yields 10^7 channels over 8.4 MHz with a resolution of 1 Hz or 10^7 channels over 268 MHz with a resolution of 32 Hz.

Figures 3 and 4 show schematic block diagrams of the sky survey and discrete source survey devices which consist of two stages of digital bandpass filters followed by digital FFT (Fast Fourier Transform) processors. The primary spectral resolutions originating in this design are 8.4 MHz, 65.5 kHz, 1 kHz, 32 Hz and 1 Hz. Synthetic spectral resolutions may be generated by combining samples in frequency and in time, and the MCSA will be designed to output power spectra over the range of spectral resolution from 1/4 Hz to 4 kHz in steps which are multiples of 2. This resolution tree allows a more nearly optimum match to a wide range of continuous and pulsed signal bandwidths. The bandpass filter design ensures spectral isolation to the 1-kHz level (256 Hz counting synthetic frequencies); i.e., a strong interfering signal will not "splatter" more than this amount beyond its own bandwidth. The use of FFT processors at the high-resolution end of the chain minimizes memory required in the hardware. The MCSA architecture is highly multiplexed so that the actual board level parts count is minimal.

The MCSA is designed to be microprogrammable, which allows the characteristics of the bandpass filters and the hardware thresholding levels (α) to be changed through software commands; in addition the nature of the transform performed in the fast processors may be altered by software commands. The test as to whether the power appearing in a bin exceeds a preset threshold will be carried out in the MCSA at high speed. The data corresponding to threshold crossings will be passed over to the decision processor for further tests.

The MCSA and decision processor will be sensitive to three distinct classes of signals: (1) a continuously present, nondrifting signal of the order of the mean noise level, (2) a periodically pulsed signal of the order of 10 times the mean noise level and which may be drifting, and (3) a continuously present, drifting signal of the order of the mean noise level.

Class (1) signals are the easiest to detect, requiring only a threshold test on the accumulated spectrum at the end of an integration period. Class (2) signals are more demanding on the hardware/software. Their detection requires a threshold test for each sample. Data exceeding thresholds is stored over a period of observation and then the decision processor must examine the resulting matrix for periodicity and drift. The sensitivity achieved will depend upon the number of false alarms which the system can handle. Class (3) signals require large, high-speed memory modules, for each sample spectrum must be stored over some chosen period. Sensitivity is enhanced through removal of frequency drift before accumulation and thresholding. Of course, the processor must perform this manipulation over a range of drifts.

IV. Summary Remarks

It is presently believed that a number of large spectrum analyzers could be built and used at existing radio observatories to carry out a significant SETI program. While this program is still in its conceptual stages, we believe that a field test program could begin as early as 1980-1981 using a smaller version of the large spectrum analyzers and other more traditional hardware. The immediate goals are to learn more about the radio frequency background (interference) at high spectral resolution and to develop signal detection algorithms which efficiently recognize the presence of a signal and automatically attempt to identify and classify it. It is expected that full-scale instrumentation development could begin in 1982 and an operational system placed in the field in 1984.

Acknowledgment

We thank our colleagues Dr. B. Oliver and Dr. A. Peterson and members of the SETI groups at the Ames Research Center and the Jet Propulsion Laboratory for their many contributions to the ideas reflected in this paper.

References

1. Cocconi, G., and Morrision, P., "Searching for Interstellar Communications," *Nature*, 184, pp. 844 (1959).

2. Oliver, B. M., "Rationale for the Water Hole," *Acta Astronautica*, 6, No. 1-2, pp. 71-79 (1979).

3. Seeger, C. L., "Strategic Considerations in SETI, and a Microwave Approach," *Acta Astronautica*, 6, No. 1-2, pp. 105-127 (1979).

4. Murray, B., Gulkis, S., and Edelson, R. E., "Extraterrestrial Intelligence: An Observational Approach," *Science*, 199, pp. 485-492 (1978).

5. Oliver, B. M., and Billingham, J., *Project Cyclops*, NASA CR114445 (1972).

6. Morris, G. A., and Wilck, H. C., "JPL 2^{20} Channel 300 MHz Bandwidth Digital Spectrum Analyzer," DSN Progress Report 42-46, Jet Propulsion Laboratory, Pasadena, Calif., pp. 57-61 (1978).

Table 1. Search strategy observing parameters

Parameter	All-sky survey	Selected site survey
Coverage	4π steradians	~800 beam areas
Sensitivity limit	$\sim 10^{-23}\sqrt{f_{GHz}}$ W/m^2	10^{-25} -10^{-27} W/m^2
Frequency range	1 – 10 GHz + spot bands	1 – 3 GHz + spot bands
Spectral resolution	32 Hz	1 Hz
Integration time/beam area	0.3 – 3 s	100 – 1000 s
Total integration time for survey	1.6 yr	~0.5 yr
Aperture	34-m	$\geq$ 64-m

Table 2. Typical telescope sensitivities

Telescope	T_s, K	A, m^2	ϕ(W/m^2) τ = 1 s	ϕ(W/m^2) τ = 1000 s
Arecibo	40	35633	1.55×10^{-25}	4.89×10^{-27}
Greenbank 93-m	30	6808	6.07×10^{-25}	1.92×10^{-26}
Parkes or DSN 64-m	20	3217	8.58×10^{-25}	2.71×10^{-26}
Ohio State	40	2221	2.48×10^{-24}	7.86×10^{-26}
Stanford 5-element interferometer	20	1313	2.10×10^{-24}	6.65×10^{-26}
DSN 34-m	20	908	3.04×10^{-24}	9.61×10^{-26}
Greenbank or DSN 26-m	20	527	5.24×10^{-24}	1.66×10^{-25}
Stanford 18-m	20	263	1.05×10^{-23}	3.32×10^{-25}

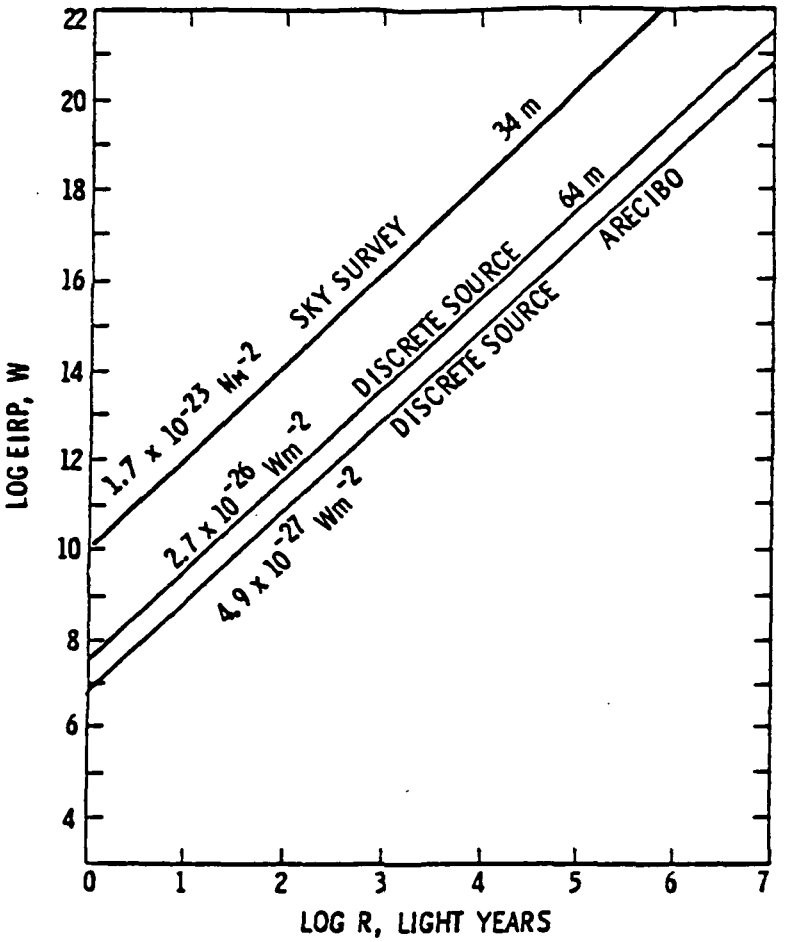

Fig. 1. The minimum equivalent isotropic radiated power detectable as a function of distance from the transmitter for a signal-to-noise ratio equal to five. The all-sky survey is assumed to be carried out at a spectral resolution of 32 Hz and a 1-s integration period on a 34-m telescope. The discrete source survey is assumed to be carried out at a spectral resolution of 1 Hz and a 1000-s integration period on a 64-m telescope and the Arecibo telescope

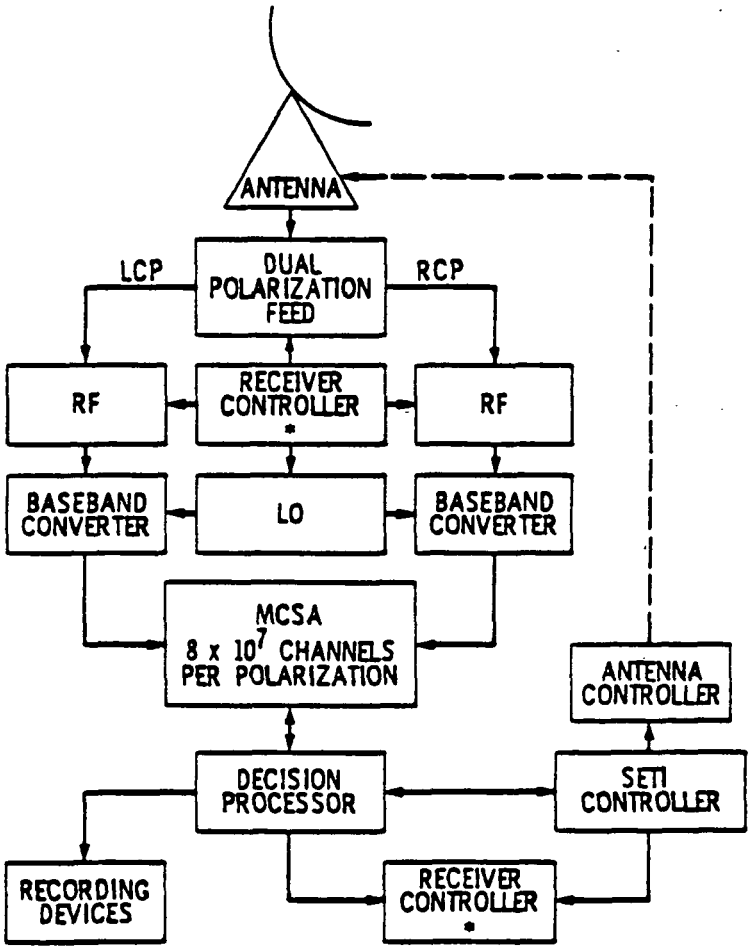

Fig. 2. A block diagram of a system instrumented to carry out a search for extraterrestrial intelligence. The system must be capable of processing data on-line to discard data of no archival value

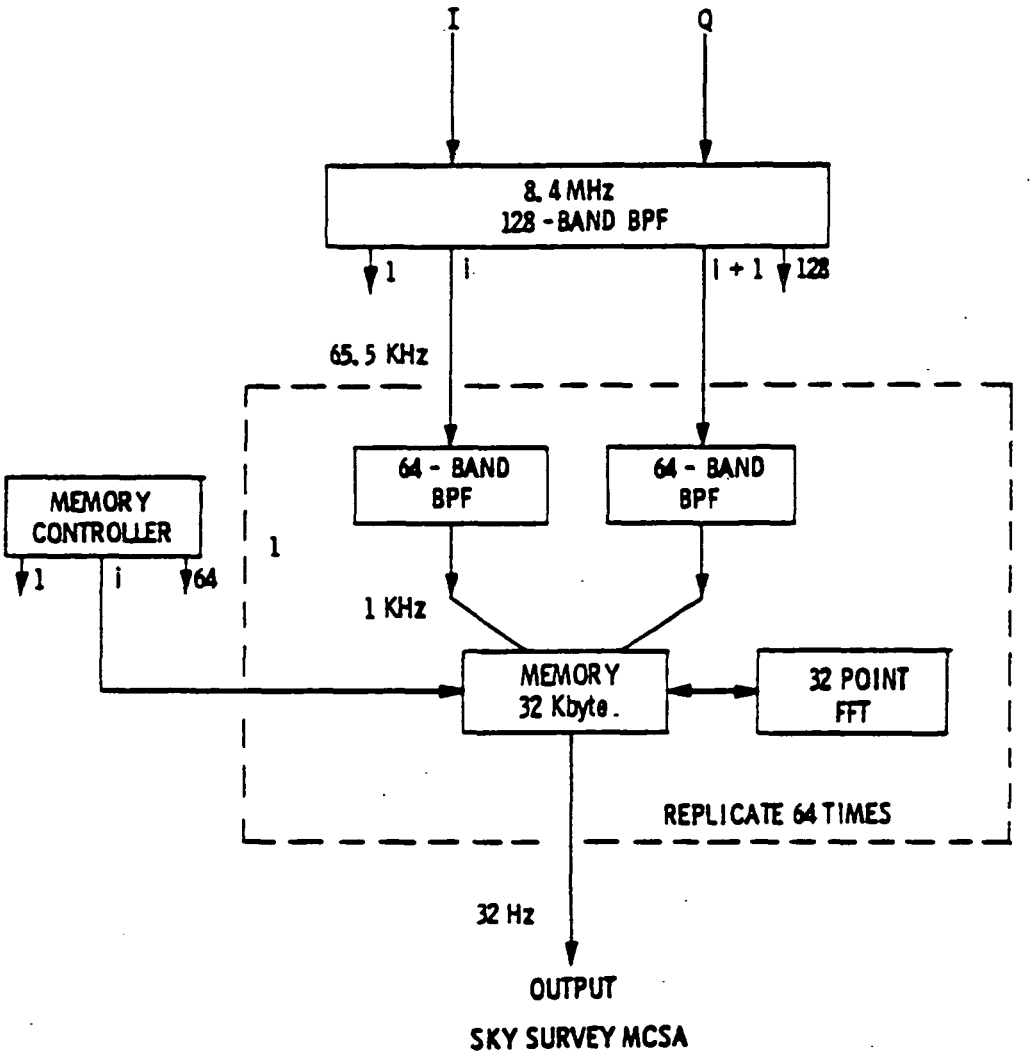

Fig. 3. A schematic block diagram of the multichannel spectrum analyzer designed for the all-sky survey. It is designed to cover a 268.4-MHz instantaneous bandpass at 32-Hz resolution

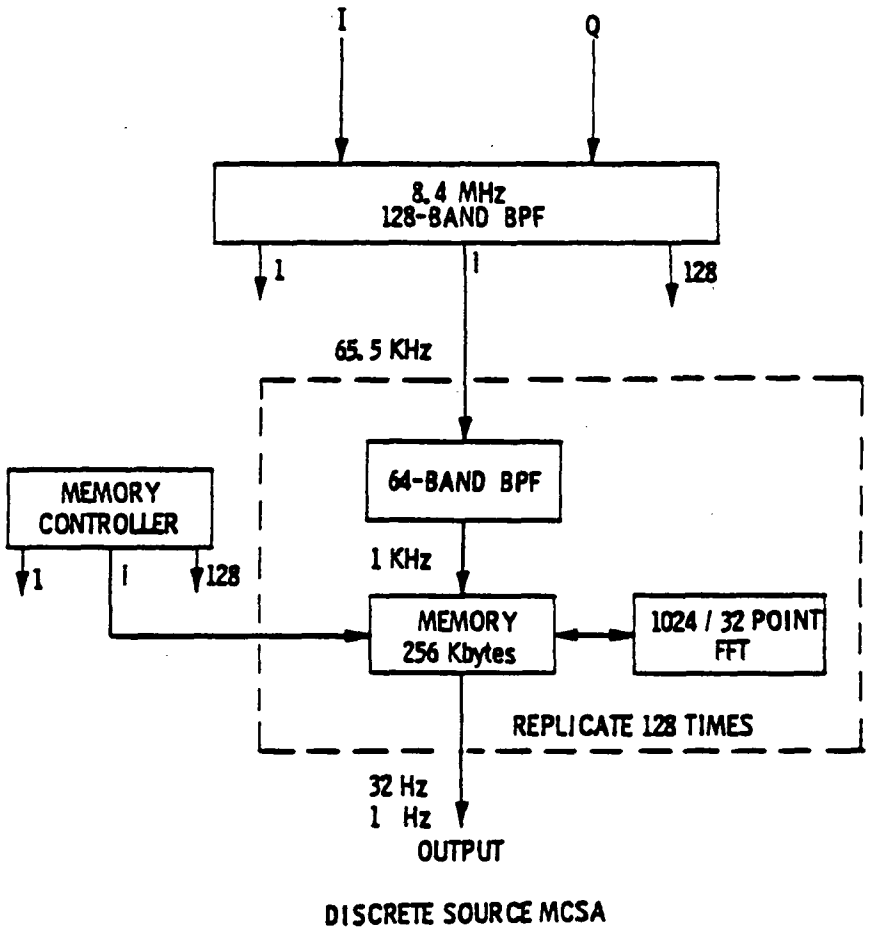

Fig. 4. A schematic block diagram of the multichannel spectrum analyzer designed for the discrete source survey. It is designed to cover a 8.4-MHz instantaneous bandpass at 1-Hz resolution

N80-33432

ORION S-Band Data Acquisition for S-X Calibration

S. C. Wu
Tracking Systems and Applications Section

To calibrate for ionospheric charged particle effects, ORION will include both X- and S-band data links. This report studies the performance of S-band receiver and the optimum allocation of data volume between S- and X-band observations. It is found that the requirements on the S-band receiver are not very stringent.

I. Introduction

Covariance analyses have been performed to estimate the effects of possible error sources on ORION baseline determination (Ref. 1). In the analyses, the ORION observations were assumed to be taken only at X-band frequencies. In other words, no S-X calibration was considered; the effects of ionospheric charged particles were assumed partially calibrated for by a global model. Such a global model requires an independent measurement of the ionosphere, such as by Faraday rotation measurement, and relies on a mapping scheme to obtain line-of-sight calibrations.

With the inclusion of an S-band link, ionospheric calibration becomes simple and complete through the combination of S- and X-band observations. However, it is costly to have an S-band receiver performing as well as the primary X-band receiver. An S-band receiver with a system temperature a factor of 2 higher than that of the X-band receiver is available at a much lower cost. In this report, we shall compare the performance of S-band receivers with different system temperatures. Also, the optimum allocation of data volume between S- and X-band observations will be studied.

II. Analysis

In the following analysis, we shall assume that all 14 pairs of the Mark III VLBI data channels are available for maintaining high delay precision. In other words, no channel pairs are to be placed at reduced span bandwidths for ambiguity resolving. It appears that the smaller span bandwidth of 100 MHz at S-band (in comparison with 400 MHz at X-band) may be used to resolve the ambiguity of the X-band delays. Parameters to be used in the analysis are listed as follows:

Quasar correlated flux density $S = 2$ janskys

Span bandwidth $f_{span} = 400 \times 10^6$ Hz (X-band)
$= 100 \times 10^6$ Hz (S-band)

Total channel bandwidth $B = 14 \times (2 \times 10^6)$ Hz

Integration time per observation $T = 600$ s

Antenna efficiencies:

At co-site $e_1 = 0.5$ (S and X)

At mobile site $e_2 = 0.5$ (X-band)
0.4 (S-band)

Antenna diameters:

At co-site D_1 = 9 m or 26 m

At mobile site D_2 = 5 m

System temperatures:

At co-site T_1 = 40 K (S and X)

At mobile site T_2 = 100 K (X-band)
60 - 240 K (S-band)

The 1-σ error of delay observation due to receiver system noise is (Ref. 1)

$$\sigma_\tau = \frac{\sqrt{2}c}{2\pi f_{span}} \left(\frac{1}{SNR}\right) \tag{1}$$

where SNR is the fringe signal-to-noise ratio,

$$\text{SNR} = 2.05 \times 10^{-4} S D_1 D_2 \left(\frac{e_1 e_2 BT}{T_1 T_2}\right)^{1/2} \tag{2}$$

and c is the speed of light. When all 14 pairs of the data channels are used for X-band only, the delay observations will have a 1-σ error of 0.89 cm due to the system noise with a 9-meter antenna at the co-site. To account for different system parameters, the 1-σ delay error can be written as

$$\sigma_\tau = 0.89 \left(\frac{400}{f_{span}}\right) \left(\frac{9}{D_1}\right) \left(\frac{T_2}{100}\right)^{1/2} \left(\frac{0.5}{e_2}\right)^{1/2} \text{cm} \tag{3}$$

where f_{span} is in MHz and D_1 in meters.

A covariance analysis following Ref. 1 shows that an error σ_τ = 1 cm results in a 3-D baseline error of 1.3 cm:

$$\epsilon_{BL} = 1.3\, \sigma_\tau \tag{4}$$

when solving for 16 parameters (three baseline components, epoch offset and 12 segments of clock rate offsets) from 32 observations. On the other hand, the effect of an uncalibrated ionosphere on baseline determination is estimated to be about 4 cm (at X-band) per 1000-km baseline. The root-sum-square (RSS) baseline errors due to system noise and to ionospheric effects are shown in Fig. 1 as slanted curves for D_1 = 9 m and 26 m.

When part of the 14 pairs of data channels are allocated to S-band observations, S-X calibration can be performed to remove the ionospheric effects. However, system noise effects will be increased, partly due to the decrease in data volume at X-band and partly due to additional effects from S-band observations. The S-X calibrated delay observable can be expressed as a linear combination of X- and S-band observations:

$$\tau_{s-x} = \left(\frac{1}{1-\alpha^2}\right) \tau_x - \left(\frac{\alpha^2}{1-\alpha^2}\right) \tau_s$$

$$\doteqdot 1.08\, \tau_x - 0.08\, \tau_s \tag{5}$$

where α = 3/11 is the ratio of S- and X-band frequencies. The effect of system noise on such delay observable is then

$$\sigma^2_{\tau s-x} = 1.08^2\, \sigma^2_{\tau,x} + 0.08^2\, \sigma^2_{\tau,s} \tag{6}$$

An attempt to reduce $\sigma_{\tau,x}$ calls for a larger data volume to be allocated to X-band observations; this leaves a smaller data volume for S-band and thus increases $\sigma_{\tau,s}$ and vise versa. Hence a compromise between S- and X-band data volume allocation needs to be made to keep $\sigma_{\tau,s-x}$ low.

Let the fraction of data volume allocated to X-band be V_x and that to S-band be $V_s = 1 - V_x$; then

$$\sigma^2_{\tau,x} = \left(\frac{1}{V_x}\right) \sigma^2_{\tau,x\text{-only}} \tag{7}$$

$$\sigma^2_{\tau,s} = (20)\left(\frac{T_{2,s}}{100}\right)\left(\frac{1}{1-V_x}\right) \sigma^2_{\tau,x\text{-only}} \tag{8}$$

where the factor 20 accounts for different f_{span} and e_2 for the S-band receivers. With the substitution of Eqs. (7) and (8), Eq. (6) can be written as

$$\frac{\sigma^2_{\tau,s-x}}{\sigma^2_{\tau,x\text{-only}}} = 1.08^2 \left(\frac{1}{V_x}\right) + 0.08^2 \left(\frac{T_{2,s}}{5}\right) \left(\frac{1}{1-V_x}\right) \tag{9}$$

which is minimum when

$$V_x = \frac{1.08}{1.08 + 0.08\, (T_{2,s}/5)^{1/2}} \tag{10}$$

with a minimum value of

$$\frac{\sigma^2_{\tau,s\text{-}x}}{\sigma^2_{\tau,x\text{-}only}} = \left[1.08 + 0.08\left(\frac{T_{2,s}}{5}\right)^{1/2}\right]^2 \qquad (11)$$

In other words, the 3-D baseline error due to the system noise in both S- and X-band receivers will be

$$\epsilon_{BL} = (1.3)(0.89)\left(\frac{9}{D_1}\right)\left[1.08 + 0.08\left(\frac{T_{2,s}}{5}\right)^{1/2}\right] \qquad (12)$$

Figure 2 shows the variations of baseline errors as functions of V_x. Since there are 14 pairs of data channels, V_x can have a value only of integral multiples of 1/14. Hence the *theoretical* minimum 3-D baseline error ϵ_{BL} of (12) is not always attainable. The *realizable* minimum 3-D baseline error is calculated from (9), with V_x calculated from (10) but quantized to the nearest integral multiples of 1/14. However, as shown in Fig. 2, the sensitivity of the error to V_x is small near the optimum V_x. Thus, Eq. (12) is very close to the realizable minimum 3-D baseline error due to system noise.

Another concern is the requirement of exceeding a minimum signal-to-noise ratio (SNR $\geq$ 7) for phase detection. Such a criterion can easily be met with a 26-meter antenna at the co-site. With D_1 = 9 meters and $T_{2,s}$ = 240 K, an SNR $>$ 7 at S-band calls for $V_s > 0.41$. The closest realizable $V_s > 0.41$ is 6/14, leaving V_x = 8/14 = 0.57 instead of the optimum 0.66 as calculated from (10). In view of Fig. 2(c), however, the 3-D baseline error will be only slightly higher than that given by the theoretical minimum of (12). In Fig. 2 the errors are shown as broken lines for those values of V_s and V_x resulting in SNR $<$ 7.

The realizable minimum 3-D baseline errors due to system noise for the three different S-band system temperatures at the mobile site are shown in Fig. 1 as horizontal lines. It It is seen that an increase in S-band system temperature at the mobile site by a factor of 4 increases the baseline error only slightly, provided that S/X data volume ratio is not far from optimum.

III. Conclusions

The system temperature of the ORION S-band receiver has a very small effect on baseline determination accuracy. It is unwise to pay a high cost for an S-band receiver with a low system temperature; a system temperature as high as 240 K is tolerable. Only 20 to 40 percent of data volume is to be allocated to S-band observations for minimum baseline error. The error remains low over a rather wide range of data volume ratio. Hence precise allocation of the 14 pairs of the Mark III VLBI data channels between S- and X-band observations is not critical.

Reference

1. Wu, S. C., "Error Estimation for ORION Baseline Vector Determination," *TDA Progress Report 42-57*, Jet Propulsion Laboratory, Pasadena, Calif., June 15, 1980, pp. 16-31.

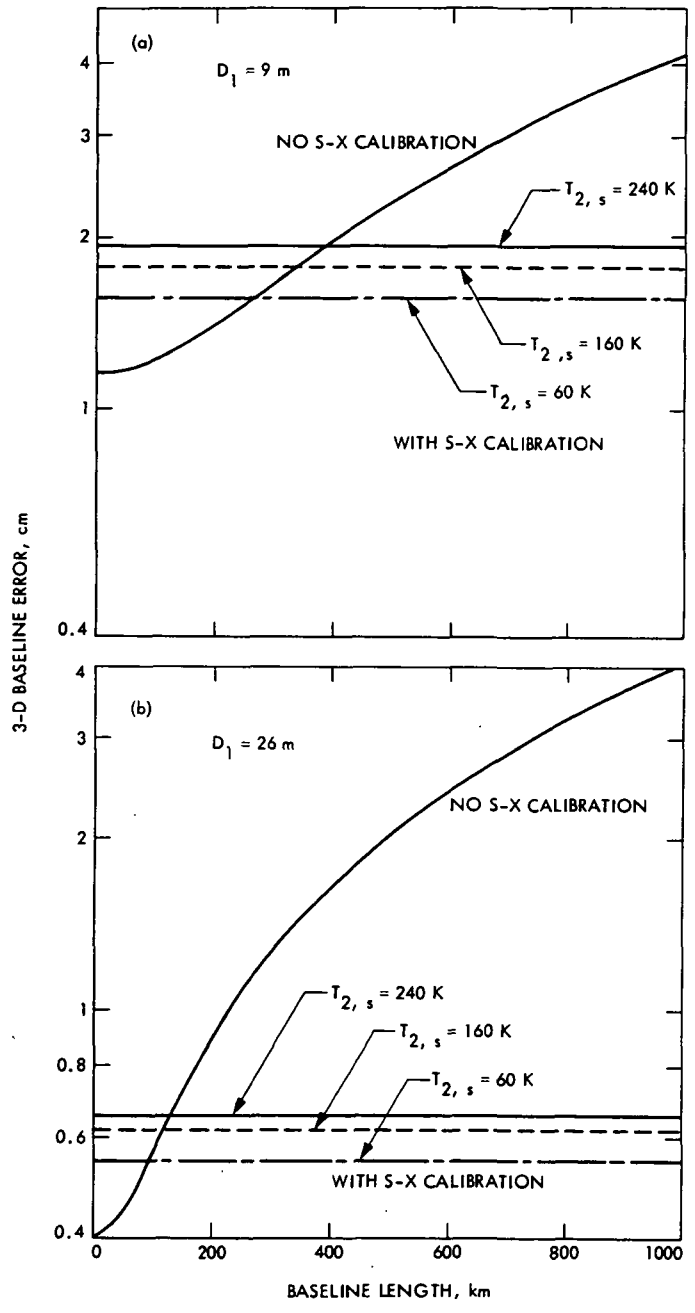

Fig. 1. RSS effects of system noise and ionosphere on baseline determination

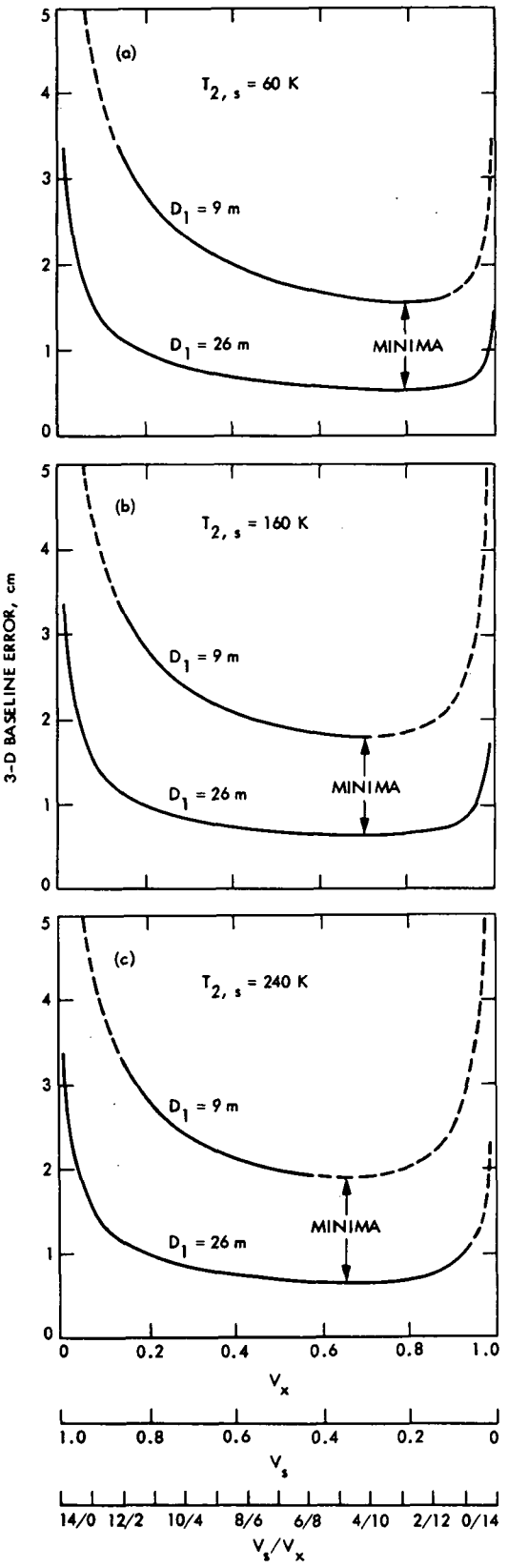

Fig. 2. Effects of S-X relative data volume on baseline errors due to system noise

N80-33433

Network Functions and Facilities

N. A. Renzetti
Office of Tracking and Data Acquisition

The objectives, functions, and organization of the Deep Space Network are summarized; deep space station, ground communication, and network operations control capabilities are described.

The Deep Space Network was established by the National Aeronautics and Space Administration (NASA) Office of Space Tracking and Data Systems and is under the system management and technical direction of the Jet Propulsion Laboratory (JPL). The network is designed for two-way communications with unmanned spacecraft traveling approximately 16,000 km (10,000 miles) from Earth to the farthest planets and to the edge of our solar system. It has provided tracking and data acquisition support for the following NASA deep space exploration projects: Ranger, Surveyor, Mariner Venus 1962, Mariner Mars 1964, Mariner Venus 1967, Mariner Mars 1969, Mariner Mars 1971, and Mariner Venus-Mercury 1973, for which JPL has been responsible for the project management, the development of the spacecraft, and the conduct of mission operations; Lunar Orbiter, for which the Langley Research Center carried out the project management, spacecraft development, and conduct of mission operations; Pioneer, for which Ames Research Center carried out the project management, spacecraft development, and conduct of mission operations; and Apollo, for which the Lyndon B. Johnson Space Center was the project center and the Deep Space Network supplemented the Manned Space Flight Network, which was managed by the Goddard Space Flight Center. The network is currently providing tracking and data acquisition support for Helios, a joint U.S./West German project; Viking, for which Langley Research Center provided the Lander spacecraft and project management until May, 1978, at which time project management and mission operations were transferred to JPL, and for which JPL provided the Orbiter spacecraft; Voyager, for which JPL provides project management, spacecraft development, and is conducting mission operations; and Pioneers, for which the Ames Research Center provides project management, spacecraft development, and conduct of mission operations. The network is adding new capability to meet the requirements of the Galileo mission to Jupiter, for which JPL is providing the Orbiter spacecraft, and the Ames Research Center the probe and the probe carrier. In addition, JPL will carry out the project management and the conduct of mission operations. The network is also preparing to support the planned International Solar Polar Mission (ISPM), a joint European Space Agency (ESA) and NASA project scheduled for launch in 1985.

The Deep Space Network (DSN) is one of two NASA networks. The other, the Spaceflight Tracking and Data Network (STDN), is under the system management and technical direction of the Goddard Space Flight Center (GSFC). Its function is to support manned and unmanned Earth-orbiting satellites. The Deep Space Network supports lunar, planetary, and interplanetary flight projects.

From its inception, NASA has had the objective of conducting scientific investigations throughout the solar system. It was recognized that in order to meet this objective, significant supporting research and advanced technology development must be conducted in order to provide deep space telecommunications for science data return in a cost effective manner. Therefore, the Network is continually evolved to keep pace with the state of the art of telecommunications and data handling. It was also recognized early that close coordination would be needed between the requirements of the flight projects for data return and the capabilities needed in the Network. This close collaboration was effected by the appointment of a Tracking and Data Systems Manager as part of the flight project team from the initiation of the project to the end of the mission. By this process, requirements were identified early enough to provide funding and implementation in time for use by the flight project in its flight phase.

As of July 1972, NASA undertook a change in the interface between the Network and the flight projects. Prior to that time, since 1 January 1964, in addition to consisting of the Deep Space Stations and the Ground Communications Facility, the Network had also included the mission control and computing facilities and provided the equipment in the mission support areas for the conduct of mission operations. The latter facilities were housed in a building at JPL known as the Space Flight Operations Facility (SFOF). The interface change was to accommodate a hardware interface between the support of the network operations control functions and those of the mission control and computing functions. This resulted in the flight projects assuming the cognizance of the large general-purpose digital computers which were used for both network processing and mission data processing. They also assumed cognizance of all of the equipment in the flight operations facility for display and communications necessary for the conduct of mission operations. The Network then undertook the development of hardware and computer software necessary to do its network operations control and monitor functions in separate computers. A characteristic of the new interface is that the Network provides direct data flow to and from the stations; namely, metric data, science and engineering telemetry, and such network monitor data as are useful to the flight project. This is done via appropriate ground communication equipment to mission operations centers, wherever they may be.

The principal deliveries to the users of the Network are carried out by data system configurations as follows:

(1) The DSN Tracking System generates radio metric data, i.e., angles, one- and two-way doppler and range, and transmits raw data to Mission Control.

(2) The DSN Telemetry System receives, decodes, records, and retransmits engineering and scientific data generated in the spacecraft to Mission Control.

(3) The DSN Command System accepts spacecraft commands from Mission Control and transmits the commands via the Ground Communications Facility to a Deep Space Station. The commands are then radiated to the spacecraft in order to initiate spacecraft functions in flight.

(4) The DSN Radio Science System generates radio science data, i.e., the frequency and amplitude of spacecraft transmitted signals affected by passage through media such as the solar corona, planetary atmospheres, and planetary rings, and transmits these data to Mission Control.

(5) The DSN Very Long Baseline Interferometry System generates time and frequency data to synchronize the clocks among the three Deep Space Communications complexes. It will generate universal time and polar motion and relative Deep Space Station locations as by-products of the primary data delivery function.

The data system configurations supporting testing, training, and network operations control functions are as follows:

(1) The DSN Monitor and Control System instruments, transmits, records, and displays those parameters of the DSN necessary to verify configuration and validate the Network. It provides the tools necessary for Network Operations personnel to control and monitor the Network and interface with flight project mission control personnel.

(2) The DSN Test and Training System generates and controls simulated data to support development, test, training and fault isolation within the DSN. It participates in mission simulation with flight projects.

The capabilities needed to carry out the above functions have evolved in the following technical areas:

(1) The Deep Space Stations, which are distributed around Earth and which, prior to 1964, formed part of the Deep Space Instrumentation Facility. The technology involved in equipping these stations is strongly related to the state of the art of telecommunications and flight-ground design considerations, and is almost completely multimission in character.

(2) The Ground Communications Facility, which provides the capability required for the transmission, reception, and monitoring of Earth-based, point-to-point communications between the stations and the Network

Operations Control Center at JPL, Pasadena, and to the JPL Mission Operations Centers. Four communications disciplines are provided: teletype, voice, high-speed, and wideband. The Ground Communications Facility uses the capabilities provided by common carriers throughout the world, engineered into an integrated system by Goddard Space Flight Center, and controlled from the communications Center located in the Space Flight Operations Facility (Building 230) at JPL.

The Network Operations Control Center is the functional entity for centralized operational control of the Network and interfaces with the users. It has two separable functional elements; namely, Network Operations Control and Network Data Processing. The functions of the Network Operations Control are:

(1) Control and coordination of Network support to meet commitments to Network users.

(2) Utilization of the Network data processing computing capability to generate all standards and limits required for Network operations.

(3) Utilization of Network data processing computing capability to analyze and validate the performance of all Network systems.

The personnel who carry out the above functions are located in the Space Flight Operations Facility, where mission operations functions are carried out by certain flight projects. Network personnel are directed by an Operations Control Chief. The functions of the Network Data Processing are:

(1) Processing of data used by Network Operations Control for control and analysis of the Network.

(2) Display in the Network Operations Control Area of data processed in the Network Data Processing Area.

(3) Interface with communications circuits for input to and output from the Network Data Processing Area.

(4) Data logging and production of the intermediate data records.

The personnel who carry out these functions are located approximately 200 meters from the Space Flight Operations Facility. The equipment consists of minicomputers for real-time data system monitoring, two XDS Sigma 5s, display, magnetic tape recorders, and appropriate interface equipment with the ground data communications.

D1/32

N80-33434

DSN Ground Communications Facility

R. H. Evans
TDA Engineering Section

A functional description of the GCF and its relationships with other elements of the DSN and NASCOM is presented together with development objectives and goals and comments on implementation activities in support of flight projects.

I. Introduction

The Ground Communications Facility (GCF) is one of the three elements of the DSN. The GCF provides for transmission, reception, and monitoring of Earth-based point-to-point communications between the Deep Space Stations (DSSs, one of the DSN elements), the Network Operations Control Center (NOCC, the other element) located at JPL, Pasadena, and the Mission Operations Control Center (MOC) at JPL. Voice, teletype, high-speed data, and wideband data channels of the world-wide NASA Communications Network (NASCOM) are utilized for all long-distance circuits, except those between JPL and the Goldstone Deep Space Communications Complex (GDSCC). Goddard Space Flight Center (GSFC) NASCOM Engineering has delegated the responsibilities for planning, budgeting, design, implementation, operation, and maintenance of the communications requirements between Goldstone and JPL to the DSN GCF. Additionally, the GCF provides communications services between the DSSs at each geographic communications complex (Spain, Australia and Goldstone, Calif.) via intersite microwave system capabilities, and between separated areas of the NOCC at JPL via 230-kbit/s wideband data channels. Also, voice communications are provided within the stations, between the stations, within the complexes, and within the NOCC. The GCF is comprised of eight subsystems; Voice, Teletype, High-Speed Data, Wideband Data, Monitor and Control, Data Records, Network Log Processor, and Network Communications Equipment. The DSN Tracking and Data Acquisition Engineering Office of JPL provides the technical direction and systems management of the GCF and acts as the representative of NASCOM for switching and interconnect functions on the West Coast.

II. GCF-NASCOM Interrelationships

The interrelationships at the programmatic level between JPL's DSN GCF and the NASCOM network, managed, engineered, and controlled at GSFC, are characterized as follows:

NASCOM:

(1) Provides long-haul operational ground communications in support of all NASA projects and mission activities including those supported by the DSN.

(2) Accepts and supports communications requirements established by the DSN and validated through continuing consultation and review.

(3) Establishes in consultation with the users the basic characteristics of the NASCOM systems, such as teletype line rate and block header formats for switching, and the user electrical interfaces.

GCF:

(1) Provides ground communications for all DSN missions and uses the services of NASCOM.

(2) Establishes additional characteristics of all GCF subsystems on an end-to-end basis such as block multiplexing, error correction, monitoring and control, and data records capabilities.

III. Objectives and Goals

The primary objectives of the GCF are to provide highest quality point-to-point transfer of operational data within the DSN and provide simple user and NASCOM electrical and operational interfaces. These objectives are being met by:

(1) Providing automatic message switching and routing.

(2) Providing data transmission subsystems that are as transparent to the user as possible.

(3) Minimizing project-dependent equipment within the GCF.

(4) Providing a centralized common user data records capability.

The goals of the GCF are to provide highly reliable and cost-effective data transmission while continuing an adequate capability balance for multiple mission users. These goals include the following:

(1) Equipment and routing redundancy to minimize single-point-of-failure impact.

(2) Error performance which provides essentially block-error-free throughput.

(3) Design coordinated and consistent with the NASCOM Development Program.

IV. Configuration and Functional Subsystem

The current GCF configuration, including the related NASCOM interfaces and functions, is illustrated in Fig. 1. This configuration illustrates the long-haul communication circuit services external to JPL and Deep Space Communications Complexes (except circuits between the Goldstone Complex and JPL) which are the responsibility of NASCOM. The Voice, Teletype, High-Speed Data, Wideband Data, and Monitor and Control Subsystems point-to-point communications are serviced by this Fig. 1 configuration.

A. High-Speed Data Subsystem

This subsystem shall consist of GCF assemblies that switch, transmit, record, process, distribute, test, and monitor digital data and is used for transmission of:

(1) All digital data for the DSN Command, Tracking, and Monitor Control Systems.

(2) All low or medium rate data of the DSN Telemetry, Radio Science, Very Long Baseline Interferometry (VLBI), and the DSN Test and Training System.

The High-Speed Data Subsystem provides a capability for transmitting and receiving the serial bit stream formatted data over a properly conditioned full duplex alternate voice/data channel having a 3.0-kHz bandwidth. This serial bit stream is impressed on communication circuits at a continuous line bit rate divided into message segments referred to as high-speed data blocks.

Two types of data blocks are used:

(1) Data blocks containing user data bits to be transmitted.

(2) Filler blocks containing filler data bits provided by the GCF when the user data bit/block rate is insufficient to maintain the contiguous bit/block rate required for continuous line monitoring and error control.

Current capabilities for the GCF Mark III period provide the functional capabilities illustrated in Fig. 2. The GCF High-Speed Data Subsystem is standardized on a 1200-bit block size (message segment) and a line bit rate of 7200 bit/s. Subsystem changes to bring about the Mark III capabilities included conversion from a 33-bit to a 22-bit error detection encoding/decoding polynomial code and increasing the number of bits reserved in the data block ending from 36 to 40 bits. The 40-bit block ending with the 22-bit code facilitates numerical serialization and acknowledgement numbers for error correction by retransmission for short outages or errors in GCF end-to-end data transmission.

The error correction capability has significantly reduced the post-pass time required for non-real-time replay of blocks received in error to complete the intermediate data record. Figure 3 illustrates the High-Speed Data Subsystem transitional configuration (in a simplified manner) that was planned for the CY 1977 and CY 1978 time period. The transitional configuration (old and new configurations and interfaces separately or in combinations operational and usable) was required to provide continuous support for ongoing and new

projects starting up until the conversion from the old Ground Data System to the new one was completed to support Voyager and Pioneer Venus Projects and the continued extended mission of the Viking Project through early CY 1979 (subsequent Viking mission extensions caused continuance of old system and its interfaces until March 1980). The dual-mode configuration became operable and usable to support DSN System Testing in November 1977. The added new computer-to-computer switched interface became operational in limited form in early CY 1978 serving the Pioneer Venus Project, other ongoing Pioneer Projects, and the Helios Project with the new Ames Research Center and DSN-NOCC interface in the 22-bit polynomial error detection mode. This new computer switched interface to the Mission Control and Computing Center (MCCC) became operational supporting the Voyager Project in September 1978. The Voyager Project began using the high-speed data subsystem in the error correction mode on November 11, 1978, with the Helios and Pioneer Project following suit shortly thereafter.

The Viking Project agreed to convert to the new standard 22-bit error detection code, for the final mission extension beginning in March 1980. The high-speed data subsystem CCT equipment was then reconfigured to eliminate the transitional configuration and the old 33-bit error detection encoding/decoding equipment and hardware interfaces to the NOCC and MCCC.

B. Wideband Data Subsystem

The Wideband Data Subsystem consists of assemblies that switch, transmit, receive, process, distribute, test and monitor data requiring the use of bandwidths greater than those provided by standard high-speed data channels. The GCF Wideband Data Subsystem functionally illustrated in Fig. 4, together with a listing of functional capabilities provided, includes standard wideband circuits as well as all intersite microwave (area microwave) capabilities. The Wideband Data Subsystem is used for the transmission of:

(1) All DSN Telemetry System high-rate data that exceed High-Speed Data Subsystem capabilities.

(2) Data interchange between the NOCC and GCF Communications Terminal at JPL.

(3) Data interchange between DSSs within a complex via intersite microwave, including critical timing signals and receiver baseband signals for antenna arraying and signal combining systems support.

(4) Simulation System Data from the Mission Control and Computing Center/Mission Operations Center to the DSSs.

(5) DSN Test and Training System data from the Network Operations Control Center to the DSSs.

The wideband data circuits for interchange of data between the DSSs and JPL are impressed with serial bit streams at a continuous line rate, typically 56,168, or 230.4 kbit/s, divided into 2400- or 4800-bit message segments (data blocks). The 2400-bit block size will no longer be used since the last user Viking Mission orbiting spacecraft operation was terminated in July 1980. Similar to the high-speed data subsystem, the blocks are either data blocks or filler blocks inserted when the user data load is insufficient to maintain contiguous data blocks.

Engineering planning and design effort was to begin in FY 1979 to implement error correction capability into the wideband data subsystem for inbound data from the DSSs to JPL. This task was delayed and will now be considered for inclusion in the Block IVA GCF design.

C. Voice Subsystem

The Voice Subsystem consists of GCF assemblies that switch, transmit, receive, distribute, test, and monitor transmissions originally generated in vocal form, and includes internal voice communications within the Deep Space Station Communications Complexes, DSSs, and the NOCC. The subsystem service provides capabilities between those areas and to non-DSN area interfaces as follows:

(1) NOCC and DSS.

(2) NOCC and MCCC/MOC (or remote MOC).

(3) MOC and DSS for Command System backup.

The Voice Subsystem functional capabilities and key characteristics include:

(1) Standard voice-data grade circuits for all traffic.

(2) Conferencing capability on one intercontinental circuit during noncritical periods for all deep space stations supporting a single project (individual circuits for each DSS during critical periods, resources permitting).

(3) User-controlled intercom switching.

(4) Circuits used for high-speed data transmission (backup) if required.

(5) Voice traffic recording in the central communications terminal upon request.

D. Teletype Subsystem

The teletype (TTY) subsystem was converted from 5-level Baudot format to eight-level ASCII (American Standard Code for Information Interchange) national standard. GCF and NASCOM engineering began the work in 1979 and completed the conversion of all GCF equipment terminals in August 1980.

The subsystem consists of assemblies that switch, transmit, receive, distribute, test and monitor digital signals at a TTY line rate of 100 words per minute. The operational use of teletype continues to be de-emphasized and is used primarily for emergency backup operational transmissions and administrative communications. Service functions and key characteristics include:

(1) Handling Air Force Eastern Test Range (AFETR) generated predicts for DSN initial acquisition.

(2) Transmitting nonoperational messages between the JPL Message Center and other locations.

(3) Use of standard NASCOM format and the NASCOM communications processor for message switching.

(4) Employment of time division multiplexing techniques to reduce trunk circuit costs.

E. Monitor and Control Subsystem

The Monitor and Control Subsystem consists of assemblies that collect, process, and display the status and performance of the GCF Subsytems in real-time. The Monitor and Control Subsystem with a listing of functional capabilities illustrated in Fig. 5 includes minor subassemblies located at each DSS in the CMF to interface station GCF function status and performance indicators to the CMF for monitor block formatting and transfer to the Central Communications Monitor (CCM) Processor at JPL. The CCM also receives real-time status and performance information from local GCF subsystems. All real-time status and performance information received by the CCM is processed and displayed relative to preset standards and limits to facilitate operations monitoring and technical control. Information and alarms are displayed on continuous line performance and data flow throughput error control.

F. Data Records Subsystem

The DSN requirements for the data record processing and production functions are implemented in the GCF Data Records Subsystem. The Data Records Subsystem consists of assemblies in the CCT that log in real-time, monitor, identify gaps, provide for processing and editing of data gap lists, control data gap recalls from the DSSs and the generation and accounting for Intermediate Data Records (IDRs) and fill data records selected from records of the GCF real-time log.

The existing Data Records capability is a collection of functions distributed through the Data Records Processor, the GCF Network Log and the Network Communications Equipment Subsystems, which uses the NOCC Real-Time Monitor and Network Support Processors to identify, process and edit the gap lists.

G. Network Log Processor Subsystem

The Network Log Processor (NLP) Subsystem consists of GCF miniprocessors, multiple mag tape units, and peripheral I/O assemblies that switch, transmit, receive, process, and record data. The NLP subsystem assemblies are located in the Central Communications Terminal (CCT) for interfacing the CCT with the remotely located DSN Network Data Processing Area (NDPA) and the NDPA with the Network Operations Control Area (NOCA) (see Fig. 6).

The NLP Subsystem provides a Deep Space Network Operations Control interface to monitor and log all data transferred between the DSSs and the local and remote MOCs, to receive all inbound DSS Monitor and Control Response Data, and to transmit all predicts and control messages from the NOCA to the DSSs.

H. Network Communications Equipment Subsystem

The Network Communications Equipment (NCE) Subsystem consists of GCF miniprocessors and peripheral I/O assemblies that switch, transmit and receive data. The NCE Subsystem assemblies are located in the remote NDPA (roughly three quarters of a cable mile distant from the CCT in Building 202 at JPL). The NCE assemblies comprise a GCF Area Communications Terminal located adjacent to the NDPA.

The NCE interchanges multiplexed block formatted data with the NLP subsystem processors located in the CCT over three full-duplex 230-kbit/s wideband data channels extending the GCF interface to the NDPA (see Fig. 6). This GCF-NDPA interface function provides for

(1) Processing data for transmission to and accepting data from the GCF CCT.

(2) Multiplexing/demultiplexing and buffering data for all NDPA processors.

(3) Routing data to and from NDPA processors.

V. Typical Configuration

The DSN GCF is designed for multiple mission support. Improvements and additions are integrated to meet new era and project requirements (Voyager and Pioneer-Venus requirements were completed in CY 1978) while continuing to

support the Viking, Helios, and Pioneer 6 through 11 Projects. Plans for West Coast Switching Center support of the IRAS Project are completed. Requirements for the ISPM and Galileo projects are being defined and included in ongoing plans. Figure 7 illustrates, in general, the GCF configuration for support of these projects. Additionally, remote information centers and other non-DSN NASCOM-serviced installations on the West Coast are serviced through the NASCOM West Coast Switching Center,, an integral part of the GCF 20/Central Communications Terminal at JPL.

VI. Implementation Activities

A. GCF-NOCC Reconfiguration[1]

The task to reconfigure the CCT was begun with requirements specifications established in March 1979 and a responsive design review in October 1979. In brief, the reconfigured CCT will:

(1) Reduce the number of computers in use.

(2) Provide a more timely IDR production capability.

(3) Reduce the complexity of the man/machine interface.

(4) Reduce manpower required at the CCT.

(5) Release the wideband data subsystem Coded Multiplexer/Demultiplexers for reinstallation at the 34-meter DSSs.

(6) Increase the capacity to handle simultaneous wideband data lines at the CCT.

(7) Provide a central console at the CCT for control and monitoring of all GCF subsystems.

B. Mark IVA GCF

Implementation planning and design to meet the requirements of the DSN's Mark IV Long Range Plans was begun in late 1979. The priority design and implementation effort will be to consolidate the data communications interfaces to a single communications processor interface at each of the three Deep Space Communications Complexes (DSCC). This single interface processor will accommodate the DSN's Networks Consolidation Program plans for a single signal processing center located at each DSCC. Other less significant GCF changes and additions required within the DSCC's along with minor changes at the CCT are included in this effort, which is to be completed in 1985 via a transitional phased implementation. With the consolidation of the networks the GCF will see a significant increase in data communications requirements, as both deep space and high elliptical near-earth orbiting spacecraft tracking and data acquisition data throughput will pass through the single communications processor interface with the DSCC.

[1]See Refs. 1 and 2.

References

1. McClure, J. P., "GCF-NOCC Reconfiguration," in *The Deep Space Network Progress Report 42-55*, pp. 86-89, Jet Propulsion Laboratory, Pasadena, California, February 1980.

2. Bremner, D. S., and Hung C-K, "Ground Communication Facility and Network Operations Control Center Reconfiguration," in *The Deep Space Network Progress Report 42-58*, pp. 108-109, Jet Propulsion Laboratory, Pasadena, California, August 1980.

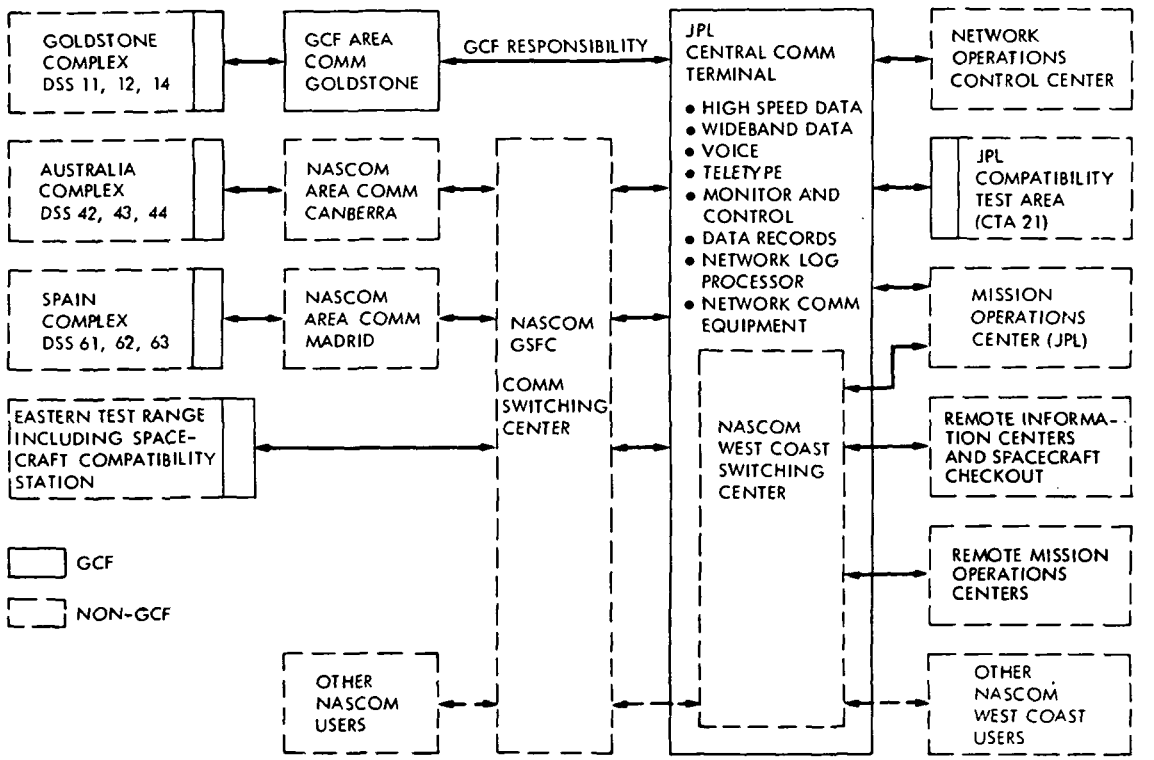
GOLDSTONE COMPLEX DSS 11, 12, 14
GCF AREA COMM GOLDSTONE
GCF RESPONSIBILITY
JPL CENTRAL COMM TERMINAL
• HIGH SPEED DATA
• WIDEBAND DATA
• VOICE
• TELETYPE
• MONITOR AND CONTROL
• DATA RECORDS
• NETWORK LOG PROCESSOR
• NETWORK COMM EQUIPMENT
NETWORK OPERATIONS CONTROL CENTER
AUSTRALIA COMPLEX DSS 42, 43, 44
NASCOM AREA COMM CANBERRA
JPL COMPATIBILITY TEST AREA (CTA 21)
SPAIN COMPLEX DSS 61, 62, 63
NASCOM AREA COMM MADRID
NASCOM GSFC COMM SWITCHING CENTER
MISSION OPERATIONS CENTER (JPL)
EASTERN TEST RANGE INCLUDING SPACE-CRAFT COMPATIBILITY STATION
NASCOM WEST COAST SWITCHING CENTER
REMOTE INFORMATION CENTERS AND SPACECRAFT CHECKOUT
REMOTE MISSION OPERATIONS CENTERS
GCF
NON-GCF
OTHER NASCOM USERS
OTHER NASCOM WEST COAST USERS

Fig. 1. GCF configuration

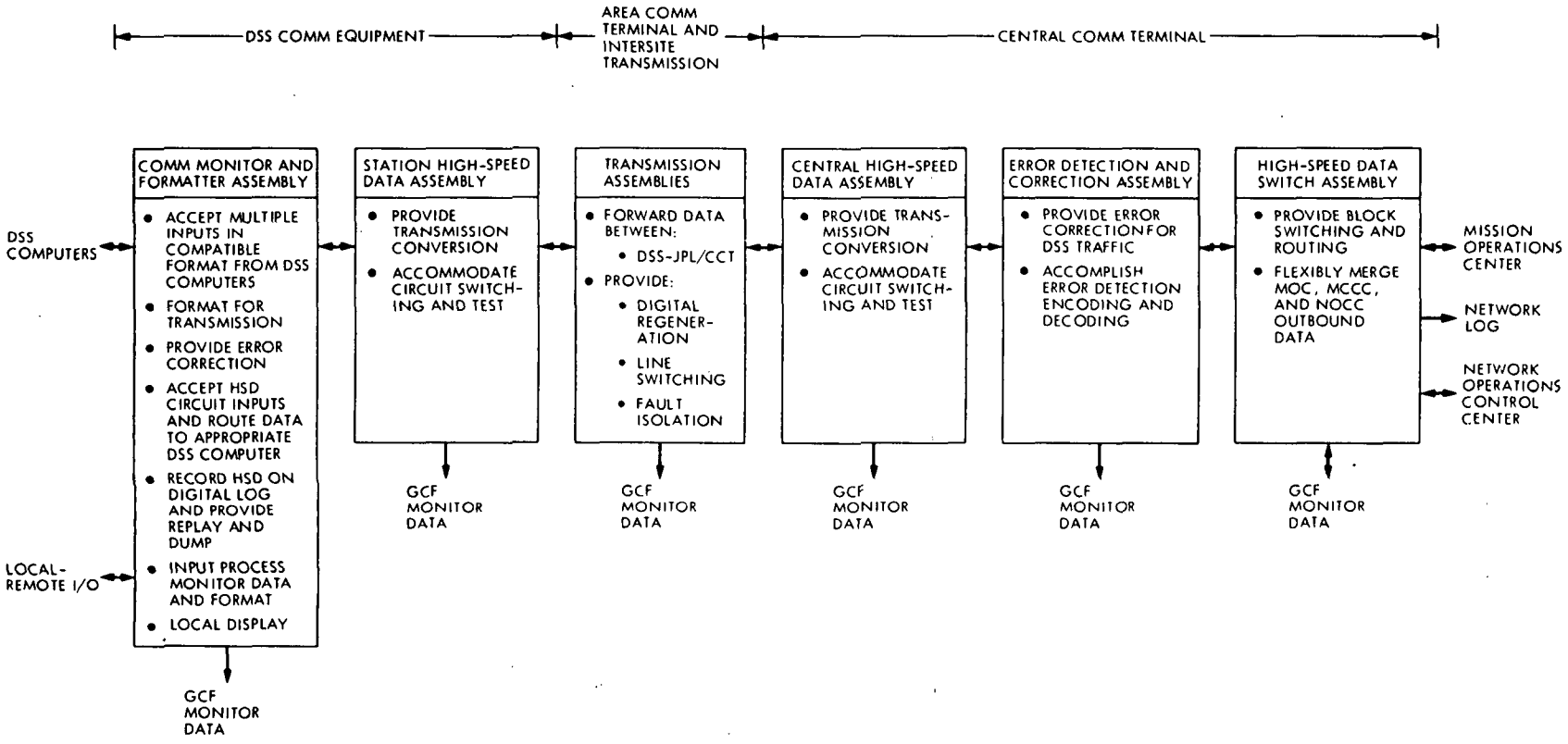
DSS COMM EQUIPMENT
AREA COMM TERMINAL AND INTERSITE TRANSMISSION
CENTRAL COMM TERMINAL
COMM MONITOR AND FORMATTER ASSEMBLY
• ACCEPT MULTIPLE INPUTS IN COMPATIBLE FORMAT FROM DSS COMPUTERS
• FORMAT FOR TRANSMISSION
• PROVIDE ERROR CORRECTION
• ACCEPT HSD CIRCUIT INPUTS AND ROUTE DATA TO APPROPRIATE DSS COMPUTER
• RECORD HSD ON DIGITAL LOG AND PROVIDE REPLAY AND DUMP
• INPUT PROCESS MONITOR DATA AND FORMAT
• LOCAL DISPLAY
DSS COMPUTERS
LOCAL-REMOTE I/O
GCF MONITOR DATA
STATION HIGH-SPEED DATA ASSEMBLY
• PROVIDE TRANSMISSION CONVERSION
• ACCOMMODATE CIRCUIT SWITCHING AND TEST
GCF MONITOR DATA
TRANSMISSION ASSEMBLIES
• FORWARD DATA BETWEEN:
• DSS-JPL/CCT
• PROVIDE:
• DIGITAL REGENERATION
• LINE SWITCHING
• FAULT ISOLATION
GCF MONITOR DATA
CENTRAL HIGH-SPEED DATA ASSEMBLY
• PROVIDE TRANSMISSION CONVERSION
• ACCOMMODATE CIRCUIT SWITCHING AND TEST
GCF MONITOR DATA
ERROR DETECTION AND CORRECTION ASSEMBLY
• PROVIDE ERROR CORRECTION FOR DSS TRAFFIC
• ACCOMPLISH ERROR DETECTION ENCODING AND DECODING
GCF MONITOR DATA
HIGH-SPEED DATA SWITCH ASSEMBLY
• PROVIDE BLOCK SWITCHING AND ROUTING
• FLEXIBLY MERGE MOC, MCCC, AND NOCC OUTBOUND DATA
GCF MONITOR DATA
MISSION OPERATIONS CENTER
NETWORK LOG
NETWORK OPERATIONS CONTROL CENTER

Fig. 2. GCF high-speed data subsystem functional capabilities

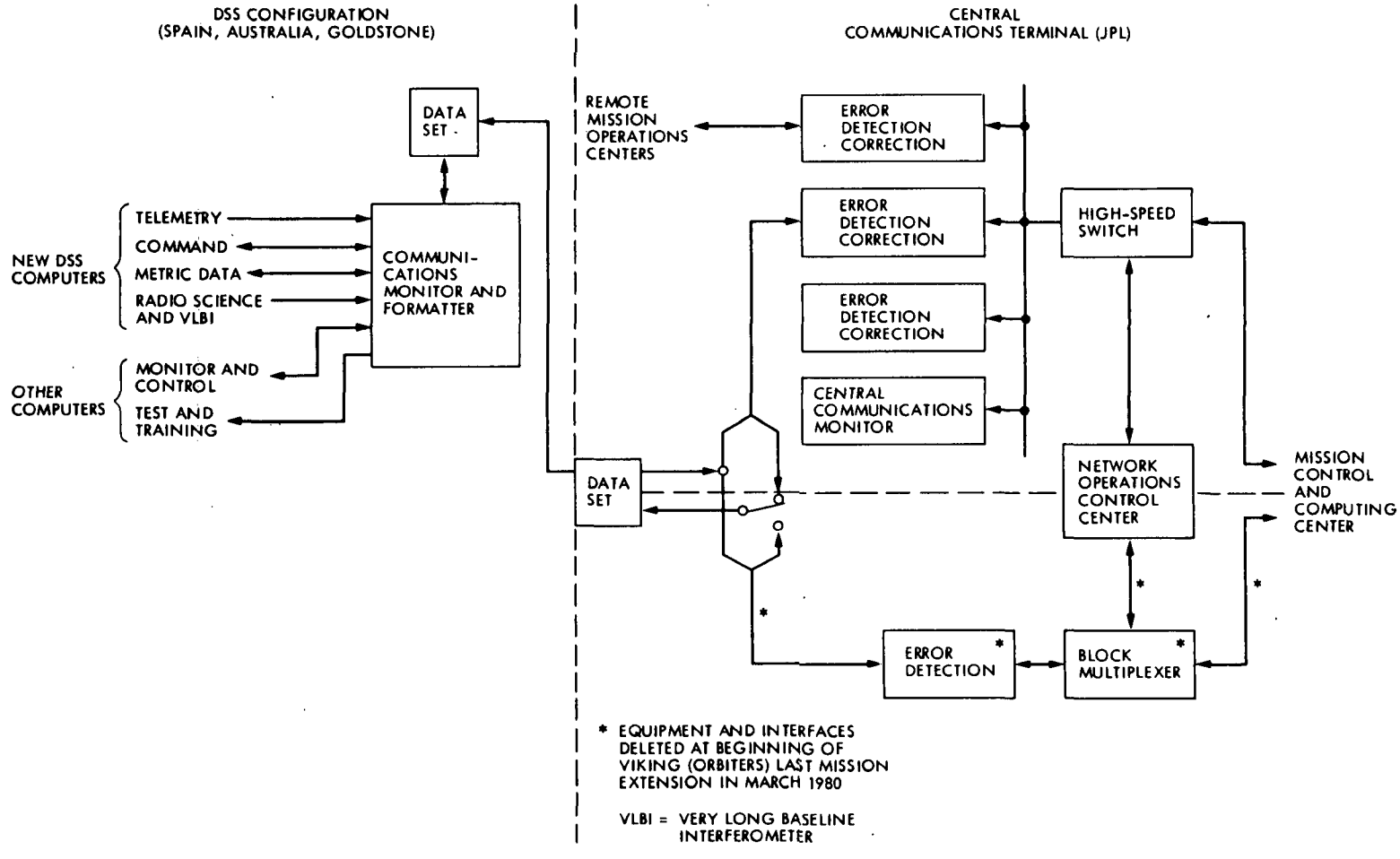

Fig. 3. GCF high-speed subsystem configuration and interface through Viking Extended Missions until March 1980

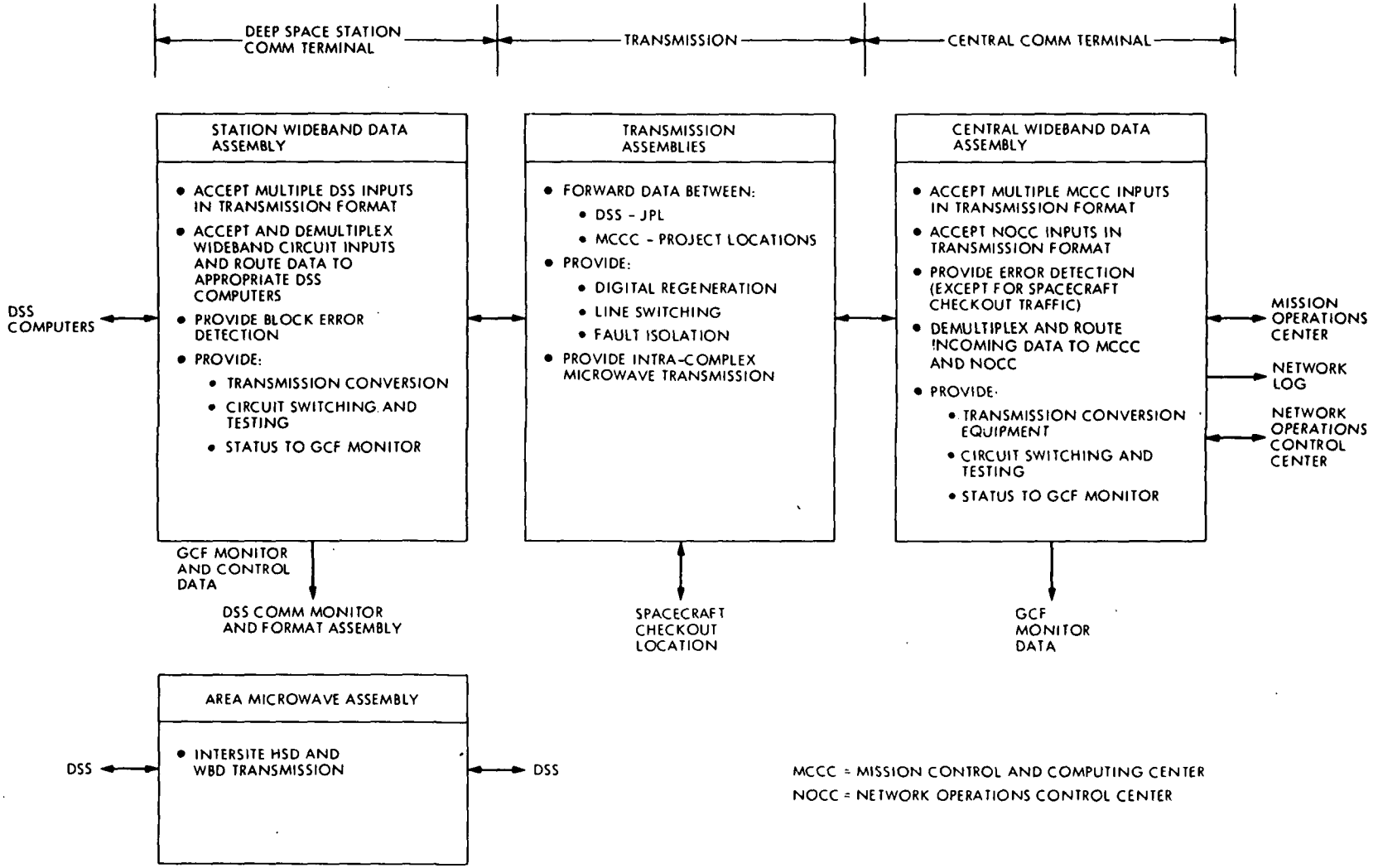
DEEP SPACE STATION COMM TERMINAL
TRANSMISSION
CENTRAL COMM TERMINAL
STATION WIDEBAND DATA ASSEMBLY
• ACCEPT MULTIPLE DSS INPUTS IN TRANSMISSION FORMAT
• ACCEPT AND DEMULTIPLEX WIDEBAND CIRCUIT INPUTS AND ROUTE DATA TO APPROPRIATE DSS COMPUTERS
• PROVIDE BLOCK ERROR DETECTION
• PROVIDE:
• TRANSMISSION CONVERSION
• CIRCUIT SWITCHING AND TESTING
• STATUS TO GCF MONITOR
TRANSMISSION ASSEMBLIES
• FORWARD DATA BETWEEN:
• DSS - JPL
• MCCC - PROJECT LOCATIONS
• PROVIDE:
• DIGITAL REGENERATION
• LINE SWITCHING
• FAULT ISOLATION
• PROVIDE INTRA-COMPLEX MICROWAVE TRANSMISSION
CENTRAL WIDEBAND DATA ASSEMBLY
• ACCEPT MULTIPLE MCCC INPUTS IN TRANSMISSION FORMAT
• ACCEPT NOCC INPUTS IN TRANSMISSION FORMAT
• PROVIDE ERROR DETECTION (EXCEPT FOR SPACECRAFT CHECKOUT TRAFFIC)
• DEMULTIPLEX AND ROUTE INCOMING DATA TO MCCC AND NOCC
• PROVIDE:
• TRANSMISSION CONVERSION EQUIPMENT
• CIRCUIT SWITCHING AND TESTING
• STATUS TO GCF MONITOR
DSS COMPUTERS
MISSION OPERATIONS CENTER
NETWORK LOG
NETWORK OPERATIONS CONTROL CENTER
GCF MONITOR AND CONTROL DATA
DSS COMM MONITOR AND FORMAT ASSEMBLY
SPACECRAFT CHECKOUT LOCATION
GCF MONITOR DATA
AREA MICROWAVE ASSEMBLY
• INTERSITE HSD AND WBD TRANSMISSION
DSS
DSS
MCCC = MISSION CONTROL AND COMPUTING CENTER
NOCC = NETWORK OPERATIONS CONTROL CENTER

Fig. 4. GCF wideband subsystem

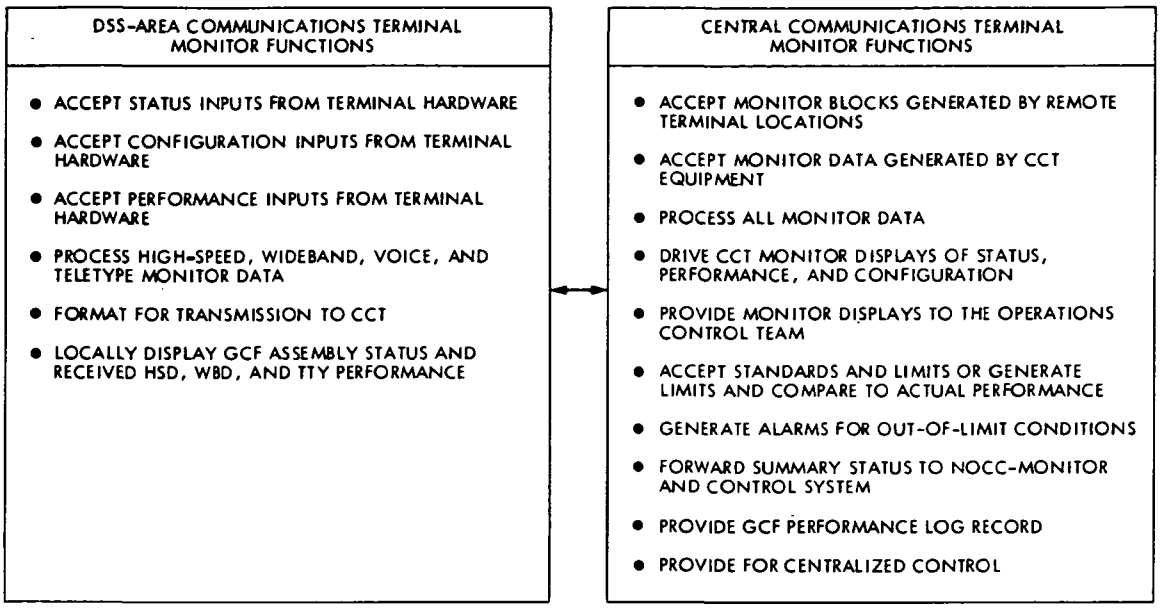
DSS-AREA COMMUNICATIONS TERMINAL MONITOR FUNCTIONS
• ACCEPT STATUS INPUTS FROM TERMINAL HARDWARE
• ACCEPT CONFIGURATION INPUTS FROM TERMINAL HARDWARE
• ACCEPT PERFORMANCE INPUTS FROM TERMINAL HARDWARE
• PROCESS HIGH-SPEED, WIDEBAND, VOICE, AND TELETYPE MONITOR DATA
• FORMAT FOR TRANSMISSION TO CCT
• LOCALLY DISPLAY GCF ASSEMBLY STATUS AND RECEIVED HSD, WBD, AND TTY PERFORMANCE
CENTRAL COMMUNICATIONS TERMINAL MONITOR FUNCTIONS
• ACCEPT MONITOR BLOCKS GENERATED BY REMOTE TERMINAL LOCATIONS
• ACCEPT MONITOR DATA GENERATED BY CCT EQUIPMENT
• PROCESS ALL MONITOR DATA
• DRIVE CCT MONITOR DISPLAYS OF STATUS, PERFORMANCE, AND CONFIGURATION
• PROVIDE MONITOR DISPLAYS TO THE OPERATIONS CONTROL TEAM
• ACCEPT STANDARDS AND LIMITS OR GENERATE LIMITS AND COMPARE TO ACTUAL PERFORMANCE
• GENERATE ALARMS FOR OUT-OF-LIMIT CONDITIONS
• FORWARD SUMMARY STATUS TO NOCC-MONITOR AND CONTROL SYSTEM
• PROVIDE GCF PERFORMANCE LOG RECORD
• PROVIDE FOR CENTRALIZED CONTROL

Fig. 5. GCF Monitor and Control Subsystem functional requirements

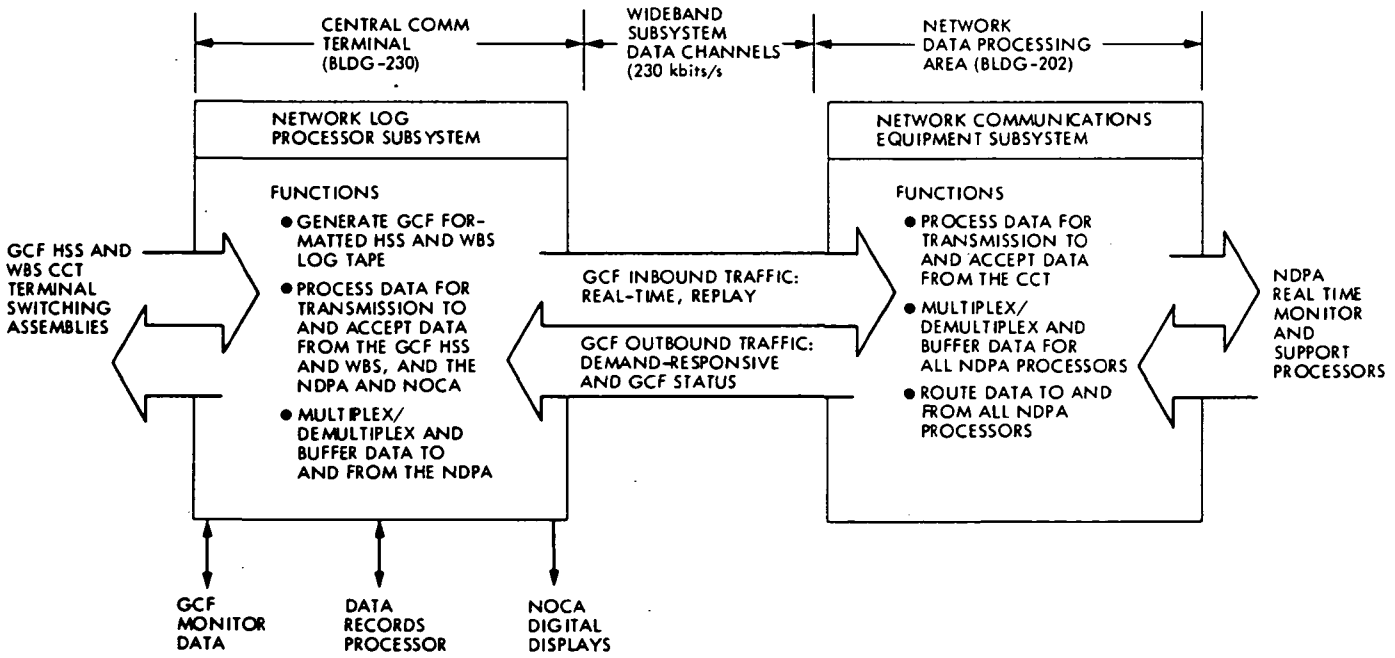
CENTRAL COMM TERMINAL (BLDG-230)
WIDEBAND SUBSYSTEM DATA CHANNELS (230 kbits/s
NETWORK DATA PROCESSING AREA (BLDG-202)
NETWORK LOG PROCESSOR SUBSYSTEM
NETWORK COMMUNICATIONS EQUIPMENT SUBSYSTEM
FUNCTIONS
• GENERATE GCF FORMATTED HSS AND WBS LOG TAPE
• PROCESS DATA FOR TRANSMISSION TO AND ACCEPT DATA FROM THE GCF HSS AND WBS, AND THE NDPA AND NOCA
• MULTIPLEX/ DEMULTIPLEX AND BUFFER DATA TO AND FROM THE NDPA
FUNCTIONS
• PROCESS DATA FOR TRANSMISSION TO AND ACCEPT DATA FROM THE CCT
• MULTIPLEX/ DEMULTIPLEX AND BUFFER DATA FOR ALL NDPA PROCESSORS
• ROUTE DATA TO AND FROM ALL NDPA PROCESSORS
GCF HSS AND WBS CCT TERMINAL SWITCHING ASSEMBLIES
GCF INBOUND TRAFFIC: REAL-TIME, REPLAY
GCF OUTBOUND TRAFFIC: DEMAND-RESPONSIVE AND GCF STATUS
NDPA REAL TIME MONITOR AND SUPPORT PROCESSORS
GCF MONITOR DATA
DATA RECORDS PROCESSOR
NOCA DIGITAL DISPLAYS

Fig. 6. GCF network logging and interface network operation and control subsystems

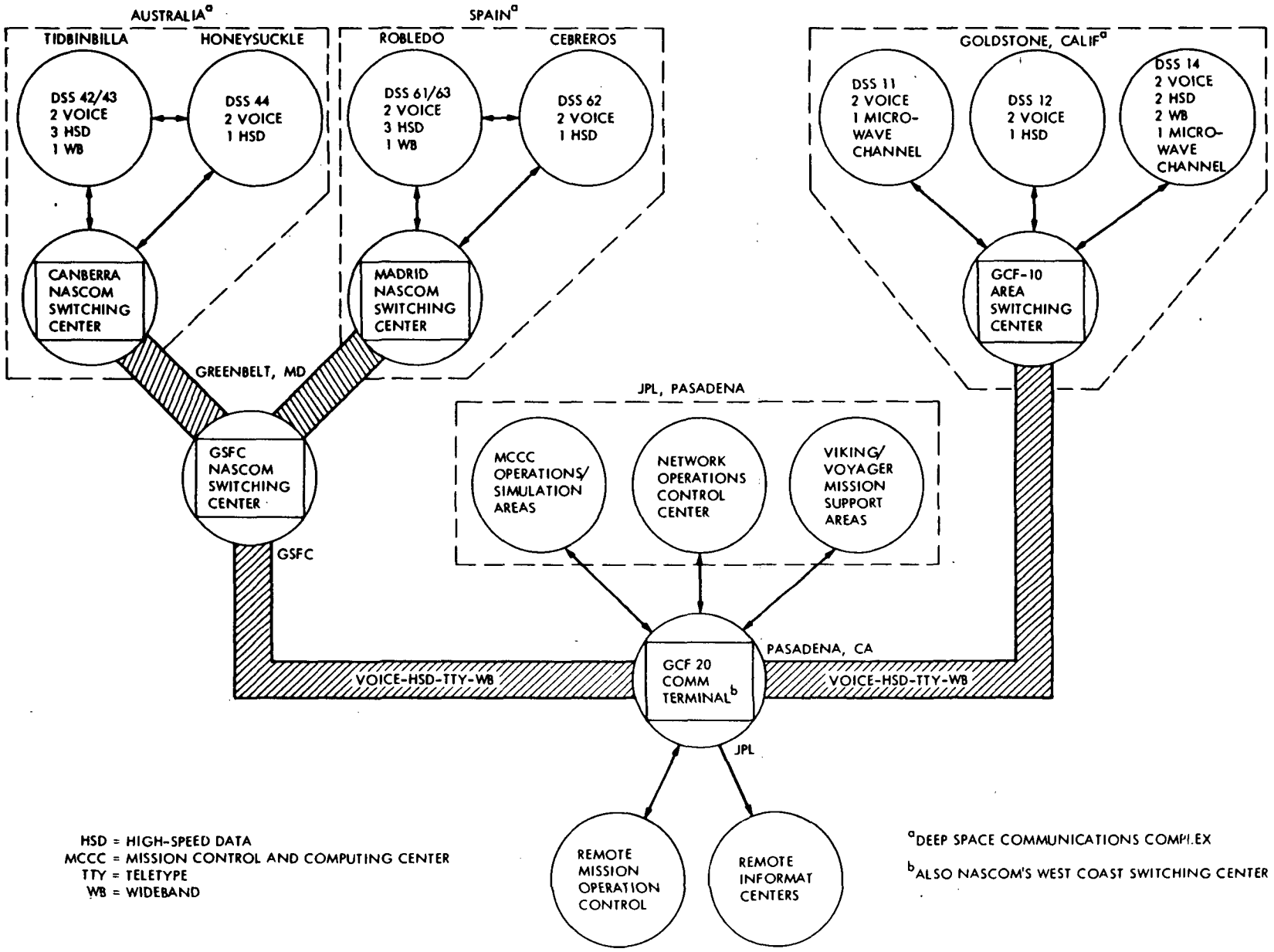

Fig. 7. DSN support locations and GCF-NASCOM circuit requirements

N80-33435

The DSN Programming System

A. P. Irvine
TDA Engineering Office

The DSN Programming System is described by a heuristic model. Interaction with two elements of that system, anomaly reporting and the MBASIC™ language, is described in detail.

I. Introduction

The DSN Programming System is composed of a body of methodologies, tools, and practices whose major components are the following:

(1) DSN Software Standard Practices.

(2) DSN standard programming languages.

(3) Software implementation aids.

(4) Management aids.

The goal of the system is to produce software:

(1) On time.

(2) Within budget.

(3) Conforming correctly to functional requirements.

(4) Of a low life-cycle cost.

Reference 1 presents a hierarchical model of the DSN Programming System, and Ref. 2 describes each major element in detail. This article will describe information flow generated from activities which provide a heuristic process for the DSN Programming System.

II. The Heuristic Model

Heuristic is defined in Ref. 3 as "pertaining to exploratory methods of problem-solving in which solutions are discovered by evaluation of the progress made toward the final result." Figure 1 shows a heuristic model of the DSN Programming System, with information source elements as well as key component elements of the end-to-end system. Also, the paths of information and feedback between the various key elements are shown.

A. Inputs

The inputs to the model, as shown in Fig. 1, consist of the following:

1. TDA planning. The Telecommunications and Data Acquisition (TDA) Planning Office is responsible for generating a DSN Programming System Long-Range Plan which will give, in broad outlines, the general direction of the system.

2. Technology development. Programs developed under the direction of the TDA Technology Development Office provide appropriate research and prototypes prior to implementation.

3. **Research from NASA Centers.** Of particular interest is work being done at the Software Quality Laboratory of the Goddard Space Flight Center and work done under the Multi-Purpose User-Oriented Software Technology (MUST) Project, led by the Langley Research Center.

4. **Other research.** Both industry and universities actively engage in research in the software area. A goal of the Programming System is to make use of research from these sources. An example of this technology transfer would be the use of Program Design Language (PDL) (Ref. 4) instead of flow charts for software documentation.

5. **Operations needs.** The operations organization provides feedback which helps to identify needed improvements to the man-machine interface and to software documentation and operating procedures.

6. **Implementation activities.** The process of implementing software helps to identify and focus needs which should indicate future activities for the Programming System. The necessity for implementation tools and the usefulness of certain procedures are examples of this kind of feedback. Other paths of feedback contain information concerning anomaly rates and schedules which are outputs of the implementation process.

7. **Work Authorization Document (WAD).** The WAD serves as an input of constraints to the Programming System for any given fiscal year.

B. Outputs

The output from the model consists of information which enables the system to direct activities of the components shown in Fig. 1 and listed in the Introduction. All outputs of the system eventually feed into the implementation process.

This article will discuss two subcomponents of the system and how the direction of their activities consists of a heuristic process. The first, anomaly reporting, is a subcomponent of management aids, but is shown as a separate feedback path in Fig. 1 because of its importance to the heuristic model. The second is the MBASIC[tm] language which is a subcomponent of DSN Software Standard Programming Languages.

1. **Anomaly reporting.** Of all the paths of feedback, that of anomaly reporting is one of the more significant. Anomalies can be reported against any discrepancy noted during verification testing and acceptance testing or subsequent transfer. Anomalies are charged against the subsystem or assembly in which the originator believes the anomaly resides. Reference 5 describes how an anomaly rate lower than industry-reported averages was experienced by the DSN Mark III Data Subsystems Implementation Project (MDS) using the DSN Programming System methodology.

The rate of anomalies incurred is only a quantitative measure for feedback. A qualitative assessment is also necessary to determine from where in the software life-cycle many of the errors originate. There are approximately 1000 reports available which are currently classified as to subsystem and severity. Severity is defined as follows:

Category A: Critical to the operation of the software. The software will not function as required.

Category B: Does not meet specifications. The software functions, but may operate in such a manner as to lead to a misunderstanding of the performance.

Category C: Does not prevent software from operating and satisfying all requirements, but is operationally undesirable.

An effort is being initiated by which causal relationships may be uncovered. This will be done by:

(1) Identifying existing software error taxonomies in use that capture meaningful data.

(2) Auditing historical anomaly reports and assigning each anomaly to the appropriate error type.

(3) Also, auditing historical anomaly reports for the time-wise occurrences in relation to the software life-cycle.

(4) Analyzing the data for trends and significant clusterings of error data.

The outcome of this analysis should point to areas where efforts of the system should be directed.

2. **The MBASIC[tm] language.** The MBASIC[tm] language is the DSN standard non-real-time language and is described in Ref. 6. Its initial implementation was as an interpreter. An interpreter essentially consists of an executive routine that, as computation progresses, translates a stored program expressed in some pseudocode or source language into machine code and performs the indicated operations by means of subroutines as they are translated. This method of code execution is much slower than directly executing machine code.

Feedback from costs expended, as reported by users, showed that for Central Processing Unit (CPU) bound jobs in production mode, an interpretive method of execution was very expensive. Based on estimated expenses incurred by the DSN in FY'79, it was determined that the implementation of the MBASIC[tm] language as a compiler was cost-effective. The

speed increase needed to pay for the implementation of the compiler is a five-fold increase in CPU execution times. Any greater increase would not appreciably affect costs. Figure 2 shows the relation between increase in speed and cost-savings.

It has been calculated (Ref. 7) that considerable savings can be realized by the user of higher-order languages. This is true in the implementation of compilers as well as real-time applications programs because compilers exhibit many of the features of a real-time program. Consequently, the PASCAL language was selected as the language of implementation for the MBASIC[tm] compiler. The University of Wisconsin implementation of this language was chosen as the most suitable compiler for this effort. This compiler was recommended by users at the Langley Research Center.

DEMOBASIC, a subset of the MBASIC[tm] language, was implemented on the MODCOMP II and was successfully demonstrated during the Configuration Control and Audit Demonstration. That activity terminated in December 1978. Feedback from the demonstration provided the information and incentive to pursue a complete MBASIC[tm] implementation for the MODCOMP II. DEMOBASIC has been upgraded to match the implementation currently available on the Univac series of computers and is scheduled to be transferred to operations September 15, 1980.

III. Conclusions

Feedback from anomaly reporting indicated that the methodology resulted in a low anomaly rate (Ref. 5) and thereby also provided positive feedback. Further analysis of anomaly reporting will provide more valuable information for future efforts. The need to reduce operating costs prompted the implementation of the MBASIC[tm] compiler, which was written in a higher order language suggested by another NASA Center.

The DSN Programming System can be considered to be both adaptive and heuristic, incorporating new technology as it is introduced and redirecting emphasis as information relevant to the evaluation of progress toward a fixed goal becomes available.

References

1. Hodgson, W. D., "The DSN Programming System," in *The Deep Space Network Progress Report 42-41*, pp. 4-9, Jet Propulsion Laboratory, Pasadena, Calif., Oct. 15, 1977.
2. Irvine, A. P., "The DSN Programming System," in *The Deep Space Network Progress Report 42-50*, pp. 4-6, Jet Propulsion Laboratory, Pasadena, Calif., Apr. 15, 1979.
3. *Computer Glossary*, The Funk and Wagnalls Library of Computer Science, Funk and Wagnalls, New York.
4. Caine, S. H., and Gordon, E. K., *PDL – A Tool for Software Design*, 1975 NCC, AFIPS Press, Montvale, N.J., 1975.
5. Irvine, A., and McKenzie, M., "Evaluation of the DSN Software Methodology," in *The Deep Space Network Progress Report 42-48*, pp. 72-81, Jet Propulsion Laboratory, Pasadena, Calif., Dec. 15, 1978.
6. *MBASIC[tm] Manual*, Volumes I and II, Jet Propulsion Laboratory, Pasadena, Calif., Aug. 1975.
7. McKenzie, M., "Cost Evaluation of a DSN High Level Real-Time Language," in *The Deep Space Network Progress Report 42-42*, pp. 214-225, Jet Propulsion Laboratory, Pasadena, Calif., Dec. 15, 1977.

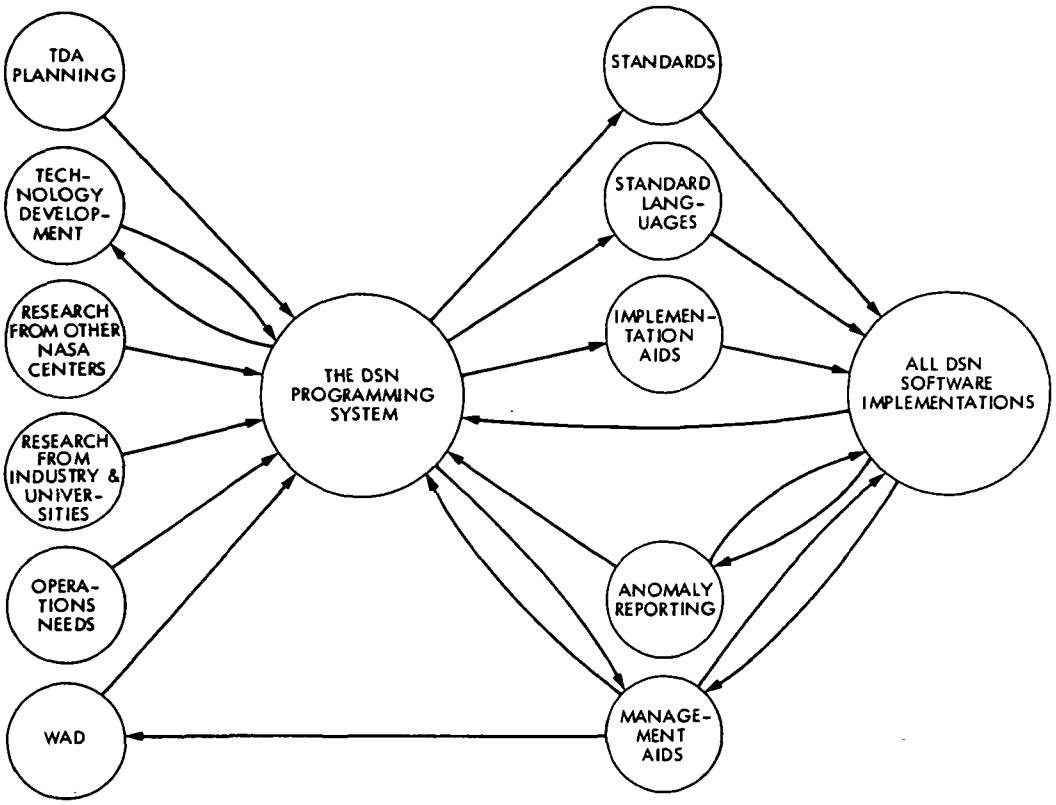

Fig. 1. Heuristic model of DSN Programming System

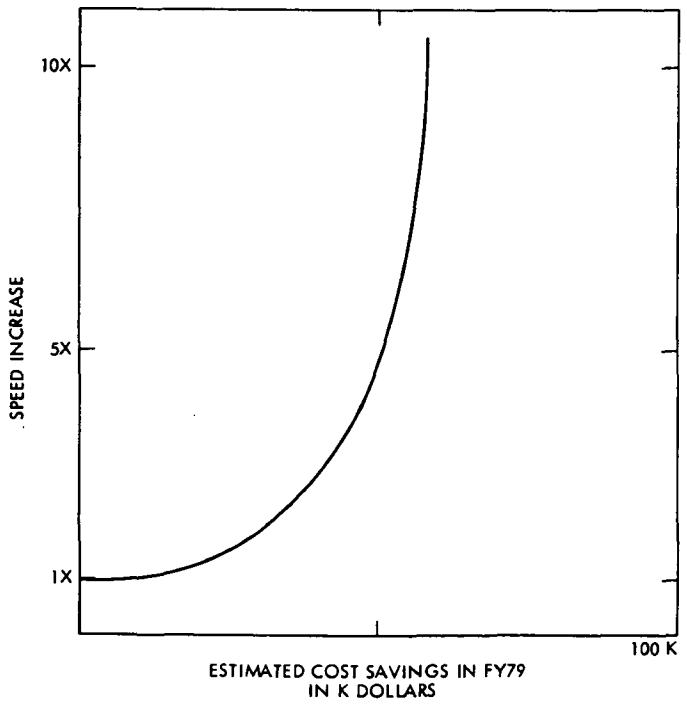

Fig. 2. Speed vs cost

N80-33436

Planning a DSN Support Section Technical Library

T. Bailey and C. C. Chatburn
Deep Space Network Support Section

This article describes the planning procedure being used to establish a technical library for the DSN Support Section. It describes the inventory and survey methods employed and discusses the preliminary results of these methods.

I. Introduction

The information needs of an engineering group cover a broad range, from specific technical information about particular components to generic information about classes of equipment. In time, the amount of information that the engineer needs and stores in personal files becomes overwhelming. The Deep Space Network Support Section is taking steps to organize and control this information by establishing the Support Section Technical Library. The methods used to plan the library can be applied by other organizations with similar problems. The purpose of this article is to outline the progress to date.

II. Technical Library Goals

Success of a technical library is achieved when its services are designed to meet the specific needs of the individual users rather than conform to traditional library services. In fact, if a library is to justify its existence, it must be fully responsive to the information needs of the personnel it serves (Ref. 1). There is no simple way to determine the information needs of potential users, and unfortunately there are no procedural manuals available for conducting user studies in these areas.

In the present situation, each engineer is responsible for the collection, storage, retrieval, and distribution of documentation associated with his or her work. There is no central control of documentation received, and as a result, it is not known how much documentation exists or to what extent it is utilized. The technical library will be established to coordinate these functions to ensure that information is being utilized in the most effective manner.

III. Information Resource Inventory

To design a technical library, it is necessary to identify the information resources presently in use and to understand the information needs of the users (Ref. 2). This process includes an inventory of the materials in use and a survey of the user needs with regard to possible library services. An inventory of all materials will enable space requirements to be estimated, and the decision to centralize or decentralize materials can be made. The survey provides information to determine which service requirements are needed by which personnel, and can help in the estimation of manpower needed to support the services.

The inventory process consists of cataloging all information materials in each staff member's collection. The end product of the inventory is a composite list that shows the location and number of copies of existing materials. The list will serve as the basis for a retrieval system that allows the sharing of such materials as reference books and periodicals, which are in an individual's personal collection. This will help eliminate unnecessary duplication of documents and serve also as a speedy means to acquire information that is presently available within the section.

IV. User Surveys

The first step in planning the Support Section Technical Library was a personal interview with each prospective user. The interview served as a means to inform personnel that a section library was being established and to introduce ideas and receive suggestions as to services and collection content.

The second step of the survey consisted of a series of questionnaires. The first questionnaire (Fig. 1) is designed to gather data on the information sources now in use, the level of importance of each source, and the level of satisfaction in acquiring, maintaining, and disseminating information. The frequency of use that the various types of documents receive is also learned. The purpose of this questionnaire is to gain understanding of the information structure that now exists in the Section.

The second questionnaire is designed to learn what information services are required to improve the existing information structure in the Section (Fig. 2). Here, use patterns of library facilities and attitudes toward library organization systems are examined. Also, questions are asked concerning previous experience in using library services and attitudes toward projected service. Results from this questionnaire will provide information necessary to plan the organization system and services that the library will implement.

A final questionnaire will be given after the library has been in operation for several months. Personnel will be requested to evaluate the new information system as to level of satisfaction with services and collection content. The results of this questionnaire will serve as a check point to see if the library is operating in an effective manner.

V. Preliminary Results

We are still in the survey phase, but certain items have been noted. The interviews found an overall positive reaction to the formation of a section library. The engineers' number-one concern is that it be designed to serve their individual needs in contrast to merely developing a collection of documents.

The inventory process revealed that duplication exists in the various collections. However, the duplicates are not necessarily of the same revision level, so some users have collections of outdated material. Each personal collection tends to be job-function oriented, and includes such information sources as textbooks and vendor catalogs. The average engineer currently uses from seven to nine linear feet of shelf space for his personal reference collection. How much of this information can be centralized is yet to be determined.

Personnel indicated in the questionnaire that they have ready access to information materials; however, they have to order the materials, and, in turn, the items become a permanent part of their personal reference collection. The staff felt that this system was satisfactory, but that they would prefer a centralized reference collection that would reduce the need to order copies and would minimize the size of their personal files.

Acquiring and maintaining documents is not thought to take a great deal of time, but the interview and inventory process demonstrated that most of the personal collections are not up-to-date, and contain materials no longer needed. Also, engineers indicated that the information they need is available but not easy to find, and that the time delay in acquiring documents disrupts their work activity. These apparent contradictions need further investigation. The most important sources of information are internal documents and personal contacts with colleagues. External documents, textbooks, handbooks, and journals ranked fairly evenly from very important to not important. The degree of importance is directly related to the individual's specific work activities.

VI. Conclusion

The need for a DSN Support Section Technical Library has been demonstrated. The details of its implementation remain to be worked out. The final survey results and implementation details will be presented in a future article.

References

1. *Contemporary Problems in Technical Library and Information Center Management: a State-of-the-Art*, edited by A. M. Rees. American Society for Information Science, Washington, D.C., 1974.
2. Batten, W. E., *Handbook of Special Librarianship and Information Work*, 4th ed., Aslib, London, 1975.

NAME _____ DATE _____

The following questions are designed to provide a general overview of your personal experience and attitudes of information usage in your work. The information will be used to help plan a section library.

1. Please agree or disagree with the following statements:

Circle the number that best describes your level of agreement.

1 = agree 100%
2 = agree 75%
3 = agree 50%
4 = agree 25%
5 = disagree 100%

a. I have ready access to all information needed for a project.	1	2	3	4	5
b. The information I need is available, but not easy to find.	1	2	3	4	5
c. Time delay in acquiring documents disrupts my work activity.	1	2	3	4	5
d. I am aware of the information services available to me that the JPL library provides.	1	2	3	4	5
e. Acquiring and maintaining documents requires a great deal of time.	1	2	3	4	5
f. Because of time pressure associated with my job, I am not able to make a thorough search for information I need to complete a project.	1	2	3	4	5

2. How important are the following information sources in the performance of your work?

	not important				very important
a. Personal contacts with colleagues in your work group	1	2	3	4	5
b. Personal contacts with colleagues at JPL	1	2	3	4	5
c. Personal contacts with outside organizations	1	2	3	4	5
d. Internal documents	1	2	3	4	5
e. External documents	1	2	3	4	5
f. Science and technical journals	1	2	3	4	5
g. Other periodicals and journals	1	2	3	4	5
h. Textbooks	1	2	3	4	5
i. Engineering handbooks	1	2	3	4	5
j. Documentation department	1	2	3	4	5
k. JPL library	1	2	3	4	5

Fig. 1. Sample document usage questionnaire

3. For what sub-systems do you need information? _____

4. How often do you use the following types of documents? (X = Yes)
Please provide an X for each document type.

	Frequently	Seldom	Never
General Specifications			
Detail Specifications			
Design Specifications			
Functional Requirements			
Test Specifications			
Test Descriptions			
Test Procedures			
Operation Procedures			
Installation Procedures			
Process Specifications			
Modification Procedures			
Technical Descriptions			
Technical Requirements			
Project Implementation Plans			
Engineering Data Lists			

	Frequently	Seldom	Never
Quality Assurance Documents			
Software & Firmware Document			
DSN Standards			
DSN Standard Instructions			
DSN Standard Procedures			
Commercial Manuals TM's			
JPL Technical Manuals			
Maintenance Procedures			
Engineering Reports			
DSN Energy Project Reports			
Vendor Catalogs			
800 Series Documents			
377/422 Section Documents			
Training Manuals			
DSN Progress Reports			

5. When the section moves off lab, will this affect the way you acquire or use information? Yes _____ No _____ Briefly explain:

_____

_____

_____

_____

Fig. 1. (contd)

NAME _____ DATE _____

The following are questions designed to provide information about what information resources and services you would like in connection with your work. The information will be used to help decide what materials should be included in the library collection and what services need to be provided. If you are not familiar with the function that the services perform, please read the definitions provided. (Feel free to include as much information about your personal information needs--write in the margins or on the back of this sheet.)

1.1 When considering a section library, what materials would you like to have in connection with your work?

	Yes	No		Yes	No
JPL documents	____	____	Aperature Cards	____	____
Reference books (e.g., dictionaries, handbooks, etc.)	____	____	Telephone Directories	____	____
			Maps/Atlases	____	____
Textb· 'ks	____	____	Other_____	____	____
Periodicals/Journals	____	____	Other_____	____	____
Vendors Catalogs	____	____	Other_____	____	____

DEFINITIONS OF LIBRARY SERVICES

Literature Search	A systematic and exhaustive search for material on a specific subject.
Bibliographies	An annotated catalog of documents that refers to writings related to a subject, period, author, or other unifying concept.
Acquisition Lists	Lists of new materials received by the library. (This would include updates)
Abstracts	A condensation of document contents which covers all pertinent points appears in the document.
Reference and Information Services	Personal assistance by the librarian to individual information
Routing of Periodicals	The systematic circulation of periodicals or other printed materials among individuals or an organization in accordance with their information needs.
Acquisition Requests	Ordering specific materials that are requested by individuals.

1.2 Of the services listed above, which do you need in connection with your work?

	Yes	No		Yes	No
Literature Searches	____	____	Reference & Information Services	____	____
Compilation of Bibliographies	____	____	Routine of Periodicals	____	____
Acquisition Lists	____	____	Acquisition Requests	____	____
Abstracts Prepared	____	____			

Fig. 2. Sample library services questionnaire

1.3 Do you feel that space and equipment should be provided so that personnel can study materials in the library? (e.g., study tables)

Yes _____ No _____

1.4 Would you please list the scientific, technical or general purpose publications that you review on a regular basis in your work: (e.g., IEE Spectrum, Business Week, etc.) Indicate with an X if JPL provides these publications.

_____ _____ _____

_____ _____ _____

_____ _____ _____

1.5 On the average how quickly do you need information? (indicate with an X)

immediately	_____	within a week	_____
within a few hours	_____	within a month	_____
by the next day	_____	time is not important	_____

****

Studies have found that engineers do not use library services to their full advantage because they are not aware of the full potential and possible applications of the services. Another deterring factor is that library resources and services are not readily accessible because of physical distance. The following questions are designed to find out your library use habits and how valuable library services and resources are in meeting your information needs.

2.1 How often do you use the library? (Concerning section library, estimate frequency of use.)

	Daily	2-3 Times a Week	Weekly	Monthly	2-3 Times a Year	Once a Year	State briefly the reason for your latest visit to the library. (e.g., general reading, to find a specific fact, etc.)
JPL Library							
Public Library							
School/Univ. Library							

2.2 When you go to the library, do you ask the librarian for assistance?

often _____ once in awhile _____ never _____

2.3 If you never use the library, please try to state why:

_____

_____

Fig. 2. (contd)

2.4 Which JPL library services have you used and how satisfactory were they in meeting your information requirements? (X=yes)

	not satisfactory				satisfactory
Reference and information service _____	1	2	3	4	5
Literature searches _____	1	2	3	4	5
Computer search services _____	1	2	3	4	5
Photocopying _____	1	2	3	4	5
Routing of periodicals _____	1	2	3	4	5
Acquisition lists _____	1	2	3	4	5
Microfilm services _____	1	2	3	4	5
Other _____	1	2	3	4	5

2.5 Which JPL library sources have you used and now useful were they in meeting your information requirements? (X=yes)

	not useful				useful
None _____	1	2	3	4	5
Periodicals and journals _____	1	2	3	4	5
Indexes and abstracts _____	1	2	3	4	5
Technical reports _____	1	2	3	4	5
Books _____	1	2	3	4	5
Other _____	1	2	3	4	5
Other _____	1	2	3	4	5

Fig. 2. (contd)

D10

N80-33437

International Solar Polar Mission

R. B. Miller
TDA Mission Support Office

The key configurations and characteristics of the two International Solar Polar Mission spacecraft are described.

I. Introduction

The International Solar Polar Mission (ISPM) is a joint activity of the European Space Agency (ESA) and the National Aeronautics and Space Administration (NASA). The NASA portion of the Project is under the Solar Terrestrial Program of the Office of Space Science. The NASA Project management is at JPL. The ESA portion of the mission is under the Scientific Program Office of the Scientific and Meteorological Programs Directorate at ESA Headquarters located in Paris, France. The ESA Project management is at the European Space Technology Center (ESTEC) located at Noordwÿk, The Netherlands. ESA will be providing one of the two spacecraft for the mission, about half of the science instruments on both spacecraft, and the spacecraft-dependent mission operations personnel and software. NASA will provide a spacecraft, science instruments on both spacecraft, the RTGs, the launch vehicles, the Mission Operations Control Center for both missions, and the TDA support. The NASA Project Manager at JPL has overall responsibility for the NASA-provided support of the mission.

The ESA spacecraft will be a European industry product using the STAR Consortium of firms, with the systems contract under the leadership of Dornier System GmbH, located near Friedrichshafen, Germany. The NASA spacecraft will also be an industry product, using a systems contract with the TRW Space Systems Group located at Redondo Beach, California.

II. Mission Description

The ISPM project uses a NASA spacecraft and an ESA spacecraft. The two spacecraft are launched from Cape Canaveral, Florida, using separate shuttles, each carrying a three-stage Inertial Upper Stage (IUS). Early this year the design of the third stage of the IUS was changed from spin-stabilized to 3-axis. The launch opportunity opens on 27 March and closes 5 May 1985. The shuttle ascends from the Cape to a 150-nautical-mile-altitude circular parking orbit. After spacecraft checkout, the IUS with its NASA or ESA payload is deployed. At the proper time, the IUS ignition sequence delivers the spacecraft on an interplanetary trajectory to Jupiter.

The NASA and ESA spacecraft travel nearly in the ecliptic to Jupiter. The spacecraft will be targeted to utilize the Jovian gravitational field to deflect both spacecraft out of the ecliptic, one north and the other south. After Jupiter flyby, both spacecraft will travel in heliocentric, out-of-ecliptic orbits with high heliographic inclination, with a simultaneous pass encompassing one solar sidereal revolution at heliographic

latitude above |70|.* At maximum latitude, the distance from the Sun will be approximately 2 AU. After the polar pass, the two spacecraft will go through perihelion at about 1 AU and then enter a second high latitude phase with the spacecraft at opposite hemispheres. The mission terminates in late 1989 at the end of the second polar pass when the two spacecraft again cross below |70| degrees heliographic latitude.

The primary mission objectives of the ISPM are to investigate, as a function of solar latitude, the properties of the solar corona, the solar wind, the sun/wind interface, the heliospheric magnetic field, solar and nonsolar cosmic rays, and the interstellar/interplanetary neutral gas and dust. In addition, instrumentation is included to detect the mysterious gamma ray bursts; it is hoped to pinpoint the sources of these bursts by using triangulation from each spacecraft and the Earth.

The secondary mission objectives include: (1) interplanetary physics investigations during the Earth-to-Jupiter phase when the separation of the two spacecraft will be approximately 0.01 AU, and (2) measurements of the Jovian magnetosphere during the Jupiter flyby phase.

III. Spacecraft Description

A. Spacecraft Characteristics

The ESA spacecraft, shown in Fig. 1, is a Radioisotope Thermoelectric Generator (RTG)-powered, spin-stabilized vehicle. The centrally located equipment compartment accommodates both engineering and science instrument equipment and supports a deployable 5.5-meter instrument boom, a deployable 72-meter dipole antenna, and a deployable 8-meter axial monopole antenna. Only a portion of the 72-meter antenna is pictured in Fig. 1. Propulsion is provided by two groups of thrusters and a single spin-centered propellant tank. The spacecraft is sized to fit within a 4.2-meter-diameter STS launch envelope with a mass on the order of 400 kg.

The NASA spacecraft, shown in Fig. 2, is also an RTG-powered, spin-stabilized vehicle with a centrally located engineering equipment compartment, which supports a deployable 13-meter instrument boom and a deployable 100-meter dipole antenna. Propulsion is provided by two groups of thrusters; telecommunications equipment includes a 2-meter high-gain antenna, which is offset from the spin axis to accommodate the despun platform. A separate science equipment compartment accommodates instrument mounting. The spacecraft is sized to fit within a 4.2-meter-diameter STS launch envelope with a mass of approximately 500 kg. The dominant physical difference between the ESA and NASA spacecraft is the despun CXX (white light, X-ray coronagraph) telescope located on the spin axis of the latter.

B. Telecommunications

The prime communication link for both spacecraft will be via a parabolic antenna parallel to the spin axis. Precession maneuvers will be periodically performed to maintain Earth pointing. X-band downlink will be the prime telemetry source with S-band used for navigation purposes and to provide a TDRSS compatible link in the near-Earth phase. The S-band and X-band downlinks may be noncoherent or coherently derived from the received uplink signal independently. The most common mode expected during the mission would be a split mode with S coherent providing radio metric data, and X noncoherent to avoid telemetry degradation due to turnaround loss. Both spacecraft can be commanded in advance into a state where X- and/or S-band downlinks will automatically switch to coherent upon spacecraft receiver lock or into a state where a command is required to go coherent. Addition of an experimental X-band receive capability on the NASA spacecraft was still undecided at the time of writing.

Pertinent spacecraft telecommunication parameters are listed in Table 1. Both spacecraft will use Viterbi compatible encoding on the telemetry with the NASA spacecraft adding a Reed-Solomon outer code. Both spacecraft will utilize PCM commanding, the NASA spacecraft consistent with NASA Planetary Command Standards and ESA consistent with the ESA Telecommand Standards. The ESA Telecommand Standards are compatible with existing and planned DSN capability but do impact the control center software. Telemetry subcarriers are square-wave; a sine-wave command subcarrier is expected from the DSN.

All antennas are RCP (right-hand circularly polarized). It is expected that the high-gain antenna will be used during the entire mission, except for near-Earth and trajectory correction maneuvers within 30 days of launch.

Both missions will use Viterbi (7, 2) coding. The ESA spacecraft will have a single engineering format and a single science format. Minor frame length will be 1024 bits with a 16-bit sync word. In the engineering format only two minor frames are required to obtain a major frame (European terminology calls a major frame a "format"). Thirty-two minor frames are required in the science format for one science major frame. Two major science frames are required (64 minor frames) to obtain an engineering major frame when in the science format.

*|70| = 70 degrees, absolute value.

The NASA spacecraft will use packet telemetry consistent with the "Multimission Packet Telemetry Guidelines and Standards for Deep Space Missions" (633-9) and a Reed-Solomon outer code. The transport frame length will be 8800 bits with a 24-bit sync word. The Reed-Solomon code is J=8, E=16, I=5. The source packet length will always be 4352 bits.

Both spacecraft will utilize tape recorders to maintain continuity during nontracking periods. The ESA spacecraft recording rates are 128, 256, and 512 b/s. Whenever the spacecraft is being tracked by a DSS, the ESA mission would like to maintain a real-time science transmission rate of 1024 b/s, although a backup rate of 512 b/s is provided. Playback takes place by interleaving real-time and playback frames at the ratios of 1 to 1, 1 to 3, or 1 to 7, resulting in transmission rates of 2048, 4096, or 8192. The ESA recorder implementation will result in playback minor frames being in reverse time order, but each individual minor frame will be forward (i.e., sync word still correct and in the same location as a real-time frame). Science, engineering, real-time, and playback frames will all look the same to DSN hardware and software.

The specific NASA spacecraft record and playback characteristics and formats are not yet established. It is known, however, that all transport packets will look identical to the DSN.

Achieving continuity of the science data for the life of the mission has been a major mission design consideration. The basic design assumes a single 34-meter 8-hour track per day per spacecraft. During the 16-hour nontrack time the onboard recorder will record science data at a reduced data rate, and during the tracking period, higher rate science will be sent in real-time along with a period of recorder dump. Although the daily track is the basic plan, the Project has been cautioned that at certain times during the mission a daily pass of the desired length may not be available due to conflicting requirements of other DSN users. In response some flexibility to take advantage of the telecommunication performance gain of a 64-meter antenna to utilize less frequent or shorter 64-meter tracks to achieve essentially the same net data return is being included in the design of the mission.

Table 1. Telecommunications parameters (all values are preliminary)

Spacecraft	Frequencies, MHz	Telemetry subcarriers, kHz	Telemetry data rates, b/s	Command subcarriers	Command data rates, b/s
ESA	S-up 2111.607253 S-down 2293.148148 X-down 8408.209876 (channel 9)	65.536 131.072	64 to 8192 in factors of 2. (128, 256, and 512 used for recording)	16.000 kHz	15.625 (125/8)
NASA	S-up 2116.040895 X-up[a] 7171.559413 S-down 2297.962963 X-down 8425.864197 (channel 22)	42.3 169.2	11.5 5,154.5 186.1 6,872.7 372.3 13,745.5 744.5 27,490.9 1,489.1 41,236.4 2,863.6 54,981.8 3,436.4	16.000 kHz	125.0 7.8125 (125/16)

	Antenna	Gain, dBi	Final power amplifier, W	Telemetry modulation index, rad
ESA	High gain (X/S) (1.65 m)	TBD/TBD	S: 5	0.56: 64 0.65: 128 to 512
	Omni (S only)	TBD	X: 20	0.9: 1024 1.18 or 1.25: 2048 to 8192
NASA	High gain (X/S) (1.98 m)	42.5/30.8 XMT TBD/30.3 RCV	S: 5	32 levels between (TBD) and (TBD)
	Medium gain (X only)	18.2 XMT	X: 22	
	Broad coverage (S only)	10.7 XMT 10.2 RCV		
	Omni (S only)	TBD		

[a]Proposed.

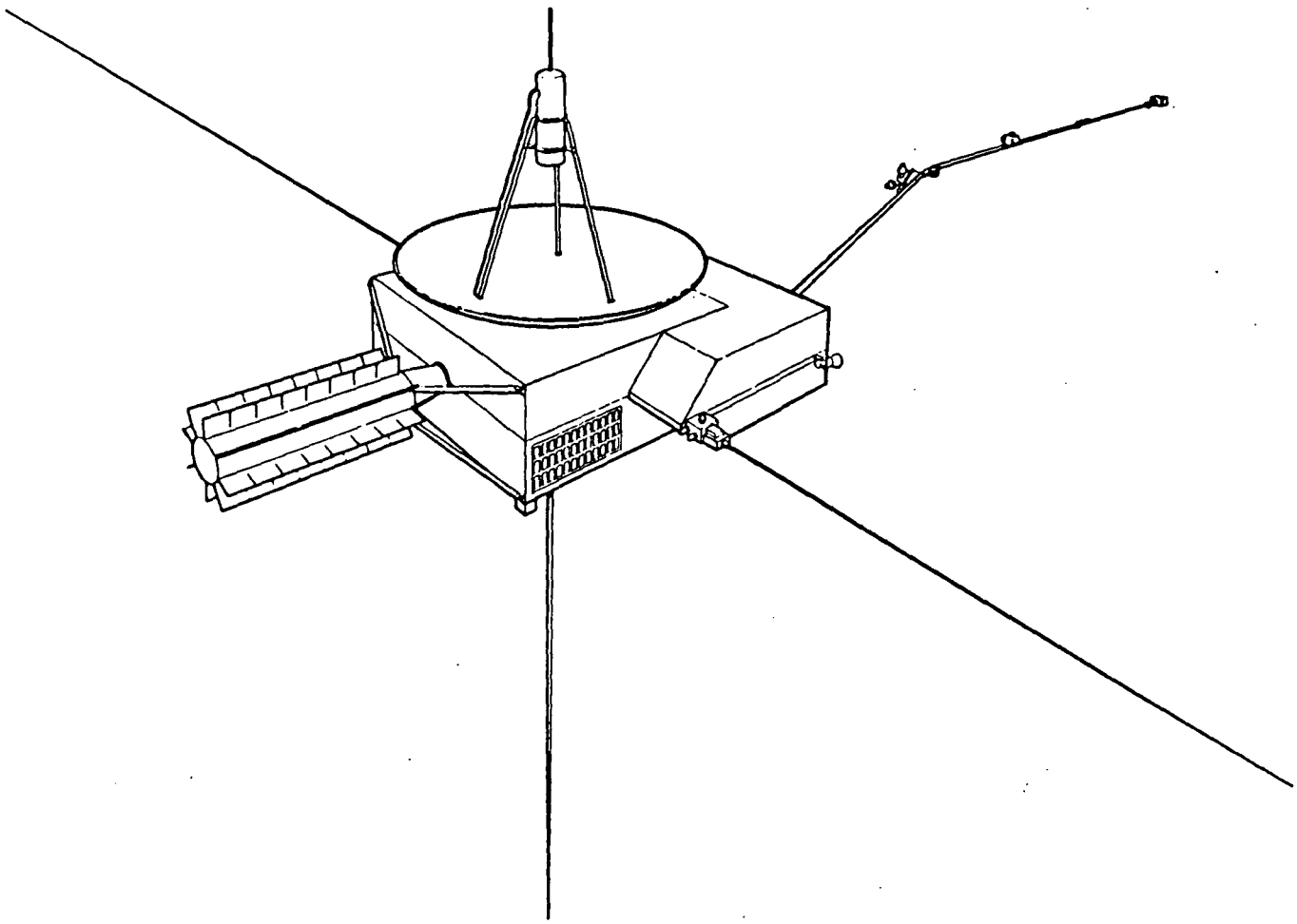

Fig. 1. ISPM spacecraft configuration

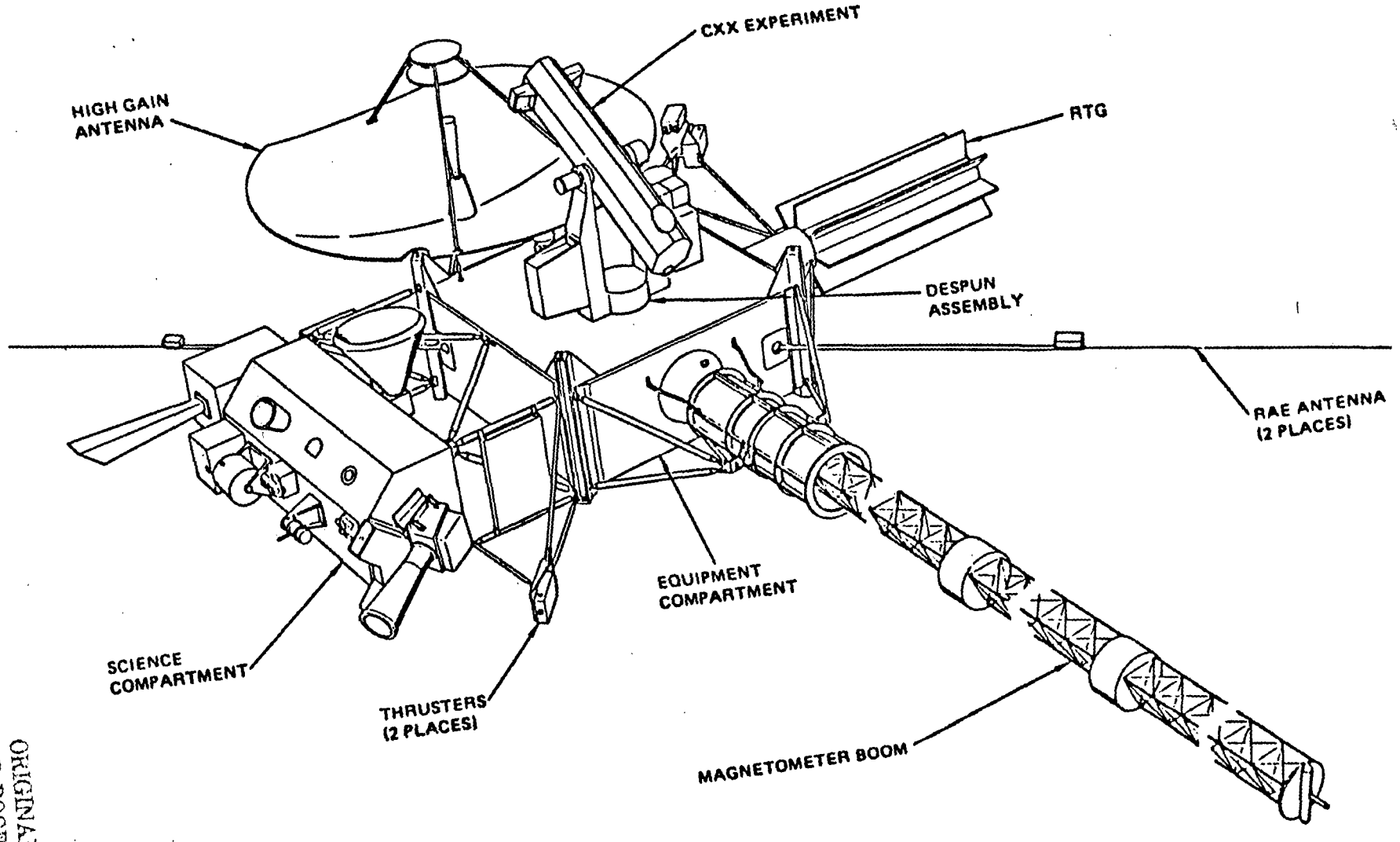

Fig. 2. NASA ISPM spacecraft configuration

ORIGINAL PAGE IS
OF POOR QUALITY

N80-33438

A Study of the Processes in the RF Hydrogen Gas Dissociator

L. Maleki
Communications Systems Research Section

The role of the RF gas dissociator in the hydrogen maser is examined. Based on collisional and plasma transport processes, the performance of the source is investigated. It is found that while the complexity of the collisional processes in the RF dissociator prohibits an easily obtained quantitative expression for the performance of the source, it is nevertheless possible to make general inferences concerning the qualitative performance based on collisional effects. An analytical expression for the efficiency of the source in atom production is obtained based on plasma transport processes. On the basis of this study some recommendations are made for the development of more efficient RF hydrogen gas dissociators for use in masers.

I. Introduction

The performance of the hydrogen gas dissociator has a significant effect on the operation of the hydrogen maser. The dissociator affects the performance of the maser in terms of power output and stability by influencing the flux of the hydrogen atoms (Ref. 1) which radiate through stimulated emission; it also affects the operation of the vacuum pumps, thereby indirectly influencing the operational life of the maser itself.

The most significant effect of the dissociator on the H-maser operation, however, is its direct influence on maser breakdown; experience has shown that the degradation of the dissociator performance is one of the primary causes of maser failure.

It therefore appears that an evaluation of the performance of the hydrogen gas dissociator would prove quite useful in extension of efforts towards optimization of H-maser operation. In particular, understanding of the processes that take place within the hydrogen source would be a valuable aid in the work toward the development of a more rugged dissociator with an improved performance.

In Section II of this report background information on the RF dissociator is given. Processes within the dissociator are outlined in Sections III and IV. Section V briefly outlines interactions with wall material and Section VI gives the summary.

II. Background

Of the number of atomic hydrogen sources used in various applications (Ref. 2) none appears more suitable for the hydrogen maser than the RF dissociator (Fig. 1). The reason for this is the strict requirements of the maser application on

the available sources. Due to the sensitivity of the maser stability to fluctuation in temperature and magnetic field in the environment (Ref. 2), sources which employ high temperatures to produce atomic hydrogen are not well suited. Furthermore, most sources employ either a heated filament or a light source to dissociate the hydrogen molecules and are therefore susceptible to frequent shutdowns necessary to replace or refurbish those elements. This leaves the RF dissociator as the most suitable hydrogen atom source for maser application. Added to the desirable features of long operational life and minimum environmental disturbances of the RF sources are such other attractive characteristics as low power requirement and small size. These latter features are particularly important in the development of spaceborne masers.

The dissociation of molecular hydrogen in all varieties of sources is brought about by inelastic collision of the molecules with other particles. In the case of the RF dissociator, collisions of the molecules with electrons are primarily responsible for atom production.

When hydrogen gas is introduced in the dissociator bulb and the RF power is turned on, any free electrons present in the bulb will oscillate in the RF field. During the course of these oscillations, electrons collide with the molecules, resulting in the production of a number of particles including atoms, ions and other electrons. The new electrons in turn participate in collisions, thereby producing, and sustaining, a plasma discharge.

Although the above outline gives the principle of the operation of the RF source, it neglects many important details of collisions and particle production. It is the study of these other, more detailed processes which would prove of value in the evaluation of the RF dissociator.

III. Collisional Processes in the Dissociator

The rate of any particular reaction between n_e electrons per cubic centimeter and target particles (molecules, atoms, or ions) of density n_i susceptible to the particular reaction in the atom source is determined by the product $(n_i\sigma)(n_e V)$, where σ is the cross section for the particular reaction and V is the relative velocity. Since the mass of the electron is many times smaller than the mass of the target particle, the relative velocity is essentially equal to the electron velocity, if the collision of electrons with other electrons is unimportant in the plasma. When a plasma fulfills certain conditions (Ref. 3), one may consider a certain distribution for the electron velocity. In particular, for the case of the RF dissociator, we consider an average distribution for the product σV, which is designated as $\langle\sigma V\rangle$ and referred to as the rate coefficient for a given reaction. This concept is brought about since the reaction cross section is a function of the reaction energy, or equivalently, of the relative velocity of the particles involved. In the case of the RF dissociator, the electrons typically have a Maxwellian velocity distribution, and reaction cross sections are of the order of 10^{-18} cm^2 for those interactions that have the highest contribution to the source processes. It is now evident that the rate of a given reaction is determined by the electron and particle densities as well as the rate coefficient for the particular reaction.

The inelastic collisions of electrons with molecular hydrogen can result in a number of processes with varied products. While simple dissociation, i.e., $e + H_2 \rightarrow H + H + e$, does occur as the result of collisions, other processes such as electron impact ionization ($e + H_2 \rightarrow H_2^+ + 2e$) and excitation, followed by photon emissions ($e + H_2 \rightarrow e + H_2^* \rightarrow e + H_2 + h\nu$) are also quite likely to occur. In general, the collision of molecules with electrons can result in four types of processes (Ref. 4), viz, dissociation, ionization, excitation, and recombination. Although all these processes do occur in the source to various degrees, a number of them occur so infrequently as to have minimal influence on the performance of the source. We can now try to characterize the significance of each of these processes in the source by studying each process individually.

(1) *Ionization.* Although ionization of particles as a result of electron impact is not the desired product in the atom source, it is nevertheless the primary process contributing to the density of the electrons and thereby affecting the reaction rates. Electron impact can ionize the hydrogen molecules in the following ways:

$$e + H_2 \rightarrow H_2^+ + 2e \quad (1)$$

$$e + H_2 \rightarrow H^+ + H + 2e \quad (2)$$

$$e + H \rightarrow H^+ + 2e \quad (3)$$

All these reactions result in the production of electrons which can now participate in interactions of their own. Process (2) is also an important source of atom production, with a relatively large cross section (Ref. 5) (about 2×10^{-18} cm^2). The contribution of each of these processes to the plasma in the source can best be illustrated by considering the processes which can ensue after the ion is produced in process (1). The H_2^+ ion can undergo additional collisions resulting in the following reactions:

$e + H_2^+ \rightarrow H^+ + H^+ + e$ dissociation ionization

$e + H_2^+ \rightarrow H^+ + H + e$ dissociation excitation

$e + H_2^+ \rightarrow H + H$ dissociation recombination

$e + H_2^+ \rightarrow H^+ + H^-$ pair production

Obviously such reactions are allowed only if energetically possible. But even with electron energies compatible with the above processes, the only reactions with a significant cross section are the dissociative excitations which produce an atom in the reaction; all others have relatively small cross sections and therefore can be neglected in this analysis.

Therefore, it is apparent that all ionization reactions (1) through (3) can occur with almost equal probability, creating secondary electrons needed to sustain the discharge. Furthermore, processes (1) and (2) can lead to reactions which themselves are a source of secondary electrons. While it is comforting that secondary electrons are created in these reactions which can enhance the electronic density in the plasma, it is not necessarily desirable to produce the ions. Ions drift from the plasma and onto the walls, causing wall damage which results in the efficiency degradation of the source. This point will be elaborated upon in Section V.

(2) *Dissociation and Excitation*. These two processes are discussed together, since oftentimes excitation of one of the product particles occurs following electron impact dissociation. In fact, while the cross section for dissociation $H_2 + e \rightarrow H + H + e$ is about 6×10^{-18} cm^2 at 15 eV impact energy, the reaction which would leave one of the atoms in an excited state (with a subsequent decay via the H_α emission) has a cross section only an order of magnitude smaller. Electron impact ionization of the hydrogen molecule may also leave one of the resulting H_2^+ ions or the H atom (as the case might be) in an excited state.

The excited atoms and molecules deexcite by emitting photons producing the light associated with the RF plasmas. Traditionally, the color of this emission is used in the evaluation of the performance of the source. A red/violet hue (primarily due to the Balmer H_α production) is interpreted to signal production of atoms, while radiation associated with molecular emission is taken to mean that the power is dissipated in molecular excitation.

We have already seen that atoms may be produced without H_α emission with cross sections comparable to unexcited atom production. In the study of recombination we shall see that molecular emission may result as molecular ions recombine with electrons; i.e.

$$H_2^+ + e \rightarrow H_2 + h\nu .$$

It should now be evident that the evaluation of the source performance by the color of the source, or other technique based on the comparison of the intensity of atomic emission with molecular emission, is only crudely related to the efficiency of the source in atom production.

(3) *Recombination*. This process leads to the production of neutral species as a result of the reaction of ions with electrons. Although electron recombination with an ion is generally regarded as an undesirable process in ion sources, under certain circumstances it may be regarded as a desired process in atom sources. The recombination of ions (density n_i) with electrons (density n_e) in the plasma is characterized by the recombination rate α where $dn_i/dt = -\alpha n_i n_e$.

Various modes of recombination have various rates associated with them, and the rates usually are a strong function of the electron energy. One of the important modes of recombination in the plasma is radiative recombination, where an ion combining with an electron yields a neutral species and a photon, viz,

$$X^+ + e \rightarrow X^0 + h\nu .$$

For the case of the plasma in the RF dissociator, the rate of radiative recombination α_r is of the order of 10^{-13} cm^{-3} s^{-1}. Another mode of recombination is the dielectronic recombination, which describes the process involving the interaction of an ion and an electron yielding a particle in a highly excited state. The excited particle may then be either ionized again or become stabilized by photon emission or by collision with other particles. In the range of the electron energies present in the RF dissociator the dielectronic recombination rate α_d is usually much larger than the radiative recombination rate for moderate electron energies.

Finally, electronic collisional radiative recombination should be mentioned, which may be described by the reaction

$$X^+ + 2e \rightarrow X + e$$

In the case of a plasma fulfilling certain conditions, Bates et al. give the following relation for the recombination of protons (Ref. 6)

$$\alpha_{eer} \simeq 10^{-8} (T_e)^{9/2} (n_e)$$

where T_e is the electron temperature in kelvin.

The dominant recombination process for the case of hydrogen dissociator is the dissociative recombination, where electron impact on a molecular ion results in the dissociation of the molecule. The process is very efficient, especially at low energies where the cross section for the process can be as large as 10^{-13} cm^2. Dissociative recombination, therefore, can yield hydrogen atoms at an appreciable rate, only if the densities of ions and electrons are not prohibitively low. Ion densities are limited not only by the ionization rate coefficients, but by other phenomena such as drift out of the plasma and wall neutralization. In fact, ion drift is usually a much larger source of ion depletion in the plasma than recombination effects.

Other modes of recombination such as neutral collisional radiative recombination, as well as processes involving charge transfer, have comparatively smaller rates and are of less significance in the study of the hydrogen gas dissociator. The study of production of negative ions and larger molecules and their ions, such as H_3^+, which can also be of significance, will be excluded here.

The significance of recombination in the dissociator is now evident. Recombination can be a source of atom production in the dissociator, as well as a source of photons. While the former effect is desirable, the latter effect contributes to the light produced by the hydrogen source, making the consideration of the color an unreliable technique for the evaluation of the performance of the source, as mentioned before.

So far we have considered the collisional processes that occur in the hydrogen gas dissociator. We can now proceed to formulate a procedure for the evaluation of the rate of atom production in the source. Such an evaluation is in principle simple. Essentially, we can evaluate the rate of atom production by summing all the processes that yield atoms and subtracting all processes that result in the loss of atoms. Specifically, dissociation of hydrogen molecules, dissociative recombination of molecular ions and neutralization of protons yield atoms, while ionization and escape of atoms from the source are the primary atom loss mechanisms. For those mechanisms which have known reaction rates such as dissociation of the molecules, or the dissociative recombination of molecular ions, one may calculate rates, assuming the density of all particles are known. Each rate would be equal to $n_t n_e \langle \sigma_{t,e} v_e \rangle$ where n_e is the density of electrons, n_t the density of the target, $\sigma_{t,e}$ the cross section for the particular process, and $\langle \sigma_{t,e} v_e \rangle$ the rate coefficient. The rate of the escape of the atoms can also be computed from the knowledge of the temperature of the gas and the confinement time. Processes such as recombination of atoms at the walls, and other wall effects are a great deal more difficult to quantify exactly.

IV. Plasma Processes

The only laboratory parameters which affect the performance of the dissociator are the pressure of the hydrogen gas in the dissociator, the RF power input, and the dissociation geometry. Ideally, then, we should look for a relationship between the efficiency of the source and these parameters. While in practice such a relationship is quite difficult to obtain, it is nevertheless possible to examine the efficiency of the source in the context of transport phenomena in the source plasma, for approximate cases. Such a relationship will fall short of an exact description. In what follows, we approximate (Ref. 7) the plasma behavior in the RF source with that of a positive column of a dc plasma.

We can start such a description by considering a source which has a cylindrical geometry with respect to the applied electric field $\vec{E}$, assumed to be parallel to the axis. We also make the following assumptions concerning the plasma in the source. We assume that at every point the net charge density is zero, that is $n_e \simeq n_i \equiv n$, and the temperature of the molecules is constant in space and time; we further assume that the plasma properties are homogeneous in the direction of the cylindrical axis and that they are time independent; furthermore, positively charged particles are produced in collisions of ground state molecules with electrons, and no negative ions are formed. Finally, we assume that the diffusion of charged particles onto the walls and their subsequent recombination is the only mechanism responsible for their loss. All these assumptions are realized to various degrees in the RF dissociator and none of them present a severe deviation from the actual case of the source.

We now can write down the following equations (Refs. 8, 9) to describe the distribution of charged particles in the source. Starting with

$$n_e = n_i \equiv n \tag{1}$$

the flux of charged particles with a drift velocity V_d can be written as

$$\phi = nV_d = D_a \nabla n \tag{2}$$

where D_a is the coefficient of ambipolar diffusion. Taking the divergence of Eq. (2) we get

$$\nabla \cdot \phi = D_a \nabla \cdot \nabla n \tag{2}$$

and since

$$\nabla \cdot \phi = \nu_i n$$

where ν_i is the collisional ionization frequency, we have

$$D_a \nabla^2 n = - \nu_i n$$

or

$$\nabla^2 n + \frac{\nu_i}{D_a} n = 0 \tag{3}$$

For a cylindrical geometry we expect that the density of charged particles is only a function of r, the radial distance from the symmetry axis. We therefore have

$$\frac{d^2 n(r)}{dn^2} + \frac{1}{r} \frac{dn(r)}{dr} + \frac{\nu_i}{D_a} n(r) = 0 \tag{4}$$

This equation has a solution of the form:

$$n(r) = n_0 J_0 \left(r \sqrt{\frac{\nu_i}{D_a}} \right) \tag{5}$$

where n_0 is the charge density on the axis and J_0 is the zeroth-order Bessel function. Imposing the boundary condition that the density of charged particles is zero at the wall, i.e., $n = 0$ at $r = R$, where R is the radius of the source, we obtain

$$\sqrt{\frac{\nu_i}{D_a}} R = 2.4 \tag{6}$$

where the numerical function 2.4 is the first root of J_0. Equation (5) gives us the condition for sustainment of the plasma in the source. We can use this equation to obtain T_e, the temperature of electrons in the plasma. To do so, we use the assumption of Maxwellian velocity distribution for electrons so that we may write down the following equation for ν_i (Ref. 9):

$$\nu_i = A p V_i^{3/2} \left(\frac{eV_i}{kT_e} \right)^{-1/2} \exp(-eV_i/kT_e) \tag{7}$$

where A is a constant characteristic of the particular gas, V_i is the ionization potential of the gas, and p is the pressure. We can write the approximate relation:

$$D_a = \frac{kT_e}{e} \mu^+ \tag{8}$$

which is valid when the electron temperature is much larger than the ion temperature (assumed to be approximately the same as the ambient temperature), with μ^+ as the mobility of the ions. Combining Eqs. (6), (7) and (8), we get

$$\frac{\exp(eV_i/kT_e)}{(eV_i/kT_e)^{1/2}} = 1.2 \times 10^7 (CpR)^2 \tag{9}$$

where C is a characteristic constant of the gas and is approximately equal to 10^{-2} in the case of H_2 (Ref. 10). Equation (9) permits us to calculate the temperature of the electrons in the plasma, when the pressure p and the radius of the source R are known. For example, for a typical source with $R = 2.5$ cm and $p = 0.1$ torr, we have in the case of hydrogen gas an electron temperature of about 35000 K. The important point of Eq. (9) is that there is essentially a relationship between T_e/V_i and the product CpR. In other words, for a given gas we have a relationship between T_e and the product pR, which can be used to obtain a desired T_e by varying p and R.

We next consider the potential at the vicinity of the wall arising from the diffusion of the charged particles. For an insulating wall a (Debye) sheath is produced at the wall to insure that the number of (faster moving) electrons arriving at the wall is equal to the number of (slower moving) ions at the wall. It can be shown that the potential across this sheath is given by (Ref. 11)

$$V_D = - \left(\frac{kT_e}{2e} \right) \ln \left(\frac{T_e m_i}{T_i m_e} \right) \tag{10}$$

where m_e and m_i are electron and ion mass, respectively. For the case of the hydrogen molecular ions, V_D is approximately 20 volts, when T_e is about 35000 K. Similarly, it can be shown

(Ref. 9) that the potential difference V_b between the axis and the boundary sheath is

$$- V_b \simeq \frac{kT_e}{e} \ln (R/1.7 \lambda_e)$$

where λ_e is the mean free path of the electrons. So, for the case of hydrogen gas dissociator, the ions created at the axis are accelerated to the wall through a potential $V_T = V_b + V_D$ with $V_T = 26$ V.

We are now in a position to determine the efficiency of the source. We can write a diffusion equation similar to Eq. (2) for the case of hydrogen atoms as produced by electron impact on the molecules:

$$\phi_H = D \nabla n_H \tag{11a}$$

Here ϕ_H is the flux of H atoms, D the diffusion constant for the diffusion of atoms through H_2 molecules, and n_H the number density of atoms. Since each electron impact resulting in the dissociation of a molecule produces two hydrogen atoms, taking the divergence of (11a) yields:

$$\nabla \cdot \phi_H = 2\nu_H n \tag{11b}$$

where ν_H is the collision frequency of electrons with molecules resulting in dissociation and n is the electron density. Equation (11b) implicitly contains the fact that the density of electrons is much smaller than the density of hydrogen molecules. We now combine Eqs. (11a) and (11b) to get:

$$D \nabla^2 n_H = n \nu_H \tag{12}$$

Similarly from Eq. (2):

$$D_a \nabla^2 n = n \nu \tag{13}$$

Solving for n in Eqs. (12) and (13), we get

$$\frac{D_a \nabla^2 n}{\nu} = \frac{D \nabla^2 n_H}{\nu_H}$$

or

$$\nabla^2 n_H = \frac{2\nu_H}{\nu} \frac{D_a}{D} \nabla^2 n ,$$

resulting in

$$D \nabla n_H = \frac{2\nu_H}{\nu} D_a \nabla_n$$

or finally

$$\phi_H = \frac{2\nu_H}{\nu} \phi \tag{14}$$

Now, the rate at which hydrogen atoms arrive at the wall is $n_H V/4$, where V is the thermal velocity of the atoms. A fraction γ of the atoms arriving at the wall then recombine to form hydrogen molecules. In order to achieve equilibrium, the rate of production of atoms and the rate of their loss have to be equal,

$$\gamma n_H \frac{V}{4} = \frac{2\nu_H}{\nu} \phi . \tag{15}$$

At this point we can relate the ion flux ϕ to the power input into the source. If we assume that the only loss mechanism in the source is due to the energy carried away by the ions falling to the wall, then we will have, at equilibrium, $P = V_T I$, where P is the power input into the source and I is the ion current. Since we have $e\phi = j$, where j is the current density, we can use Eq. (15) to obtain

$$\gamma n_H \frac{V}{4} = \frac{2\nu_H}{\nu} \frac{j}{e}$$

or using the relation for power

$$\gamma n_H \frac{V}{4} = \frac{2\nu_H}{\nu} \frac{P}{AeV_T}$$

where A is the area of the source. For a source with efficiency of atom production η, we have $n_H = 2\eta n_0$, where n_0 is the density of molecules. Combining this with the last equation we obtain an expression for the source efficiency η:

$$\eta = \frac{4\nu_H}{e\nu} \frac{P}{V\gamma n_0 A V_T}$$

or:

$$\eta = \frac{4\nu_H}{\nu} \frac{kT_H}{e} \frac{P}{AV\gamma V_T p} \tag{16}$$

If we assume $\gamma = 5 \times 10^{-5}$ (Ref. 12), $p = 0.1$ torr $= 7.49 \times 10^{-5}$ dynes/cm^2, and $P = 10$ W, the efficiency of a source with a radius of 1 inch and length of 2 inches is of the order of 5 percent, in general agreement with experimental results.

The assumptions leading to Eq. (16) for efficiency preclude the applicability of the expression for η in the regime of high pressures, where certain concepts such as the sheath potential V_D are likely to fail. The assumption of absence of negative ions (which promote volume recombination) and neglect of other loss mechanisms also limit the accuracy of η. Finally, one should bear in mind that an increase in power results in the increase of T_e, which affects most of the parameters in the expression for η.

V. Particle Interactions With Dissociator Walls

The interaction of particles in the hydrogen gas dissociator with dissociator walls is an important effect which directly influences both the atom flux from the source and the source life (Refs. 12, 13). Various ions and neutral particles in the source which drift onto walls interact in different ways with the glass walls of the dissociator. Hydrogen atoms form a layer on the wall by an adsorption mechanism which can subsequently promote the formation of molecules. It is also known that the silica glass can be permeable to H_2 molecules with very high energies. Various chemical interactions between the particles and the molecules in the glass will also be important in recombination of atoms and introduction of impurities in the plasma.

Equation (10) expresses the relationship between V_D and the electron temperature T_e. It is then clear that an increase in the electron temperature increases the energy with which ions strike the walls. The resulting ion sputtered surface is detrimental to the efficiency η, presumably because of an increase in the microscopic surface area generated by surface granules and the subsequent increase in recombination rate. Striking ions also may release other ions from the wall material, including impurities in the glass. This results in the absorption of power by the new ions and decrease in hydrogen atom production efficiency. The same consideration applies equally well to the presence of water vapor or other impurities in the source. Finally, carbon atoms present as impurities in the vacuum system may deposit on the surface and directly influence the value of surface recombination rate γ (Ref. 12).

VI. Summary, Conclusions and Recommendations

We have examined some of the processes which are important in the study of the hydrogen gas dissociator. We have seen that collisional processes in the dissociator result in the production of hydrogen atoms and other particles, as well as photons. By approximating the RF discharge with the positive column of a dc plasma source, we considered the transport properties of the plasma to obtain relationships for electron temperature and source efficiency in terms of gas pressure, input power, and geometric size of the source. Finally, we briefly outlined the influence of the wall of the dissociator on its performance.

On the basis of this study, the following conclusions regarding the design of more efficient RF hydrogen atom sources may be inferred. Since the wall recombination presents the greatest limitation at the source, care should be taken to construct the source from materials with the lowest recombination coefficient. At the present time, Pyrex is the most widely used material for this purpose. It is recommended that other materials with smaller coefficient be sought for possible application in source construction. Furthermore, sources should be acid cleaned not only to remove any surface deposits that may interfere with the development of an optimized plasma temperature, but also to leave a smooth surface to minimize the area which can enhance atom recombination at the walls. Since the wall recombination coefficient is a strong function of temperature (Ref. 12), designs should include adequate measures for the removal of the heat generated by the RF power in the dissociator bulb. While the considerations in this study were based on RF power inductively coupled to the source, it is believed that they apply equally well to the case of capacitive coupling. In either case, care should be taken to couple the RF power into the source with adequate efficiency.

Relations (9) and (16) may be used in both design and operation of the source. As indicated by these equations, the physical dimension of the dissociator strongly affects its performance. However, it should be carefully noted that while an increase in the size of the dissociator decreases the sputtering effect, it can also decrease the efficiency if power and pressure are held constant. It therefore appears that a careful design for a dissociator may employ relations (9) and (16) to seek an optimized size for the source and find a

balance between these two effects. In general, however, it can be said that for constant power and pressure, a smaller dissociator leads to more efficiency, while a larger size results in longer lifetime.

Equations (9) and (16) can also be used to optimize the performance of a dissociator by properly adjusting the pressure and power. It should, however, be kept in mind that these relations do not hold for the case of high pressures (in excess of 500 microns). Finally, it should be reemphasized that the evaluation of the source performance by examination of the color of the plasma is inadequate. Barometric methods are more direct and reliable and should be preferred.

Future studies of the RF hydrogen dissociator should include a search for wall materials with reduced recombination coefficient. It is also recommended that considerations be given to the application of an axial magnetic field on the source to confine the ions close to axis and reduce the ion bombardment of the walls, similar to RF ion sources. If a magnetic field can be applied on the source without appreciable degradation of the efficiency, it may be possible to increase the life of the source by an appreciable amount.

References

1. Kleppner, D., Berg, H. C., Crampton, S. B., and Ramsey, N. F., *Phys. Rev., 138*, A972 (1965).
2. Valyi, L., *Atom and Ion Sources*, Chapter II, John Wiley and Sons, New York, N.Y. (1977).
3. Darwin, H. W., in *Reactions Under Plasma Conditions*, M. Venugopalan, Editor, Vol. 1, Chap. 3, Wiley-Interscience, New York, N.Y. (1971).
4. Mott, N. F., and Massey, H. S. W., *The Theory of Atomic Collisions*, 3rd Ed., Oxford University Press, Oxford (1965).
5. See, for example, K. T. Dolder and B. Pent, Comments Atom. Mol. Phys. *5*, 97 (1976) and A. H. Mahan, A. Gallagher and S. J. Smith, *Phys. Rev. A, 13*, 156 (1976) and M. Misakian and J. C. Zorn, *Phys. Rev. A, 6*, 2180 (1972), G. A. Khayrallah, *Phys. Rev. A, 13*, 1989 (1976) and references therein.
6. Bates, D. R., et al., *Proc. Roy. Soc.*, A, *267*, 297 (1962).
7. Godyak, V. A., Kanneh, A. S., *Proc. XIVth ICPIG J. de. Phys.*, Suppl. *7*, Vol. 1, pp C7-147 (1979).
8. Delcroix, J. L., *Plasma Physics*, Vol. 2, John Wiley and Sons Ltd., New York, N.Y. (1967)
9. Von Engel, A., *Ionized Gases*, Second Ed. Chapter 8, Oxford University Press, Oxford (1965).
10. Cobine, J. D., *Gaseous Conductors*, Chapter IV, Dover Publications, Inc., New York, N.Y. (1958).
11. Shahin, M. H., in *Reactions Under Plasma Conditions*, M. Venugopalan, Ed., Wiley-Interscience, New York, N.Y. (1971).
12. Ritz, V. H., Bermudez, V. M., and Folen, V. J., *J. Appl. Phys., 48*, 2076 (1977).
13. Mandl, A., and Salop, A., *J. Appl. Phys., 44*, 4776 (1973).

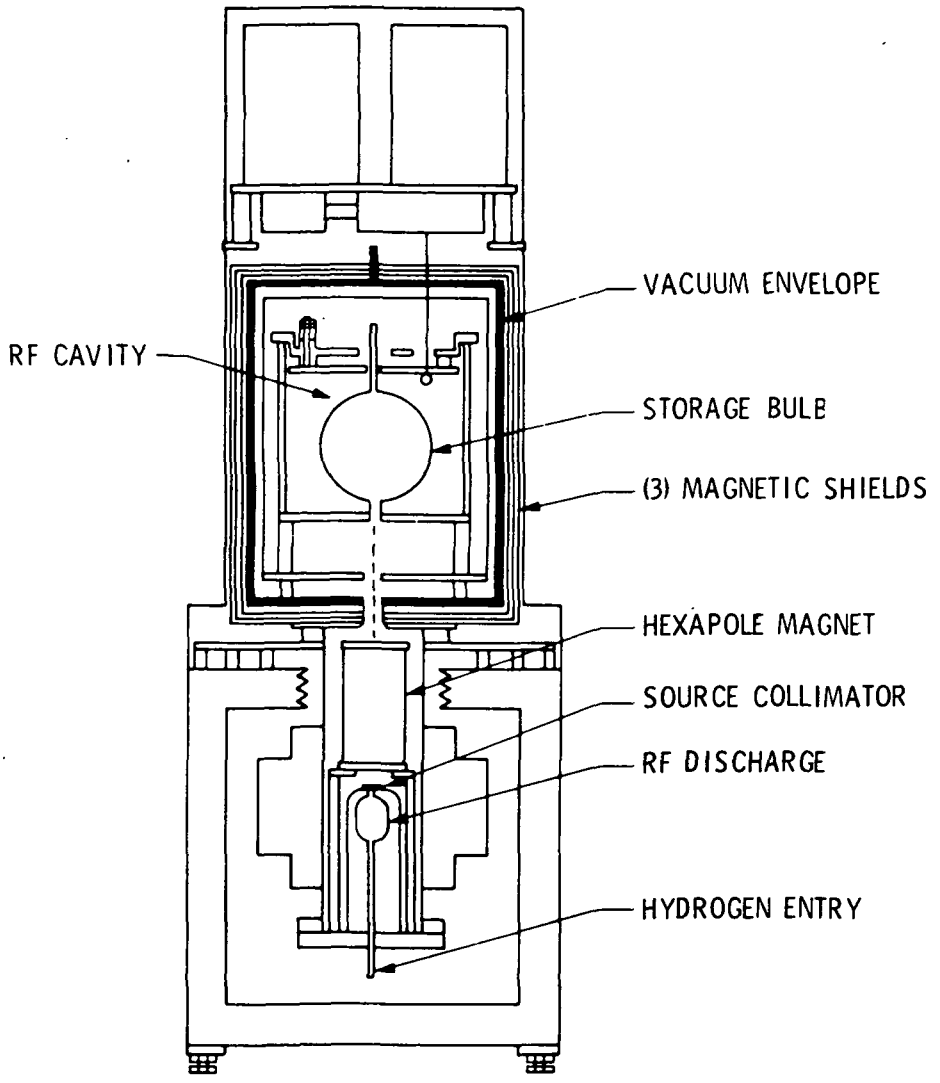

Fig. 1. Line drawing of the hydrogen maser

N80-33439

Experimental Optical Fiber Communications Link

G. F. Lutes
Communications Systems Research Section

An optical fiber communications link 1.5 kilometers in length has been installed between the Interim Frequency Standard Test Facility and the Timing and Frequency Systems Research Laboratory at JPL. It is being used to develop optical fiber technology for use in the DSN and particularly for precise time and frequency distribution.

I. Introduction

An optical fiber communications link 1.5 km in length has been installed at JPL between the Interim Frequency Standard Test Facility and the Timing and Frequency Systems Research Laboratory along the route shown in Fig. 1. It is being used to develop optical fiber technology for use in the DSN, which includes learning to install optical fiber cable and connectors, learning to weld fiber and make splices and learning to design optical fiber communications links and to measure and verify their performance.

The present effort is concentrated on the development of precise frequency and timing distribution systems, which will eliminate the need for a frequency and/or timing system in each DSN Deep Space Station.

This article describes the experimental optical fiber communications link, the installation of the link and associated problems, and the link performance.

II. Description

The optical fiber communications link consists of a commercial optical transmitter and receiver and a 1.5-km length of two conductor optical fiber cable.

The optical transmitter contains a single transverse-mode solid-state laser diode which emits infrared power at a wavelength of ≈ 830 nm. It is biased in the linear region of its emission-vs-current curve so it can be linearly amplitude modulated. The optical output power is set for about 3 mW out of each end of the laser. The power emitted from the back of the laser is detected with a photodiode, and the resultant current is used in a negative feedback loop to stabilize the optical output power level. A thermoelectric cooler is used to cool the laser diode and hold its temperature to $\approx 25°C$.

The optical carrier emitted from the front facet of the laser is coupled to an optical fiber pigtail. About 50 percent of the power is lost in the coupling, resulting in a net optical carrier power of ≈ 1.5 mW launched into the fiber.

The optical receiver consists of an avalanche photodiode detector (APD) followed by a variable gain, dc to 3-GHz wideband amplifier. The gain of the APD is compromised in order to obtain the wide bandwidth. This results in a responsivity for the APD of only ≈ 25 amperes/watt.

The optical fiber cable was made up of a cable 1225 meters long, which was the longest continuous length available, and a cable 348 meters long spliced onto the end of it.

The cable contains two optical fibers enclosed in separate tubes. Each of these tubes is surrounded by strength members and a larger-diameter tube. These latter tubes are surrounded by more strength members, and the whole assembly is enclosed in an outer jacket (Fig. 2).

The fibers are of the multimode graded index type with a bandwidth of 400 MHz-km and 6 dB/km loss. The outside diameter of the fibers is 125 μm with a 62.5-μm core diameter. Each fiber is protected by a coating of lacquer.

III. Installation

The optical fiber cable was installed in the existing cable troughs and conduits with no special precautions taken. However, because the splice in the cable was too large to go through the existing conduit opening, the cable installation was made through a manhole near the Interim Frequency Standard Test Facility and pulled through the conduit in both directions from there.

Several delays occurred during the installation, due to heavy rain and/or construction, and the part of the cable not yet installed was left outside exposed to the elements for two weeks. When the installation was completed, an optical continuity test indicated that one of the two fibers was broken.

An optical time domain reflectometer (TDR) was designed and fabricated and used to locate a break in the open fiber about 260 meters from the end of the cable in the Timing and Frequency System Research Lab building. About 230 meters of this distance was contained in a roll of excess cable near the end. It was later determined that the break was between the third floor and the junction box on the second floor of the lab building. The cable was cut at the junction box and the broken fiber was pulled out of the cable and the length measured. An identical length of cable from the roll of excess cable in the lab was pulled through the junction box and cut off, exposing the ends of the fibers. No damage to the jacket was observed near the break.

After verifying continuity through both fibers back to the lab, the ends of the cable were welded together. Measurement of the physical distance between the end of the cable and the splice indicated an error in the TDR measurement of 3 meters out of 260 meters.

Continuity was again tested and there was still no continuity in the same fiber; this time the TDR did not indicate a break. It was concluded that this break was too far from the end of the cable in the lab building to be detected. The TDR was taken to the Interim Frequency Standard Test Facility, where a measurement indicated a break $\approx$ 240 meters from that end of the cable.

Difficulty was encountered in trying to determine the physical location of this break because the cable was accessible only at manholes spaced from 25 to 50 meters apart. The cable was cut in three adjacent manholes before the break was physically located. It was impossible to verify the TDR measurement with a physical measurement in this case. The cable was visibly damaged at this break, which turned out to be about a foot from the commercial splice. The commercial splice was removed so as to have only one splice at that location.

In order to gain experience the cable was welded at all three manholes even though the option of installing a new piece of cable between the outer two manholes and eliminating one splice was available. Upon completing these splices, continuity was verified through both fibers.

IV. Time Domain Reflectometer (TDR)

A block diagram of the previously mentioned time domain reflectometer (TDR) is shown in Fig. 3. The TDR consists of an optical transmitter and receiver, an optical directional coupler, and the required power supplies. The transmitter and receiver are identical to the ones used in the optical fiber communications link. The directional coupler is a commercial unit and has a directivity of 52 dB.

A pulse generator and oscilloscope are used with the TDR and are connected as shown in Fig. 3. A pulse from the pulse generator modulates the optical carrier emitted from the transmitter, producing an optical pulse that travels through the directional coupler and down the fiber. A pulse traveling in this direction is isolated from the receiver by the 52-dB isolation in the directional coupler. When this optical pulse arrives at a fiber end, break or termination, some of the power in the pulse ($< 4\%$) is reflected back down the fiber toward the TDR, where it passes through the directional coupler and is detected by the receiver.

The oscilloscope is used to measure the time delay between the resultant electrical pulse from the receiver and the original pulse from the pulse generator. This time delay is used to calculate the distance from the TDR to the fiber end.

There is no other practical way to find a break in a fiber contained in a cable.

V. Splices

Splices are made in a 19- X 12- X 5.5-cm commercial aluminum box. A standard watertight electrical conduit connector with a rubber compression grommet is installed on each end of the box, offset from the center as shown in Fig. 4.

The end of each optical cable to be spliced is pulled about 60 cm through one of the connectors. The end of each cable is stripped back to expose the fiber and the appropriate fibers are welded together. A clamp is installed to relieve tension on the weld and the weld is coated with a protective coating. The cables are pulled back through the connectors until about 3 or 4 centimeters of the outer jacket remains in the box and the fibers form a loop. The connector shells are tightened so that the grommets are compressed and clamp the cable firmly.

Silicon rubber cement is applied around the connectors and to the cover of the box, which is then installed, completing the splice.

VI. Tests

The two fibers were welded together at the far end of the cable and the transmitter and receiver were installed on the ends of the fibers in the Timing and Frequency Systems Research Lab. This gave a round trip path length of 3 km, with a total of 11 welded splices in the fiber. All of the following tests were performed with the optical fiber link in this configuration.

The instantaneous bandwidth of the link is limited by the fiber to 130 MHz (Fig. 5). Signal loss in the fiber is 24 dB. The power spectral density of phase noise (Ref. 1) is ≈ 120 dBc in a 1-Hz bandwidth, 10 Hz from a 100-MHz signal (Fig. 6). Intermodulation distortion products are down more than 40 dBc for two signals separated by 1 kHz around 25 MHz and with a modulation depth of 70 percent (Fig. 7).

The input and output impedances of the link are shown in Figs. 8 and 9. The phase across the link has been monitored overnight and found to have a maximum peak-to-peak variation of <1 degree at 100 MHz. This is <30 ps variation in propagation delay. Previous tests on propagation delay vs temperature indicate a change of ≈ 10 ppm/°C for multimode fiber.

Our tests verified that there are variations in loss and propagation delay as a function of flexure of optical fibers. This effect has been analyzed by Lau (Ref. 2) and the Timing and Frequency Systems Research Group is presently doing experiments to verify the analysis.

An Allan variance curve, phase stability vs sampling time, was conducted on the nonstabilized link with the results shown in Fig. 10. This data indicates that propagation delay stability in multimode optical fibers is as good as the best coaxial cable and much better than microwave communications links. It is suspected that single-mode fiber is more stable than multimode fiber, particularly as a function of flexure, and work is being done to verify this.

VII. Data and Signal Transmission Demonstration

A 60-MHz bandwidth digital signal, a 4-MHz bandwidth television signal and a narrowband test signal were transmitted simultaneously on different radio frequency carriers over the optical fiber link to demonstrate its low loss and wide bandwidth capabilities. The bit error rate of the digital signal and the television picture quality were not significantly affected by the optical fiber link.

VIII. Advantages of Optical Fibers

Optical fibers generally have greater bandwidth and lower loss than do coaxial cables. This is shown in Figs. 11 and 12, where attenuation and bandwidth data from manufacturer specifications for common types of optical fibers and coaxial cables have been plotted together.

The 7/8-inch air dielectric coaxial cable mentioned in Figs. 11 and 12 and in Table 1 is the lowest-loss, widest-bandwidth coaxial cable that data was available for. The fat fiber mentioned is a step-index-type multimode optical fiber with a 100-μm core diameter. It is generally used for short distance (<1 km) and small bandwidth (<20 MHz-km) applications. The large-diameter core makes it easier to adequately couple light-emitting diode sources ino it.

Optical fibers do not radiate or pick up RFI or EMI. Electrical isolation may be maintained between an optical transmitter and receiver, thereby eliminating ground loops and reducing the possibility of short circuits.

Optical fiber cables are small, lightweight and corrosion resistant. A high level of transmission security can be achieved in an optical fiber communication system because of the extreme difficulty of intercepting the signal without appreciably disturbing it. The cost of optical fiber cables is very low when compared to the cost of coaxial cables if the performance is considered. The costs of the various optical fibers and coaxial cables previously mentioned are compared in Table 1 and are given in terms of cost per meter as well as cost per meter per MHz bandwidth. It can be seen that the cost of

optical fiber cables is extremely small if the full bandwidth capability is utilized.

IX. Conclusion

Optical fiber communications systems are superior in some applications to alternative types of communications systems, such as coaxial cable, and terrestrial microwave systems. The optical fiber transmission medium has much lower loss and greater bandwidth than the best coaxial cable. The propagation delay is as stable as that of the best coaxial cable and an order of magnitude more stable than a microwave link. Optical fiber cable is also much less expensive than coaxial cable with equivalent stability.

It was found that the installation of optical fiber cables is comparable to coaxial cables; that discontinuities can readily be located using an optical time domain reflectometer; and that they can be repaired by welding even in an adverse field environment. Welded connections are no more difficult to make than installing coaxial or optical fiber connectors and are more stable and reliable.

Optical fiber communications systems are adequately developed for many applications and should be considered a viable alternative to established communications technologies.

References

1. Meyer, R., and Sward, A., "Frequency Generation and Control: The Measurement of Phase Jitter," in *The Deep Space Network, Space Programs Summary 37-64*, Vol. II, pp. 55-58, Jet Propulsion Laboratory, Pasadena, Calif., August 31, 1970.
2. Lau, K., "Propagation Path Length Variations Due to Bending of Optical Fibers," to be published.

Table 1. Cost of optical fiber cables and coaxial cables

Type	Number	Bandwidth	Cost/meter, $	Cost/MHz (BW) • meter, $
1-A	RG223U	1.22 MHz-km	1.05	0.86
1-B	RG214U	4.57 MHz-km	3.05	0.67
1-C	See notes	91 MHz-km	20.00	0.22
2	See notes	1000 MHz-km	2.50	0.0025
3	See notes	140,000 MHz-km	6.00	0.00004
4	See notes	500 MHz-km	0.90	0.0018

Notes:

Type 1A	Coax–0.216 in.–diameter, double shielded.
Type 1B	Coax–0.425 in.–diameter, double shielded.
Type 1C	7/8 in.–diameter air dielectric coaxial cable.
2	Multimode fiber optic cable, utilizing Corning 250-10D fiber.
3	Single-mode fiber optic cable, special order.
4	Telephone fiber optic cable.

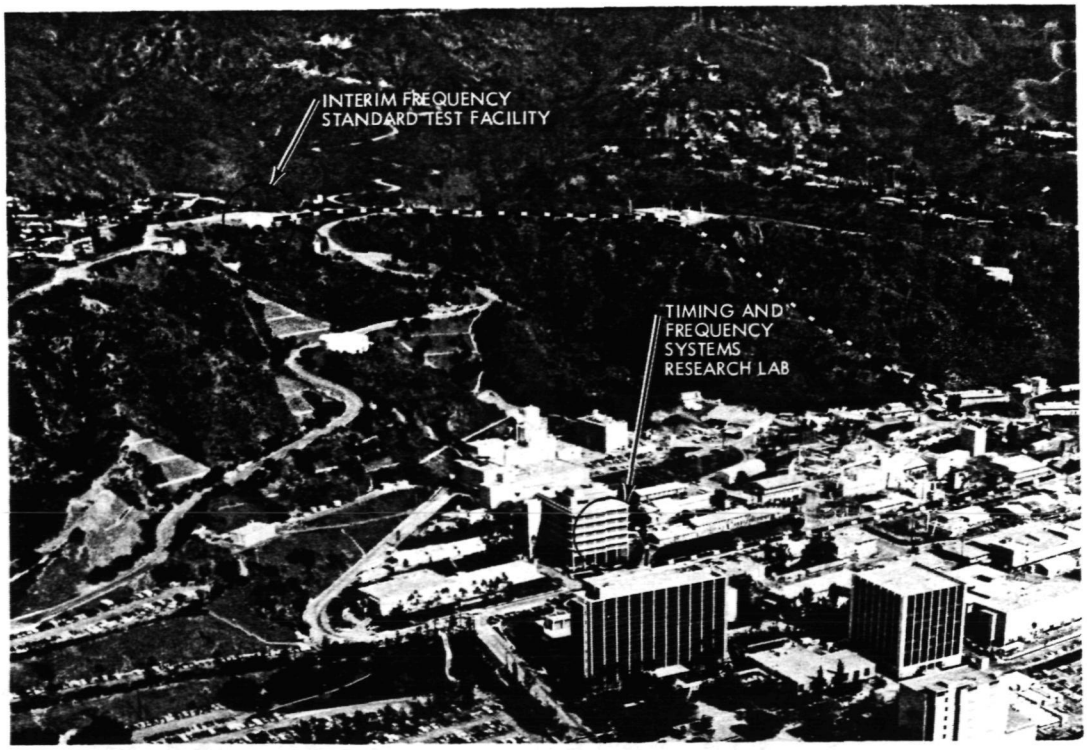

Fig. 1. Optical fiber cable route

ORIGINAL PAGE
OF POOR QUALITY

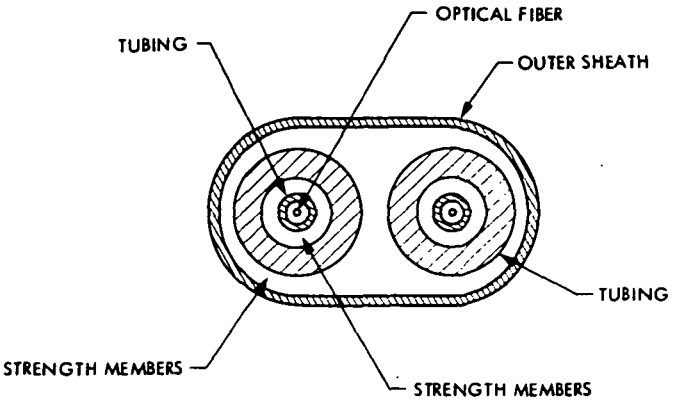

Fig. 2. Cross section of optical fiber cable

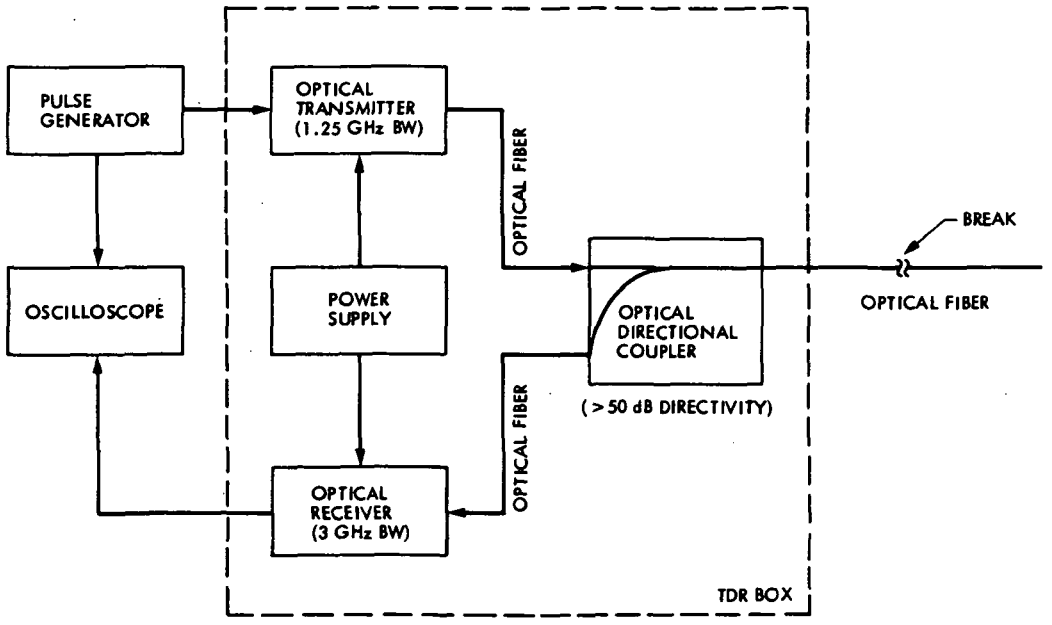

Fig. 3. Time domain reflectometer (TDR) block diagram

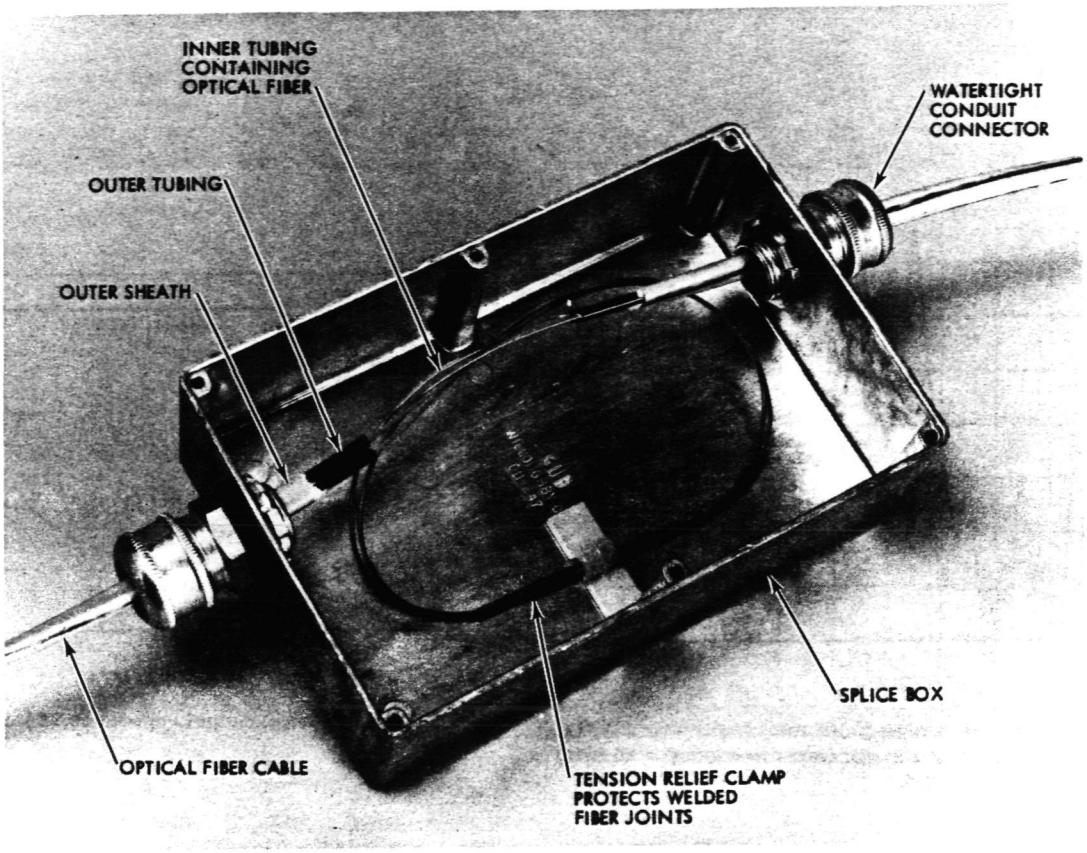

Fig. 4. Splice box

ORIGINAL PAGE IS OF POOR QUALITY

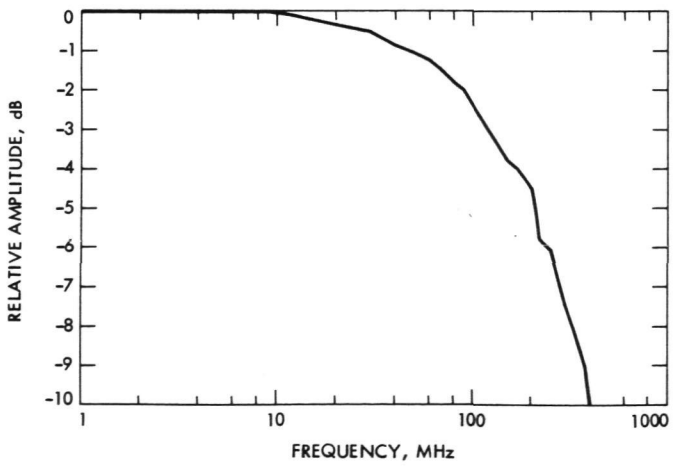

Fig. 5. Optical fiber bandwidth for a 3-km length

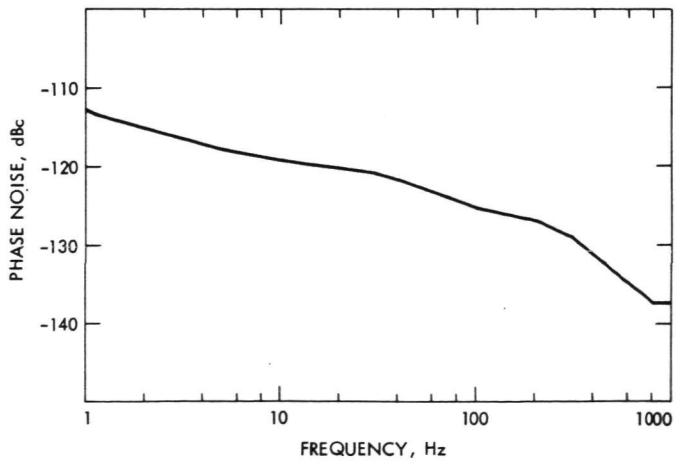

Fig. 6. Power spectral density of phase noise vs frequency (single sideband)

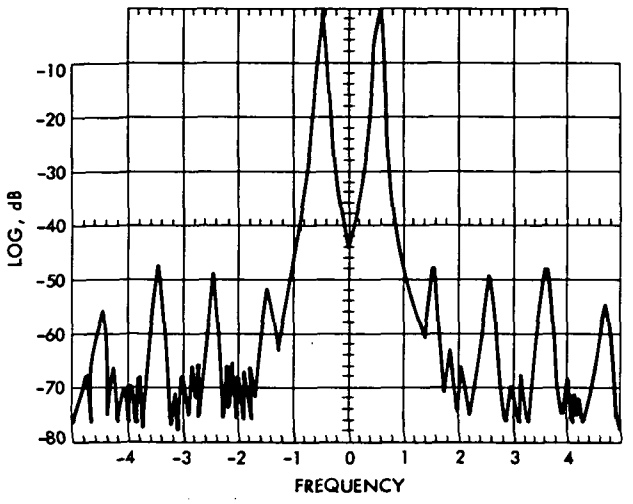

Fig. 7. Intermodulation distortion (horizontal scale = 1 kHz/div; vertical scale is relative in dB; center frequency = 25 MHz; modulation depth = 70%

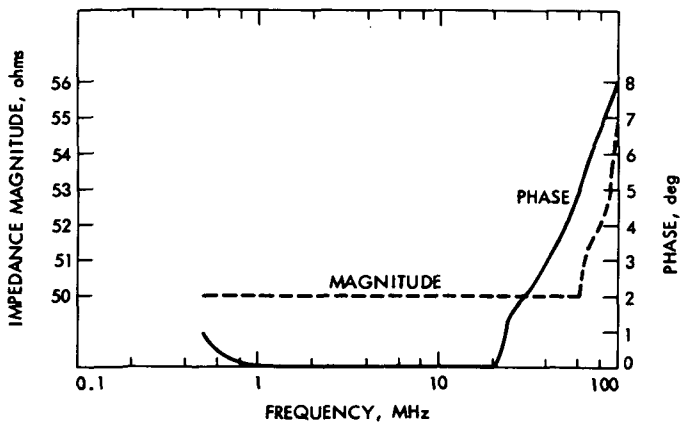

Fig. 8. Optical transmitter input impedance vs frequency (modulation input port)

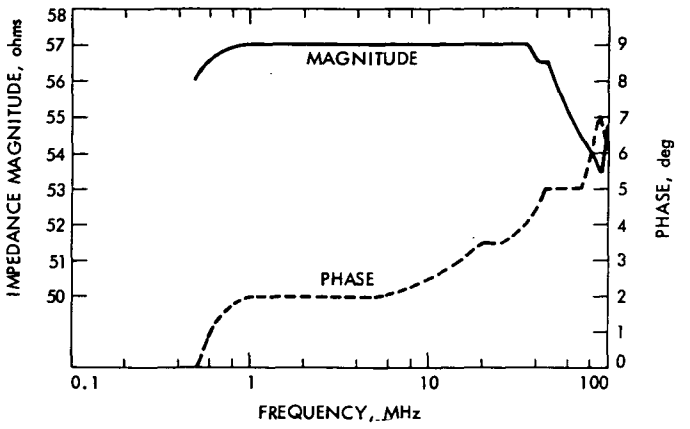

Fig. 9. Receiver output impedance vs frequency

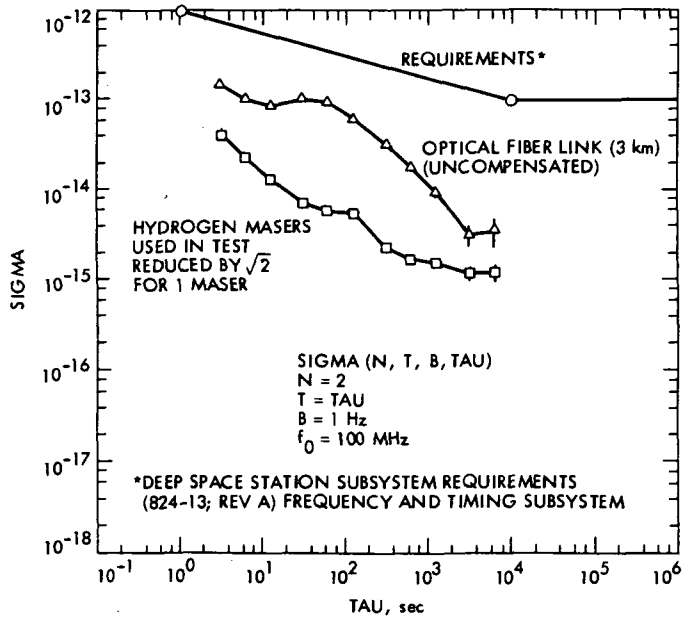

Fig. 10. Allan variance curve

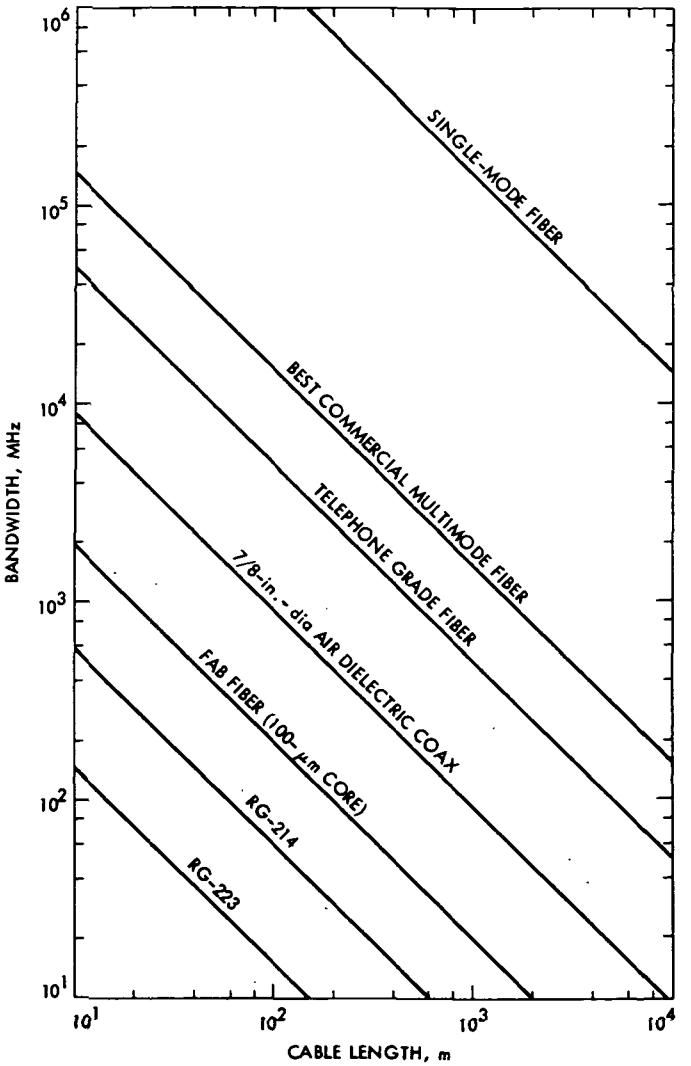

Fig. 11. Bandwidth vs cable length for some optical fibers and coaxial cables

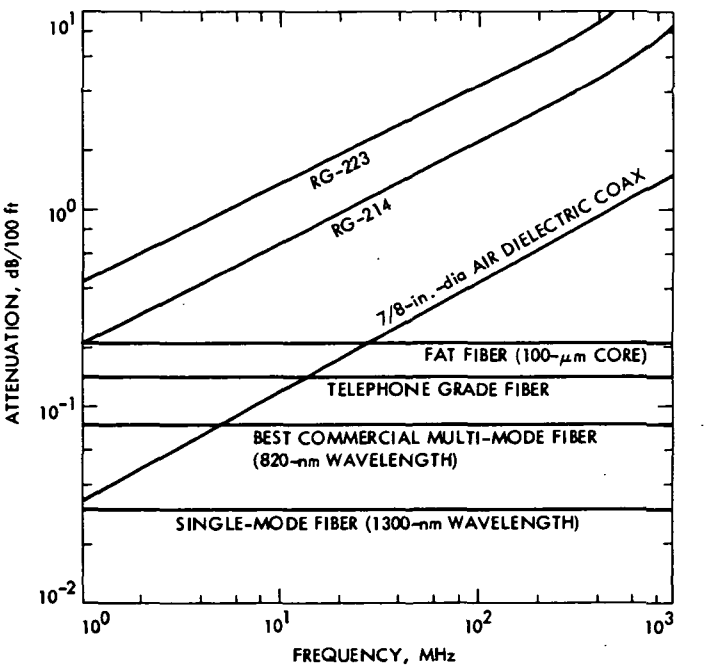

Fig. 12. Attenuation vs frequency for some optical fibers and coaxial cables.

N80-33440

Open-Loop Radio Science With a Suppressed-Carrier Signal

C. A. Greenhall
Communications Systems Research Section

When a suppressed-carrier signal is squared, the carrier reappears in doubled form. An open-loop receiver can be used to deliver a recording of a band-limited waveform containing this carrier, whose amplitude and phase can be tracked by the radio science experimenter.

I. Introduction

In conventional radio science, a spacecraft transmits a sine-wave signal through a medium, which perturbs the signal in phase and amplitude. Inferences about the medium are made from observations of these phase and amplitude variations. Because the present DSN telemetry system uses a residual carrier, open-loop or closed-loop radio science can be carried out in the presence of telemetry modulation. Figure 1 shows an open-loop processor.

The multimegasymbol telemetry system now under development can use a suppressed-carrier signal having no discrete spectral component at the carrier frequency. Doppler phase and signal amplitude can be extracted by a Costas-loop receiver; hence, closed-loop radio science can be carried out as before. In fact, as Ref. 1 shows, this scheme enjoys a 15- to 30-dB advantage over the residual-carrier scheme (with an 80-deg modulation index and no subcarrier) because the latter uses only 1/33 of the total signal power.

Our purpose is to ask whether open-loop radio science can also be carried out with a suppressed-carrier signal. After some tentative investigation into the structure of the optimal receiver for extracting the phase and amplitude of the suppressed carrier, we decided to take a more practical turn. Since the Costas loop has the same performance as a squaring loop (Ref. 2), why not use an open-loop heterodyne receiver to process the square of the residual-carrier waveform? Such a processor is shown in Fig. 2. The recorded waveform contains a doubled version of the carrier.

The comparison between this scheme, which we call squared-suppressed-carrier (SSC), and open-loop reception of a residual carrier (RC), almost duplicates the closed-loop comparison in Ref. 1. The reason for this is that the tape recording of the squared waveform is analyzed by a phase-locked loop in computer software to extract the phase and amplitude of the recovered doubled carrier. In effect, this is nothing but a squaring loop. Nevertheless, we have taken some care to examine exactly what information (and noise) is contained in the square of the suppressed-carrier waveform, as influenced by the dispersion of the medium and of the presquaring filter.

The comparison between RC and SSC is based on the noise variances of the measurements of the phase and amplitude of the perturbed carrier. In the SSC case, there is, of course, no discrete carrier for the medium to perturb, yet we shall see that the reconstructed doubled carrier in the squared waveform contains almost the same information about the medium as the perturbed residual carrier. In fact, if the dispersion of the medium over the bandwidth of the suppressed-carrier

ORIGINAL PAGE IS OF POOR QUALITY

signal can be neglected, then the SSC receiver of Fig. 2 delivers a signal whose phase is twice the RC phase and whose amplitude is the square of the RC signal amplitude. Therefore, the experimenter must halve the phase and take the square root of the amplitude to obtain phase and amplitude information equivalent to what the RC setup gives. The effect of dispersion is assessed in Section V.

We shall show that the SSC scheme enjoys a considerable signal-to-noise-ratio (SNR) advantage over the RC scheme for the measurement of phase and amplitude. The results can be summarized here. The RC and SSC output tapes (Figs. 1 and 2) are both analyzed by phase-locked loops in software to recover phase and amplitude; let the loop bandwidth in both cases be B_L. Assume that both the RC and SSC received waveforms (the inputs in Figs. 1 and 2) have total signal power A_e^2 and noise spectral density $\frac{1}{2} N_0$. Denoting the estimated carrier phase by $\hat{\psi}_e$, we have

$$\frac{1}{\sigma^2(\hat{\psi}_e)} = \frac{A_e^2}{N_0 B_L} \cos^2\theta \quad \text{(residual carrier)}$$

$$\frac{1}{\sigma^2(\hat{\psi}_e)} = \frac{A_e^2}{N_0 B_L} \beta' \qquad \text{(squared suppressed carrier)}$$

For RC, θ is the modulation index. For SSC, β' is a degradation factor, given in Eq. (30) below, caused by the distortion of the presquaring filter $G_i(\omega)$ (Fig. 2) and the noise induced by the squaring operation. These equations are also found in Ref. 1, which compares RC and Costas-loop tracking in the multimegasymbol telemetry environment. For $\theta = 80$ deg and a symbol SNR between 0 dB and 10 dB, we have

$$\cos^2\theta = -15.2 \text{ dB}, -3.1 \text{ dB} < \beta' < -0.8 \text{ dB}$$

for a proper choice of the bandwidth of the presquaring filter (see Fig. 3). It follows that SSC has an advantage of 12 dB to 14 dB over RC for the measurement of phase. The same conclusion holds for the measurement of log-amplitude. This advantage can be used either to decrease the total noise variance of the measurement or to increase the measurement bandwidth B_L.

II. Models

We shall set up conceptual models for open-loop reception of RC and SSC signals. To be most fair to the RC setup, we shall assume that a subcarrier is used. In what follows, ω and λ denote radian frequency.

A. Transmitted Signals

These are

$$\sqrt{2}\cos\theta\cos\omega_c t \qquad \text{(residual carrier)} \tag{1}$$

$$\sqrt{2}\, d(t)\cos\omega_c t \qquad \text{(suppressed carrier)} \tag{2}$$

where θ = modulation index, $d(t)$ = data modulation, modeled by independent random ±1's with a symbol time T. In our situation, 0.1 MHz $\leq 1/T \leq$ 30 MHz. The spectral density of $d(t)$ is

$$S_d(\lambda) = T\,\text{sinc}^2(\tfrac{1}{2}\lambda T) \tag{3}$$

The random Fourier expansion of the stationary process $d(t)$ can be written symbolically* as

$$d(t) = \int_{-\infty}^{\infty} D(\lambda) e^{i\lambda t}\, d\lambda \tag{4}$$

B. External Medium and Received Waveforms

This is what the radio science experimenters want to probe. We represent it by a time-varying transfer function $G_e(\omega, t)$, the "external filter." It operates as follows: Any RF exponential $Ae^{i\omega t}$ emerges from the medium as the narrowband waveform $G_e(\omega, t)Ae^{i\omega t}$, and the principle of superposition holds for linear combinations of complex exponentials. Further, $G_e(\omega, t)$ is scaled so that it accounts for the power transmitted by the spacecraft, the space loss, and the gains of the transmitting and receiving antennas. Thus, the received residual-carrier waveform is

$$\frac{1}{\sqrt{2}}\cos\theta\, G_e(\omega_c, t)\, e^{i\omega_c t} + \text{c.c.} + n_w(t)$$

$$= \sqrt{2}\cos\theta\, A_e(t)\cos(\omega_c t + \psi_e(t)) + n_w(t) \tag{5}$$

where c.c. means complex conjugate, $G_e(\omega_c, t)$ has amplitude $A_e(t) > 0$ and phase $\psi_e(t)$, and $n_w(t)$ is white Gaussian noise with spectral density $\frac{1}{2} N_0$. We presume that the desired radio science information is contained in $A_e(t)$ and $\psi_e(t)$.

*Actually, $D(\lambda)\, d\lambda$ represents a process with orthogonal increments. In the Appendix, we shall approximate $d(t)$ by a process with a discrete Fourier expansion.

Applying G_e to Eq. (2), with $d(t)$ given by Eq. (4), we obtain the received suppressed-carrier waveform as

$$\frac{1}{\sqrt{2}} d_e(t) e^{i\omega_c t} + \text{c.c.} \tag{6}$$

where

$$d_e(t) = \int_{-\infty}^{\infty} G_e(\omega_c + \lambda, t) D(\lambda) e^{i\lambda t} d\lambda \tag{7}$$

is the data waveform after distortion by the baseband filter $G_e(\omega_c + \lambda, t)$. If

$$G_e(\omega_c - \lambda, t) = \overline{G_e}(\omega_c + \lambda, t)$$

were to hold (the bar means complex conjugate), then $d_e(t)$ would be real. In general, $d_e(t)$ is complex.

C. Open-Loop Receivers

Stripped to its conceptual essentials, an open-loop receiver for the residual-carrier waveform Eq. (5) is shown in Fig. 1. The heterodyne frequency f_h is chosen such that $0 < f_c - f_h < B_v$, where B_v is the "video" bandwidth, ranging from 100 Hz to 50 kHz in the DSN Multi-Mission Receiver (Ref. 3). The video waveform is sampled at $2B_v$ and recorded.

To process the suppressed-carrier waveform Eq. (6), the receiver of Fig. 2 is suggested. Before being squared, the waveform passes through an "internal" bandpass filter G_i with a nominal passband $f_c \pm B$. We shall show that the squared waveform contains a discrete component at $2f_c$ containing the radio science information. Mixing this with $2f_h$ gives another video waveform with bandwidth $2B_v$. This processor will be called the *squared-suppressed-carrier receiver*.

III. Analysis of the Squared-Suppressed-Carrier Receiver

Let $G(\omega, t) = G_e(\omega, t)G_i(\omega)$, the overall filter. In analogy with Eq. (7), set

$$d_G(t) = \int_{-\infty}^{\infty} G(\omega_c + \lambda, t) D(\lambda) e^{i\lambda t} d\lambda \tag{8}$$

The output of the internal filter in Fig. 2 is $x(t) = s(t) + n(t)$, where

$$s(t) = \frac{1}{\sqrt{2}} d_G(t) e^{i\omega_c t} + \text{c.c.} \tag{9}$$

$$n(t) = g_i(t) * n_w(t) \tag{10}$$

and $g_i(t)$ is the impulse response of G_i. Then

$$x^2(t) = s^2(t) + 2s(t)n(t) + n^2(t) \tag{11}$$

Let us first examine the S X S signal $s^2(t)$. In the Appendix it is shown that $s^2(t)$ is the sum of two components, one with discrete spectral lines and the other with a spectral density. The discrete component has spectral lines at frequencies $2f_c + n/T$ ($n = 0, \pm 1, \pm 2, \cdots$) plus a *DC* term that we ignore.

The central component at $2f_c$, the reconstructed doubled carrier, is the narrowband waveform

$$1/2\, Y(0,t) e^{i2\omega_c t} + \text{c.c.} \tag{12}$$

where

$$Y(0,t) = \int_{-\infty}^{\infty} G(\omega_c + \lambda, t) G(\omega_c - \lambda, t) \operatorname{sinc}^2(\tfrac{1}{2}\lambda T) \frac{T d\lambda}{2\pi} \tag{13}$$

(a special case of the function $Y(\omega, t)$ defined in the Appendix). If $G(\omega, t)$ were equal to $G_e(\omega_c, t)$ for all ω, then, because $\operatorname{sinc}^2(\tfrac{1}{2}\lambda T)$ integrates to 1, Eq. (13) would become $Y(0, t) = G_e^2(\omega_c, t)$. This means that Eq. (12) would carry the same radio science information as the residual-carrier signal in Eq. (5) except that here the carrier would appear in doubled form; Eq. (12) would be

$$A_e^2(t) \cos(2\omega_c t + 2\psi_e(t)) \tag{14}$$

In practice, G will have dispersion due to the external medium and the receiver, especially the $\pm B$ bandpass. The actual Eq. (13) gives $Y(0, t)$ as a weighted average of $G(\omega_c + \lambda, t)G(\omega_c - \lambda, t)$. We shall say more about this in Section V.

The spurious S X S components at $2f_c + n/T$ ($n \neq 0$) will be ignored because we assume that the video bandwidth $2B_v$ is less than $1/T$. As with Costas loop tracking, one must be careful not to mistake a spur for the main component (Ref. 4).

The continuous-spectrum component of $s^2(t)$, the S × S noise, is almost small enough to be ignored in this study. Nevertheless, we shall set down its spectral density here for the record. Let $\omega_1 = 2\pi/T$. Define the function

$$\Phi(0, \lambda, t) = \sum_{k=-\infty}^{\infty} G(\omega_c + \lambda + k\omega_1, t)\, G(\omega_c - \lambda - k\omega_1, t)$$

$$\times \operatorname{sinc}^2 (\tfrac{1}{2}(\lambda + k\omega_1)T) \qquad (15)$$

(a special case of the function $\Phi(\omega, \lambda, t)$ defined in the Appendix). This function (of λ) is ω_1-periodic, and its average over a period is just $Y(0, t)$. The spectral density of the S × S noise at $2f_c$ is now

$$S_{ss}(2\omega_c, t) = \frac{T}{2} \int_0^{\omega_1} |\Phi(0, \lambda, t) - Y(0, t)|^2 \, \frac{Td\lambda}{2\pi} \qquad (16)$$

which is $T/2$ times the mean-square variation of Φ over a period. This is a time-dependent, short-term spectral density, valid for integration times that are short compared to the fluctuations of $G_e(\omega, t)$.

Equation (16) is equivalent to Eq. (17) of Ref. 5.

The spectral densities of $s(t)$ and $n(t)$ in Eqs. (9) and (10) for frequencies near f_c are

$$S_s(\omega_c + \lambda, t) = \tfrac{1}{2}|G(\omega_c + \lambda, t)|^2 \, T \operatorname{sinc}^2 (\tfrac{1}{2}\lambda T)$$

$$S_n(\omega_c + \lambda) = \tfrac{1}{2} N_0 |G_i(\omega_c + \lambda)|^2 \qquad (17)$$

Therefore, the spectral densities at $2f_c$ of the S × N noise $2s(t)n(t)$ and the N × N noise $n^2(t)$ are (Ref. 6)

$$S_{sn}(2\omega_c, t) = N_0 \int_{-\infty}^{\infty} |G(\omega_c + \lambda, t)\, G_i(\omega_c - \lambda)|^2$$

$$\times \operatorname{sinc}^2 (\tfrac{1}{2}\lambda T) \, \frac{Td\lambda}{2\pi} \qquad (18)$$

$$S_{nn}(2\omega_c, t) = \tfrac{1}{2} N_0^2 \int_{-\infty}^{\infty} |G_i(\omega_c + \lambda)$$

$$\times G_i(\omega_c - \lambda)|^2 \, \frac{d\lambda}{2\pi} \qquad (19)$$

(Because $n(t)$ is Gaussian, the spectral density of $n^2(t)$ is $2S_n(\omega)*S_n(\omega)$.)

IV. Comparison of Open-Loop Receivers

A. Ratio of Power to Noise Spectral Density

Before proceeding to the comparison of the noise variances of phase and log-amplitude, it is convenient to compute power/noise ratios for the RC and SSC receivers. For the RC receiver, the ratio of signal power to one-sided noise spectral density (NSD) of the waveform Eq. (5) is

$$\frac{\text{Power}}{\text{NSD}} = \frac{A_e^2}{N_0} \cos^2 \theta \qquad \text{(residual carrier)} \qquad (20)$$

We have dropped the dependence of A_e on time.

To get a simple expression for the squared-suppressed-carrier (SSC) receiver, let us assume that

$$G_e(\omega_c \pm \lambda, t) = G_e(\omega_c, t), \quad (|\lambda| < 2\pi B) \qquad (21)$$

$$G_i(\omega_c + \lambda) = 1, \quad (|\lambda| < 2\pi B)$$

$$= 0, \quad \text{otherwise} \qquad (22)$$

This means that we are neglecting the dispersion of the external filter over the passband of the internal filter, which is assumed ideal. Then the doubled reconstructed carrier, Eq. (12), is

$$A_e^2(t) \propto \cos(2\omega_c t + 2\psi_e(t)) \qquad (23)$$

where

$$\alpha = \int_{-2\pi BT}^{2\pi BT} \operatorname{sinc}^{2i}(\tfrac{1}{2}x) \, \frac{dx}{2\pi} \qquad (24)$$

This α (the same as in Ref. 1) measures the signal loss due to the distortion of $d(t)$ by the receiver.

The noise spectral densities from Eqs. (18), (19), and (16) become (with time dependence dropped)

$$\begin{aligned} &N_0 A_e^2\,\alpha && \text{(S X N)} \\ &N_0^2\,B && \text{(N X N)} \\ &\tfrac{1}{2} A_e^4\,T\mu_2 && \text{(S X S)} \end{aligned} \tag{25}$$

where μ_2, a function of BT, is the mean-square oscillation of Φ/A_e^4 over a period $2\pi/T$. In the cases given below, the S X S density is almost negligible.

Now let $R = A_e^2 T/N_0$, the symbol SNR. Equations (23) and (25) give

$$\frac{\text{Power}}{\text{NSD}} = \frac{\tfrac{1}{2} A_e^4 a^2}{2(N_0 A_e^2\,\alpha + N_0^2\,B + \tfrac{1}{2} A_e^4 T\mu_2)}$$

$$= \frac{A_e^2}{N_0}\,\tfrac{1}{4}\,\gamma \quad \text{(squared-suppressed-carrier)} \tag{26}$$

where the degradation factor γ is given by

$$\gamma = \frac{R\alpha^2}{R\alpha + BT + \tfrac{1}{2} R^2\,\mu_2} \tag{27}$$

which is the same as β' of Ref. 1 (see Eq. (30) below) except for the small S X S noise term $\tfrac{1}{2} R^2\mu_2$. The next subsection will show why the factor 1/4 in Eq. (26) is not counted as a degradation.

B. Amplitude and Phase Noise Variances

Consider now the actual quantities of interest, namely A_e and ψ_e. Let us suppose that for both RC and SSC the phase of the signal in the video waveform is tracked (in nonreal time) by a phase-locked loop with one-sided bandwidth B_L. For RC (the waveform of Eq. (5) heterodyned to video), the variance of the loop phase estimate $\hat{\psi}_e$ is given by

$$\frac{1}{\sigma^2(\hat{\psi}_e)} = \frac{A_e^2}{N_0 B_L}\cos^2\theta \quad \text{(residual carrier)} \tag{28}$$

For SSC we must remember that the signal being tracked is the doubled carrier Eq. (23) (heterodyned to video). Thus, the usual linear-loop phase error variance is really the variance of $2\hat{\psi}_e$. Computing the variance of $\hat{\psi}_e$ introduces a factor of four that cancels the 1/4 in Eq. (26) and gives

$$\frac{1}{\sigma^2(\hat{\psi}_e)} = \frac{A_e^2}{N_0 B_L}\,\beta' \quad \text{(squared-suppressed-carrier)} \tag{29}$$

where, as in Ref. 1 (also see Refs. 2 and 5),

$$\beta' = \frac{R\alpha^2}{R\alpha + BT} \tag{30}$$

The S X S noise, small to begin with, has been suppressed by the coherent phase detection.

Because the SSC receiver does not have to deliver telemetry, the presquaring filter bandwidth $2B$ can be chosen to minimize the phase noise variance. It can be assumed that the symbol rate $1/T$ is set so that the nominal symbol SNR $R = A_e^2 T/N_0$ has some reasonable value, say between 0 dB and 10 dB. Given R, one can choose BT to maximize β'. (Recall that α is a function of BT from Eq. (24).) The resulting BT and β' are given as functions of R in Figs. 3 and 4 for $-4\text{ dB} \leqslant R \leqslant 12\text{ dB}$. (At a value of R slightly more than 12 dB, the optimal BT jumps discontinuously to a value greater than 1.) Also shown is the residual carrier suppression $\cos^2\theta$ for several values of the modulation index θ; the ratio $\beta'/\cos^2\theta$ is the advantage of SSC over RC.

Let the amplitude of the signal in the video waveform be extracted by a coherent amplitude detector (Fig. 5) whose low-pass filter has one-sided noise bandwidth B_A. With perfect phase tracking, the noise variance of the amplitude estimate $\hat{A}$ is

$$\sigma^2(\hat{A}) = N_A B_A \tag{31}$$

where N_A is the one-sided spectral density of the baseband noise from the amplitude detector.

For RC we have $A = A_e\cos\theta$, $N_A = N_0$; hence

$$\frac{A_e^2}{\sigma^2(\hat{A}_e)} = \frac{A_e^2}{N_0 B_A}\cos^2\theta \quad \text{(residual carrier)} \tag{32}$$

For SSC we have $A = (\alpha/\sqrt{2})\, A_e^2$, $N_A = 2N_0 A_e^2 \alpha + 2N_0^2 B + 2A_e^4 T\mu_2$. Since $\sigma(\hat{A})/A \approx 2\sigma(\hat{A}_e)/A_e$, the ¼ factor in Eq. (26) again goes away, and

$$\frac{A_e^2}{\sigma^2(\hat{A}_e)} \approx \frac{A_e^2}{N_0 B_A} \frac{R\alpha^2}{R\alpha + BT + R^2\mu_2}$$

(squared suppressed carrier) (33)

The degradation factor in Eq. (33) is the same as γ (Eq. (27)) except that the small S X S noise term has been doubled by the coherent detection. It can still be ignored in this context. Again, one can use Fig. 4 to compare SSC to RC.

V. The Effect of Dispersion

The suppressed-carrier signal, although its bandwidth may be as much as 60 MHz, is still a narrowband signal because the carrier frequency is at least 2.3 GHz. Dispersive effects of the medium may therefore be negligible. Nevertheless, let us measure the dispersion of the external filter $G_e(\omega, t)$ near ω_c by the function

$$H(\lambda, t) = \frac{G_e(\omega_c + \lambda, t)}{G_e(\omega_c, t)} \tag{34}$$

Then $G(\omega_c + \lambda, t) = G_e(\omega_c, t)\, G_i(\omega_c + \lambda) H(\lambda, t)$. If $H(\lambda, t)$ does not depend on t, then by Eq. (13) the complex amplitude $Y(0, t)$ of the reconstructed doubled carrier is still proportional to $G_e^2(\omega_c, t)$. In any case, assume that for $\omega_c + \lambda$ in the passband of G_i we have the development

$$H(\lambda, t) = 1 + h_1(t)\lambda + h_2(t)\lambda^2 + \cdots \tag{35}$$

Assume that $G_i(\omega, t)$ is known. Neglecting the remainder in Eq. (35), we have

$$Y(0, t) = G_e^2(\omega_c, t) \left[\int_{-\infty}^{\infty} G_i(\omega_c + \lambda) \times G_i(\omega_c - \lambda) \operatorname{sinc}^2(\tfrac{1}{2}\lambda T) \frac{Td\lambda}{2\pi} + \frac{4(2h_2 - h_1^2)}{T^2} \int_{-\infty}^{\infty} G_i(\omega_c + \lambda) \times G_i(\omega_c - \lambda) \sin^2(\tfrac{1}{2}\lambda T) \frac{Td\lambda}{2\pi} \right] \tag{36}$$

The second term carries the dispersive effect. Although one cannot measure the dispersion by observing $Y(0, t)$, one could use prior bounds on h_1 and h_2, and their variation with time, to estimate how much the ratio $Y(0, t)/G_e^2(\omega_c, t)$ varies with time.

VI. Conclusions

By squaring a suppressed-carrier signal, it is possible to provide the radio-science experimenter with a tape containing the reconstructed doubled carrier. For measuring amplitude and phase, this scheme has typically a 12-dB to 14-dB advantage over the present residual-carrier scheme.

If the dispersion of the medium over the presquaring filter passband is neglected, then the reconstructed doubled carrier yields the same information as the residual carrier; one merely takes the square root of the amplitude and halves the phase. There is a phase ambiguity of π instead of 2π. This is of no consequence if the phase is tracked continuously.

It is anticipated that the effect of media dispersion on the doubled carrier reconstruction will be small because the bandwidth of the suppressed-carrier signal is small compared to, for example, the difference between S band and X band. The effect of this dispersion can be estimated.

References

1. Lesh, J. R., "Tracking loop and modulation format considerations for high rate telemetry," *DSN Progress Report 42-44*, Jet Propulsion Laboratory, Pasadena, California, 1978.

2. Lindsey, W. C., and Simon, M. K., *Telecommunication Systems Engineering*, Prentice Hall, 1973.

3. Donnelly, H., and Nishimura, H., "Multi-Mission Receiver (MMR)," *DSN Progress Report 42-52*, Jet Propulsion Laboratory, Pasadena, California, 1979.

4. Hedin, G. L., Holmes, J. K., Lindsey, W. C., and Woo, K. T., "Theory of False Lock in Costas Loops," *IEEE Trans. Commun.*, COM-26, 1-12, Jan. 1978.

5. Simon, M. K. and Lindsey, W. C., "Optimum Performance of Suppressed Carrier Receivers with Costas Loop Tracking," *IEEE Trans. Commun.*, COM-25, 215-226, Feb. 1977.

6. Davenport, W. B., Jr. and Root, W. L., *An Introduction to the Theory of Random Signals and Noise*, McGraw Hill, 1958.

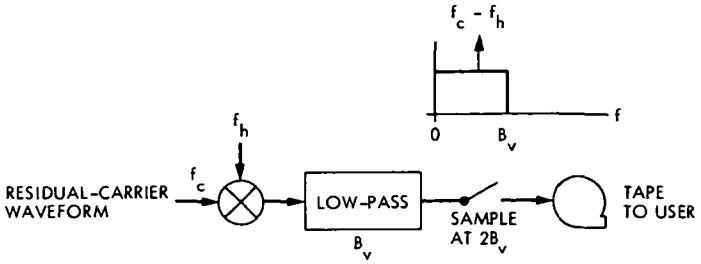

Fig. 1. Conceptual model of residual-carrier, open-loop receiver

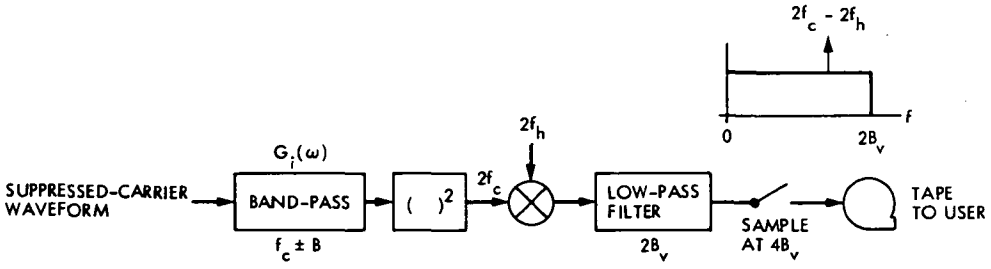

Fig. 2. Conceptual model of square-suppressed-carrier, open-loop receiver

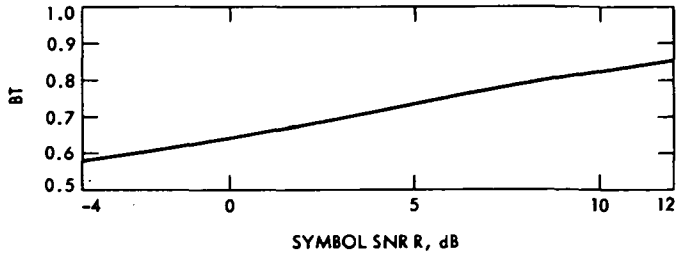

Fig. 3. Finding the optimal presquaring filter bandwidth $2B$ for the squared-suppressed-carrier (SSC) receiver (T = symbol time)

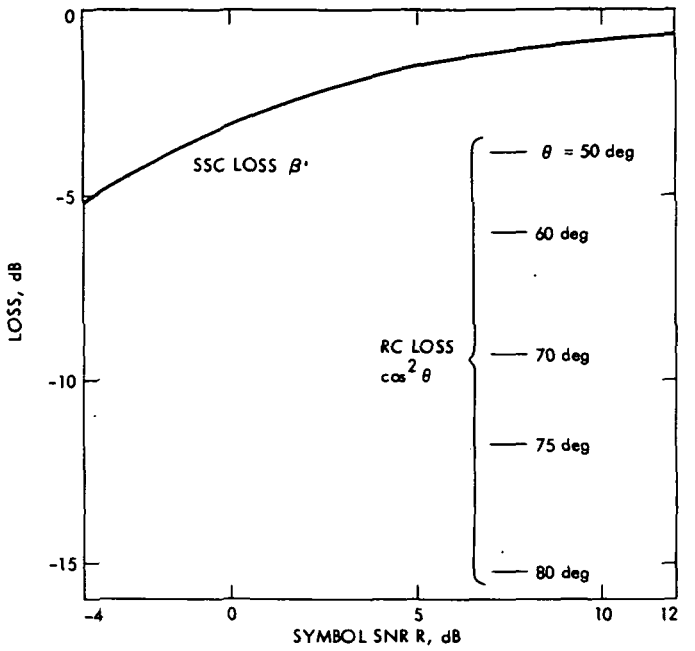

Fig. 4. Comparative losses of the SSC and residual-carrier (RC) receivers for several RC modulation indices θ

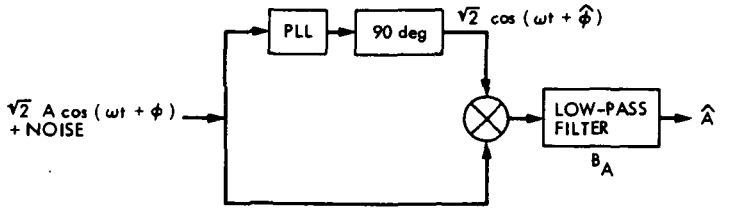

Fig. 5. Coherent amplitude detector

Appendix

S × S Components

Our aim here is to compute the discrete-spectrum and continuous-spectrum components of $s^2(t)$, where $s(t)$ is given by Eq. (9). To do this, we have found it expedient to approximate $d(t)$ by a waveform $d_N(t)$ of period NT, defined by

$$d_N(t) = d_j \quad (jT < t < (j+1)T), 0 \leqslant j \leqslant N-1)$$

$$d_N(t+NT) = d_N(t) \quad (\text{all } t) \tag{A-1}$$

where $d_0, \cdots, d_{N-1}$ are independent random variables taking the values 1 and -1 with probability 1/2. Then $d_N(t)$ has the discrete Fourier expansion

$$d_N(t) = \sum_{\lambda} D(\lambda) e^{i\lambda t} \tag{A-2}$$

where the λ spacing is $\Delta\lambda = 2\pi/(NT)$. Results will be obtained by letting $N \to \infty$.

Let $d(t)$ be replaced by $d_N(t)$. Ignoring DC components, we have

$$s^2(t) = \tfrac{1}{2} e^{i2\omega_c t} y(t) + \text{c.c.}$$

where

$$y(t) = \left[\sum_{\lambda} G(\omega_c + \lambda, t) D(\lambda) e^{i\lambda t}\right]^2$$

$$= \sum_{\omega} Y(\omega, t) e^{i\omega t} \tag{A-3}$$

The ω spacing is $\Delta\omega = 2\pi/(NT)$.

From Eq. (A-3),

$$Y(\omega, t) = \sum_{\omega} G(\omega_c + \lambda, t) G(\omega_c + \omega - \lambda, t)$$

$$\times D(\lambda) D(\omega - \lambda) \tag{A-4}$$

To compute the mean and variance of $Y(\omega, t)$ we need the second and fourth moments of the $D(\lambda)$ process. Let $\omega_1 = 2\pi/T$. From Eqs. (A-1) and (A-2),

$$D(\lambda) = \frac{e^{-i\lambda T} - 1}{-i\lambda T} \frac{1}{N} \sum_{j=0}^{N-1} d_j e^{-ij\lambda T}$$

$$(\lambda = k\omega_1/N, -\infty < k < \infty)$$

Then

$$E[D(\lambda_1)D(\lambda_2)] = \frac{(-1)^k}{N} \operatorname{sinc}(\tfrac{1}{2}\lambda_1 T) \operatorname{sinc}(\tfrac{1}{2}\lambda_2 T),$$

$$(\lambda_1 + \lambda_2 = k\omega_1)$$

$$= 0, \quad (\lambda_1 + \lambda_2 \neq 0 \bmod \omega_1) \tag{A-5}$$

$$E[D(\lambda_1)D(\lambda_2)D(\lambda_3)D(\lambda_4)]$$

$$= E[D(\lambda_1)D(\lambda_2)]E[D(\lambda_3)D(\lambda_4)] \quad \text{(part 1)}$$

$$+ E[D(\lambda_1)D(\lambda_3)]E[D(\lambda_2)D(\lambda_4)] \quad \text{(part 2)} \tag{A-6}$$

$$+ E[D(\lambda_1)D(\lambda_4)]E[D(\lambda_2)D(\lambda_3)] \quad \text{(part 3)}$$

$$+ \text{part 4}$$

$$\text{part 4} = -\frac{2}{N^3} (-1)^k \operatorname{sinc}(\tfrac{1}{2}\lambda_1 T) \cdots \operatorname{sinc}(\tfrac{1}{2}\lambda_4 T),$$

$$(\lambda_1 + \lambda_2 + \lambda_3 + \lambda_4 = k\omega_1)$$

$$= 0, \quad (\lambda_1 + \lambda_2 + \lambda_3 + \lambda_4 \neq 0 \bmod \omega_1)$$

If $d(t)$ were a Gaussian process, then part 4 would be zero.

From Eq. (A-4),

$$EY(\omega, t) = \sum_{\lambda} G(\omega_c + \lambda, t) G(\omega_c + \omega - \lambda, t)$$

$$\cdot E[D(\lambda)D(\omega - \lambda)]$$

$$E|Y(\omega,t)|^2 = \sum_{\lambda}\sum_{\lambda'} G(\omega_c+\lambda,t)G(\omega_c+\omega-\lambda,t)$$

$$\cdot \bar{G}(\omega_c+\lambda',t)\bar{G}(\omega_c+\omega-\lambda',t)$$

$$\cdot E[D(\lambda)D(\omega-\lambda)D(-\lambda')D(\lambda'-\omega)] \quad \text{A-7)}$$

where the bars mean complex conjugate. It is convenient to use the notation

$$F(\omega,\lambda,t) = G(\omega_c+\lambda,t)G(\omega_c+\omega-\lambda,t)$$

$$\times \operatorname{sinc}(\tfrac{1}{2}\lambda T)\operatorname{sinc}(\tfrac{1}{2}(\omega-\lambda)T) \qquad \text{(A-8)}$$

in terms of which the expectation of $Y(\omega, t)$ is:

$$EY(n\omega_1,t) = \frac{(-1)^n}{N}\sum_{\lambda} F(n\omega_1,\lambda,t) \quad (n=0,\pm1,\cdots)$$

$$EY(\omega,t) = 0 \quad (\omega \neq 0 \bmod \omega_1)$$

When Eq. (A-6) is used to compute the fourth moments in Eq. (A-7), the variance of $Y(\omega, t)$ takes the form

$$E|Y(\omega,t)|^2 = \sum_{i=1}^{4} \text{part } 1$$

where

$$\text{part } 1 = |EY(\omega,t)|^2$$

$$\text{part } 2 = \text{part } 3\,\frac{1}{N^2}\sum_{\lambda}\sum_{k=-\infty}^{\infty} F(\omega,\lambda,t)\bar{F}(\omega,\lambda+k\omega_1,t)$$

$$\text{part } 4 = -\frac{2}{N^3}\left|\sum_{\lambda} F(\omega,\lambda,t)\right|^2$$

We are going to interpret these by letting $N \to \infty$. When we do this, all the sums become integrals in which $1/N$ becomes $Td\lambda/(2\pi)$. Parts 2, 3, and 4 are all $O(1/N)$. For $\omega = n\omega_1$ we have in the limit

$$EY(n\omega_1,t) = (-1)^n\int_{-\infty}^{\infty} F(n\omega_1,\lambda,t)\,\frac{Td\lambda}{2\pi}$$

$$E|Y(n\omega_1,t)|^2 = |EY(n\omega_1,t)|^2$$

which says that the variances of the real and imaginary parts of $Y(n\omega_1, t)$ are zero, and hence

$$Y(n\omega_1,t) = (-1)^n\int_{-\infty}^{\infty} F(n\omega_1,\lambda,t)\,\frac{Td\lambda}{2\pi} \qquad \text{(A-9)}$$

a nonrandom quantity. When $n = 0$ we get Eq. (13) for the complex amplitude of the recovered doubled carrier; when $n \neq 0$ we get the spurs, which are expected to be smaller than the main peak because the functions $\operatorname{sinc}(\tfrac{1}{2}(\lambda - n\omega_1)T)$ are orthonormal. These discrete components necessarily have nonrandom amplitudes, otherwise $s^2(t)$ would have strange nonergodic properties.

Let $\omega \neq 0 \bmod \omega_1$. Then $EY(\omega, t) = 0$ and $E|Y(\omega, t)|^2 = O(1/N)$. This means that as $N \to \infty$ the discrete spectrum near ω tends to a spectral density. We can let $1/N = T\,\Delta\omega/(2\pi)$. Then

$$S_{ss}(2\omega_c+\omega,t) = 1/4\lim_{\Delta\omega\to 0}\frac{E|Y(\omega,t)|^2}{\Delta\omega/(2\pi)}$$

$$= \frac{T}{2}\int_{-\infty}^{\infty} F(\omega,\lambda,t)\sum_{k=\infty}^{\infty}\bar{F}(\omega,\lambda+k\omega_1,t)\,\frac{Td\lambda}{2\pi}$$

$$-\frac{T}{2}\left|\int_{-\infty}^{\infty} F(\omega,\lambda,t)\,\frac{Td\lambda}{2\pi}\right|^2 \qquad \text{(A-10)}$$

Define

$$\Phi(\omega,\lambda,t) = \sum_{k=-\infty}^{\infty} F(\omega,\lambda+k\omega_1,t)$$

which is an ω_1-periodic function of λ. In terms of it, Eq. (A-10) becomes

$$S_{ss}(2\omega_c+\omega,t) = \frac{T}{2}\int_0^{\omega_1}|\Phi(\omega,\lambda,t)|^2\,\frac{Td\lambda}{2\pi}$$

$$- \frac{T}{2} \left| \int_0^{\omega_1} \Phi(\omega, \lambda, t) \frac{Td\lambda}{2\pi} \right|^2$$

$$= \frac{T}{2} \int_0^{\omega_1} |\Phi(\omega, \lambda, t) - Z(\omega, t)|^2 \frac{Td\lambda}{2\pi} \tag{A-11}$$

where

$$Z(\omega, t) = \int_{-\infty}^{\infty} F(\omega, \lambda, t) \frac{Td\lambda}{2\pi} = \int_0^{\omega_1} \Phi(\omega, \lambda, t) \frac{Td\lambda}{2\pi} \tag{A-12}$$

Note that $Z(n\omega_1, t) = (-1)^n Y(n\omega_1, t)$ $(n = 0, \pm 1, \cdots)$. The special case $\omega = 0$ gives Eq. (16) of the text for the S X S noise spectral density at $2f_c$.

N80-33441

Noise Adding Radiometer Performance Analysis

C. Stelzried
Radio Frequency and Microwave Subsystems Section

The DSN noise adding radiometer (NAR) measurement accuracy is analyzed. The NAR capability is part of the Precision Power Monitor function recently introduced in the DSN. The potential system noise temperature measurement accuracy is estimated to be about 1.5% (1σ) with the 1 kelvin noise diode. Performance verification requires comparison noise temperature measurements with the manual Y *factor method and* routine *monitoring of critical elements in the NAR system such as system linearity and noise diode calibration. A technique is presented to calibrate and reduce the effects of the receiving system nonlinearity. Unsatisfactory performance or degradation of these critical NAR elements would require appropriate system upgrading.*

I. Introduction

A noise adding radiometer (NAR) is being implemented (Fig. 1) in the DSN as an integral part of the Precision Power Monitor (PPM). The NAR is required to convert signal-to-noise ratio (SNR) measurements to signal power. In addition the NAR is available with stand-alone capability.

II. Theory

The fundamental equation for the NAR is (Refs. 1, 2):

$$T_{OP} = T_N/(Y - 1) \tag{1}$$

where

T_{OP} = system operating noise temperature, K (defined at system input reference plane)

T_N = noise diode injected noise temperature, K (defined at system input reference plane)

$Y = (V_2 + \alpha V_2^2)/(V_1 + \alpha V_1^2)$, ratio

V_2 = detector output voltage, noise diode on, V

V_1 = detector output voltage, noise diode off, V

α = detector nonlinearity constant, V^{-1} (=0 in an ideal detector)

The NAR noise temperature measurement resolution is given by Ref. 1.

$$\Delta T_{OP} = 2T_{OP}(1 + T_{OP}/T_N)/\sqrt{\tau B} \tag{2}$$

where

τ = measurement time, s

B = predetection bandwidth, Hz

For example, if $T_{OP} = 20$ K, $\tau = 10$ s, $B = 10^7$ Hz, $T_N = 100$ K, then

$$\Delta T_{OP} \simeq 0.005 \text{ K}$$

T_N can be calibrated by connecting the receiver input to the ambient termination. With T_{OP} known, the NAR is used to solve

$$T_N = T_{OP}\Big|_{AMB}(Y - 1) \tag{3}$$

using (assuming a perfectly matched system with transmission line at temperature T_p)

$$T_{OP}\Big|_{AMB} = T_p + T_E \tag{4}$$

where

T_E = equivalent noise temperature of the receiver, K

$= T_M + T_F$

T_M = maser noise temperature, K

T_F = follow-up receiver noise temperature, K

T_P = physical temperature of ambient temperature, K

In the above, T_P is measured, T_M* is assumed known from laboratory measurements and T_F is determined from the maser on-off method.

$$T_F \simeq T_P / Y_{00} \tag{5}$$

where

Y_{00} = receiving system Y factor with maser turned off and on, ratio

The calibration resolution of T_N is given by (see Appendix A)

$$\Delta T_N = 2T_N(1 + T_{OP}/T_N)/\sqrt{\tau B} \tag{6}$$

For example, if T_{OP} = 300 K, τ = 10 s, B = 10^7 Hz, T_N = 100 K, then

$$\Delta T_N = 0.08 \text{ K} = 0.08\%$$

However, if T_N = 1 K in this example, then

$$\Delta T_N \simeq 0.06 \text{ K} = 6\%$$

which is unsuitable since a 6% error in T_N results in a 6% error in T_{OP}, Eq. (1), (i.e., a "low" noise diode cannot be calibrated directly using the ambient termination technique with "short" integration time). If T_N is small it is useful to use a larger T_N with a calibration transfer technique using both the ambient termination and the antenna. This calibration technique consists of:

(1) Calibrating T_{NH} using the ambient termination with Eq. (4)

$$T_{NH} = T_{OP}\Big|_{AMB}(Y - 1) \tag{7}$$

(2) Calibrating the system operating noise temperature on the antenna

$$T_{OP}\Big|_{ANT} = T_{NH}/(Y - 1) \tag{8}$$

(3) Calibrating T_{NL} using the known T_{OP} from step 2

$$T_{NL} = T_{OP}\Big|_{ANT}(Y - 1) \tag{9}$$

where

T_{NH} = "high" noise diode, K

T_{NL} = "low" noise diode, K

Using Eq. (6), the resolution of T_{NL} (step 3 alone), assuming T_{OP} = 20 K, τ = 10 s, $B = 10^7$ Hz, T_N = 1 K is 0.004 K.

Now, using $T_{OP}|_{AMB}$ = 300 K, $T_{OP}|_{ANT}$ = 20 K, T_{NH} = 100 K, T_{NL} = 1 K, B = 10^7 Hz and going through the calibration steps above, the calibration resolution, using Eqs. (2) and (6), is

(1) ΔT_{NH} = 0.025 K (τ = 100 s)

(2) $\Delta T_{OP\ ANT} = \sqrt{(0.005)^{2*} + (0.005)^{2**}}$ (τ = 10 s)

$\simeq$ 0.007 K

and

(3) $\Delta T_{NL} = \sqrt{(0.007)^2 + (0.004)^2} \simeq 0.01$ K (τ = 10 s)

This analysis neglects all bias errors and antenna/receiver system instabilities and interference. However, the analysis does indicate the basic calibration resolution limit. A 1% resolution (0.01 K) can also be obtained with the low noise diode for this example by calibrating on the ambient termination directly and integrating for approximately 6 minutes.

*If $T_{OP}|_{AMB}$ = 300 K and T_M = 3 K, a 10% error in T_M results in only = 0.1% error in $T_{OP}|_{AMB}$ (Refs. 3, 4).

*From Step 2, $\Delta T_{OP}|_{ANT} = (\Delta T_{NH})/(Y - 1) = 0.025/5 = 0.005$ K.

**From Eq. (2).

The primary "accuracy" concerns for the NAR are measurement resolution, repeatability as discussed above, bias errors, and "short" and "long" term measurement accuracy deterioration. Measurement resolution is obtained by selecting the system operating parameters (primarily measurement time) to satisfy Eq. (2). The primary concerns regarding bias errors and accuracy deterioration are receiving system linearity and noise diode calibrations.

System non-linearity effects are analyzed in Appendix B and, for example (1), $[T_{ND}(M)|_{AMB} - T_{ND}(M)|_{ANT} \simeq 0.1$ K], results in $\Delta T_{OP}|_{ANT} \simeq 0.1$. If the actual receiver nonlinearity is unacceptable, lower the maser gain (results in higher T_E), upgrade the receiver, use algorithm equation B-3 to reduce the effect or combine techniques to obtain acceptable performance.

III. NAR Performance

The expected noise temperature measurement accuracies (1σ) on the antenna for the NAR (assuming $T_{OP}|_{ANT} \simeq 20$ K, $T_{OP}|_{AMB} \simeq 300$ K, $B = 10^7$ Hz and $\tau = 10$ s) are summarized in Table 1 for 1 and 100 K noise diodes. It is assumed that the noise diode waveguide coupler has satisfactory directivity. This can be verified by $T_{ND}(M)|_{AMB} = T_{ND}(M)|_{ANT}$ with reduced maser gain.

The function of the NAR is to measure the receiving system operating noise temperature to a specified resolution and accuracy at a prescribed data rate. A manual Y factor method is available in the DSN for comparison noise temperature measurements with the NAR. The manual method consists of switching the receiving input between the antenna and an ambient termination and using a manually operated precision IF waveguide beyond cutoff attenuator to measure the Y factor. The 1σ accuracy of the manual method is about 2 percent (Ref. 3).

Comparison of the NAR with the manual Y factor method should be performed on a *routine* basis to detect NAR degradation. In addition, the NAR performance is verified by *routine* testing of the critical component elements of the NAR system. These are:

(1) Measurement resolution (evaluate the noise temperature measurement scatter).

(2) Linearity verification (using an auxiliary noise diode on the antenna and ambient termination, Appendix B).

(3) Noise diode calibration (long-term noise temperature calibration monitoring).

The analysis summarized in Table 1 indicates that the NAR has about 1.5 percent (1σ) accuracy potential with the 1 K noise diode (assuming no pathological problems such as RF interference). This level of measurement accuracy requires monitoring of the critical measurement elements indicated above. This analysis assumes satisfactory performance of these critical NAR elements. Unsatisfactory performance (i.e., unstable noise diode waveguide coupler or transmission line connectors, receiver nonlinearity, or RFI) would require appropriate system upgrading.

Indication of unsatisfactory performance should be investigated by monitoring the noise diode calibration over a 24-hr period and correlating with ambient temperature. In addition, the system should be stressed by moving and braking the antenna, manual cable movement, etc.

Acknowledgments

J. Hall suggested this study. B. Seidel, D. Bathker, L. Howard, and C. Foster made useful suggestions. J. Ohlson (Naval Postgraduate School, Monterey, Calif.) made suggestions and verified concepts and analysis.

Table 1. Summary of NAR measurement errors of system noise temperature on the antenna

	Case	
	1	2
Error source	T_N = 1 K	T_N = 100 K
Resolution, Eq. (2)	0.08	0.005
ΔT_N(Resolution, Eq. (6))	0.20[a]	0.016[b]
ΔT_N(bias error; assume 0.5%)	0.10	0.10
Receiver nonlinearity, Eq. (B-9) using 10 K auxiliary noise diode	0.10	0.10
$\Sigma\|\text{error}\|$	0.05 (2.5%)	0.22 (1.1%)
$\sqrt{\Sigma\|\text{error}\|^2}$	0.26 (1.3%)	0.14 (0.7%)

[a] Assumes ΔT_N = 0.01 K.

[b] Assumes ΔT_N = 0.08 K.

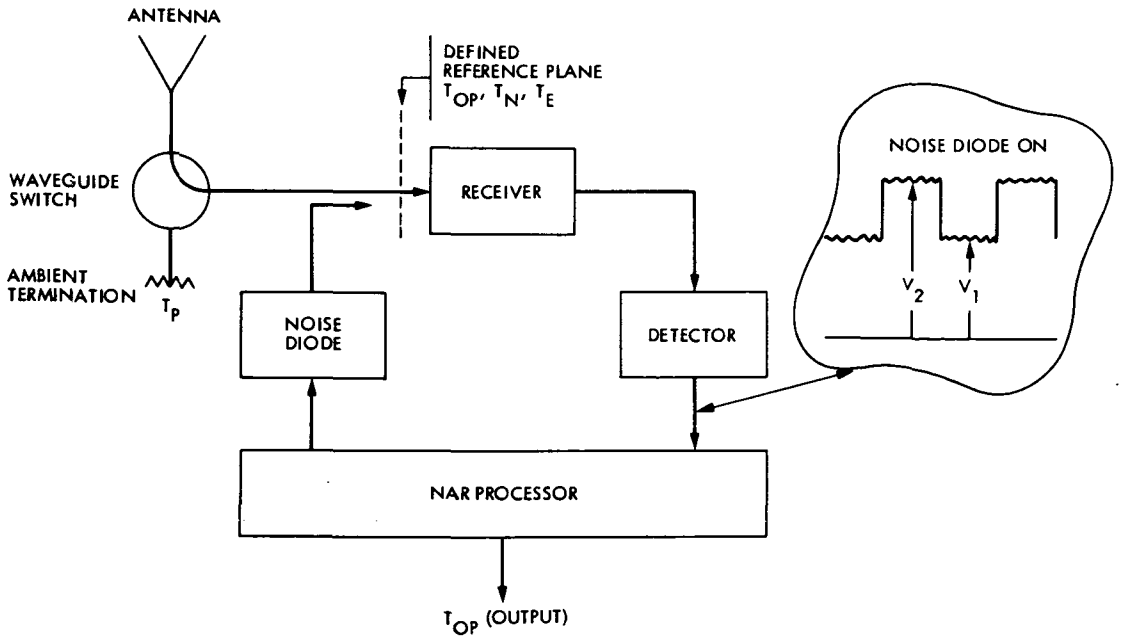

Fig. 1. Microwave receiving system showing NAR configuration

Appendix A

Noise Diode Calibration Resolution

The NAR noise diode can be calibrated (assuming T_{OP} is known) using*

$$T_N = T_{OP}\,[(V_2/V_1) - 1] \qquad \text{(A-1)}$$

where

$V_1 = GT_{OP}$, V

$V_2 = G(T_{OP} + T_N)$, V

G = system gain

Use

$$\sigma^2_{T_N} = \left(\frac{\partial T_N}{\partial V_1}\right)^2 \sigma^2_{V_1} + \left(\frac{\partial T_N}{\partial V_2}\right)^2 \sigma^2_{V_2} \qquad \text{(A-2)}$$

$$= T_N^2 \left(1 + \frac{T_{OP}}{T_N}\right)^2 \left[\left(\frac{\sigma V_1}{V_1}\right)^2 + \left(\frac{\sigma V_2}{V_2}\right)^2\right] \qquad \text{(A-3)}$$

From total power radiometry theory,

$$\left(\frac{\sigma V_1}{V_1}\right)^2 = \left(\frac{\sigma V_2}{V_2}\right)^2 = \frac{1}{(\tau/2)\,B} \qquad \text{(A-4)}$$

where

B = bandwidth, Hz

τ = total measurement time, s (measuring V_1 or V_2 only 1/2 the time)

Then

$$\Delta T_N = 2T_N\,(1 + T_{OP}/T_N)/\sqrt{\tau B} \qquad \text{(A-5)}$$

*For calculation of resolution, α in Eq. (1) can be approximated as 0.

Appendix B
Receiving System Linearity Verification

The NAR system can be used with an auxiliary noise diode to determine the receiving system nonlinearity. This is done by turning an auxiliary noise diode on and off with the receiving system connected alternately to the antenna and then to the ambient termination. The degree of system nonlinearity is indicated by the difference between the increase in system noise temperature with the different input noise power levels represented by the antenna and the ambient termination.

The auxiliary noise diode increases the system noise temperature by (receiving system input connected to the antenna or ambient termination, respectively)

$$T_{ND}\Big|_{ANT} = \widetilde{T}_{OP}\Big|_{ANT} - T_{OP}\Big|_{ANT} \tag{B-1}$$

$$T_{ND}\Big|_{AMB} = \widetilde{T}_{OP}\Big|_{AMB} - T_{OP}\Big|_{AMB} \tag{B-2}$$

where

T_{OP} = system operating noise temperature (auxiliary noise diode off), K

$\widetilde{T}_{OP}$ = system operating noise temperature (auxiliary noise diode on), K

Assume that the corrected and measured system noise temperatures (Ref. 5) are related by (all measured temperatures are identified by M)

$$T_{OP} = \gamma T_{OP}(M) - \beta T_{OP}^2(M) \tag{B-3}$$

where

$T_{OP}(M)$ = measured system noise temperature, K

T_{OP} = corrected system noise temperature, K

β = system non-linearity factor, V^{-1} (= 0 in ideal system)

γ = system nonlinearity factor, ratio (= 1 in ideal system)

Since

$$T_{ND}\Big|_{ANT} = T_{ND}\Big|_{AMB} \tag{B-4}$$

we have

$$\widetilde{T}_{OP}\Big|_{ANT} - T_{OP}\Big|_{ANT} = \widetilde{T}_{OP}\Big|_{AMB} - T_{OP}\Big|_{AMB} \tag{B-5}$$

From the NAR calibration technique, Eqs. (3) and (4),

$$T_{OP}(M)\Big|_{AMB} = T_{OP}\Big|_{AMB} \tag{B-6}$$

and with Eq. B-3

$$\gamma = 1 + \beta T_{OP}\Big|_{AMB} \tag{B-7}$$

Substituting Eq. (B-3) into (B-5) and solving using Eq. (B-7)

$$\beta = \frac{T_{ND}(M)\Big|_{AMB} - T_{ND}(M)\Big|_{ANT}}{\widetilde{T}_{OP}(M)\Big|_{AMB} T_{ND}(M)\Big|_{AMB} + T_{OP}\Big|_{AMB} T_{ND}(M)\Big|_{ANT} + T_{OP}^2(M)\Big|_{ANT} - \widetilde{T}_{OP}^2(M)\Big|_{ANT}} \tag{B-8}$$

The error in T_{OP} due to the system nonlinearity is (using $\Delta T_{OP} = T_{OP} - T_{OP}(M)$, with Eqs. B-3 and B-7),

$$\Delta T_{OP} = \beta T_{OP}(M) \left[T_{OP}(M)\Big|_{AMB} - T_{OP}(M)\right] \quad \text{(B-9)}$$

For example (1),

$$T_{OP}(M)\Big|_{ANT} = 20\ \text{K}, T_{OP}\Big|_{AMB} = 300\ \text{K}, T_{ND}(M)\Big|_{ANT}$$

$$= 10\ \text{K}, T_{ND}(M)\Big|_{AMB} = 10.1\ \text{K}.$$

This results in

$$\beta = \frac{0.10}{(310.1)(10.1) + 300(10) + (20)^2 - (30)^2}$$

$$= 1.776 \times 10^{-5}$$

$$\gamma = 1 + (1.776 \times 10^{-5})\, 300 = 1.0053$$

$$\Delta T_{OP}\Big|_{ANT} = 1.776 \times 10^{-5}\,(20)\,(300\text{-}20) = 0.1\ \text{K}$$

This example is typical of a highly linear receiving system.

Equation (B-3) can be used as in the example for error estimates or alternately as a method to reduce the effects of the receiving system nonlinearity. In the latter case, β and γ are determined from calibrations using the auxiliary noise diode and a corrected T_{OP} is computed from Eq. (B-3). In this case the linearity error is greatly reduced. This can be verified in practice with the same auxiliary noise diode.

For example (2)

$$T_{OP}(M)\Big|_{ANT} = 20\ \text{K}, T_{OP}\Big|_{AMB} = 300\ \text{K}, T_{ND}(M)\Big|_{ANT}$$

$$= 10\ \text{K}, T_{ND}(M)\Big|_{AMB} = 12\ \text{K}.$$

This results in $\beta \simeq 3.203 \times 10^{-4}$, $\gamma = 1.096$ and $\Delta T_{OP}\Big|_{ANT} \simeq$ 1.8 K. Equation (B-3) is shown plotted in Fig. B-1 for this example, chosen to illustrate a highly nonlinear receiving system.

Poor directivity of the waveguide coupler used to inject the noise diode, T_N, could result in $T_{ND}\Big|_{ANT} \neq T_{ND}\Big|_{AMB}$. This is due to the difference in coupling factor of the waveguide coupler when connected to the antenna and ambient load, which in general will not have identical VSWRs. Therefore, if $T_{ND}\Big|_{ANT} \neq T_{ND}(M)\Big|_{AMB}$ it will be necessary to distinguish between poor waveguide coupler directivity and receiver nonlinearity. This can be done using an independent method from the above derivation for receiver linearity verification: (1) calibrate system noise temperatures with normal system gain; (2) recalibrate system noise temperature, with reduced (approximately 10 dB) maser gain accounting for increased maser followup noise temperature (Eq. 5). No change in the calibrations would indicate a linear system.

If low system noise temperature is not critical in a particular application, then maser gain reduction could be a simple operational solution to receiver system nonlinearity.

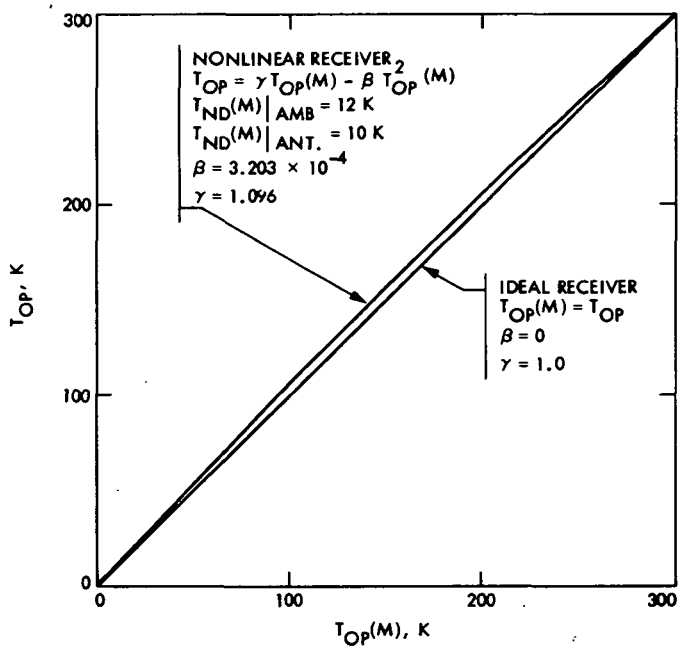

Fig. B-1. T_{op} vs $T_{op}(M)$ for a highly nonlinear receiving system

References

1. Batelaan P. D., Goldstein R. M., and Stelzried, C. T., "A Noise Adding Radiometer for Use in the DSN," Space Programs Summary 37-65, Vol II, Jet Propulsion Laboratory, Pasadena, Calif.

2. Software Definition Document, DSS Receiver Subsystem Precision Power Monitor SDD-DOI-5132-OP Rev. A, Code ID No. 23835, Nov. 27, 1979.

3. Stelzried, C. T., "Operating Noise-Temperature Calibrations of Low-Noise Receiving Systems," *Microwave Journal*, Vol. 14, No. 6, June 1971, p. 41.

4. Stelzried, C. T., "Post Amplifier Noise Temperature Contribution in a Low Noise Receiving System," *Proceedings of the IRE*, Vol. 52, No. 1, Jan. 1964, p. 77.

5. Freiley, A. J., Ohlson, J. E., and Seidel, B. L., "Absolute Flux Density Calibrations: Receiver Saturation Effects," DSN Progress Report 42-46, May/June 1978, p. 123, Eq. (19), Jet Propulsion Laboratory, Pasadena, Calif.

N80-33442

Networks Consolidation Program

M. L. Yeater and D. T. Herrman
Office of Telecommunications and Data Acquisition

G. E. Sanner
Bendix Field Engineering Corporation

The Networks Consolidation Program (NCP) was established by NASA in the fall of 1979 to implement the recommendations of the Networks Planning Working Group, which had been presented at NASA Headquarters in October of that year. The goals of the NCP were defined to include the planning, designing, and implementing of a single network of ground tracking stations.

The proposed consolidated network will make use of facilities that are now included in the Goddard Ground Spaceflight Tracking and Data Network as well as the existing JPL Deep Space Network. These facilities will be combined and modified to provide a consolidated network that is capable of supporting the set of planetary and Highly Elliptical Earth Orbiter missions that are planned for the Tracking and Data Relay Satellite System era.

This report traces the history of activities and events that led to the decision to consolidate the NASA ground tracking and data networks. It also presents a summary of the management and planning activities that have taken place at the Jet Propulsion Laboratory, Goddard Space Flight Center, and at the NASA Headquarters Office of Space Tracking and Data Systems, with respect to the NCP, from the time of decision in October 1979 to the present.

I. Introduction

The Deep Space Network (DSN) provides radio metric data and acquisition support for unmanned spacecraft engaged in the scientific investigation of both the planets and interplanetary space. Communication with and tracking of Earth-orbiting spacecraft have been performed by a world-wide network of ground-based tracking stations known as the Spaceflight Tracking and Data Network (STDN). This network has traditionally handled all Earth orbiters including Highly Elliptical Earth Orbiter (HEEO) and near-Earth missions. The latter class will be serviced by the Tracking and Data Relay Satellite System (TDRSS) when it becomes operational as a part of the STDN early in 1984. The few remaining HEEO missions would be serviced by a portion of the Ground Spaceflight Tracking and Data Network (GSTDN). As shown in Fig. 1, GSTDN stations are located at twelve separated geographical positions. Because of both limited numbers of such future planned missions, and continued high cost of GSTDN maintenance and operations (M&O), a TDRSS era planning study was directed by NASA to identify possible economic alternatives.

The TDRSS was conceived as an alternative means of providing tracking and data relay support for a large class of Earth-orbiting satellies by using a set of satellite relay stations in stationary orbit above Earth's equator. With its two operational satellites (Fig. 1), the TDRSS will provide the potential for near-global, real-time coverage (at least 85 percent of each orbit) for most users. But current and future planned HEEO missions will operate above, or outside of the TDRSS zone of coverage. In many respects, such missions have operational parameters that are similar to those missions that are supported by the DSN. Thus, the question was raised, "was there any combination of GSTDN and DSN that could result in more economical support for those missions that could not be supported by the TDRSS?"

To address this question, NASA Headquarters determined that a study effort should be conducted jointly by its Office of Space Tracking and Data Systems (OSTDS), by the Jet Propulsion Laboratory (JPL), and by the Goddard Space Flight Center (GSFC). Known as the Networks Planning Working Group, the study commenced in May 1979 and concluded in October 1979. The results of the study are summarized here. For more detail, Ref. 1 should be consulted.

II. Background

The OSTDS Networks Planning Working Group included representatives from OSTDS, GSFC, and JPL in addition to members from the Spanish Instituto Nacional de Tecnica Aerospacial (INTA) and the Australian Department of Science and Environment (DSE).

A Networks Planning Workshop was held on June 11 to 15, 1979, at GSFC. At that time identified options were reviewed, compared, and ranked. Three were selected and presented to NASA's Associate Administrator for OSTDS on June 13, 1979. General encouragement to proceed with the detailing of three primary options was indicated. These options were: (1) the current plans for the DSN and GSTDN (as a baseline), (2) a hybrid network, which would retain the separate identities of the two present networks, but which would provide enhanced cross-sharing of facilities between them, and (3) a single consolidated network, presumably under the management of JPL.

A. Goals and Objectives

The explicitly stated goal of the 1979 planning effort was to devise a technical and managerial approach that would: (1) provide adequate support for flight projects that cannot be supported by the TDRSS; (2) not preclude other potential NASA missions (e.g., geodynamics); (3) make best use of existing NASA facilities; (4) be consistent with realistic NASA resources; and (5) provide appropriate and useful roles for the several involved organizations, which include NASA Headquarters, GSFC, JPL, INTA, and DSE.

Throughout the planning effort, it was assumed that the TDRSS would provide support for all low Earth-orbiting spacecraft by 1984. GSFC would continue to manage the TDRSS including its associated ground station and control center. Also, any proposed consolidation of the GSTDN and DSN was not to take place until the TRDSS was operational and all GSTDN support of low Earth-orbiting spacecraft was complete. Phasedown of the unneeded GSTDN facilities would also be completed by GSFC before consolidation.

There were two main drivers considered in developing the study. One was economy. The second was the 1986 Voyager encounter at the planet Uranus, as shown in Fig. 3. Enhancement of the X-band telemetry capability, an essential part of the networks' consolidation, would be repaid in additional data from this never-before-explored planet, if the enhancement could be completed before late 1985.

B. Baseline for Separate Networks

The GSTDN plans for the TDRSS era called for a gradual phasedown of the network, as shown in Fig. 1, with the following exceptions: (1) the GSTDN main sites, consisting of Orroral Valley (ORR), Australia, Goldstone-Mojave (GDS), California, and Madrid (MAD), Spain, are approximately colocated with DSN sites as shown in Fig. 2; (2) stations in Florida (MILA) and Bermuda (BDA), which provide shuttle launch, landing, and range safety support; and (3) the station located at GSFC (ETC) would be dedicated to support of geosynchronous spacecraft.

The baseline plan for the GSTDN also included some automation of the main sites after phasedown was complete. This automation was expected to achieve operational savings in the 1985 to 1987 time period. Also, the baseline plan for the DSN's evolution into the late 80s would result in the Mark IV DSN (1988) configuration. Enhanced navigation, telemetry, and radio science capability were to be concentrated in the Goldstone complex. Overseas tracking would be provided by the present conjoint stations with only minor improvements in their existing capability complement.

C. A Consolidated Network

In the 1979 study, the Consolidated Network, composed of elements from the present DSN and the GSTDN main sites, showed markedly less cost and more capability than the sum of the separate networks. This option was planned around the then-existing plan for the Mark IV DSN augmented by GSTDN facilities and resources to support the HEEO missions, to

enhance the deep space telemetry capability, and to reduce future maintenance and operations costs. Figure 2 is a top-level overview of that Consolidated Network. Each of the complexes contained all of the DSN and GSTDN antennas planned for each locale. The 26-meter antennas were, in all cases, to be expanded to 34-meters for increasing X-band telemetry capability. The enhanced features of the DSN plan for Goldstone were also included. A Signal Processing Center (SPC) would be established at each of the three complexes and provide economies through the concentration of functions, with a corresponding reduction in manpower required by the stations at each complex.

D. Selection Criteria

The selected approach had to fit within both the projected NASA resources and the institutional capabilities of the "doing" organizations. Also, it needed to be acceptable to the participating organizations. The network life-cycle costs needed to be minimized, subject to a constraint of limited initial funding. Also, the approach would need to make the best use of existing NASA facilities and costs that had already been incurred.

Further, the selected approach was not to inhibit radio astronomy and radio science. If possible, it was not to preclude OSTDS support of future NASA initiatives, such as geodynamics.

E. Recommendations

On August 1, 1979, the Networks Planning Working Group presented their recommendations at a JPL Formal Review, which included members of the JPL Senior Staff and the Office of Telecommunications and Data Acquisition (TDA) Advisory Council. With their support, the working group concluded the OSTDS review on August 13, 1979, with a series of recommendations. It was suggested that the Networks Consolidation Plan (NCP), as presented, be adopted as a baseline plan for the ground tracking networks and that OSTDS and JPL Program Managers be appointed with responsibility for the networks' consolidation. Work leading to the Mark IV DSN was to be continued insofar as it contributed to the networks' consolidation. The plans to phase down GSTDN support of low Earth orbiters were to be continued.

The working group further recommended that system engineering and management studies should be supported in FY 80 to: detail improvements, such as centralized control and signal processing; prepare a detailed Networks Consolidation Implementation Plan that considers life-cycle costs in view of schedule; integrate network combining with other implementation plans; prepare a Networks Consolidation Management Plan; and prepare a Mission Support Plan for the consolidation period. Design engineering and implementation would begin in FY 81 according to detailed plans developed in FY 80, along with system contracting preparations needed to support the NCP.

III. Management Planning

Pursuant to these recommendations of the Networks Planning Working Group and the subsequent approval of those recommendations by NASA Headquarters, steps were taken to establish both the NCP and a program management structure. The latter was to include representatives from each of the participating organizations.

By January 1980, an NCP Office was established at JPL in the TDA Office. Simultaneously, program offices were established at GSFC and in the OSTDS. JPL and GSFC management and technical counterparts were identified, and monthly working sessions were initiated.

A. NCP Flight Mission Set

The JPL Program Manager began discussions with GSFC and OSTDS in February 1980, in an effort to establish a meaningful flight mission set that the Consolidated Network would need to fulfill its support role, and upon which the design of the total network would depend. Figure 3 shows the mission set currently under consideration.

B. Organization

The NCP is organized within the TDA office in JPL, under the NCP Manager. He directs the accomplishment of the networks' consolidation, together with the OSTDS and GSFC NCP Managers. Additional management support will be provided by the Spanish INTA and Australian DSE agencies. This multiagency organizational structure is depicted in Fig. 4. In addition to these participating organizations, a steering committee and a review board have been formed at JPL to support the NCP Manager. A Planning Team and a System Design Team have been organized to conduct the initial planning and system engineering activities required prior to the detailed design and implementation phase. The Planning Team organization consists of representatives from the key technical divisions within JPL that support the DSN, together with representatives from the organizations in the TDA Office.

The System Design Team also comprises both Technical Division and TDA personnel. Each of several task areas is headed by a Task Leader from a Technical Division with assistance from a Systems Engineer in TDA Engineering (Office 430).

At GSFC, accomplishment of the NCP is supported by the Networks Directorate and the Mission and Data Operations Directorate.

C. Schedule

The near-term schedule shown in Fig. 5 covers the initial planning phase of NCP activity. This first phase, comprising Program Planning and Systems Engineering, occurs basically in CY 1980. Development of high-level and detailed program plans, performance of special engineering studies, and establishment of a baseline system design are scheduled to be accomplished during this phase.

The overall schedule drivers are: the date on which the TDRSS is declared fully operational (presently estimated to be not later than January 1984), and the Voyager encounter at the planet Uranus beginning in November 1985.

D. Program Directives

The Networks Consolidation Program directives consist of technical and managerial guidance derived primarily from the OSTDS Networks Planning for the TDRSS Era Study (Ref. 1). Planning assumptions, Consolidated Network design strategy, and technical and managerial option selection criteria have been adopted from this study. They are to be used as the constraints, assumptions, and design strategy to be adhered to in accomplishing the NCP.

The program constraints include the following: the Consolidated Network will not support low Earth-orbital spacecraft, which are by design and policy to be supported exclusively by the TDRSS; the networks' consolidation cannot be completed until the TDRSS is fully operational and GSTDN support of low Earth-orbiting spacecraft is terminated; the consolidation of the networks must be accomplished within a relatively fixed NASA budget; management of the NCP should not preclude provision of tracking services by other host countries or other agencies; and the networks' consolidation is not intended to compensate for the decrease in ground station support of Earth-orbiting spacecraft that will occur because pre-NCP GSTDN stations are being closed. This decrease in ground station support is the result solely of the decision to support such spacecraft by TDRSS and is not related to the networks' consolidation effort.

The program assumptions include the following: TDRSS will be fully operational and providing support for low Earth-orbiting spacecraft not later than January 1984 (GSFC has the management responsibility for TDRSS); phasedown of unneeded GSTDN stations will have been started before the networks are consolidated; equipment from other closed GSTDN stations can be made available for incorporation into the Consolidated Network as the GSTDN is phased down; equipment obtained from GSTDN stations will be configured to make it compatible with the DSN mode of operation; existing staff will be available and can be trained to operate and maintain the developing Consolidated Network, so that additional station and complex personnel will not be needed; and CTA 21 and MIL 71 will continue to exist as functional entities, CTA 21 shall be revised to simulate an SPC and its associated Front End Areas (FEA), and MIL 71 shall be reduced to the configuration that is needed for spacecraft-network compatibility tests and will be activated only when needed for specific flight projects.

The preliminary design strategy is discussed in the baseline system development section later in this article. It is also based upon the following important criteria: the primary means of increasing aperture for enhancing deep-space telemetry reception shall be the arraying of multiple antennas that shall be provided at each of the three complexes; all antennas together with their associated FEA subsystems shall operate in the unattended mode for all normal tracking; signal processing equipment shall be interchangeable between planetary and HEEO spacecraft communications links; design shall plan for a minimum operational lifetime of 10 years; standard data interface protocols and formats that are compatible with TDRSS spacecraft interfaces shall be established; redundancy shall be incorporated only to the extent that it is necessary to provide required schedule and functional availabilities; the Consolidated Network shall provide the same radio science and radio astronomy capabilities that are present in the pre-NCP DSN, i.e., the capabilities that are designated in the Support Instrumentation Requirements Documents (SIRDs) for these activities; consider using turn-key contractors to convert 26-m antennas to 34-m antennas in order to expedite the conversion; economize in the usage of energy from nonrenewable sources by using an energy cost inflation factor that is at least twice that used for other costs when estimating life-cycle costs; accommodate command rates up to at least 1 kbits/s in various modes; and incorporate the ability to detect direct carrier modulation.

E. Reviews and Reports

NCP reviews are conducted by a Formal Review Board convened by the JPL Assistant Laboratory Director for TDA. NCP status reports are presented periodically at the Director's Report and Discussion (DRD) to acquaint upper levels of JPL management with the NCP. On-going reviews of program directions and progress are conducted by an NCP Steering Committee chaired by the JPL Manager of TDA Special Projects and is composed of JPL experts and external consultants.

Also, two categories of reviews are held at NASA Headquarters to insure that OSTDS Management is kept informed of the status and progress of the program with respect to both budgets and technical matters. First, budgetary reviews are scheduled in six-month intervals as a part of the Work Authorization Document (WAD) review cycle. Second, technical reviews are scheduled on a quarterly basis to provide the OSTDS NCP Manager with a current status report on all aspects of program progress.

Standard NASA/JPL reports are used for program-level reporting and include the Network Management Report (NMR), which is prepared monthly. Also, Implementation Schedule (IMPSKED) Reports are generated quarterly for NASA management, and periodic inputs are provided to the TDA Progress Report.

IV. System Design Approach

The approach used in designing the system for the networks' consolidation has been one of developing a baseline design that is in conformity with the constraints, assumptions, and design strategy set forth in the Management Plan. Desirable alternatives are then studied to determine their effect on the cost and schedule of the baseline system. Constrained by overall budget effects, the optimum NCP system resulting from this approach will then be selected, developed, and implemented.

A. Baseline System Development

The baseline system that is being developed for the three complexes (Goldstone, Canberra, and Madrid) includes all of the DSN and GSTDN antennas previously in existence, or planned for in each of those locations. In particular, the GSTDN 9-meter and 26-meter antennas, near each of the DSN complexes in California, Australia, and Spain will become part of the Consolidated Network. These complexes are shown in Fig. 2. Typical DSN and GSTDN stations are shown in Fig. 6 prior to consolidation. The DSN 64-, 34- and 26-meter subnets utilize separate signal processing facilities, generally located at a distance of 5 to 20 km from the Communications Terminal of NASCOM. Also, radio metric signal data, from the GSTDN 9-meter and 26-meter antennas are directed to GSFC via NASCOM.

Figure 7 shows the general complex configuration after the networks' consolidation. A central Signal Processing Center (SPC) will be established at each of the three complexes. Each center provides signal processing and monitor and control facilities for all antennas in the complex, as well as all other functions that are centralized there. The objective of these centers is to provide maintenance and operations cost savings through concentration of functions and a corresponding reduction in manpower. In the Consolidation Network being developed, the front-end area (FEA) of each antenna is to be located at a distance that is less than 1 km from the SPC. This enables RF signal combining, which enhances arraying of multiple antennas. The resulting increase in aperture is useful for improving deep-space telemetry reception. Antenna arraying capability is to be provided at each of the three complexes. Received RF signals are amplified and down converted in the FEA, where all antenna functions are also monitored. Both the 64-meter and the present 34-meter antennas at each complex will be used to track planetary and interplanetary spacecraft. When appropriate, tracking of planetary spacecraft will be augmented by arraying one or more converted DSN or GSTDN 26-meter antennas. An example of this is the planned future support of the Voyager encounter with Uranus. The GSTDN 9-meter antennas are not intended to be used to support planetary and interplanetary missions. However, the GSTDN 26-meter and the present DSN 26-meter DSN antennas will be converted to 34-meter, high-efficiency, S- and X-band listen-only antennas. These antennas will be capable of supporting either deep-space or GSTDN missions.

B. Special and Alternative Studies

In developing the baseline system, special studies have been conducted in an effort to establish the parametric requirements of the NCP. A special assessment is being made of NCP capability to support HEEO missions in terms of possible special navigation requirements. Additionally, NCP mission support requirements are being analyzed in view of existing mission scheduling resources.

Because of the antenna arraying objective for NCP, certain alternative studies are also being conducted. The results of these studies are necessary to make high-level decisions, including "to move or not to move" certain antennas. Arraying may be enhanced by relocation of some of the antennas within any given complex. Accordingly, cost tradeoffs are being determined for relocation of certain antennas vs possible reconfiguration for remote operation. Also, RFI and performance degradation of antennas colocated in high-density arrangements are under investigation, along with possible weather effects. Microwave link and fiber optic techniques are being considered as a possible means for transmitting received RF data from some of the antenna FEAs to the SPC for possible RF combining. This would further enhance antenna arraying.

C. Present NCP System

Current study and planning for the Consolidated Network is directed towards selection of a final system design. In general, the configuration has been developing in the direction

shown in Fig. 8. The three complexes, Goldstone, Canberra, and Madrid, provide output data from their SPC to the Central Communications Terminal at JPL. There the data is further distributed to the Network Operations Control Center (NOCC), the Mission Control and Computing Center (MCCC), and other Project Operation Control Centers (POCCs).

As shown, the three complexes will have basically the same capability. The Goldstone complex will include the DSN Deep Space Stations (DSSs) 11, 12 and 14, and the GSTDN 9- and 26- (converted to 34-) meter stations. The transmit (XMT) and receive (RCV) capabilities in S-band (S) and X-band (X) are shown in Fig. 8 for the various stations. Also, a microwave relay link connects DSS 12 and the SPC because of their geographic separation. Capabilities at the Australian (Canberra) and Spain (Madrid) complexes are similar. At all three complexes, the GSTDN 9-meter stations have an S-band transmit capability, since these stations will provide for command of HEEO missions. In all Deep Space Stations shown, an objective is to make the FEA (Fig. 7) operate in an unattended environment.

V. Future Plans

As the system design for the Consolidated Network proceeds, planning for its implementation is also progressing. This includes the important supporting areas of transition and mission support. Planning activity, to date, is reported below. As progress is made, it will be presented in future reports.

A. Implementation Plan

The NCP Implementation Plan is currently being developed to provide the more detailed technical and managerial approaches to the work that must be performed on the present GSTDN and DSN elements to convert them into the fully operational Consolidated Network.

The plan will provide the processes and approaches to be followed for accomplishing the networks' consolidation during the detailed design, production, installation, and test phases. It will specifically define the constraints on, and assumptions for, NCP implementation, and the interrelationships between participating organizations and program plans. When completed, it will also describe the organizational structure, responsibilities, authorities, and communication interfaces for NCP implementation management. Finally, it will present the orderly sequence of events to be followed at all network facilities and locations for accomplishing implementation of the Consolidated Network. Preliminary planning, to date, is typical of that shown on the target schedule of Fig. 9.

B. Transition Plan

As an interrelated part of the implementation process, the objective of the Transition Plan is to provide directions for transferring, from GSFC to JPL, the network responsibility for the GSTDN missions to be supported by the Consolidated Network. This change must be accomplished without adversely impacting ongoing flight projects support.

The plan will address three general transition areas including management, operations, and configuration. In the management and operations areas, specific functions to be transferred are being identified. Thereafter, detailed transfer criteria will be developed. Described in detail will be hardware and software elements required from GSFC (if applicable), staffing and budget requirements, and the JPL organization(s) to be responsible after transfer of responsibility from GSFC. In the configuration area, the equipment arrangements that are unique to the transition period will be developed.

C. Mission Support Plan

Also importantly related to the implementation process is the Mission Support Plan. It will provide the detailed technical and managerial requirements for maintaining adequate support of the flight projects that will be using the Consolidated Network during its transition, implementation, and fully operational stages.

When completely developed, the plan will describe how the DSN will support each of the users of the Consolidated Network. Each mission will be described in terms of the technical characteristics required by NCP planners and designers for network capacity planning and network configuration establishment.

Network user interfaces are being developed as part of the plan. Network scheduling, predicts generation, data delivery, and network operations support will be defined to allow potential users an understanding of the requirements for accessing and obtaining Consolidated Network support.

The Mission Support Plan will specify the user support strategy to be followed during transition to the Consolidated Network. In particular, the specific activities required to demonstrate operational readiness will be delineated in the plan, along with initial planning phase network user interfaces and mission support strategy. The interfaces and commitments specified in the plan will be finalized in the Network Operations Plan (NOP) and Network Support Plan (NSP) prepared for each network user.

Reference

1. Layland, J. W., *OSTDS Networks Planning for the TDRSS Era*, OSTDS Report, January 1980.

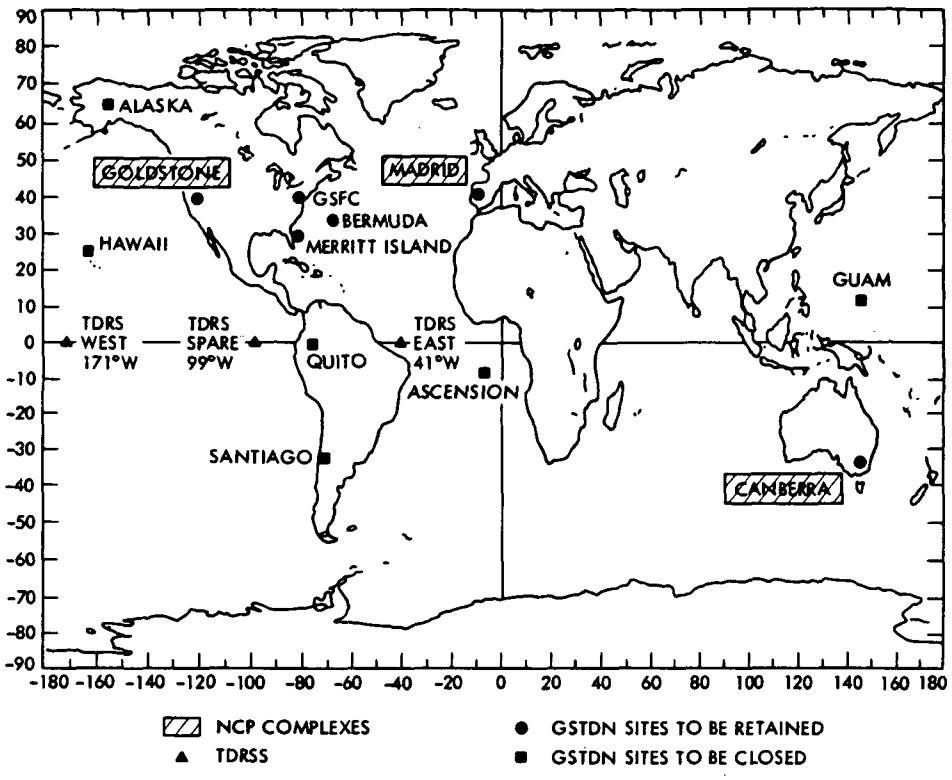

Fig. 1. Location of NASA ground stations

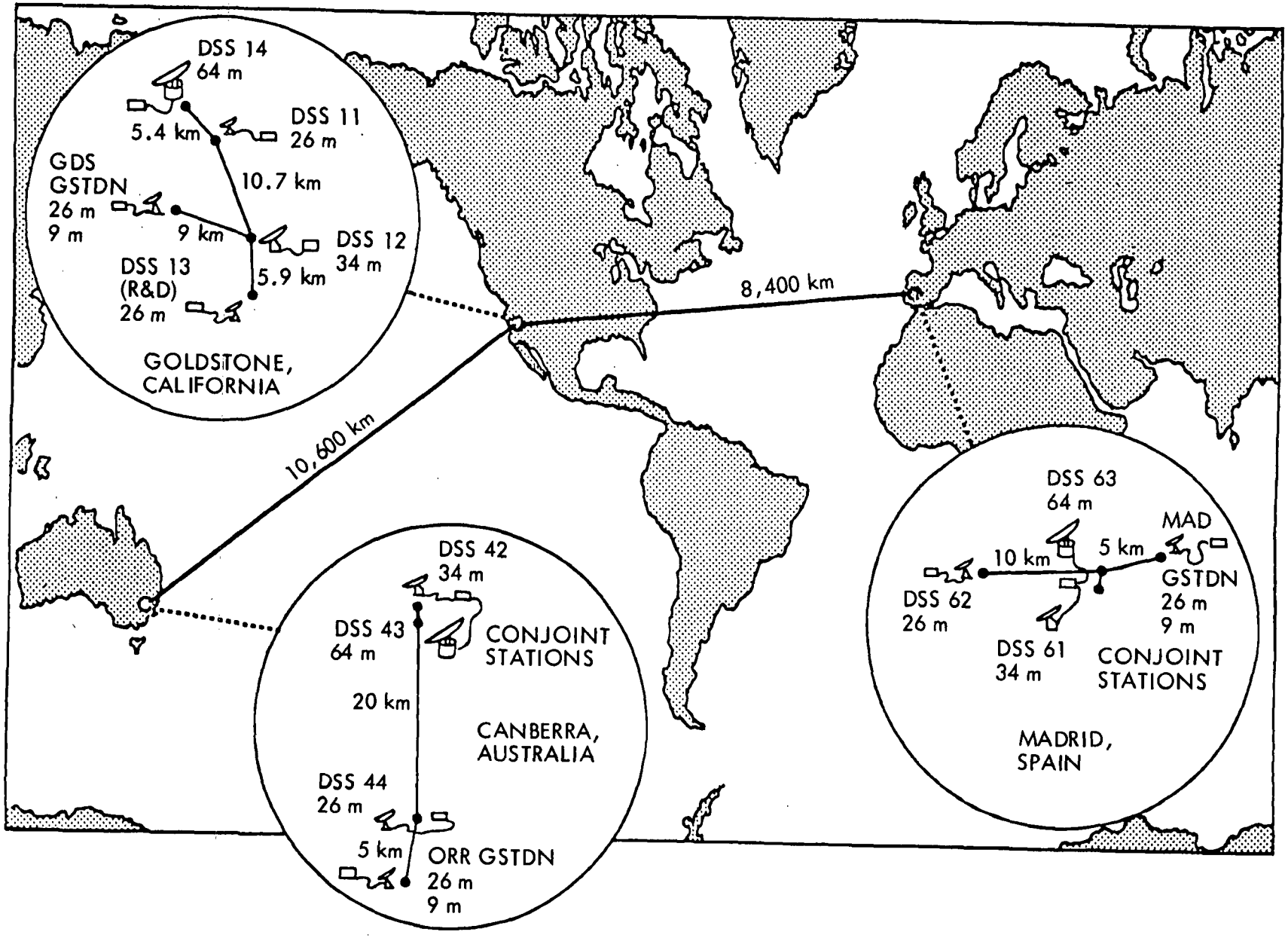

Fig. 2. Deep Space Network complexes

ORIGINAL PAGE IS
OF POOR QUALITY

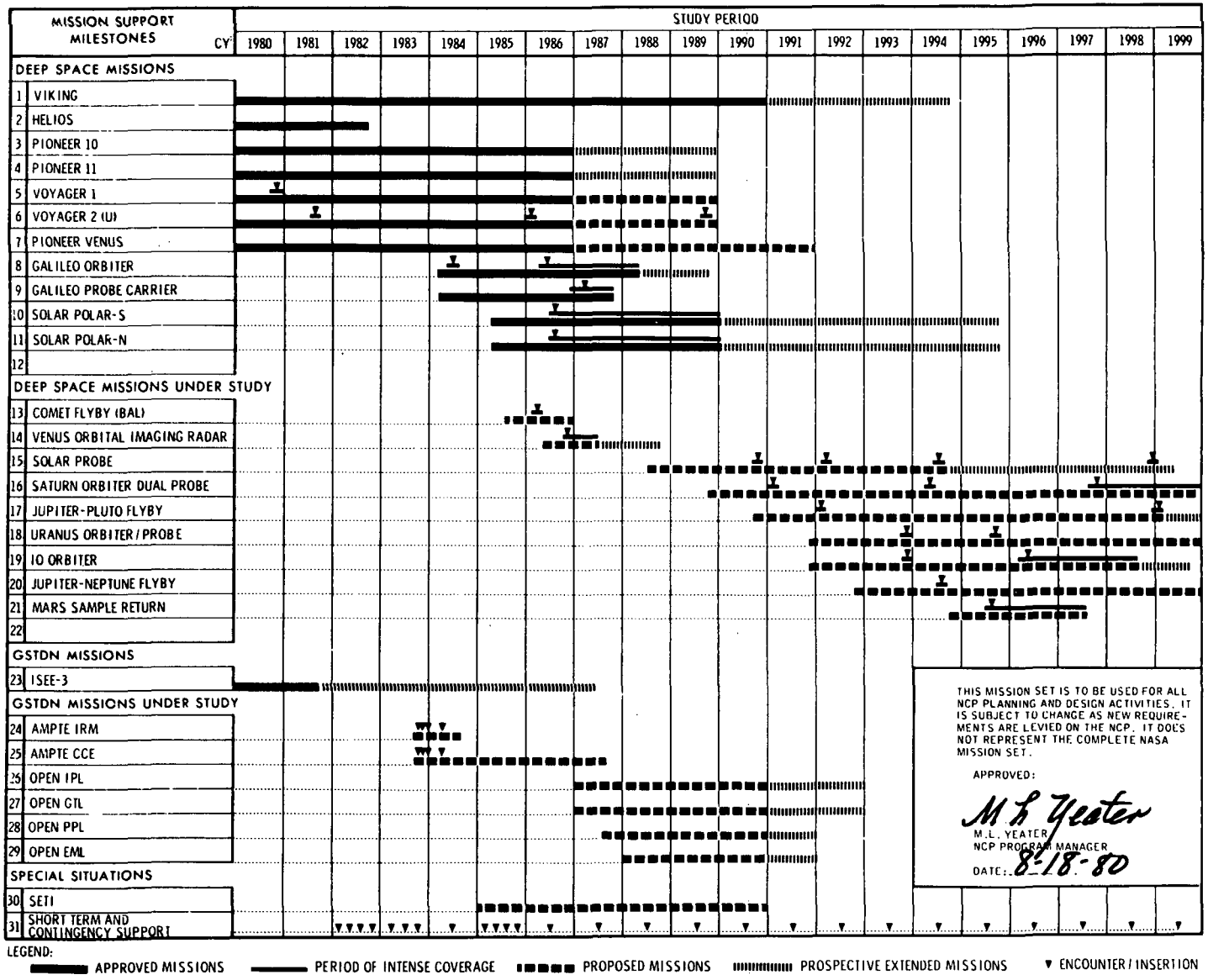

Fig. 3. NCP flight mission set

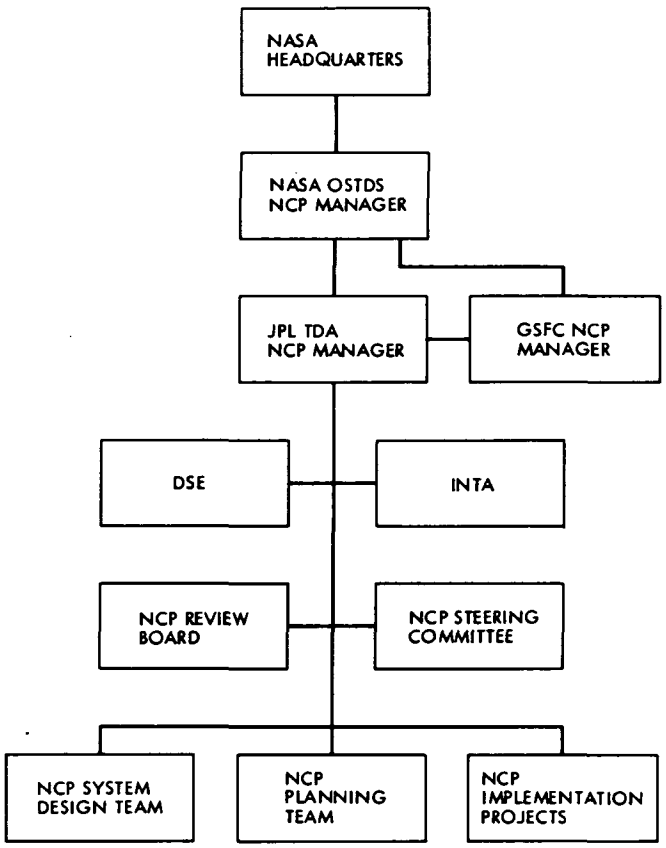

Fig. 4. NCP organization

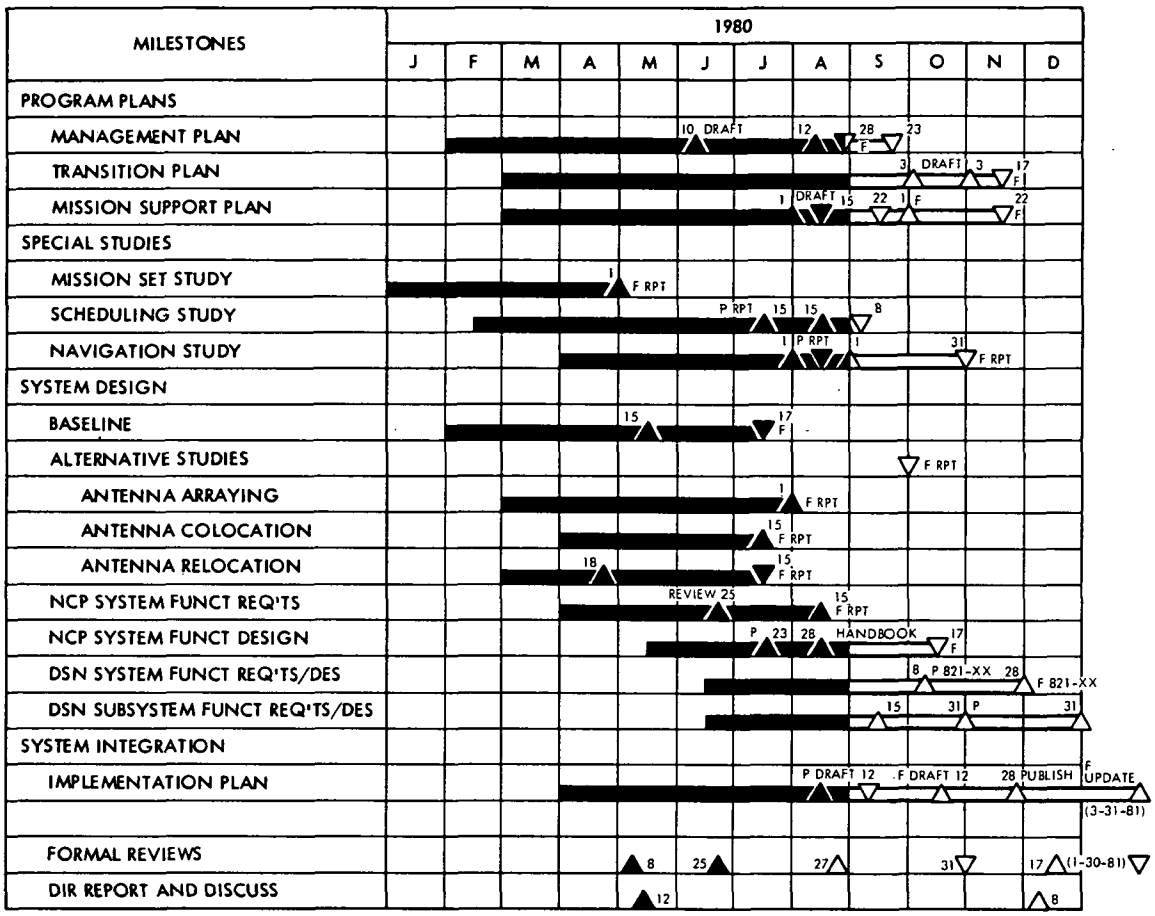

P = PRELIMINARY F = FINAL

Fig. 5. Planning and design schedule

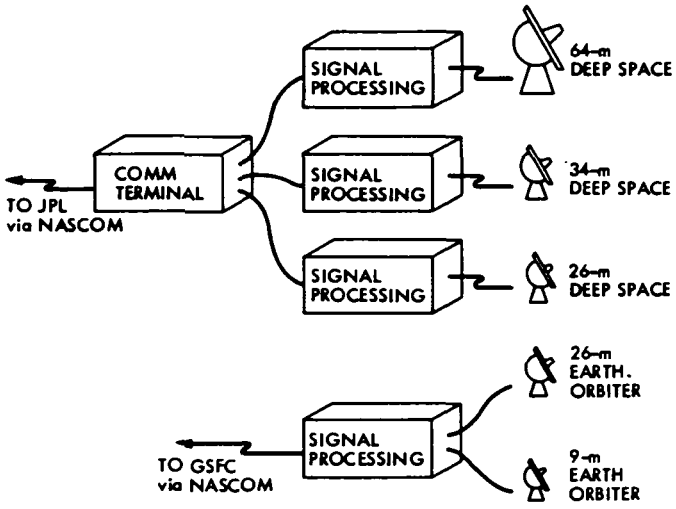

Fig. 6. Typical complex before the networks' consolidation

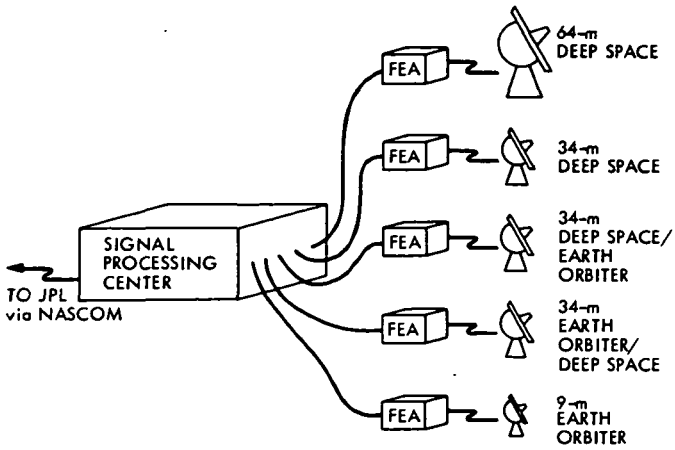

Fig. 7. Typical complex after the networks' consolidation

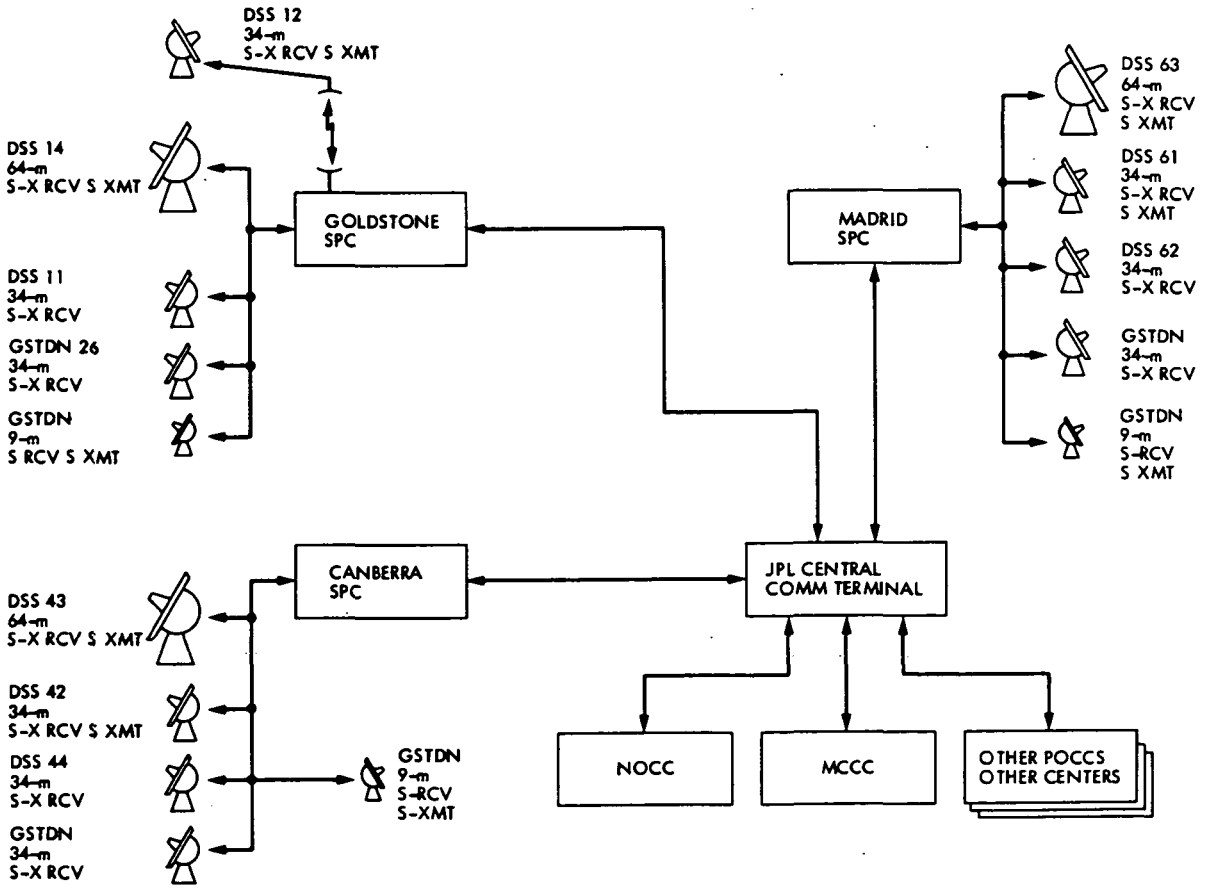

Fig. 8. Consolidated network configuration

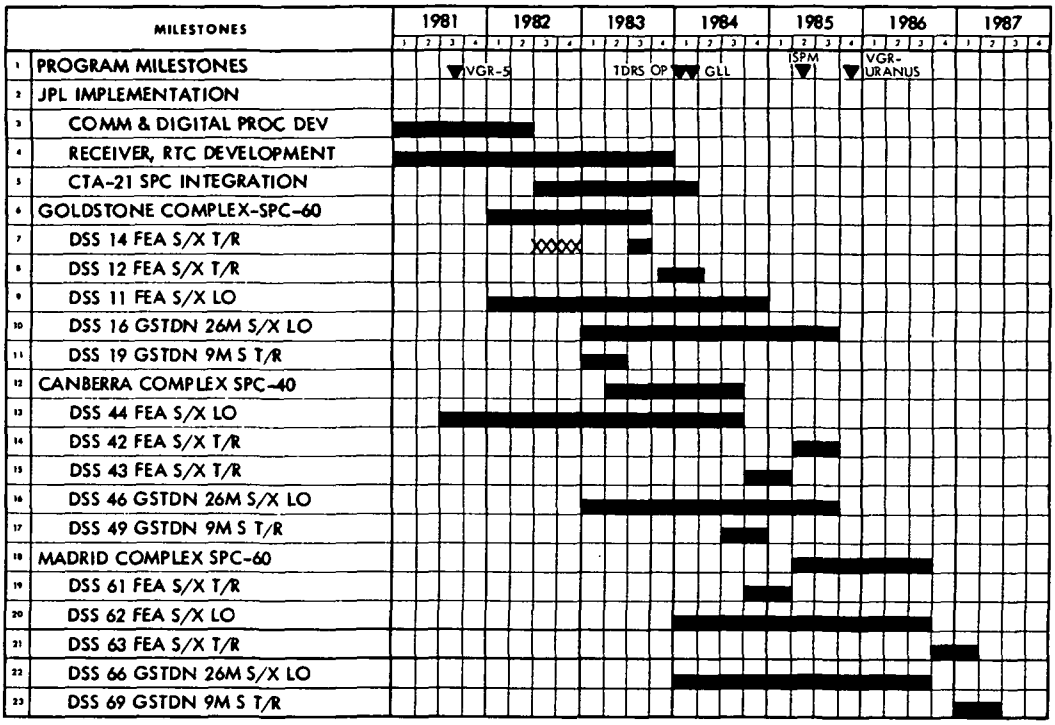

Fig. 9. Network Implementation Schedule

N80-33443

DSN System Performance Test Software

F. B. Leppla
Deep Space Network Support Section

The Software Support Group of the Deep Space Network Support Section is continuing the development of System Performance Test (SPT) software for the Deep Space Network. During the past two and one-half years, test software has been developed for a new system, Radio Science, and many new features have been added to existing software. Plans are underway for implementation of test software for the Very Long Baseline Interferometry (VLBI) system and the Network Data Processing Area. A description of the elements of the SPT software is provided.

I. Introduction

In April of 1975 the Software Support Group was given the assignment of developing System Performance Test (SPT) software as part of the DSN Mark III Data System (MDS) Project. The implementation was successful in that the test software was used for the SPTs to verify system operation and performance.

The three areas that drive the development of SPT software are:

(1) New system implementations.

(2) Modifications to existing systems.

(3) Modified test techniques.

A test capability was implemented during 1978 for the then new narrow- and wide-bandwidth Radio Science System. The test software was used to verify system performance prior to the Voyager Jupiter encounters. In 1979 and 1980, the Radio Science test software was expanded to include test capabilities for the medium-bandwidth Radio Science System features. This SPT software is now being used to test the Radio Science System in preparation for Voyager Saturn encounters.

Since the completion of the MDS implementation, the test software has been modified and enhanced to meet changing system requirements and performance characteristics. The Tracking, Telemetry, and Command SPT software packages have all been modified to match operational system software or hardware changes. In some cases, the test software has to be changed to accommodate anomalies that exist in the operational software.

During the past few years, the majority of the Software Support Group's workload has been in the area of providing modifications to and sustaining existing test software. The workload emphasis changes when requirements for new systems such as Very Long Baseline Interferometry (VLBI) and the Network Data Processing Area (NDPA) are introduced. Two years hence, the initial effort for the Networks Consolidation Project (NCP) will begin.

II. Description

The SPT software consists of two basic types of software packages. The first is devoted to real-time testing and consists of a Test Executive and several individual test tasks where each task is designed to test a particular system. The second type is non-real-time oriented and is directed towards mathematical performance evaluation where large amounts of data need to be processed.

The real-time test software is contained on one 2.5-MByte disk. This disk is presently 97 percent full and contains software and procedure files to test the Tracking, Telemetry, Command, and Monitor and Control Systems in the DSN. The Test Executive is the main program and controls all activity during execution by activation and deactivation of tasks, reading and routing of operator directives, routing of input and output data, control of peripheral devices, and performing data block dumps upon request.

The operation of the Test Executive is governed by the SPT Standard Operating System (SPTSOS) which contains I/O handlers and common software required by the executive and the test tasks. This operating system is a modified version of the computer-manufacturer-supplied operating system, which has been customized for DSN unique features and disk partitioning requirements. In actuality, four versions of the SPTSOS exist in order to be able to operate the test software in any one of four computer systems in the DSN. System generations are needed whenever the disk configurations need to be modified.

The non-real-time type of SPT software presently consists of three test packages designed for Radio Science System testing. Various types of mathematic techniques are implemented. Digital filtering and Fast Fourier Transform techniques are utilized. Data input is from Original Data Records on magnetic tapes. Planning is underway for implementation of test software for the VLBI system.

III. System Performance Test Executive

The purpose of the SPT Test Executive (EXEC) is to coordinate the processing of Monitor, Command, Telemetry, Tracking, and ODR Validation System Performance Test Tasks. The EXEC is responsible for routing of all input directives, standard subsystem blocks (SSB), high-speed data (HSD) and wideband data (WBD) blocks to and from the proper test task. The EXEC is also responsible for activating the test tasks and configuring the communication process by operator directives. Another function of the EXEC is to transmit and dump HSD, SSB and WBD blocks as required. The EXEC in combination with the Operating System maintains communication protocols with other processers in the Deep Space Station (DSS). Finally, the EXEC coordinates the output of operator messages, test reports and data block dumps from either the Test Tasks or from the EXEC itself.

Communication with peripheral devices (disc drives, magnetic tapes, and the operator console) and control of system resources (central processor time and memory) are all maintained by the SPTSOS. The SPTSOS is a modified version of Modular Computer Corporation's MAX III operating system. Modifications have been made to the Modcomp operator console handler and the magnetic tape handler. Special software has been added to interface with the DSN communication buffers, Frequency and Timing System and the Star Switch Controllers. Common data handling routines have been added for features such as Get Bit, Put Block, and GMT time conversions.

Currently, the SPTSOS can run in four different computers in a DSS. The SPT software is normally run in the backup Communication Monitor and Formatter Assembly (CMFA), but it is capable of running, with restrictions, in a Command Processor Assembly (CPA), a Telemetry Processor Assembly (TPA), or a Metric Data Assembly (MDA). Running in any assembly other than the CMFA eliminates the reception of high-speed data.

One of the most important features of the EXEC is the capability to read test procedures (files of operator directives) from disk storage. This capability allows system test personnel to define and use standard, repeatable test conditions which are semiautomatic during execution. The test procedure capability contains basic logical features such that procedures may start, wait, loop, and branch based on time, data conditions, or sense switch positions either in hardware or software. The procedures may call other subprocedures for execution. The procedures control the test process as well as the test software by activating tasks, informing computer operators of required actions, configuring test equipment, and timed generation and transmission of simulated data blocks.

The automatic test procedure capability allows for most cost-effective utilization of test time in the DSN. The test procedures presently contain approximately 23,000 lines of directives.

IV. Monitor System Performance Test Task

The test software designed to verify system performance of the Monitor System is capable of simulating approximately 250 parameters in various types of data blocks. The test

software is capable of performing automatic verification on most of these parameters which are available in data block output. The simulation feature may be used to output data either as high-speed data or standard subsystem blocks.

The test procedures in combination with the test software are also used to verify all visual displays output by the system. This is accomplished by outputting detailed checklists for computer operator use and then simulating data to drive various display devices at convenient output rates. Erroneous information is also presented to the system to test system responses.

Specific test routines are coded to test (1) text data handling, (2) Antenna Pointing System drive tape preparation, and (3) backfeed data test.

The Monitor SPT software has not been updated during the past two years. The Monitor System has been stable in the DSN for that time period. Some minor changes have been made to the test procedures.

V. Telemetry System Performance Test Task

The telemetry test software is a table-driven multimission test program capable of processing six telemetry channels simultaneously. This program, as well as all others noted in this article, may be operated either in a manual mode or through use of the automatic procedure capability. The program can control the Simulation Conversion Assembly (SCA) by generating and transmitting text and control blocks. The SCA is used to generate simulated telemetry data for testing.

Telemetry testing requires that a data path be looped to the test computer. This may be accomplished by patching of HSD lines or using computer control to configure Star Switch Controllers. The test software, either in manual or automatic mode, configures the Telemetry Processor Assembly (TPA), instructs the SCA to simulate telemetry for a particular spacecraft, and then performs various test functions on the system data. The test program may perform block header checks, block serial number sequence tests, GMT time comparisons, receiver lock tests, AGC and SNR limit checks, sync or word or bit error rate tests, and distribution curve calculations. Y-factor values may also be computed.

Anomalies in the input data are reported to the test operator. Test reports are output on periodic intervals with a final report output at the completion of a test. Test periods may be defined as a time interval or as a total number of bits to process.

The sync bit error rate test feature has recently been added to the software. Requirement definitions are being finalized for modifications to support the Galileo and International Solar Polar Mission telemetry testing requirements.

VI. Tracking System Performance Test Task

The Tracking System Performance Test software is a multitask program which is implemented to test the three basic functions of the Tracking System. These functions are doppler, range, and angles.

The test software provides the basic capabilities to (1) validate all tracking data, as defined in the detailed Interface Design Document 820-13 (TRK 2-14) against Standards and Limits, (2) generate and transmit, via HSD or SSB, DSN Tracking System predictions, (3) simulate Monitor System inputs to the Tracking System, and (4) analyze doppler, range, and angle data types.

The doppler function is evaluated by verifying data formats, calculating long-term drift and phase jitter, computing theoretical jitter and S-band Programmed Oscillator Control Assembly (POCA) ramp delay and noise characteristics.

The range function is tested by verifying data formats and by determining range and differenced range versus integrated doppler (DRVID) characteristics. The angle data are evaluated by generating and transmitting angle predictions and then using these predictions to point the antenna. The system data output is then compared against the predicted values. Upon completion of data evaluation, a test report is generated showing test configuration, test data, and test results.

The Tracking SPT software is presently being modified to add various data analysis techniques. The Software Requirements Document (SRD) and Software Definition Document (SDD) have been completed. Development and acceptance of the software program should be completed by March 1981.

VII. Command System Performance Test Task

There are two SPT programs for the Command System, one for the Mark III-74 Command System and another for the Command Store and Forward System. The two command systems while retaining similar characteristics are significantly different in data format, content, and timing. These basic differences and the fact that the systems were developed three years apart necessitated the development of two distinct test programs.

Both SPT programs function similarly in that they allow simulation of the DSN Operations Control Center by sending control messages to the CPA for radiation and receiving messages from the CPA consisting of acknowledgements, confirmations of radiated commands, and status reports.

Both programs maintain models of the command stacks in the CPA and predict events on the basis of received data. The SPT software predicts confirmations of radiated commands. For the store and forward capability, the software also predicts such things as the Bit-1 radiation times of commands waiting to be radiated, expected time of the next event message and contents thereof, status of the Prime Command file, Command Modulation Assembly (CMA) mode status, queue formation, and the files in the file director.

The predicted events are validated against reported events and the results indicate system performance. Test procedures have been designed to test various mission configurations. Error messages are output upon occurrence and a summary report is output at the conclusion of a test sequence. The test software is very time-critical.

The Command SPT software has been updated three times in the past two years. The design has been completed and coding has begun on modifications for Galileo and the International Solar Polar missions.

VIII. Original Data Record Validation Task

The ODR validation software runs under the Executive Task even though the testing is not real-time oriented. The software may therefore be controlled via an Automatic Procedure File. This software provides a means for validating the CMFA-produced ODR, which is a record of all system data transmitted from a DSS.

The validation process consists of verifying the block sequences and time sequences and performing selected block dumps to a line printer. Options are available to validate all data on a tape or selected data streams. Error messages are output for missing or duplicated blocks, and a summary output is available noting percentages of data blocks available. The data content of the blocks cannot be verified.

This software, being mission-independent in nature, has not been modified in some time.

IX. Data Block Translator Task

The Data Block Translator (DBT) task is a general-purpose table-driven software package used to format HS, WB or SSB data blocks to readable outputs on a display device. The Test Executive controls operation of this task. Transmitted or received blocks may be dumped.

Conversion routines are available for such things as (1) output ASCII string, (2) convert to decimal output, (3) convert to integer output, and (4) GMT time conversion. Fifteen different conversion routines are available. Five other routines are included to define table start and end, do logical jumps within the table, adjust data block pointers, and load alternate tables.

The tables are stored on disk with unique block identifier so they can be located rapidly when needed. A spooler file is maintained on the system disk to buffer output data at high block dump rates.

The last release of SPT software contained tables for display of 65 different data blocks.

X. Radio Science System Performance Test Software

Three Radio Science SPT programs have been delivered to the DSN. Each program has been designed to process data from a unique type of Radio Science System data output. These types are commonly called narrow, medium, and wide bandwidth. Each program performs the same basic function on the system data tape. These programs do not need to operate in a real-time environment as the other SPT programs do. The same basic operating system is used but the disk configuration is much different for data storage requirements.

The basic process performed is to read Radio Science data from magnetic tape or tapes, decimate the data, pass the data through a Fast Fourier Transform, and store the results; then read a tracking system data tape for the same time period, extract the signal frequency, and store the results. S- or X-band data may be processed. A comparative analysis is then performed to determine relative performance of the Radio Science System. Test reports are printed and a basic spectrum analysis plot is available for output.

Some new processing techniques are being explored to be able to process more data in a shorter time span and provide better resolution. At the same time, the three Radio Science SPT programs are being combined into one program.

XI. Summary

The SPT software is an integral part of system performance testing in the DSN. The development and use of automatic test procedures enhances the overall test capability by providing

repeatability of test configurations in a fast and efficient manner. The procedures and software have been developed in a modular manner. They may be used in total to provide a complete system test. Selected subsets may be used by DSS personnel to troubleshoot isolated system problems.

The SPT software consists of approximately 175,000 lines of source code. During the past two years many modifications have been made, especially in the areas of telemetry, tracking, and command software. New capabilities have been implemented for the Radio Science System.

The design is complete and coding has begun for a major update to the Tracking System test software. The design is complete for new test software for the VLBI System. This effort will result in approximately 20,000 new lines of code. The initial design effort is underway for software to test the NDPA.

The development of SPT software is an ongoing effort in the DSN. The basic goal is to provide a capability which provides a computerized method of verifying system performance in a repeatable, rapid and efficient manner.

TRISCAN: A Method of Precision Antenna Positioning

R. C. Bunce
Deep Space Network Support Section

TRISCAN is a method of improving the alignment between the boresight of the Deep Space Network antennas and a particular target, spacecraft, or radio source (star). For stars, the method works in conjunction with the noise-adding radiometer and the Antenna Pointing System to form estimates of the alignment offset coordinates. This information is then used to position the antenna for improved target alignment. A comparison with CONSCAN is included since a CONSCAN study led to TRISCAN development.

I. Introduction

TRISCAN was conceived after an exhaustive study of CONSCAN disclosed that the latter (using normal parameters) was effective only on relatively strong signal inputs. With strong inputs, the CONSCAN gain uncertainties and continual loss during scan were negligible, as was the antenna positioning noise. However, with weak signal inputs, as with weak stars and transient spacecraft dropouts, CONSCAN lost effectiveness. The major causes of this ineffectiveness were determined and a simplified system designed that avoided the bulk of the CONSCAN weak-signal error sources. The new system is called TRISCAN for triangle (antenna) scan, and is the subject of this article.

A detailed comparison of TRISCAN and CONSCAN appears later in the text. First, however, a general description of TRISCAN is given.

II. Description

TRISCAN functions to estimate the coordinate errors in hour angle and declination between the predicted (boresight) location and the true location of a subject star or spacecraft.

TRISCAN for stars is based on a set of measurements made by the noise adding radiometer (NAR). This device yields temperature readings proportional to the system background noise power plus any noise power present in the antenna pattern; the latter is attenuated by the antenna boresight offset. This total power is normalized to temperature, K. When the background temperature is subtracted from the total reading while the boresight is in the vicinity of a star, the result is the *effective star temperature* at its given offset from boresight and is a measure of the star input power (Fig. 1).

TRISCAN uses the measure of three effective star temperatures from the same star. The first (TO) is the measure at the star predicts or best-known location. The second and third (T1 and T2) are taken at the two base-points of the TRISCAN triangle. The triangle height is a downward excursion in hour angle (*HA*), while its base is a plus (+) and minus (-) (side ways) excursion in declination (±*DEC*). The antenna boresight is moved to these locations, but offset dimensions are precalculated so that boresight shift is an integer number of positioning increments. Thus, the positions are exact. The resulting triangle is always isosceles, but only approximately equilateral; it must accommodate the exact increments. The algorithm incorporates the triangle as it occurs.

Using the three effective star temperatures and the triangle geometry, the algorithm calculates estimated offsets from the predict point to the star. These are read as $HA*$ and $DEC*$ for final antenna positioning. The process is theoretically valid at stars of 1 K; it has been feasibility tested at a level of 5.6 K. A TRISCAN run requires roughly five minutes.

III. Comparison of TRISCAN and CONSCAN

TRISCAN is, literally, a fresh development that grew out of an exhaustive study of CONSCAN. While the study was in process, the VLBI project found that CONSCAN was inadequate for that use. The CONSCAN study was redirected at that time to discover those characteristics of CONSCAN that were causing the limitation, and possibly to design a new system of similar nature that would work under conditions such as those experienced by the VLBI Project.

The major CONSCAN drawbacks for low magnitude stars are as follows:

(1) CONSCAN loop gain is signal dependent, and this parameter is normally an estimate. The estimate error directly multiplies the positioning coordinate errors.

(2) CONSCAN generates analog commands while the Antenna Positioning System (APS) steps in digital, or incremental, jumps. Also, when the commands are accepted, an inherent APS error occurs proportional to the command, but asymptotic to an upper range mean of 0.010 degree. *If a command is carried out manually, in a step-by-step fashion, the error is much less.* However, for example, when a straight 0.004-degree radius is commanded by CONSCAN, the full transient is typically 0.007-degree for the boresight, an overshoot of 75 percent.

(3) To keep up with the drifts, external and self-generated, CONSCAN must operate continuously. Because of the radius mean offset, this results in a continuous signal attenuation down the pattern by the radius. A typical result is a 10- to 25-percent power loss.

(4) Because of the analog/digital APS action mentioned above, the CONSCAN integration circle is an irregular polygon (Fig. 2). The main effect is an additional gain/position error.

All of these effects combined (plus minor additions not mentioned) lead to a degradation of CONSCAN threshold, together with a steady-state decrease in signal-to-noise ratio (SNR). The result is that with tolerable steady-state parameters (R = 0.004 degree to 0.008 degree) the CONSCAN process bottoms out in the neighborhood of 10 K, thus proving unacceptable for star tracks in the neighborhood of 1 K.

As the listed CONSCAN characteristics became evident, a new scanning method of the same or lesser complexity was sought that would handle stars to this 1 K level. It seemed reasonable simply to conceive a method that bypassed the CONSCAN drawbacks, in hopes that the new system would have the required 10-dB sensitivity increase. The net result was TRISCAN. In one-by-one fashion, TRISCAN avoids the CONSCAN star problems as follows:

(1) TRISCAN is independent of loop gain and signal strength. It accomplishes this by using temperature ratios in which the source level divides out of the expressions. It does require, however, an accurate measure of the system temperature (for subtraction), but this is commonly available. CONSCAN integrates this away; it is thus needed for TRISCAN only.

(2) The TRISCAN triangle uses only integer increments of the APS for positioning. Further, these increments are manually stepped one at a time for maximum accuracy, and through only one coordinate at a time. They are called "exact" in this article, for data indicated no deviation from the input commands.

(3) TRISCAN is presently described as one shot for single runs. However, the runs could be sequenced if desired. The important consideration is that runs start and finish at the best known star location, analogous to the CONSCAN scan center. There is no scan loss after the triangle is transversed. If sequenced at intervals, this means no mean loss between scans (no continuous offset).

(4) As mentioned, the triangle is nearly exactly known and absorbs the digital nature of the APS inherently. The points are static during NAR integration, so position/level irregularities are minimized during measure.

With these known difficulties avoided, we make the assumption that the only TRISCAN errors arise from the NAR variance, as from the biorthogonal integrator in CONSCAN. The NAR noise effect, discussed later in this article, causes the TRISCAN 1-K bottom.

IV. TRISCAN Algorithm

A. Algorithm Inputs

We designate the points of the CONSCAN triangle as $P0$ (predict point), $P1$ ($P0 + \Delta HA$, $+ \Delta DEC$), and $P2$ ($P0 + \Delta HA$, $- \Delta DEC$). Any temperature $TN(PN)$ refers to the total temperature as read from the NAR. TN alone refers to the star equivalent temperature, or the NAR reading with the system (cold sky) reading subtracted.

A single TRISCAN run requires nine inputs:

(1) The star (approximate) declination, $DEC*$.

(2) The antenna beamwidth, W.

(3) The system (cold sky) temperature *near* the star, by NAR, TS, K.

(4) The ΔDEC excursion (the base), an integer number of antenna positioning increments, degree. This is an operator choice, typically 0.007 degree. The parameter affects signal loss during scan, and may be chosen smaller if loss is a critical effect. Scan accuracy may be degraded on weak stars (< 5 K) (probabilistic).

(5) $T0(P0)$, K, the predict-point NAR read-out (first).

(6) $T1(P1)$, K, at $P1$ as defined, NAR total.

(7) $T2(P2)$, K, at $P2$ as defined, NAR total.

(8) $T0'(P0)$, same as $T0(P0)$ but a second reading upon return after triangle "circuit", NAR total.

(9) $T\#(P*$ est), the NAR readout after final boresight positioning to star location estimate using TRISCAN offset calculations; $T\#$ by the NAR.

B. Triangle Size

The TRISCAN triangle lies with its center line, or height, along the predict; the HA axis, + downward. The triangle base is a DEC coordinate line, orthogonal to the HA line, with + to the right, and zero at the intersection. Thus ΔDEC as chosen is one-half the triangle base. For a perfect equilateral great-circle triangle, considering conversion of HA degrees to a great-circle dimension, the ΔHA readout for triangle height, and the triangle side P, would be:

$$\Delta HA^\circ = \frac{\sqrt{3}}{\cos(DEC*)}\ \Delta DEC^\circ \text{ (ideal)}$$

$$\rho = \sqrt{(\Delta HA \cos(DEC*)^2 + (\Delta DEC)^2}$$

The value of ΔHA as given is irrational in general, and not likely to be an integer multiple of the positioning increment. It is therefore automatically rounded in the algorithm to an integer value to obtain exact boresight locations at $P1$ and $P2$. This deviates the triangle from equilateral to isosceles so that the value of the two upper sides differ somewhat from 2 ΔDEC. This changes the qualifier on ΔHA from ideal to nearest integral positioning increment. The, we rewrite:

$$\Delta HA = \frac{\sqrt{3}}{\cos(DEC*)}\ \Delta DEC^\circ \quad \text{(Rounded to nearest antenna positioning increment)}$$

$$\Delta \widehat{HA} = \Delta HA \text{ (Rounded)} \times \cos(DEC*) \quad \text{(Great circle length of } \Delta HA\text{) (Noninteger)}$$

$$\rho = \sqrt{(\Delta \widehat{HA})^2 + (\Delta DEC)^2}$$

In this way, the algorithm defines an error-free triangle for TRISCAN. All additional deviations (such as angular curvature) are negligible for the small angular distances involved. The key purpose is to obtain dimensions for the scan that are integer steps in the Antenna Positioning System (APS). This eliminates ambiguity from this source (±0.001 degree at 64-m sites). The effect on final positioning error varies with offset; it reduces this error 20 percent (rough estimate), near the half-power point, over random dimensioning. The above estimate does neglect the *HA-DEC/AZ-EL* conversion error, which is presently unspecified.

C. Star Equivalent Temperatures

All star equivalent temperatures are obtained in the same way. The system temperature is subtracted from the given total temperature, as read out by the NAR. Thus:

$T0(P0) - TS = T0$, the equivalent star temperature at $P0$, K

$T1(P1) - TS = T1$

$T2(P2) - TS = T2$

$T0(P0) - TS = T0$

$T\#(P*$ est.) $- TS = T\#$, final equivalent star temperature after TRISCAN positioning is complete.

D. Equivalent Temperatures and the Antenna Pattern Model

The equivalent temperatures obtained at the triangle points (neglecting NAR variance for the moment) may be related to the star location by the angular distance from the point to the star. Let Z be the $P0$ predict distance, $R1$ and $R2$ the base-point distances, $R1$ to the right, or $+DEC$. Let $T*$ be the unknown star temperature at star-boresight alignment, the maximum equivalent value. We assume the antenna power pattern is of the Gaussian form near boresight, and down to the one-half power point. Equivalent temperatures are related to the antenna (Gaussian model) pattern by the theoretical mean set (see Fig. 3):

$$T0, T0' = T* \epsilon^{-K(Z)^2}$$

$$T1 = T* \epsilon^{-K(R_1)^2}$$

$$T2 = T* \epsilon^{-K(R_2)^2}$$

$T\# = T* \epsilon^{-K(\Delta Z)^2}$

$T*$ = star temperature at exact alignment

ΔZ = positioning error

Z, R_1, R_2 = angular distances as given on Fig. 3.

K = antenna pattern constant

$= 2.773/W^2$

W = antenna beamwidth, degrees

$T\#$ = post-TRISCAN equivalent temperature: the TRISCAN result.

E. TRISCAN Triangle Geometry

The preceding dimensions, and those required to fill out the algorithm, are given in Fig. 3. Note in particular that the polar form of the final positioning result is Z at the angle theta. Thus, the great-circle HA correction is Z cos (theta), while the DEC correlation is Z sin (theta). This correction set plays a key role in the remainder of the algorithm (subsection F).

F. Algorithm Offset Computations

To complete the algorithm and obtain the required offsets, the following computations take place in condensed form:

(1) Three items from subparagraph C combine by ratio to eliminate $T*$:

$$\overline{T0} = \frac{T0 + T0'}{2}$$

$$\frac{1}{K} \log_e \left\{\frac{\overline{T0}}{T1}\right\} = (R_1^2 - Z^2) = a_1$$

$$\frac{1}{K} \log_e \left\{\frac{\overline{T0}}{T2}\right\} = (R_2^2 - Z^2) = a_2$$

(2) The triangles bounded by Z, P, and R_1 or R_2 may be written:

$$R_1^2 - Z^2 = \rho^2 - 2\rho Z \cos(\theta - \alpha) = a_1$$

$$R_2^2 - Z^2 = \rho^2 - 2\rho Z \cos(\theta + \alpha) = a_2$$

(two equations in two unknowns, Z and θ)

or

$$\frac{\rho^2 - a_1}{2\rho} = Z \cos\theta \cos\alpha + Z \sin\theta \sin\alpha = A_1$$

$$\frac{\rho^2 - a_2}{2\rho} = Z \cos\theta \cos\alpha - Z \sin\theta \sin\alpha = A_2$$

or

$$Z \cos\theta = \frac{A_1 + A_2}{2 \cos\alpha} = \Delta\widehat{HA}*$$

$$Z \sin\theta = \frac{A_1 + A_2}{2 \sin\alpha} = \Delta DEC*$$

Only ρ, α, a_1, a_2, A_1, and A_2 must be calculated and combined. These give the position estimates required. For implementation, $\Delta HA* = \Delta\widehat{HA}*/\cos(DEC*)$. Rounded integer increments are used by necessity.

After positioning from $P0$ through $\Delta HA*$, $\Delta DEC*$, the power gain obtained may be determined by:

$$G = 10 \log \left\{\frac{T\#}{T0}\right\}, \text{dB}$$

G. Algorithm Outputs

By way of summary, the algorithm yields eight outputs during the course of a run:

(1) ΔDEC: this is one-half the triangle base. It is normally a repeat of the algorithm input, except when the input is a noninteger in the positioning increment, or is outside the useable triangle limits (0.001 degree, 0.007 degree). Then, the program recycles.

(2) ΔHA, the triangle height: best integer positioning increment for (scaled) near-equilateral triangle. $\Delta\widehat{HA}$ is used in the algorithm.

(3) $\overline{T0}$, K: predict point star equivalent temperature (average of two).

(4) $T1$, K: star equivalent temperature at $P1$, triangle base, RH.

(5) $T2$, K: star equivalent temperature at $P2$, triangle base, LH.

(6) $\Delta HA*$ degree: correction in HA from $P0$ to star, estimated.

(7) $\Delta DEC*$ degree: correction in *DEC* from *P*0 to star, estimated.

(8) *G*, the gain of the run in dB: if the run was successful, *G* is always positive or zero, but its absolute value has no direct meaning, except as operational information. *G* has an upper limit: the dB increase on the antenna pattern from the predict point to exact boresight-star alignment. This normally ranges from 0 dB to about 3-dB maximum.

These outputs, interlaced properly with the inputs given previously, define the operator interaction with the algorithm. It is important that the ΔHA and ΔDEC excursions be mechanized properly, as shown on the triangle, and that they be taken incrementally, step-by-step, with each step the size of the positioning increment. ΔHA and ΔDEC increments should be stepped off separately: down and over, over two, over and back up; *P*0/*P*1/*P*2/*P*0, recording the NAR reading at each point. That completes the TRISCAN algorithm and its general implementation.

V. TRISCAN Feasibility Test

The TRISCAN method was tested for feasibility on June 25, 1980 at DSS 14. The first run went smoothly and within expectations; it is reported in Fig. 4 as a feasibility example. Later runs experienced difficulties resulting mostly from hardware anomalies. In particular, the maser was failing. These runs were for data for statistical evaluation; only one check-out run was planned, and obtained. All data (and the statistical variability measure) were finally put aside from the test results of all but the first run.

The star was 3C123, at an hour angle of 328.5 degrees and a declination of 29.6 degrees, was used for the feasibility run. Elevation was 38.756 degrees, and effective temperature at alignment was 5.855 K (calculated). System temperature was 22.919 K (Fig. 4). TRISCAN temperatures for the star (*T*0, *T*1, *T*2) were 4.876 K, 5.247 K, and 4.753 K. When these were placed in the algorithm, offsets of +0.010 $HA*$ and +0.002 $DEC*$ degree were obtained. A subsequent high-resolution CONSCAN run was taken, and it yielded the same $HA*$ offset, and +0.003 $DEC*$ degree in close agreement. The triangle was 0.014° (*HA*) and 0.007 (*DEC*).

When the TRISCAN correction was mechanized, the star level gained about 0.65 dB, out of a possible 0.7 dB. This indicates that TRISCAN pulled in to about 0.001 degree from an initial error of about 0.009 degree. The conclusion of feasibility appears valid.

VI. TRISCAN Error Sources

The TRISCAN method is subject to several error sources, with error defined as the absolute miss in boresight-star alignment after completion of a run and subsequent final positioning. There are two major sources of error:

(1) Inaccurate boresight positioning on the triangle.

(2) Inaccurate temperature readouts from the NAR, including the system (cold sky) reference.

The first, boresight positioning error can result from APS instability, atmospheric displacements, and simple beam distortion due to antenna mechanical movements. In TRISCAN, APS instability is theoretically controlled by integerizing antenna displacements, taking them one at a time, and designating "home base" as the predict point, to minimize the correction excursions. These processes were adopted after a study of CONSCAN, where the consistent error effects were of the magnitude that random noninteger commands would bring about 1.0 M-deg, 1 sigma. Other distance error sources have not been considered; little can be done to minimize these sources that is not already incorporated in the hardware. Low-frequency random residual error sources are present, but can be minimized by a fast run.

The second error source, inaccuracies in the NAR readouts, is tangible and can be analyzed (except under exceptional circumstances, as when a maser fails). The NAR samples the total noise in the receiver channel, and converts this Gaussian input to a voltage proportional to power using a square-law detector (SLD). The detector output is integrated over 5000 samples/s for 30 seconds. Using Chi-square theory as a model, normalized to the sample count, the power standard deviation is less than 0.1 K when converted to temperature (30-K base). The device is gain-stabilized with a pulsed noise diode. Straight data analysis performed at DSS 14 indicated a standard deviation even less than that predicted above (0.06 K), 60 samples. However, the DSS 14 data does indicate an anomaly; the system temperature jumps at points by about 1.0 K, and holds. No explanation is evident.

In view of all the above, we assume (with apprehension) that the only remaining error source in TRISCAN is the NAR variance after integration. We disregard jumps, which are detectable by the dual *P* 0 reading.

Conversion of the NAR variance to the TRISCAN final positioning error is a complicated transcendental function. It was therefore carried out by machine for a full noise set (straight DSS 14 jump-free readouts), and a sequence of possible star positions. Since the position vectors were nearly Gaussian, the error distributions were all considered to be

Rayleigh in form. Initial offsets of 0.002, 0.004, 0.008, and 0.016 degree were investigated, permuted with equivalent aligned star temperatures of 1 K, 4 K, and 16 K. The mean final errors are shown in Fig. 5. The Rayleigh 80-percent limits around these means are large: (mean) X (1.92), (mean) X (0.44). Only the 1-K star leaves questions when the initial offset exceeds 0.010 degree. Two scans are suggested in these cases to bring the final position error to 0.003 degree or less.

VII. TRISCAN For Spacecraft

TRISCAN is as theoretically applicable for spacecraft antenna positioning as for star use. The major differences are that spacecraft-received power replaces star-effective power, and system temperature may be neglected (set to zero), since spacecraft power is normally well above the threshold level.

The NAR is not used in the spacecraft algorithm. The key quantity is spacecraft level in dB. This is converted to a convenient relative power level, replacing star temperature in the algorithm, by:

$$TN = WN = 10^{\frac{\mathrm{dBm}_N + K}{10}}$$

The triangle is taken as for star acquisition, with N given the corner "tip" values 0, 1, 2, and 0′. The parameter K is given any convenient value for scaling; it drops out as power ratios are calculated. A typical value for K is 150. In the algorithm, the system temperature TS is considered negligible ($TS = 0$).

The major problem in TRISCAN application to spacecraft is that the signal level sometimes varies rapidly for various reasons. TRISCAN will yield poor results if this variation approaches the antenna pattern attenuation during the TRISCAN run, which is some small fraction of a dB. It is necessary that the TRISCAN process be performed rapidly. Exact figures are not available, however, it is known that spacecraft signal level changes occur as rapidly (in cruise) as 1.0 dB/min. This would require the TRISCAN process to be performed in less than 12 seconds and indicates that the process would have to be automated.

Also, the dBm readout is physically remote from the APS. Automation would require some hardware implementation.

VIII. Summary and Conclusions

TRISCAN is without doubt a fresh method to position the antenna boresight at DSN locations, with unusual accuracy, in alignment with target stars and possibly spacecraft. Though presently a manual process, it could be automated as need occurs.

The key procedure used by TRISCAN is careful, incremental boresight adjustment about a triangle, with tip positions maintained in static state while the star (or target) equivalent temperatures (power levels) are obtained from NAR (or receiver AGC/dBm) readings.

TRISCAN mechanization has been chosen to minimize the effects of APS errors and system gain variations, hopefully leaving only the NAR variance as a residual source of error. On stars, this error causes the process to bottom out at very weak radio source levels.

A mechanization test at DSS 14 proved the process feasible. On a 5.6-K star, TRISCAN closed from about 0.009 degree to less than 0.001 degree. CONSCAN, run in parallel, required its maximum sensitivity condition to equal the TRISCAN run. CONSCAN used a radius of over 0.015 degree and an integration time of about 10 minutes.

The VLBI Project had discarded CONSCAN because of the low sensitivity under reasonable parameter limitations; it bottoms at about 10 K under such conditions. TRISCAN, comparably can theoretically close on stars around 1 K.

It is therefore reasonable to say that (all losses and errors considered) TRISCAN has a threshold that is up to 10 dB better than CONSCAN, and obtains this with a method that also improves present procedures at a strong signal, for its stable tracking condition centers on the nominal target, rather than at some distance from it. The steady-state loss is less.

TRISCAN has possible application as a CONSCAN inter-scan drift corrector and as a manual emergency backup procedure.

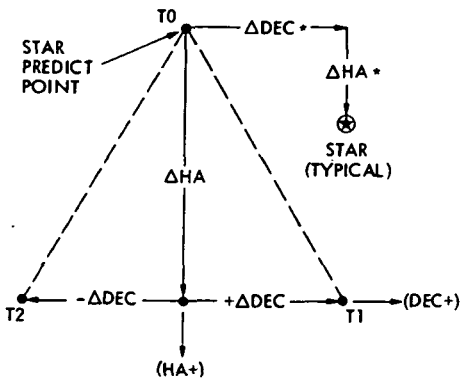

Fig. 1. TRISCAN method: basic triangle

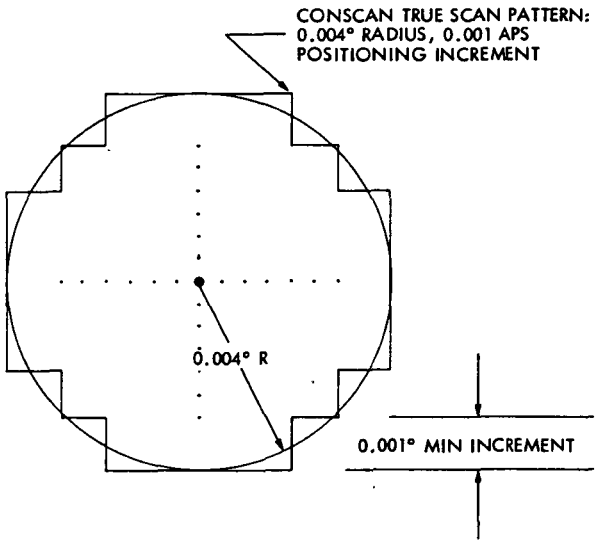

Fig. 2. CONSCAN true pattern with given parameters

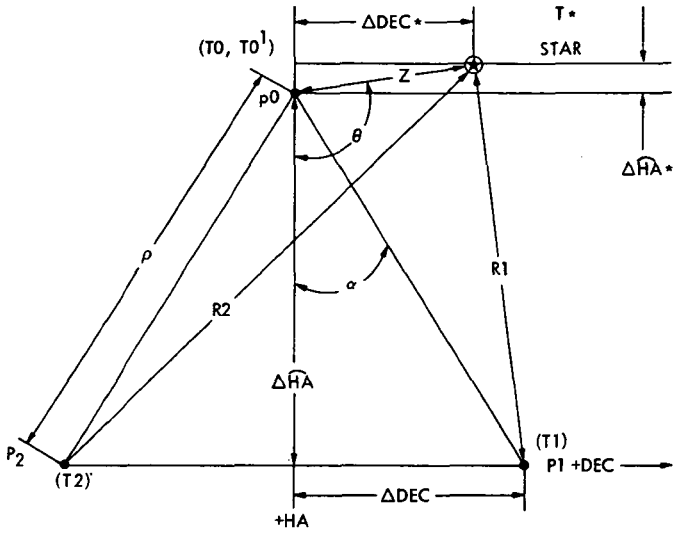

NOTE: ĤA IS THE GREAT-CIRCLE EQUIVALENT DIMENSION OF A CORRESPONDING HA MEASURE.

Fig. 3. TRISCAN algorithm model

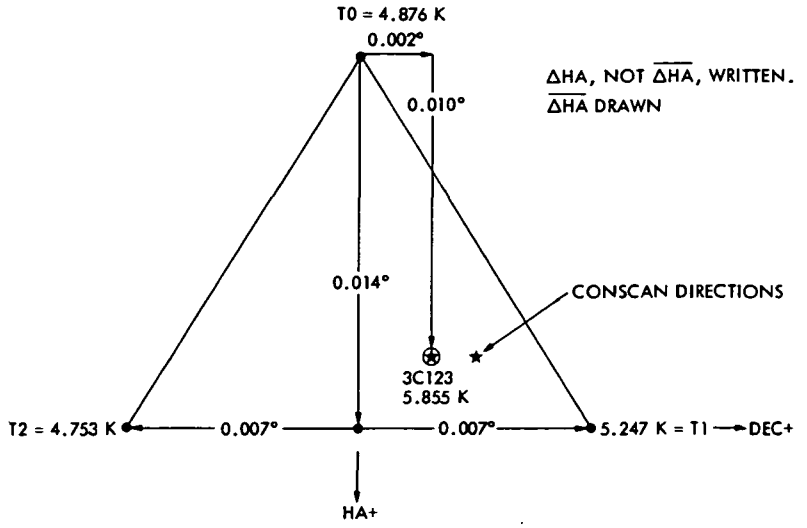

Fig. 4. TRISCAN triangle feasibility run

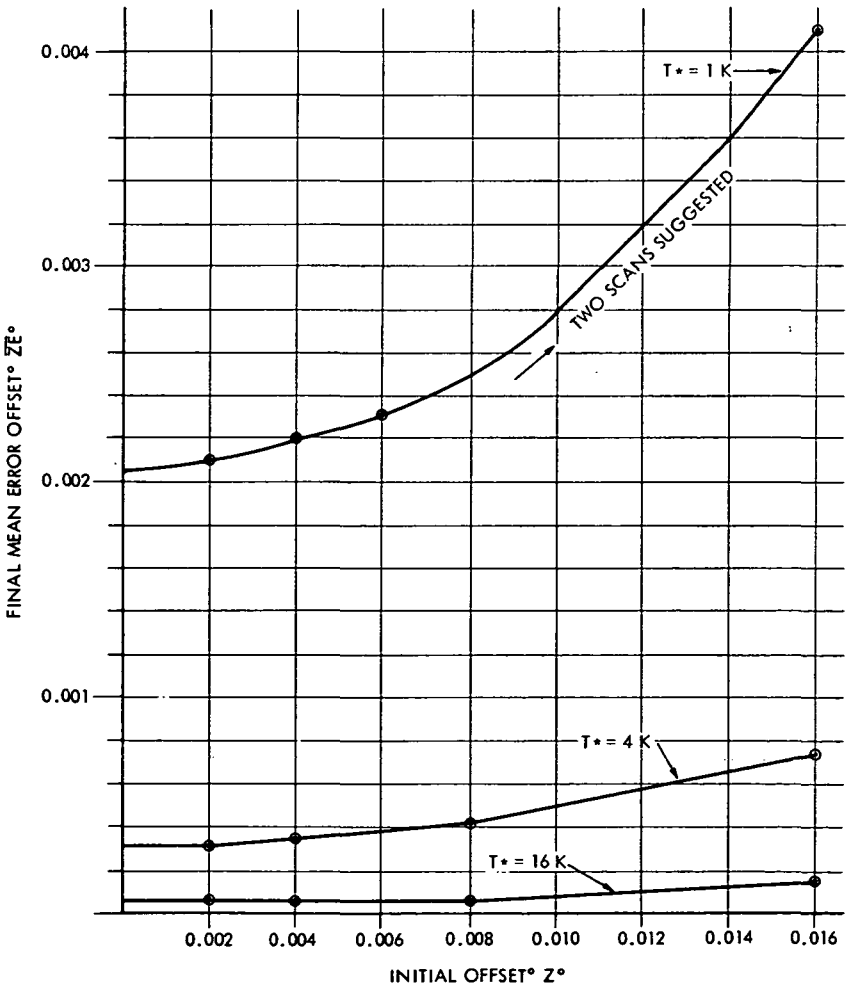

Fig. 5. TRISCAN error offset predictions

JPL P-141

Alternative to Surge Chambers for Goldstone Water Supply Distribution

J. L. Koh
Deep Space Network Support Section

When three of the six pressure-surge chambers in the Goldstone Water Supply Distribution System became inoperative, a study was undertaken to determine whether the surge chambers are a necessarily integral part of the system to safeguard against water hammering. An alternate cost effective method of safeguarding against this phenomenon was found, and is expected to be implemented in the system by the end of Calendar Year 1980.

I. Introduction

The Water Supply Distribution System (Ref. 1) at the Goldstone Deep Space Communications complex consists essentially of two supply lines. The source of the water supply is from the 3,800-m^3 (1,000,000-gallon) tank at Fort Irwin. Normally, water is pumped from this tank to an elevated 675-m^3 (177,000-gallon) tank at Venus Site. From Venus Site, water gravity feeds each tank at Echo Site, Apollo Site, Pioneer Site, and Mars Site. Water from Venus Site also gravity feeds the Microwave Test Facility (MTF) directly. If required, water from Fort Irwin could be selectively pumped into each site tank (Echo, Apollo, Pioneer and Mars) and/or supply MTF directly. Six pressure-surge chambers are installed (in groups of three) at the maximum operating pressures of 34 kg/cm^2 (450 psig) at the Fort Irwin pump house, and 5.5 kg/cm^2 (80 psig) at the Microwave Test Facility. Currently, one surge chamber at Fort Irwin, and two at the Microwave Test Facility are inoperative due to damaged internal rubber bladders.

The high repair and replacement costs of the damaged bladders, and technical considerations, prompted the effort to find an alternate means of handling water pressure surges.

II. Pressure Surge Chambers for Water Systems

Pressure surge chambers prevent "water hammer" in the pipeline. Water hammer is caused by either a sudden stoppage or a fast deceleration of the water flow in the pipeline. The instantaneous flow stoppage generates a pressure wave that propagates at the speed of sound, upstream from a valve (or blockage), until it reaches a larger diameter riser chamber (or tank); the pressure wave is then reflected back to the valve (or blockage) causing an increase in the line pressure. The pressure rise (dp) due to the hammer, however, can occur only if the stoppage time is equal to or less than $2L/a$ seconds; where L is the pipe length in meters (feet) and a is the pressure wave speed in water, having an average value of 1,220 m/s (4,000 ft/s).

III. Surge Pressures

Figure 1 shows two simple water systems consisting of a water tank, pipeline, and a shut-off valve. Figure 2 shows a steady-state system and Fig. 3 shows the instant when the

valve was completely closed. At the instant of blockage, the water mass, immediately adjacent to the valve, decelerates to zero. The momentum (kinetic energy) of the water is converted to a pressure rise that, in turn, compresses the water and expands the pipe walls. The kinetic energy then sets up a pressure wave traveling upstream to the end of the pipe at sonic speed a of propagation. This pressure wave takes L/a seconds to reach the tank and $2L/a$ seconds to return back to the valve. This $2L/a$ turnaround time is referred to as "critical valve closing time".

The surge phenomenon (water hammer) repeats with decreasing pressure amplitudes until the total original kinetic energy is absorbed.

The pressure rise is given as (Refs. 2 and 3):

$$dP \simeq \frac{Wav}{10g} \text{ kg/cm}^2$$

where

W = specific weight of water (1 kg/l)

v = initial velocity of water in pipe (m/s)

a = pressure wave speed averaging (1220 m/s in water)

g = acceleration due to gravity (9.82 m/s/s)

Therefore,

$$dP \simeq \frac{1 \times 1220 \times v}{10 \times 9.82} \text{ kg/cm}^2$$

$$\simeq 12.42\, v \text{ kg/cm}^2$$

The maximum surge pressure (P_{max}), at the point of blockage, with a static pressure (P_s) is:

$$P_{max} = dP + P_s \text{ (kg/cm}^2\text{)}$$

The relationship of maximum surge pressures, occurring at a given static pressure with specific flow rates, is shown in Fig. 4. Figures 5 and 6 show the basic piping configuration at Goldstone. The Appendix shows the calculations for the specific flow condition under normal mode of operations. The flow rates of 0.76 m/s (2.5 ft/s) from Fort Irwin to Venus Site and 1.35 m/s (4.5 ft/s) from Venus Site to Microwave Test Facility (MTF) could create a maximum surge pressure of about 43 kg/cm² (615 psig) and 22.3 kg/cm² (320 psig), respectively. The adverse conditions when pumping suddenly stops (power failure) with maximum reversal of flow occurring when the check valve (or any valve) is shut within the $2L/a$ time period are shown in Figs. 47, 59, and 60 of Ref. 4. At a pressure head of about 300 m (1000 ft), a flow rate of about 2.9 m/s (9.5 ft/s) can be expected. At this rate, the flow when suddenly stopped could create a surge pressure of about 67.7 kg/cm² (970 psig) (Refs. 4 and 5).

IV. Surge Control

The maximum surge pressures are minimized with the use of three 200-1 (80-gal) pressure-surge chambers at each location. The pressure-surge chambers at Fort Irwin are designed for conditions up to 100 kg/cm² (1430 psig). At MTF, the design is for 34 kg/cm² (490 psig). The existing water supply distribution design arrangement at Goldstone has the following drawbacks:

(1) Expensive: six pressure vessels rather than four relief valves, and one short 2.5-cm (1-in.) diameter line and valves.

(2) System does not warrant such equipment for relieving pressure surges because of the difficulty in stopping the flows within the critical times.

(3) Difficult to check for equalizing air/nitrogen pressure in the surge chambers.

(4) Difficult to locate leakage.

(5) Cumbersome and difficult to repair and maintain.

(6) Apparent nonavailability of replacement parts because the manufacturer is out of business.

Methods that could be used to control the surge at Goldstone are:

(1) By gradually closing the valve, the chance of water hammer is minimized. This action slows the water flow (i.e., v is reduced); hence the maximum pressure ($P_{max} = P_s + dP$) is reduced.

(2) A controlled minimal by-pass or a relief valve could be used to dissipate the excessive surge pressures to the atmosphere or into a low-pressure reservoir.

(3) A combination of the above methods may be employed.

Before deciding on an alternate method to control surge, the causes of pressure surge should be identified. The typical causes are (1) quick closing plug valves (check valve), and hydro and pneumatic emergency control valves and (2) positive displacement pumping, intermittent pumping (partial loss of suction), and interrupted pumping (power failure).

Conditions that could trigger a pressure wave in the Goldstone Deep Space Communication Complex (GDSCC) Water Supply Distribution System are when the 15 cm or 20 cm (6 in. or 8 in.) gate valves in the system are shut off quickly, or during power failure when a reversal of flow from the Venus Site tank to the Fort Irwin pump house occurs, or when the surge control valve in the discharge line is suddenly closed. For the gate valves, the critical condition is that the valves must be shut within 8.0 seconds and 8.5 seconds at Venus Site and MTF, respectively, to create pressure waves. From a practical standpoint, it is manually impossible to completely shut the valves against the system normal flow rates within the critical time period to generate water hammering. When power failure occurs, the only energy momentarily available to drive the pumps in the forward direction at Fort Irwin is the kinetic energy due to the inertia of the rotating elements. As soon as the flow stops, reversal of flow occurs, and the check valve will instantaneously close. These rapid changes inside the line cause a series of water hammer waves that may result in a head rise at the check valve from 1.1 to 1.9 times the normal head pressure (Ref. 4). The intensity of the pressure waves depend on the time the check valve shuts after power failure. Normally, the check valve shuts the instant the reverse flow occurs and with a pump pressure head of about 300 m (1000 ft) (between Fort Irwin and Venus Site tank). If friction and pipe losses are neglected, pressure waves ranging from

$$\frac{1.1 \times 300}{9.76} + 1 \simeq 35 \text{ kg/cm}^2 \text{ (500 psig)}$$

to

$$\frac{1.9 \times 300}{9.76} + 1 \simeq 60 \text{ kg/cm}^2 \text{ (860 psig)}$$

can be expected at the check valve. A maximum pressure of about 36 kg/cm^2 (520 psig) was noted when a series of power failure situations were simulated. This small rise in pressure indicates that the system at GDSCC may not be prone to high-pressure surges during power failure. The relationship between head rise and transient conditions after power failure with some typical pressures identified are shown in Figs. 47 and 59 of Ref. 4.

V. Corrective Measures

The study revealed that for pressure surges to occur, instantaneous blockage or reversal of water flow is necessary. It was determined that instantaneous blockage of full flow is not possible within the distribution system under normal operating mode. With power failure, the chances of a pressure wave in the magnitude of about 67.7 kg/cm^2 (980 psig) at Fort Irwin is possible, due to the reversed flow from the Venus tank to the pump and closure of the check valves that stops the reverse flow. However, this possibility did not seem to exist when the system was tested with a series of power failure simulations. The entire Water Distribution System could be protected from possible water hammer pressure surges with the following alternative devices:

(1) Provide a 2.5-cm (1-in.) bypass line from upstream of the valve at the inlet to the Venus Site tank a line that discharges into the tank. The scheme is as shown in Fig. 7.

(2) At the Microwave Test Facility, provide a 2.5-cm (1-in.) full-flow relief valve set to open at the 11.5 kg/cm^2 (170 psig) upstream of the valve in the supply line with the discharge of the relief valve going to the atmosphere as shown in Fig. 8.

(3) At Fort Irwin, provide three parallel 1.25-cm (1/2-in.) full-flow relief valves set to open at 36 kg/cm^2 (520 psig) downstream of pump check valves with the discharge going to the suction line of the pumps as shown in Fig. 9

In the existing design, there is, in addition to the surge chambers, a pressure surge valve at the Fort Irwin pump house; also, the various site tanks have the capability of taking some pressure surges. The use of a 2.5-cm (1-in.) bypass line and relief valves will not only adequately relieve excess hydraulic pressure rise in the system, but will also provide the added protection for the system. While there is no need for replacing the damaged surge chambers with new ones, the existing surge chambers will be used as added protection from water hammer pressure waves. The damaged chambers at Fort Irwin are to be modified and used as an air/water surge chamber without a bladder. The two damaged bladders at the Microwave Test Facilities are to be replaced with heavy-duty truck tire tubing, and the chambers be recommissioned in the system.

VI. Conclusion

The steps that are being taken to safeguard the Goldstone Water Supply Distribution System have been accepted in principal by the outside consultants (Ref. 6), Facility Engineering, and GDSCC Engineering. The savings to be realized by using the alternative devices described above amount to approximately $100k ($10k vs the $110k required to replace the inoperative surge chambers).

A test run will be carried out to ensure that the system is adequately protected from water hammer phenomena after the changes have been implemented.

References

1. *DSN Facility Status and Planning Journal*, TD505944, B Vol. (1) Section II, pp. 2-3, 2-4, Issue B, Jet Propulsion Laboratory, Pasadena, Calif., July 1, 1974, (JPL internal document).

2. Zahid, Z., "Surge Control in Water Systems," paper reprinted from *Water and Sewage Works*, Cleveland, Ohio, February, 1973 issue.

3. Linsley, Jr., R. K. and Franzini, J. B., *Elements of Hydraulic Engineering*, p. 271, McGraw Hill, New York, 1955.

4. Parmakian, J., *Waterhammer Analysis*, pp. 74-76, 93-95, Dover Publication, New York 14, New York, 1955.

5. *Cameron Hydraulic Data*, Edited by Westaway, C. R. and Loomis, A. W., p. 3-21, Ingersol-Rand, Woodcliff Lake, N. J., 1977 Edition.

6. *Alternate Recommendations for Water System Surge Chambers*, Report by Architects and Engineers Collaborative, North Figueroa St., L. A., CA. 90041, January 29, 1980.

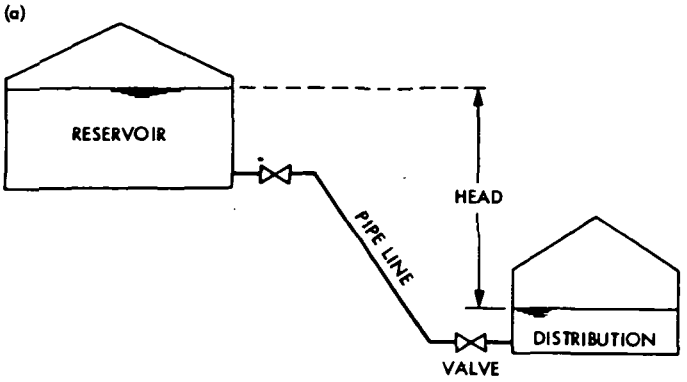

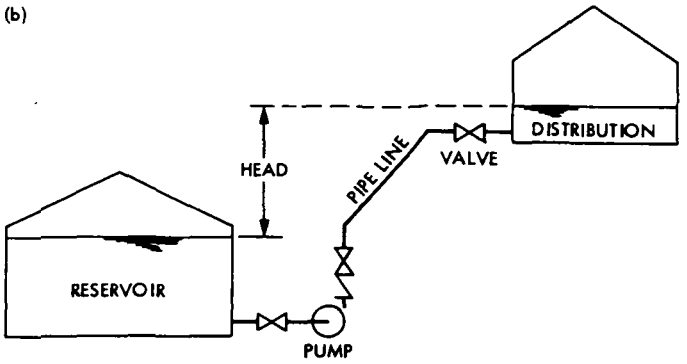

Fig. 1. Simple water supply distribution systems: a) gravity-fed system; (b) pump-fed system

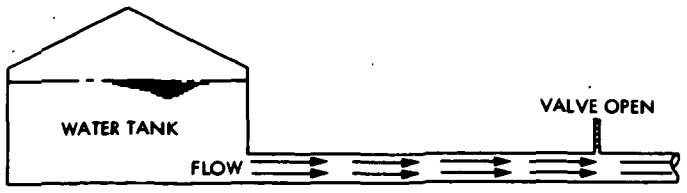

Fig. 2. Steady-state condition

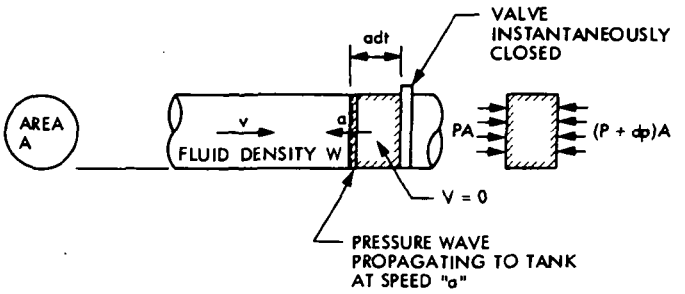

Fig. 3. Sudden stoppage of water flow (creation of water hammer)

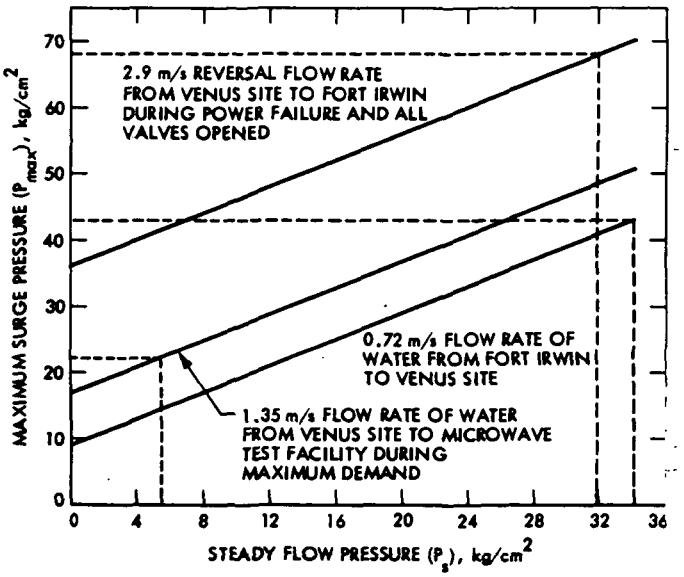

Fig. 4. $P_{max} = dP + P_s$

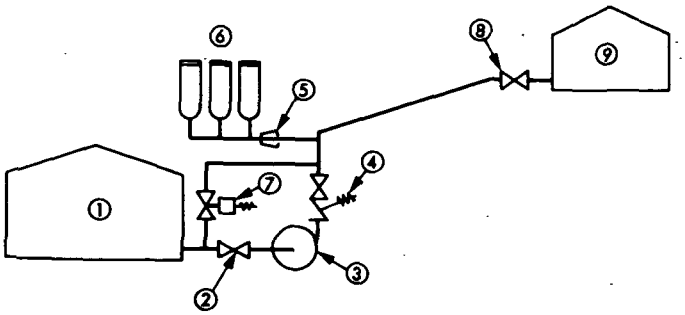

① FORT IRWIN TANK
② 20-cm GATE VALVE
③ MULTISTAGE PUMPS
④ 15-cm ANGLE GLOBE PRESSURE OPERATED VALVE
⑤ ENERGY ABSORBING ORIFICE
⑥ SURGE PRESSURE CHAMBERS
⑦ PRESSURE SURGE CONTROL VALVE
⑧ 15-cm GATE VALVE
⑨ VENUS SITE TANK

Fig. 5. Water supply from Fort Irwin to Venus Site tank

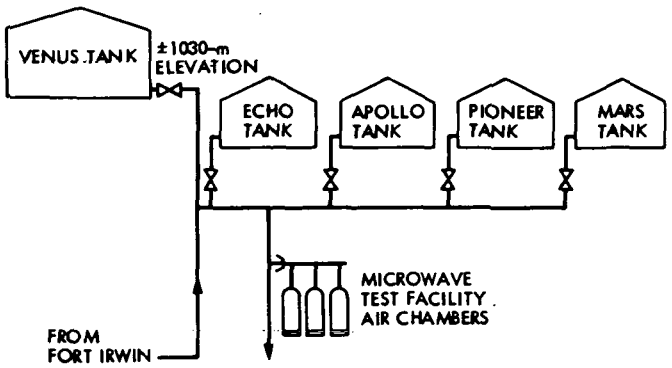

Fig. 6. Gravity-fed water supply distribution at GDSCC

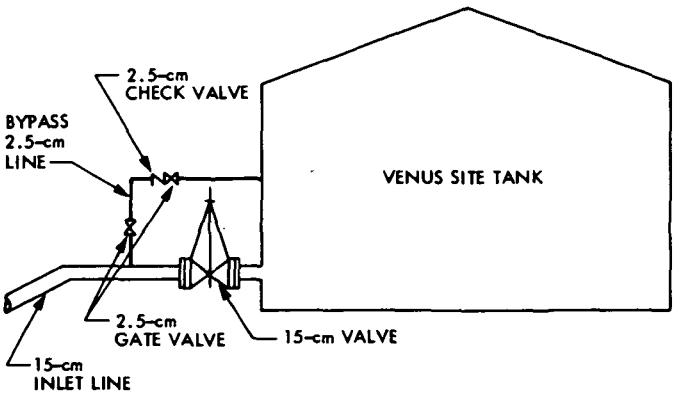

Fig. 7. 2.5-cm bypass line at inlet to Venus Site tank

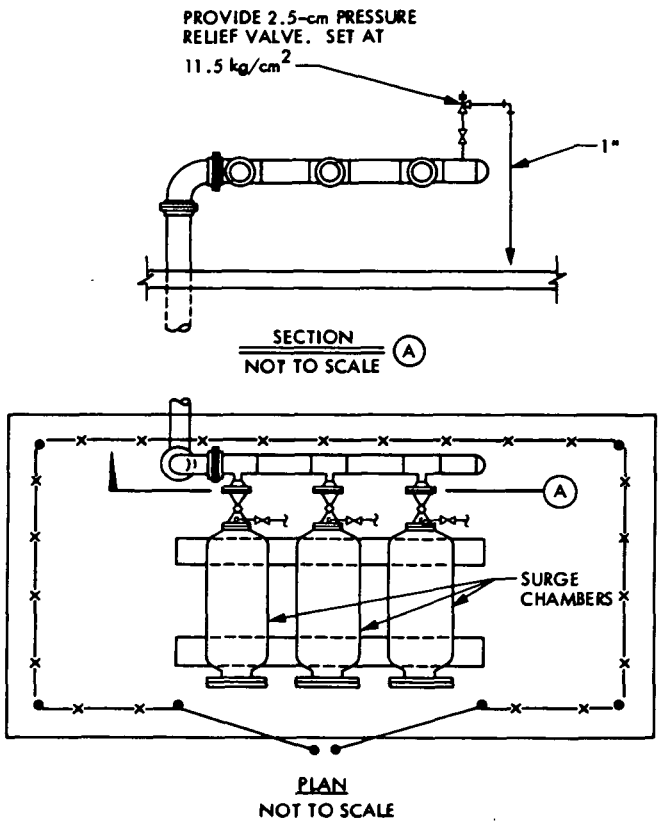

Fig. 8. MTF Station surge chambers

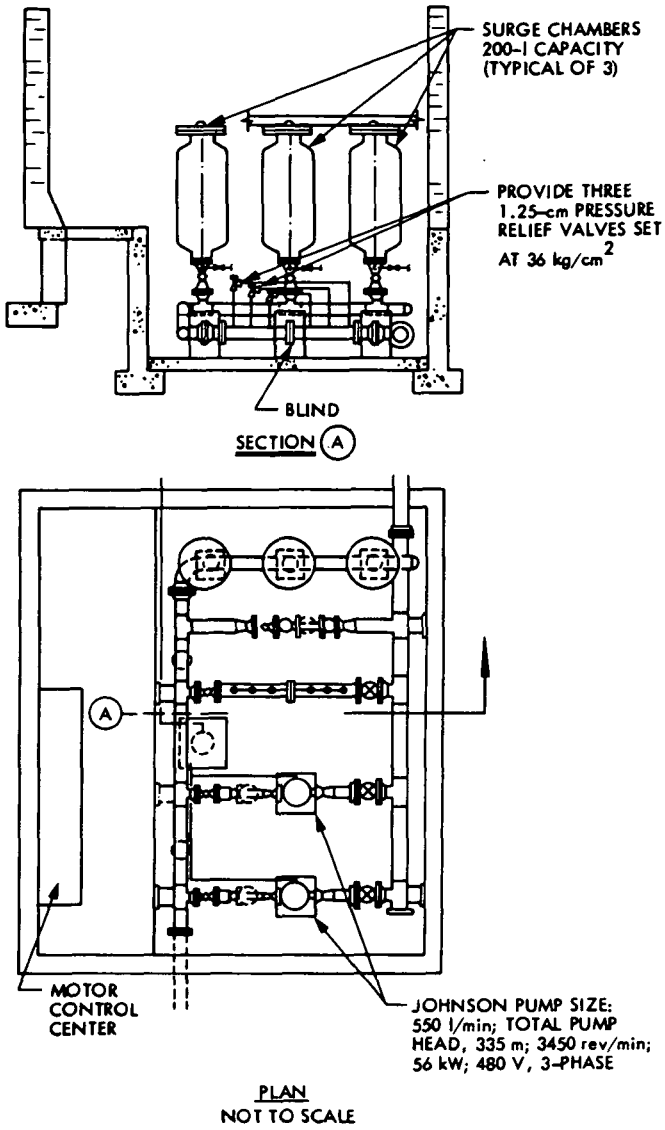
SURGE CHAMBERS 200-l CAPACITY (TYPICAL OF 3)
PROVIDE THREE 1.25-cm PRESSURE RELIEF VALVES SET AT 36 kg/cm2
BLIND
SECTION (A)
A
MOTOR CONTROL CENTER
JOHNSON PUMP SIZE: 550 l/min; TOTAL PUMP HEAD, 335 m; 3450 rev/min; 56 kW; 480 V, 3-PHASE
PLAN
NOT TO SCALE

Fig. 9. Booster pumps station at Fort Irwin

Appendix
Calculation for Water Hammer Analysis

From Figs. 5 and 6,
Basic Data and Assumptions:

Pump maximum discharge	34 kg/cm^2	(490 psig)
Average pumping rate	570 l/min	(150 gal/min)
	9.5 l/s	(2.5 gal/s)
Fort Irwin tank water level	7.6 m	(25 ft max)
Fort Irwin tank elevation	760 m	(2400 ft)
Venus tank water level	6.5 m	(20 ft max)
Venus tank elevation	1030 m	(3400 ft)
Discharge line outside diam.	15 cm	(6 in.)
Discharge line inside diam.	13 cm	(5 in.)
Fort Irwin to Venus pipe length	4.82 km	(3 mi)
Cross section of inside diam.	133 cm^2	(0.1364 ft^2)
One gallon water	3.7851 l	(0.1337 ft^3 water)
Pressure at MRF air	5.5 kg/cm^2	(80 psig)
Venus to MTF pipe length	5.15 km	(3.2 mi)
Max flow occurs when three 6.3-cm (2.5-in.) fire hoses are in use at 6 l/s each	18 l/s	(5 gal/s)

Calculations:

Flow velocity $= \dfrac{\text{volume/s}}{\text{cross-section area of pipe}}$ m/s

Average pump discharge velocity $= \dfrac{9.5 \times 1000}{133 \times 100}$ m/s

$= 0.72$ m/s (2.5 ft/s)

Average discharge velocity at MTF $= \dfrac{18 \times 1000}{133 \times 100}$ m/s

$= 1.35$ m/s (4.5 ft/s)

With power failure, there is the possibility of flow from the Venus Site Tank to the Fort Irwin tank; if all valves remain opened, the reversal flow rate for a 13-cm (5-in.) inside diam. pipe with 300-m (1000-ft) hydraulic head is about 2230 l (590 gal) per min or a flow velocity of 2.9 m (9.5 ft) per s.

Critical Time:

Time period in which the flow is stopped creating water hammer $= \dfrac{2 \times \text{length of pipe}}{\text{speed of pressure wave}}$ s

For pump to Venus tank $= \dfrac{2 \times 4820}{1220}$ s

$= 7.9$ s

$\simeq 8.0$ s

For Venus tank to MTF $= \dfrac{2 \times 5150}{1220}$ s

$= 8.44$ s

$\simeq 8.5$ s

Static Pressures (P_s):

Pressure at upstream of Venus tank gate valve is ~6.5 m (20 ft) water $= \dfrac{6.5}{9.76} + 1$ kg/cm^2

$= 1.67$ kg/cm^2 (24 psig)

Pressure at booster pumps with ~300 m (1000 ft) water $= \dfrac{300}{9.76} + 1$ kg/cm^2

$= 31.73$ kg/cm^2 (450 psig)

Surge Pressure (P_{max}):

When valves are shut within the critical time of 8.0 s at Venus tank gate valve P_{max} $= (12.42 \times 0.72) + 1.67$ kg/cm^2

$= 10.6$ kg/cm^2 (150 psig)

At booster pump P_{max} $= (12.42 \times 0.72) + 34$ kg/cm^2

$= 43$ kg/cm^2 (615 psig)

At booster pump, any discharge line valves during power failure P_{max} $= (12.42 \times 2.9) + 31.73$ kg/cm^2

$= 67.7$ kg/cm^2 (970 psig)

At MTF air chambers P_{max} $= (12.42 \times 1.35) + 5.5$ kg/cm^2

$= 22.3$ kg/cm^2 (320 psig)

N80-33445

Planetary Radar

R. M. Taylor
Deep Space Network Operations Section

This article reports on the radar astronomy activities supported by the Deep Space Network during June, July, and August 1980. The planetary bodies observed were Venus, Mercury, and the asteroid Toro. Data were obtained at both S- and X-band, and the observations were considered successful.

The high power S- and X-band transmitters at the Goldstone 64-m station were used to support five different radar observations during this period:

(1) Venus S- and X-band alternating.

(2) Venus tristatic.

(3) Venus rain.

(4) Mercury bistatic.

(5) Asteroid Toro.

I. Venus S- and X-Band Alternating

This was the first time that this particular experiment had been tried. The objective is to do ranging on Venus at two different wavelengths, one of which is not significantly absorbed by the planet's atmosphere and the other which is absorbed greatly by the atmosphere, e.g., only 10 percent returns.

To be successful, it is essential that the ranging for both wavelengths be done on the same day so that the same "windows" of atmosphere are viewed. Also necessary for this absorption measuring experiment is the accurate calibration of station operating parameters such as system noise temperature, transmitter output powers, and antenna pointing accuracy.

This differential absorption observation attempts to utilize the fact that the synodic period of Venus is very nearly in synchronism with the orbital period and so there should be a high correlation between the planetary figure and the orbital parameters. If the planet could be monitored for a full rotation, this would yield continuity of coverage and closure. How does this help?

If the atmospheric constituents are known, then ranging can be done very accurately. It may be possible to measure and monitor the local surface gravity. There is very little known to date about the lowest few kilometers of atmosphere surrounding the planet. This experiment could help to "calibrate" the atmosphere and determine the absorption of the clouds.

There are a couple of technical problems in the way of total success of the experiment, namely:

(1) The X-band transmitter has only one klystron final amplifying tube at this time, the second one being with the manufacturer undergoing repair, so the output power is degraded by 3 dB.

(2) All the X-band spectra are not accumulated because the XDS 930 computer has insufficient memory, which appears as a lack of bandwidth and is overcome by folding over these X-band spectra.

In addition, due to scheduling difficulties, it was not possible to obtain coverage of one full planetary rotation, but the data acquisition was considered fairly successful and, at the present time, analysis and calibration programs are being developed. There are no definite answers from this first Differential Absorption Experiment. How well the algorithms work will be tested soon and the experiment procedures will become less "experimental." After looking at just a couple of segments of data, the planet appears incredibly smooth.

In the future, we hope to calibrate the atmospheric profile of Venus, determine some of the surface properties of the planet, and even detect debris scale size differences. In 1981 and 1982 there is reason to hope that the scheduling pressures will abate sufficiently to permit a full rotation to be observed.

This Deep Space Network capability at the Goldstone 64-m antenna station is the only radar calibrated well enough to give the power sensitivity accuracy required by this experiment.

II. Venus Tristatic

This activity utilizes, in addition to the high-power, S-band transmitter at the Goldstone 64-m, antenna station, the S-band receiving systems at the Goldstone 64-m and the two 26-m antenna stations. The received echoes are down-converted in frequency and modulated on to a microwave channel from the remote 26-m antenna stations to the 64-m antenna station for common formatting, timing, and recording.

The objective is to measure relatively high-resolution simultaneous altitudes and reflectivities to further understand the geology of the planet.

The altimetry is accurate enough to detect small volcanoes not seen by the Pioneer-Venus spacecraft. Pioneer pixel resolution is a 30-km square, whereas tristatic radar can resolve to an 8-km square. Because the altimetry is so good, it is possible to see isostatic compensation of the surface; for example, the outer slopes of a couple of volcanoes appear to be compensated. Questions that arise are: How big are the slopes? How well are they compensated? How smooth?

Data for this experiment, which has been going for several years, are now coming in at handling rate and modelling can start. For the first time, good reflectivity and altimetry data are being acquired simultaneously.

The reflectivities are very dependent upon the area of the surface and can be used to determine something of the surface roughness and dielectric constant of the surface material. During this series of experiments, it was hoped to study the effects of angular dependence on the surface and to measure accurately the position of features, using their repeatability to help refine the spin axis. On June 14, a crater was observed exactly as it had been observed in 1972; these are the longest radar repeat scans. The exactitude and eight-year span takes care of the orbital geometry in these measurements. It may be possible to increase resolution by optimization of doppler resolution.

The Deep Space Network is the only network in the world having three systems with adequate sensitivity and baselines to perform this experiment.

In the future, it is hoped to achieve resolution improvement down to 1-km squares. The technological improvements necessary to support science of this quality include a high-speed computer, an array processor, and a high-speed data recorder.

III. Venus Rain

This activity utilizes the facilities of the Goldstone 64-m antenna station only, including the high-power X-band transmitter, which is temporarily capable of outputting only half its rated power because one of the two final amplifier klystron tubes is at the manufacturer's for repair.

The objective of this experiment is to determine if there is any rain in the upper atmosphere of Venus and, if there is, what can be determined about its distribution size and backscattering properties?

It is a difficult experiment because Venus scatters back an immense amount of power on its own account. What is needed is the use of a superspectrum analyzer in the hope of detecting "stuff" (back-scattered power) at the skirts of the planet, although our "stuff" is dwarfed by the planet's "stuff". Scattering from the drops of rain is predicated to have a Rayleighian distribution, which would indicate very small drops; therefore, the shortest wavelength available, presently X-band, is used.

During this series of observations, unexplained power has been detected at the sides of the spectrum; it is too early to state that this is rain; extensive calibrations and more development work are being done to determine the cause of this power.

In the future it is planned to do more of the same type of experiments, and the chances of detection would be enhanced by improving the X-band capability, i.e., restoring the second klystron tube, and by the introduction of a K-band capability.

IV. Mercury Bistatic

This experiment utilized the S-band receive capabilities of the Goldstone 64-m antenna station and the Goldstone 26-m antenna Research and Development station as well as the high-power S-band transmitter.

The objective of this activity was to acquire sufficient data to be able to resolve the planet's spin vector. The spin vector is not known well, the rotation rate being fairly well defined, but the pole direction is only known to within ±6.5 deg. It is hoped that the pole is perpendicular to the orbital plane, but it will be exciting to try and explain it, should it prove to be otherwise. The spin vector is assumed perpendicular to the orbital plane.

The method used is measurement of the velocity and direction of the diffraction pattern received at earth, at two stations operating as an interferometer, using a continuous wave transmission. Early results indicate that interference fringes were found and the correlation function is more flat-topped than had been expected.

In the future, it is proposed to do the same experiment using two techniques: (1) collect old data with limb-to-limb bandwidth measurements and (2) to improve X-band sensitivity, collect more limb-to-limb data, then attempt to fit these data. Possibly an improvement could be effected in the use of the interferometer, e.g., could doppler data yield more than continuous wave?

The Deep Space Network offers the advantage of long observing periods in experiments of this type, and many more such observations will be requested in the future.

V. Asteroid Toro

This asteroid is a small one that was radar detected in 1972. It returns to earth's vicinity every eight years or so. The activity involves only a single station, that being the Goldstone 64-m antenna station including the high-power X-band transmitter and two receiving systems, each looking at a different polarization.

The objective of radar probes of asteroids is to determine what they are, where they come from, and what are they made up of. Optical observations of asteroids only reveal information about the first few microns of the surface. Radar, we hope, will be able to tell more by taking advantage of the close approach to beam pulses of energy at the body and then track the echoes. Asteroids may be left-over pieces of comets, just big pieces of "clinker" with all the volatiles boiled out. One objective is to see in what ways they differ from terrestrial surfaces and the surfaces of the moons of Jupiter.

These bodies are moving so fast at closest approach that, to track them, an ephemeris-tuned oscillator must be used. Such an oscillator exists at the Goldstone 64-m antenna station and it is to be found in the Advanced Systems area; however, for this particular observation, dual polarization was required, and this capability exists only in the operational area of the station, thus it was necessary to make some engineering changes to support the activity. These changes were planned and configured very smoothly, but the attempt to run two polarizations encountered another problem; it takes about 30 seconds to refocus the subreflector each time. This time was lost from each echo, quite an impact with a round-trip light time of the order of 150 seconds.

The experiment requires the use of X-band because asteroid echoes are incredibly weak. The cross-polarized component is expected to be about one-quarter the strength of the normal component. It is essential to have both klystron tubes functional for the next time such an observation is scheduled.

In the future, it is desirable to probe as many close-passing asteroids as possible and, eventually, as the technique and technology improves, to study comets by the same means. This activity may require fast scheduling and reaction time by the Deep Space Network as exemplified in the probe of comet 1979L Bradfield earlier in the year.

The advantages of using Deep Space Network facilities for this work are in tracking time (one evening is sufficient to observe a full rotation of most asteroids) and the shorter wave length of X-band.

In summary, a very successful season has been enjoyed in data acquisition for this activity. A total of some 700 hours of support by stations left some data processing to be done and results and publications are eagerly awaited.

N80-33446

Deep Space Network Energy Program

S. E. Friesema
TDA Technology Development Office

If the Deep Space Network is to exist in a cost-effective and reliable manner in the next decade, the problems presented by international energy cost increases and energy availability must be addressed. The Deep Space Network Energy Program has been established to implement solutions compatible with the ongoing development of the total network.

I. Introduction

The question of energy availability and burden of increased energy cost is affecting the Deep Space Network (DSN) just as it is every segment of our nation's activities. Each of the three DSN complexes has an average base power requirement of between 1.5 and 2.0 megawatts. During 1979, the cost of fuel to supply this power more than doubled in one day at Madrid, escalated approximately 80 percent in eight months in Australia, and increased 25 percent in one month at Goldstone, California. While each of these conditions may not be repeated in the near future, there is little question that costs will continue to escalate and the finite available resources will be placed under significant additional strain.

While these recent developments have heightened concern within the DSN, they have also added significant impetus to expanding and accelerating the already existent DSN Energy Program. This program, officially begun in 1976, actually had its roots in studies and energy conservation activities begun in early 1974.

II. Goals and Objectives

It is the goal of this program to support national energy policies, such as the President's recent conservation directive. In addition, the DSN must manage NASA energy resources so that implementation of energy reduction procedures and solar power augmentation equipment minimizes life cycle costs and keeps them in balance with other costs. The goals are being achieved by tasks supporting long term objectives. These objectives are:

(1) To save money by cost-effective and operationally acceptable energy conservation implementation.

(2) To carry out renewable energy augmentation demonstration projects to provide data on existing low risk technology and its applicability to the DSN environment.

(3) To implement solar energy augmentation when new technology meets the DSN Energy Program requirements for reliability and cost effectiveness.

(4) To implement an energy data management system.

The objectives of the program are being put into effect under a phased schedule, with the Goldstone Deep Space Communications Complex (GDSCC) in California generally preceding the overseas stations.

III. DSN Energy Characteristics

The DSN is, in fact, a network of decentralized communities (Fig. 1). Each complex represents a significantly different set of political, socioeconomic, and environmental conditions. In the application of solar power generation solu-

tions, these communities present three uniquely different distribution problems.

The GDSCC creates the question of centralized vs decentralized power as a result of having an existing power grid. However, decentralized power generation capability also exists by virtue of backup power generators located at each site. The question requires careful examination both from operational reliability and maintenance requirements standpoints.

In Australia, the conjoint Deep Space Stations 42 and 43 will be similar to GDSCC if a proposed power grid is built to replace existing separate diesel generators. However, Deep Space Station 44 resides in a national preserve area, and present information indicates no electric power lines will be permitted into that facility. Distributed power capability is a necessity.

In Spain, the complex is also considering the introduction of a power grid. At this complex, the question of extending it beyond the conjoint Deep Space Stations 61 and 63 to Deep Space Station 62 is posed for a different reason. The results of energy conservation, including the introduction of waste heat utilization at DSS 62, have been so successful (a 50 percent reduction of power requirements) that the introduction of the electric power may have questionable merit. If the waste heat locally available is not used, additional energy must be provided to replace this source. Several interesting solutions are apparent.

The DSN is a fascinating distributed environment well oriented to verifying concepts of both centralized and distributed methodology in an effort to supply power from renewable sources. However, as a result of its primary commitment of communicating with deep space vehicles, constraints limit the DSN Energy Program to investigative studies, conservation procedures and modifications, and low risk exploratory demonstrations of new technology utilizing only proven equipment. Within these constraints the program still has many innovative aspects, some of which are discussed below.

IV. Program Activities

The program has completed studies or has under investigation a full range of alternative energy conservation and power augmentation projects. The projects developed to support energy conservation activities are generally near term; that is, they are planned for implementation within the next five years since this technology is furthest in its commercial development. The projects planned for power augmentation, such as photovoltaic and solar thermal electric generators, are generally long term and planned to begin in a phased implementation about 1984-1985. The exception to these long-range plans would be the implementation of earlier solar power generation capability with funding provided by other government agencies from presently authorized programs, such as the Federal Photovoltaic Utilization Program and the Solar in Federal Building Demonstration Program. Proposals are submitted as part of a NASA package, with the proposal data derived from DSN studies and energy planning. An implementation of this type at Goldstone could involve the augmentation of existing power from the Southern California Edison Company grid. This would be followed by a major solar power generation project patterned after the earlier prototype.

Hybrid systems using a variety of solar power generating techniques are also under investigation. Among these, a hybrid biogeneration and conversion process holds promise as a long-term solution to the alternate fuel problem created by the use of transportation vehicles and backup power generators. Biodegradable garbage and sewage would supply the base material for aquatic biomass ponds, and anaerobic digesters would provide the methane to be stored as a major source of fuel. This method of energy generation could provide up to 18 percent of anticipated energy requirements at Goldstone in 1985. One of the more exciting features of the methane generation capabilities would be its anticipated utilization in fuel cells and the inherent increase in conversion efficiency derived from this use. The study of fuel cell status and the applicability of fuel cells to the DSN environment is to be completed by the end of September 1980.

An engineering study to evalute the potential of a photovoltaic array for direct electric power at Goldstone was completed in 1979. In addition, a proposal to study the Canberra, Australia, site and its photovoltaic array potential was submitted to the Department of Energy's Photovoltaic Utilization Program.

A proposal for a solar still at GDSCC to produce distilled water has been accepted by the Department of Energy under the Solar in Federal Buildings Program (SFBP). The system will provide cooling water for the klystrons at DSS 13 and DSS 14.

Wind data from the Goldstone site indicates that the potential exists for constructing low-speed windmills. These could be used to pump water or to generate electric power for feeding the existing power grid at Goldstone.

Each area of study has a potential for decreasing DSN dependence on fossil fuels. It is highly improbable that any one method of power augmentation will be adequate alone. But, a balanced system, utilizing multiple renewable sources of energy, may be capable of meeting the majority of DSN energy needs.

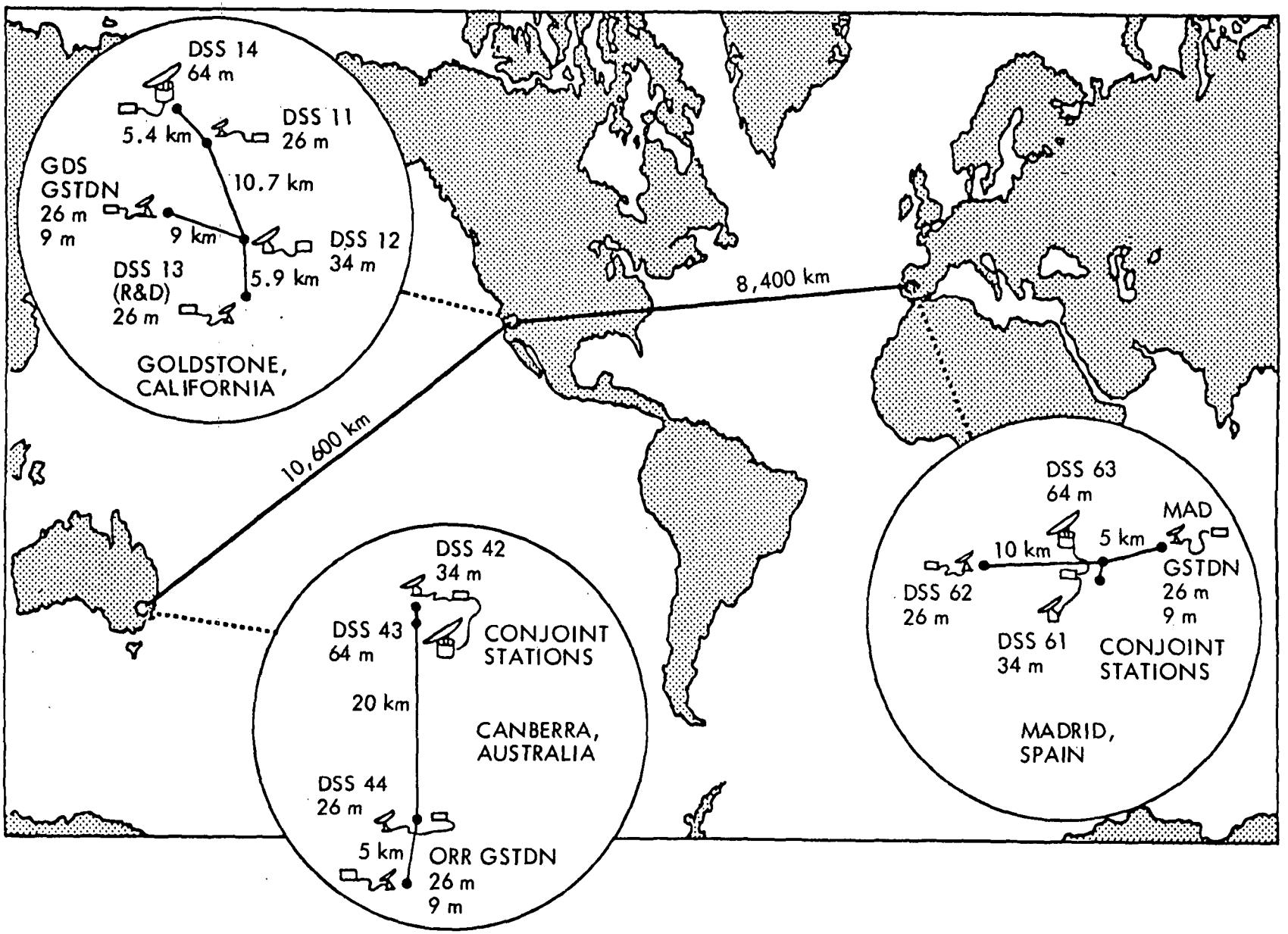

Fig. 1. Deep Space Network Complexes

SETI Bibliography

I. Comprehensive Listing Through February 1977

A Bibliography on the Search for Extraterrestrial Intelligence, NASA Reference Publication 1021, NASA, Scientific and Technical Information Office, March 1978.

II. Open Literature and TDA Progress Report Update Through July 1980

A. Open Literature

Billingham, J., Oliver, B. M., and Wolfe, J. H., "A Review of the Theory of Interstellar Communication," *Acta Astronautica*, 6, No. 1-2, pp. 47-57, 1979.

Black, D., Tarter, J., Cuzzi, J., Conners, M., and Clark, T., "Searching for Extraterrestrial Intelligence: The Ultimate Exploration," *Mercury*, 6, pp. 3-7, 1977.

Cocconi, G., and Morrison, P., "Searching for Interstellar Communications," *Nature*, 184, pp. 844-846, 1959.

Edelson, R., "At the Technological Frontier: The JPL Search for Extraterrestrial Intelligence," *Mercury*, 6, pp. 8-12, 1977.

Edelson, R. E., "An Observational Program to Search for Radio Signals from Extraterrestrial Intelligence Through the Use of Existing Facilities," *Acta Astronautica*, 6, No. 1-2, pp. 129-143, 1979.

Edelson, R. E., "An Experiment Protocol for a Search for Radio Signals of Extraterrestrial Intelligent Origin in the Presence of Man-Made Radio Frequency Sources," *Acta Astronautica*, 6, No. 1-2, pp. 145-162, 1979.

Gulkis, S., Olsen, E. T., and Tarter, J., "A Bimodal Search Strategy for SETI," in *Strategies for the Search for Life in the Universe*, D. Reidel (in press).

Healy, T. J., Seeger, C. L., and Stull, M. A., "On the Design of a Post Processor for a Search for Extraterrestrial Intelligence (SETI) Systems," *Acta Astronautica* (in press).

Morrison, P., Billingham, J., and Wolfe, J., "The Search for Extraterrestrial Intelligence: SETI," *NASA Publication SP-419*, 1977.

Morrison, P., Billingham, J., and Wolfe, J. H., "The Search for Extraterrestrial Intelligence – SETI," *Acta Astronautica*, 6, No. 1-2, pp. 11-31, 1979.

Murray, B., Gulkis, S., and Edelson, R. E., "Extraterrestrial Intelligence: An Observational Approach," *Science*, 199, pp. 485-492, 1978.

Oliver, B. M., "Project Cyclops," *NASA Publication CR 114445*, 1972.

Oliver, B. M., "Rationale for the Water Hole," *Acta Astronautica*, 6, No. 1-2, pp. 71-79, 1979.

Peterson, A. M., Narasimba, M., and Narayan, S., "System Design for a Million Channel Digital Spectrum Analyzer (MCSA)," in *Proceedings IEEE 13th Asilomar Conference on Circuits, Systems, and Computers*, IEEE Cat. No. 79 CH 1468-8C, pp. 14-17, 1980.

Seeger, C. L., "Strategic Considerations in SETI, and a Microwave Approach," *Acta Astronautica*, 6, No. 1-2, pp. 105-127, 1979.

Seeger, C. L., "The Recognition of Extraterrestrial Artificial Signals," in *Proceedings IEEE 13th Asilomar Conference on Circuits, Systems, and Computers* IEEE Cat. No. 79, ch 1468-8C, pp. 18-22, 1980.

Tarter, J., and Zuckerman, B., "Is Anyone Out There?," *Nature*, 281, pp. 528, 1979.

Tarter, J. C., "The Search for Extraterrestrial Intelligence," in *Enclyclopaedia of the 21st Century*, Macmillan Press (in press).

Tarter, J., and Zuckerman, B., "Strategies for the Search for ETI through Radiowaves: Programs in the U.S.A. and Canada," in *Strategies for the Search for Life in the Universe*, D. Reidel (in press).

Tarter, J., Cuzzi, J., Black, D., Clark, T., and Drake, F., "SETI: High Sensitivity Searches at NASA with High Speed Tape Recorders," *Acta Astronautica* (in press).

Tarter, J., Cuzzi, J., Black, D., and Clark, T., "A High-Sensitivity Search for Extraterrestrial Intelligence at 18 cm," *Icarus 42*, pp. 136-144, 1980.

B. TDA Progress Report

Berman, A. L., "The SETI Observational Plan," in *The TDA Progress Report 42-57*, Jet Propulsion Laboratory, Pasadena, Calif., pp. 9-15, June 15, 1980.

Edelson, R. E. and Levy, G. S., "The Search for Extraterrestrial Intelligence: Telecommunications Technology," in *The TDA Progress Report 42-57*, Jet Propulsion Laboratory, Pasadena, Calif., pp. 1-8, June 15, 1980.

Morris, G. A., and Wilck, H. C., "JPL 2^{20} Channel 300 MHz Bandwidth Digital Spectrum Analyzer," in *The DSN Progress Report 42-46*, Jet Propulsion Laboratory, Pasadena, Calif., pp. 57-61, April 15, 1978.